

Elucidating Microstructural Contributions to Hydrogen Embrittlement Susceptibility in Ni-base Alloys

A Dissertation

Presented to

the faculty of the School of Engineering and Applied Science

University of Virginia

in partial fulfillment
of the requirements for the degree

Doctor of Philosophy

by

Zachary Daniel Harris

December 2018

APPROVAL SHEET

This Dissertation
is submitted in partial fulfillment of the requirements
for the degree of
Doctor of Philosophy

Author Signature: Zachary Harris

This Dissertation has been read and approved by the examining committee:

Advisor: James Burns

Committee Member: Sean Agnew

Committee Member: John Scully

Committee Member: Richard Gangloff

Committee Member: Patrick Hopkins

Committee Member: Brian Somerday

Accepted for the School of Engineering and Applied Science:



Craig H. Benson, School of Engineering and Applied Science

December 2018

Dedication

This dissertation is dedicated to my grandparents, Anita (1933-2016) and Hubert Harris. Grandpa, thank you for always reminding me about the value of integrity, work ethic, and a can-do attitude. I am incredibly grateful for your love and encouragement – it is an honor to be your grandson. Nini, thank you for genuinely loving me with all of your heart and for always encouraging me to chase bigger dreams. I miss you so much, but I can feel you watching over me and I hope that I have made you proud.

Summary

Despite over a century of study, hydrogen-induced premature failure of structural metals continues to negatively impact critical industries spanning the aerospace, marine, transportation, and energy sectors. Efforts to mitigate this deleterious effect are undermined by an incomplete understanding of the microscale processes governing hydrogen-induced degradation. Recent literature has posited that the governing mechanism for hydrogen embrittlement is hydrogen-induced decohesion of grain boundaries principally driven by hydrogen-deformation interactions. However, there is a lack of experiments which quantitatively establish the predominant contribution of hydrogen-deformation interactions to hydrogen-induced intergranular cracking. Additionally, the extension of such mechanisms into more complex, industrially-relevant alloys is hindered by the uncertain contribution of alloy metallurgy to hydrogen-induced degradation. Numerous studies have attempted to ascertain the relative influence of different microstructural features on hydrogen embrittlement susceptibility, with parameters of interest being: grain boundary impurity content, grain size, grain boundary character, yield strength, slip character, and hydrogen-metal interactions. However, isolating the contribution of a particular microstructural feature is complicated by the likelihood that several parameters impact susceptibility, demonstrating the need for a study in which the variation in numerous microstructure features is carefully controlled.

The objective of this dissertation is to address these knowledge gaps by focusing on the following research questions:

- To what extent do hydrogen-deformation interactions govern hydrogen-induced intergranular fracture?
- What influence do microstructural parameters have on hydrogen embrittlement susceptibility?
- What is the role of important metallurgical features in the context of proposed microscale mechanisms governing hydrogen embrittlement?

Towards this end, the dissertation is divided into two separate research thrusts. First, the contribution of hydrogen-enhanced deformation to the conditions required for hydrogen-induced intergranular fracture is assessed using polycrystalline Ni. By quantitatively evaluating the relative contribution of hydrogen-deformation interactions, this study will better inform the extent to which dislocation-based factors like bulk slip morphology may contribute to embrittlement susceptibility in more complex alloys. Second, a series of studies which seek to evaluate the role of microstructural variation on hydrogen environment-assisted cracking susceptibility are completed using a model Ni-base superalloy, Monel K-500. Differences in fracture morphology, crack growth rates, and threshold stress intensity across five engineering-grade

heats of Monel K-500 are correlated with observed variations in metallurgy and hydrogen-metal interactions, thereby enabling a broad assessment of the metallurgical features which may contribute to an alloy's intrinsic resistance to embrittlement. Based on these experiments, targeted heat treatment variations are employed on a single heat of Monel K-500 to produce four aging conditions which result in carefully controlled differences in bulk slip morphology, grain boundary sulfur content, and yield strength. Correlation of these microstructural differences with measured crack growth rates and threshold stress intensities indicates that bulk slip morphology plays a prominent role in hydrogen embrittlement susceptibility in Monel K-500. The effect of hydrogen on bulk slip processes across the aging conditions is then explored through a detailed assessment of work hardening behavior in the presence and absence of hydrogen, thus providing mechanistic insight on how hydrogen may alter deformation processes. In particular, hydrogen is observed to induce the particle shearing-to-looping transition in Monel K-500 at a smaller precipitate size, suggesting that hydrogen perceptibly affects bulk slip processes. Given this importance of bulk slip morphology, as well as the evidence for hydrogen-modified dislocation-precipitate interactions, these results motivate the examination of the deformation proximate to the crack path so as to mechanistically evaluate the contribution of these processes to hydrogen-induced fracture. Towards this end, the dissertation concludes with the development and initial results of a multiple length-scale characterization strategy which couples (1) broad-scale electron backscatter diffraction (EBSD), (2) high-resolution EBSD (HR-EBSD), (3) focused ion beam (FIB) sample preparation, and (4) scanning transmission electron microscopy (STEM) techniques to assess the near-fracture surface deformation.

Considering the practical impact of the current dissertation, results indicate that an over-aged heat treatment can significantly reduce the embrittlement susceptibility of Monel K-500 without compromising strength, thereby providing a possible pathway for reducing the observed heat-to-heat variation in hydrogen-assisted cracking behavior. Additionally, the database of cracking kinetics and microstructural data generated for six material heats of Monel K-500 in this dissertation can be utilized to inform improvements in the Monel K-500 material specification. Considering scientific impacts, the direct assessment of the relative contribution of mobile hydrogen-deformation interactions to intergranular cracking provides critical insights into the operative microscale mechanisms governing embrittlement susceptibility. This work also demonstrates that hydrogen can modify dislocation-precipitate interactions; improved understanding of these interactions could be utilized as the scientific basis for designing hydrogen-resistant precipitation-hardened alloys. Finally, a multiple length-scale characterization strategy was developed to provide a comprehensive evaluation of the deformation proximate to the fracture surface. This approach is expected to provide additional insights into the microscale processes governing hydrogen embrittlement, which can then be utilized to improve current models for hydrogen-assisted cracking.

Acknowledgements

First, I would like to sincerely thank my dissertation advisor, Prof. James Burns. I can only imagine how challenging I must have been to have as a student, but know that I will always hold dear the lessons that you taught me. In particular, your commitment to excellence and integrity are two qualities that I will always strive to emulate. I am incredibly grateful for your ready encouragement of my curiosity, even when it led nowhere, and for your patience, as I don't know how many times I barely made a paper (or thesis) deadline! I have grown tremendously as a scientist under your tutelage and I am extremely thankful for your support, encouragement, and advice over the past few years. It has truly been an honor and privilege to be your graduate student.

I would also like to thank my dissertation committee: Prof. Sean Agnew, Prof. John Scully, Prof. Richard Gangloff, Prof. Patrick Hopkins, and Dr. Brian Somerday. I am tremendously fortunate to have been mentored by such an outstanding collective of scientists and people. In particular, I want to thank Prof. Agnew for his assistance in understanding deformation behavior and Prof. Scully for his assistance with understanding hydrogen-metal interactions and environment-assisted cracking. I owe a debt of gratitude to Prof. Gangloff and Dr. Somerday, who have both effectively served as co-advisors throughout my dissertation. Prof. Gangloff, I learned a tremendous amount from our discussions and I will always value the lessons that you taught me – thank you for always encouraging me to think bigger. Brian, thank you for giving me a chance as an intern all those years ago – I never would have learned about environmental cracking without that opportunity. My appreciation for your encouragement, support, and advice as I worked on my dissertation cannot be overstated.

I have had the privilege to collaborate with many excellent institutions and scientists during my dissertation: Dr. Samantha Lawrence (LANL), Dr. Douglas Medlin (SNL), Dr. Joseph Ronevich (SNL), Dr. Chris San Marchi (SNL), Denny Paul and Dr. John Hammond (Physical Electronics, USA), Dr. Tim Ruggles (NASA Langley), and Keith Knipling (NRL). I also owe many thanks to the staff members at Sandia National Laboratories who assisted with the portion of my dissertation completed during my summer internships: Jeff Campbell, Ken Lee, Andy Gardea, Ryan Nishimoto, and Nancy Yang. Additionally, I would never have gotten far without the support of the staff at the University of Virginia: Barry Baber, Richard White, Kari Werres, Helge Heinrich, Kim Fitzhugh-Higgins, Sherri Sullivan, and Tanner Fitzgerald. Thank you for all of your support.

I am grateful to the Department of Defense – Technical Corrosion Collaboration for their financial support. Additionally, I am appreciative for additional support provided by the Alcoa Graduate Fellowship,

Volkswagen Group of North America Fellowship, Virginia Space Grant Consortium Fellowship, TMS Superalloys Scholarship, and UVA SEAS Teaching Fellowship.

To the many friends (past and present) in CESE and MSE who made graduate school such a fun experience, thank you for your encouragement, support, and friendship. In particular, I am grateful for the friendship of Jay Srinivasan, R.J. Santucci, Cam Volders, and Mary Lyn Lim. To the Burns Group, it has been a blast working with you over the past few years – thank you for helping me laugh, being there when I needed to complain, and for all your support and friendship. Graduate school wouldn't have been the same without Noelle Co, Mike McMurtrey, Ryan Donahue, Matt McMahon, Patrick Steiner, Allison Popernack, Adam Thompson, Andrew Jamieson, Luke Brown, Kristyn Ardrey, and Carly Cocke. In particular, Adam Thompson deserves a medal for all of the late nights we spent polishing and running microscopes.

To my family, thank you for all of your love and support. Mom and Dad, I can't put into words how grateful I am to have you as my parents – thank you for listening to my gripes, for your steadfast encouragement, and for making such an effort to come see us here in Virginia. Lastly, but certainly most importantly, I want to thank my lovely wife, Michelle, for all of her support, encouragement, and sacrifice while I pursued my graduate degree. I am so incredibly grateful for everything that you do – thank you so much for listening to my blabbering about research, for your patience when I had to run to the office to check on experiments, and for your encouragement when I was running out of steam. Words cannot adequately describe my heartfelt appreciation for you.

Table of Contents

<i>Summary</i>	<i>i</i>
<i>Acknowledgements</i>	<i>iii</i>
<i>List of Figures</i>	<i>x</i>
<i>List of Tables</i>	<i>xviii</i>
Chapter 1. Introduction and background	1
1.1. Hydrogen embrittlement – status of the problem	1
1.2. Knowledge gaps	6
1.3. Research Questions	6
1.4. Dissertation overview	7
1.5. References	7
Chapter 2. Mechanistic assessment of hydrogen-induced cracking in Ni	13
2.1. Overview	13
2.2. Introduction	14
2.2.1. Chapter objective and research questions.....	15
2.3. Experimental methods and material	15
2.3.1. Material	15
2.3.2. Mechanical Testing.....	15
2.3.3. Hydrogen Charging.....	17
2.3.4. Microscopy.....	17
2.4. Results	19
2.4.1 Testing to Failure.....	19
2.4.2. Evaluation of Intergranular Microcracks in Interrupted Specimens.....	22
2.4.3. Quantifying the Variability of Intergranular Microcrack Metrics.....	23
2.4.4. Evaluation of Deformation Microstructure and Dislocation-Grain Boundary Interactions at RT and 77 K	27
2.5. Discussion	30
2.5.1. Justification of Critical Assumptions	30

2.5.2. Quantifying the Relative Contribution of Mobile Hydrogen-Deformation Interactions to Intergranular Cracking	33
2.5.3. Mechanistic Interpretations and Comments on Current Literature	35
2.6. Conclusions	36
2.7. Suggested Future Research Directions.....	36
2.8. Acknowledgements.....	37
2.9. References	37
<i>Chapter 3. Effect of microstructural variation on HEAC of Monel K-500</i>	<i>40</i>
3.1. Overview	40
3.2. Introduction	41
3.2.1. Chapter objectives and research questions	44
3.3. Experimental methods and material	44
3.3.1. Material.....	44
3.3.2. Fracture mechanics-based environmental testing.....	46
3.3.3. Characterization.....	49
3.4. Results	49
3.4.1. Inert (dry N ₂) environment testing	49
3.4.2. Aqueous chloride electrolyte testing.....	53
3.4.3. Characterization of grain size and grain boundary character distribution.....	60
3.4.4. Characterization of hydrogen-metal interactions	61
3.5. Discussion	63
3.5.1. Effect of microstructure variations on HEAC at mild and aggressive applied potentials.....	64
3.5.2. Correlating the variation in microstructural features with HEAC susceptibility.....	67
3.5.3. Modeling K _{TH} for heat-to-heat variations in yield strength and composition	77
3.6. Conclusions	80
3.7. Suggested Future Research Directions.....	81
3.8. Acknowledgements/Statement of Contribution	82
3.9. References	82
<i>Chapter 4. Effect of heat treatment variation on HEAC in Monel K-500.....</i>	<i>91</i>
4.1. Overview	91

4.2. Introduction	92
4.2.1. Chapter objective and research questions.....	93
4.3. Experimental methods and material	93
4.3.1. Material and heat treatment protocol.....	93
4.3.2. Fracture mechanics testing	94
4.3.3. Characterization.....	96
4.4. Results	97
4.4.1 Variation in yield strength with isothermal aging time	97
4.4.2. Quantifying HEAC kinetics as a function of isothermal aging time	98
4.5. Discussion	108
4.5.1. Grain size and grain boundary character	109
4.5.2. Grain boundary impurity segregation.....	114
4.5.3. Yield strength and strain hardening	115
4.5.4. Precipitate morphology	117
4.5.5. Summary and identified mechanistic knowledge gaps.....	124
4.6. Conclusions	125
4.7. Suggested Future Research Directions.....	126
4.8. Acknowledgements.....	127
4.9. References	127
<i>Chapter 5. Effect of hydrogen on deformation behavior in Monel K-500.....</i>	<i>131</i>
5.1. Overview	131
5.2. Introduction	132
5.2.1. Chapter objective and research questions.....	134
5.3. Experimental methods and material	134
5.3.1. Material.....	134
5.3.2. Mechanical Testing.....	135
5.3.3. Hydrogen Charging.....	137
5.3.4. Microscopy.....	137
5.4. Results	138
5.4.1 Effect of H on stress-strain behavior and fractography	138
5.4.2. Effect of H on work hardening behavior	142

5.5. Discussion	144
5.5.1. Verification of similar precipitate morphologies between non-charged and H-charged conditions.....	144
5.5.2. Effect of hydrogen on the mechanical behavior of Monel K-500 as a function of heat treatment	146
5.5.3. Mechanistic interpretations.....	149
5.6. Conclusions	151
5.7. Suggested Future Research Directions.....	151
5.8. Acknowledgements.....	152
2.9. References	152
<i>Chapter 6. Initial assessment of near-crack wake deformation structure</i>	<i>156</i>
6.1. Overview	156
6.2. Introduction	157
6.2.1. Chapter objective and research question	158
6.3. Experimental methods and material	159
6.3.1. Material.....	159
6.3.2. Bulk specimen preparation.....	159
6.3.3. Electron backscatter diffraction and calculation of geometrically necessary dislocation density maps .	160
6.4. Results	163
6.5. Discussion	167
6.6. Conclusions	168
6.8. Acknowledgements.....	168
6.9. References	168
<i>Chapter 7. Summary and conclusions.....</i>	<i>172</i>
7.1. Overview	172
7.2. Summary and Key Conclusions.....	172
<i>Appendix I: Mitigation of focused ion beam-induced damage.....</i>	<i>174</i>
A.1. Overview.....	174
A.2. Introduction.....	174
A.3. Material and Methods.....	176

A.4. Results	178
A.5. Discussion	182
A.5.1 Effect of Pt Deposition Approach on Damage Depth.....	183
A.5.2 Effect of Pt Deposition Approach on Damage Character	185
A.5.3 Implications on the Characterization of Near-Surface Microstructure	186
A.6. Conclusions.....	187
A.7. Acknowledgements.....	187
A.8. References.....	187
<i>Appendix II: Relevant publications and presentations.....</i>	<i>191</i>
A2.1. Published/Submitted Peer-Reviewed Journal Articles.....	191
A2.2. Published Peer-Reviewed Conference Proceedings.....	194
A2.3. Contributed Conference Presentations.....	195

List of Figures

Figure 1 – Comparison between (a) scanning electron micrograph and (b) inverse pole figure (IPF) map via EBSD of a non-strained tensile specimen of Ni-201 charged with hydrogen. Note the presence and location of the pore-like features (white arrows), particularly with respect to grain boundaries. 18

Figure 2 - (a) Engineering and (b) calculated true stress-strain curves for both H-charged and non-charged Ni-201 specimens strained to failure at room temperature (RT) and 77 K using an applied strain rate of $4 \times 10^{-4} \text{ s}^{-1}$. Note that the curves for testing at 77 K are estimated using the actuator displacement and that the true stress-strain curves are truncated at the stress corresponding to the onset of necking. 20

Figure 3 – Low and high magnification fractographs of the non-charged (a,b) and H-charged (c,d) Ni-201 specimens tested to failure at RT. 21

Figure 4 – Low and high magnification fractographs of the non-charged (a,b) and H-charged (c,d) Ni-201 specimens tested to failure at 77 K. 21

Figure 5 – Representative backscattered electron SEM micrographs demonstrating intergranular (IG) microcrack locations for H-charged specimens strained to a true strain of 0.15 at (a) RT and (b) 77 K. High magnification images of the areas in (a) and (b) outlined by the red boxes are shown in (c) and (d), respectively. 22

Figure 6 – Plots of (a) CPA, (b) CLPA, (c) average crack length, and (d) cracked grain boundaries per area versus true strain for interrupted testing conducted on H-charged specimens at RT and 77 K. 26

Figure 7 – DC-STEM electron micrographs of deformation structures observed in specimens charged with H to 3000 appm and deformed to a true strain of 0.10 at 77K (a-d) and RT (e-h). Image contrast is inverted for clarity. Examples of the dislocation “packet” morphologies at grain boundaries are highlighted by white arrows in (d) 77 K and (h) RT. 28

Figure 8 – Cumulative probability distributions for intercept lengths characterizing the dislocation cell configurations. 8 images were analyzed for each temperature (red: deformed at room temperature; blue: deformed at 77K). The distributions follow an inverse Gaussian function, with parameter fits given in Table 4. The distributions for the two deformation temperatures as essentially indistinguishable. 29

Figure 9 - Effect of testing condition on true strain for H-induced intergranular (IG) microcrack initiation. 34

Figure 10 – Crack growth rate versus total K for five lots of peak-aged Monel K-500 stressed under two different dK/dt protocols in a dry nitrogen ($\text{RH} < 5\%$) environment. Closed symbols represent specimens

tested at $dK/dt = 1 \text{ MPa}\sqrt{\text{m/hr}}$, while open symbols were tested at $dK/dt = 0.33 \text{ MPa}\sqrt{\text{m/hr}}$. Expected false da/dt produced by crack tip plastic deformation for each dK/dt are represented by the solid ($1 \text{ MPa}\sqrt{\text{m/hr}}$) and dashed ($0.33 \text{ MPa}\sqrt{\text{m/hr}}$) lines. 50

Figure 11 – Fractographs illustrating the (a) dimpled, ductile fracture morphology observed in the center (b) of inert environment-tested specimens. 51

Figure 12 – Fractograph of an NRL HS specimen tested in dry N₂ at $dK/dt = 0.1 \text{ MPa}\sqrt{\text{m/hr}}$. The white solid line and dashed line represent the end of the fatigue precrack and the dcPD-indicated crack length after slow rising-K testing, respectively, while the black line represents the end of the post-test fatigue region. Adapted from [55]. 52

Figure 13 – Comparison of the change in dcPD-measured voltage and actuator displacement with applied force for a smooth dog-bone tensile specimen of NRL HS, with the force corresponded to the alloy proportional limit and yield stress denoted by (a) and (b), respectively. Adapted from [55]. 53

Figure 14 – Crack growth rate versus total K for five lots of peak-aged Monel K-500 stressed in NaCl solution at a constant applied potential of -950mVSCE. The dashed line represents the expected false da/dt produced by crack tip plastic deformation for $dK/dt = 0.33 \text{ MPa}\sqrt{\text{m/hr}}$ 54

Figure 15 – Fractography of the intergranular (IG) fracture morphology observed for (a) Allvac, (b) TR1, (c) TR2, (d) TR3, and (e-f) NRL HS when tested in 0.6M NaCl solution with an applied potential of -950mVSCE. In addition to the IG morphology, NRL HS (e-f) also exhibited some transgranular features. 55

Figure 16 – Fractographs of facet slip traces for (a) Allvac, (b) TR1, (c) TR2, (d) TR3, and (e-f) NRL HS when tested in 0.6M NaCl solution with an applied potential of -950mVSCE. 56

Figure 17 – Crack growth rate versus total K for five lots of peak-aged Monel K-500 stressed in NaCl solution at a constant applied potential of -850mVSCE. The dashed line represents the expected false da/dt produced by crack tip plastic deformation for $dK/dt = 0.33 \text{ MPa}\sqrt{\text{m/hr}}$ 57

Figure 18 – Fractography of samples tested at an applied potential of -850 mVSCE in 0.6M NaCl: (a) overview of TR2 fracture surface and the fracture morphology observed at the crack length where $K = 40 \text{ MPa}\sqrt{\text{m}}$ for (b) TR1, (c) TR2, and (d) TR3. The black dashed line and solid line indicate the end of the fatigue precrack and slow rising-K test, respectively. 58

Figure 19 – Comparison of (a) crack growth kinetics data for NRL HS tested in dry N₂ and 0.6M NaCl at -850 mVSCE and fractographs of the (b) dimpled, ductile fracture morphology observed in the center (c) of the 0.6M NaCl at -850 mVSCE specimen. 59

Figure 20 – Orientation maps for (a) Allvac, (b) TR1, (c) TR2, (d) TR3, and (e) NRL HS collected using electron backscatter diffraction. Grain boundaries (black lines) were defined by misorientations greater than 15°	61
Figure 21 – Effect of hydrogen overpotential on total and diffusible hydrogen concentrations for the Allvac, TR2, and NRL-HS. Error bars represent 95% confidence interval.	62
Figure 22 – Sensitivity analysis conducted on the modeling to determine the effect of (a) a ± 250% change in diffusible hydrogen concentration relative to the baseline value found for Allvac, (b) a ± 25% change in the Griffith toughness of the grain boundary (k_{IG}) relative to the baseline value of 0.88 MPa \sqrt{m} , and (c) a ± 15% change in the yield strength from the Allvac yield strength (786 MPa) on the calculated threshold stress intensity.	65
Figure 23 – Sensitivity analysis conducted on the modeling to determine the effect of (a) a ± 250% change in diffusible hydrogen concentration relative to the baseline value found for Allvac and (b) a ± 15% change in the yield strength from the Allvac yield strength (786 MPa) on the calculated H-diffusion limited crack growth rate, da/dt_{II}	67
Figure 24 - Average maximum grain boundary sulfur concentration (in atomic fraction) for four different heats of Monel K-500. Error bars represent the standard deviation from 5-6 facets (3 for TR2).	70
Figure 25 – The process for establishing the fractal dimension included: (a) obtaining an orientation map via electron backscatter diffraction, (b) identification of high (black lines) angle grain boundaries and low (red lines) angle grain boundaries, (c) isolating high angle grain boundaries by removing all low angle grain boundaries, (d) measuring the maximum connected network (highlighted red lines) and overlaying a square grid with a known side length.	73
Figure 26 – Variation in hydrostatic stress with distance from the crack tip for the tested Monel K-500 heats calculated using the HRR solutions assuming plane strain conditions.	76
Figure 27 – Plot of the calculated threshold stress intensity versus applied potential curves for each heat of Monel K-500 using previously validated parameters with experimental data points included for -950 and -850 mV _{SCE} . Black arrows extending upward represent experimental observations of HEAC immunity at the tested potential.	79
Figure 28 – Plot of the calculated threshold stress intensity versus applied potential curves for each heat of Monel K-500 using new parameters with experimental data points included for -950 and -850 mV _{SCE} . New parameters include the effects of grain boundary impurity segregation of sulfur (β) and boron (γ).	

Black arrows extending upward represent experimental observations of HEAC immunity at the tested potential. 80

Figure 29 – Variation in yield strength of Monel K-500 as a function of aging time at 923 K. 98

Figure 30 – Crack growth rate versus total K for specimens heat-treated to the non-aged condition tested under slow-rising K in 0.6 M NaCl at -1100 and -1200 mV_{SCE} using a constant dK/dt = 0.33 MPa√m/hr. 99

Figure 31 – Micrographs of the fracture morphologies observed in non-aged specimens tested at -1200 (a-c) and -1100 mV_{SCE} (d) in 0.6 M NaCl. The white arrows in (a-d) denote fractographic features consistent with crack-tip blunting, which occurred at a distance similar to the targeted precrack (PC) depth from the EDM notch (white dashed line in (a-b), left). The yellow arrow in (d) indicates a transgranular (TG) feature in the post-test fatigue (PTF) region that separates the blunting features and the IG/TG fatigue fracture morphology. Crack growth occurs from left to right in all images, as shown by the dashed white arrow. 100

Figure 32 – Crack growth rate versus total K for specimens heat-treated to the under-aged condition tested under slow-rising K in dry N₂ (RH < 5%) and in 0.6 M NaCl at -1000, -1100, and -1200 mV_{SCE} using a constant dK/dt = 0.33 MPa√m/hr. The dashed line corresponds to the linear fit of the log(da/dt) vs. K_I data measured during dry N₂ testing. 102

Figure 33 – Overview micrographs of the fracture morphologies observed in under-aged specimens tested at (a) -1200, (b) -1100, and (c) -1100 mV_{SCE} in 0.6 M NaCl. The white dashed line in (a-c) denotes the location of the EDM notch, while the red dashed line in (a-c) indicates the transition from the fatigue precrack (PC) to HEAC. A representative high magnification micrograph of the fracture morphology in the HEAC region is shown in (d), with example intergranular (IG) and transgranular (TG) features noted by the white arrows. Crack growth occurs from left to right in all images, as shown by the dashed white arrow. 103

Figure 34 – Crack growth rate versus total K for specimens heat-treated to the peak-aged condition tested under slow-rising K in dry N₂ (RH < 5%) and in 0.6 M NaCl at -1000, -1100, and -1200 mV_{SCE} using a constant dK/dt = 0.33 MPa√m/hr. The dashed line corresponds to the linear fit of the log(da/dt) vs. K_I data measured during dry N₂ testing. 104

Figure 35 – Overview micrographs of the fracture morphologies observed in under-aged specimens tested at (a) -1200, (b) -1100, and (c) -1100 mV_{SCE} in 0.6 M NaCl. The white dashed line in (a-b) denotes the location of the EDM notch, while the red dashed line in (a-b) indicates the transition from the fatigue precrack (PC) to HEAC. Evidence of ductile fracture due to an overload induced by an unexpected power

outage is highlighted by the white arrows. A representative high magnification micrograph of the fracture morphology at the transition between the PC and HEAC regions for -1100 mV_{SCE} is shown in (d), with an example intergranular (IG) facet in the PC region noted by the white arrow. A high magnification micrograph of the transition from the precrack to the ductile overload region at -1000 mV_{SCE} is shown in (e). Crack growth occurs from left to right in all images, as shown by the dashed white arrow..... 105

Figure 36 – Crack growth rate versus total K for specimens heat-treated to the over-aged condition tested under slow-rising K in dry N₂ (RH < 5%) and in 0.6 M NaCl at -1100 and -1200 mV_{SCE} using a constant dK/dt = 0.33 MPa√m/hr. The dashed line corresponds to the linear fit of the log(da/dt) vs. K_I data measured during dry N₂ testing 107

Figure 37 – Overview micrographs of the fracture morphologies observed in over-aged specimens tested at (a) -1200, (b) -1100 mV_{SCE} in 0.6 M NaCl. The white dashed line in (a-c) denotes the location of the EDM notch, while the red and yellow dashed lines in (a) indicates the transition from the fatigue precrack (PC) to HEAC and HEAC to post-test fatigue (PTF), respectively. Ductile damage induced during an unexpected power outage is noted by the white arrows in (b). A higher magnification micrograph of the -1100 mV_{SCE} is shown in (c), with the white arrows noting a fractographic feature consistent with crack-tip blunting, while (d) shows a representative high magnification micrograph of the fracture morphology in the HEAC region for OA -1200 mV_{SCE}. Crack growth occurs from left to right in all images, as shown by the dashed white arrow. 108

Figure 38 – The measured variation in (a) K_{TH} and (b) da/dt_{K=45} as a function of applied potential for the under-aged, peak-aged, and over-aged heat treatments. Non-aged is excluded due to a lack of HEAC susceptibility across all tested potentials. Arrows point either upward (a) or downward (b) indicates that HEAC was not observed at the respective applied potential..... 109

Figure 39 – OIM maps for the non-aged, under-aged, peak-aged, and over-aged conditions. The white arrows indicate examples of grains in the peak-aged and over-aged condition which have undergone abnormal grain growth..... 110

Figure 40 – Measured average and standard deviation (noted by error bars) in grain size for the non-aged, under-aged, peak-aged, and over-aged conditions, calculated from ~1000 grains in OIM maps collected using EBSD..... 111

Figure 41 – Cumulative distribution of grain boundary fraction as a function of grain boundary misorientation angle based on the evaluation of ~10,000 grain boundaries from OIM maps collected using EBSD..... 113

Figure 42 – Length fraction of $\Sigma 3$ and $\Sigma 9$ CSL boundaries as a function of heat treatment. Data is calculated from the observation of ~ 42.5 mm of grain boundary length from OIM maps collected using EBSD.	113
Figure 43 – Measured average and standard deviation (noted by error bars) of the maximum sulfur concentration measured via Auger electron spectroscopy on 2-3 intergranular facets as a function of heat treatment.	115
Figure 44 – Variation in hydrostatic stress with distance from the crack tip for the tested heat treatments calculated using the HRR solutions assuming plane strain conditions.	117
Figure 45 – (a) Plot of the γ' size distribution for each age-hardened heat treatment, based on the measurement of 500 precipitates, and representative micrographs of the γ' precipitate morphology for the (b) under-aged, (c) peak-aged, and (d) over-aged heat treatments.	118
Figure 46 – Bright-field micrographs of representative bulk slip morphologies for the (a-b) under-aged, (c-d) peak-aged, and (e-f) over-aged heat treatments. The red arrows in (b) highlight two dislocation pairs, while the red arrows in (e-f) indicate evidence of looping. The diffraction vector associated with each condition is shown by the white arrows and the white dashed lines in (c) indicate the trace of the $\{111\}$ planes.	122
Figure 47 – Bright field micrograph of the bulk slip morphology in the non-aged condition, with the utilized diffraction vector indicated in lower right corner.	124
Figure 48 – Plot of the work hardening rate (θ) versus flow stress increase ($\sigma_T - \sigma_{YS}$) for the H-charged, under-aged specimen tested to failure as well as two tests which were interrupted at lower strains. The dashed black line represents the fit to the three data sets using a second-order exponential function.	136
Figure 49 – True stress-true strain curves for the H-charged and non-charged specimens strained to failure for each heat treatment.	139
Figure 50 – Fractographs of the (a) non-aged, (b) under-aged, (c) peak-aged, and (d) over-aged heat treatments tested to failure in the non-charged condition.	140
Figure 51 – Fractographs of the (a) non-aged, (b) under-aged, (c) peak-aged, and (d) over-aged heat treatments tested to failure in the hydrogen-charged condition.	141
Figure 52 – High-magnification fractographs of the slip traces observed on intergranular facets in the (a) non-aged, (b) under-aged, (c) peak-aged, and (d) over-aged heat treatments tested to failure in the hydrogen-charged condition.	141

Figure 53 – Work hardening rate versus flow stress increase for the H-charged and non-charged specimens strained to failure for each heat treatment.....	142
Figure 54 – Schematic demonstrating the graphical assessment of θ_{\max} and $d\theta/d\sigma$ based on a linear fit to the Stage III work hardening region.....	143
Figure 55 – Plot of (a) θ_{\max} and (b) $-d\theta/d\sigma$ as a function of aging time and hydrogen. Parameters were obtained using the graphical method shown in Figure 54.....	144
Figure 56 – Comparison of the γ' size distribution for the hydrogen-charged and non-charged specimens heat-treated to the peak-aged condition.....	145
Figure 57 - Observed increase in yield strength versus hydrogen concentration. Note that the linear relationship for solid solution hardening is adapted based on the work of Ulmer and Altstetter [37].	147
Figure 58 - Bright-field micrographs of the bulk slip morphology in the hydrogen-charged (a,b) and non-charged (c,d) peak-aged specimens tested to failure. The red arrow in (a) and (c) indicates planar slip bands oriented along the trace of the $\{111\}$ plane, while the red arrows in (b) indicate examples of dislocation looping.....	149
Figure 59 – Example of the cross-section exposed after Ar broad-beam ion milling. The red arrow notes the impingement direction of the Ar ions, while the white dashed line reflects the location of the fracture surface.....	160
Figure 60 – Schematic documenting the cross-correlation calculation procedure. Taken from [31].	163
Figure 61 – Micrograph of the ion-mill cross-section, with the white dashed lines indicating the bounds of the HR-EBSD characterization and are consistent with the black dashed lines in Figure 62.....	164
Figure 62 – Plot showing the total stress intensity (K_I) sampled over the exposed cross-section. Note that the crack length is measured relative to the end of the fatigue precrack (see Chapter 4 for additional details of testing). The black dashed lines correspond to the white dashed lines in Figure 61.....	165
Figure 63 – (a) Inverse pole figure map with grain orientations relative to the Z-axis (out of the page) and (b) kernel average misorientation map for the peak-aged specimen tested in 0.6 M NaCl at $-1200 \text{ mV}_{\text{SCE}}$. Note that the kernel average misorientation legend is in degrees.....	166
Figure 64 – Geometrically dislocation density map calculated using cross-correlation techniques from high-resolution EBSD scans. The red arrows indicate two adjacent grains which exhibit different distributions of GND density, while the black arrow indicates the effects of poor reference pattern selection. Note that the units are in m^{-2} and that the scale is logarithmic.....	167

Figure 65 – Overview of applied Pt deposition protocols for each TEM sample.	177
Figure 66 – Overview TEM micrographs at two different magnifications for (a,b) Sample 1, (c,d) Sample 2, (e,f) Sample 3, (g,h) Sample 4, and (i,j) Sample 5.	179
Figure 67 – High magnification TEM micrographs of the Pt/Al interface for (a) Sample 1 and (b) Sample 4. Red lines indicate the transition in damage character as well as the location of interfaces between E-beam Pt, I-beam Pt, and the Al alloy.	181
Figure 68 - High magnification TEM micrographs of the Pt/Al interface for (a) Sample 5 un-tilted and (b) Sample 5 tilted to show continuity of deformation. In (a), the red dashed line indicates the transition between the E-beam Pt and I-beam Pt, while the red arrow indicates the ‘damage’ used for calculating the damage depth shown in Figure 69.	181
Figure 69 – Average damage depth for each Pt deposition strategy based on ten equidistant measurements across the TEM specimen width.	182
Figure 70 - Normalized Ga ⁺ ion distribution as a function of depth from the Pt surface calculated using Monte Carlo-based simulations for three different Pt density values. Calculations were completed using 30 keV Ga ⁺ ions impinging from a source oriented perpendicular to the Pt layer surface.	184

List of Tables

Table 1 – Mechanical properties from testing to failure.....	20
Table 2 - Results of interrupted testing.....	24
Table 3 – Analysis of variation in microcrack metrics for interrupted testing.....	25
Table 4 - Summary of fit parameters for the inverse Gaussian distribution describing the intercept distributions measured from DC-STEM images of the dislocation substructure. The error columns tabulate the standard error in the fit for the parameter estimate.....	32
Table 5 - Chemical composition of Monel K-500 heats (wt. %, except S, P, Sn, Pb, Mg, Zr, Hf, B are wppm).....	48
Table 6 - Mechanical properties of Monel K-500 heats	48
Table 7 - Grain size and grain boundary characteristics of Monel K-500 heats	60
Table 8 – Composition of the tested Monel K-500 heat (wt. % except Si, Zr, P, S, and B are in wppm)..	93
Table 9 – Measured mechanical properties for the selected aging conditions	98
Table 10 – Precipitate morphology characteristics as a function of heat treatment condition.....	119
Table 11 – Composition of the tested Monel K-500 heat (wt. % except Si, Zr, P, S, and B are in wppm)	135
Table 12 – Mechanical properties as a function of heat treatment and hydrogen condition.....	139

Chapter 1. Introduction and background

1.1. Hydrogen embrittlement – status of the problem

Structural metals, such as Al, Fe, Ni, and Ti-based alloys, exposed to hydrogen-containing/producing environments suffer from a decrease in performance that is characterized by (1) a reduction in the resistance to fracture and (2) a transition from ductile to brittle fracture morphologies. This phenomenon – termed hydrogen embrittlement – undermines decades of metallurgical optimization and compromises damage tolerant design frameworks [1]. Manifestations of hydrogen embrittlement include reduced ductility and fracture strength, enhanced crack growth rates, and the onset of subcritical crack growth at threshold stress intensities (K_{TH}) that are on order of 10-20% of reported toughness values. However, despite over a century of study [2], which has resulted in the generation of a voluminous literature database (as documented in several reviews [1,3–7]), hydrogen embrittlement continues to pose a serious engineering challenge. Such difficulties are underscored by two recent high-profile failures attributed to hydrogen embrittlement. First, 32 high-strength steel anchor rods failed within a few days of tensioning on the new eastern span of the San Francisco-Oakland Bay Bridge in March 2013 [8], which necessitated ~\$45 million in additional cost to design and implement an alternative anchor system [9]. Additional rod failures were later identified in 2015 [9], thereby demonstrating the challenge of managing the structural integrity of components exposed to hydrogen-producing environments, even when it is known to occur. Second, three steel “mega-bolts” on the new Leadenhall Building in London failed between November 2014 and January 2015, with one of the fractured bolts falling from the 15th floor to the street below [10]. These bolt failures resulted in ~\$7.5 million being spent on the testing and replacement of other susceptible bolts in the structure [10], further highlighting the significant economic cost of hydrogen-induced degradation.

In addition to these more visible component failures, hydrogen embrittlement widely impacts other industries. For example, efforts to improve vehicle efficiency by utilizing high strength steels, which would allow the use of thinner gauge sheet while simultaneously improving passenger safety, are hindered by hydrogen-induced delayed cracking of formed components [11]. Considering the oil and gas industry, it has been estimated that up to 25% of failed components can be attributed to hydrogen [12]; the failure of bolts on North Sea oil rigs, as well as aboard marine craft, due to hydrogen embrittlement has been extensively discussed in the literature [13–15]. Unexpected failures in plain carbon steel steam generator tubes, boilers, and pipelines within power plants have been attributed to hydrogen embrittlement [16,17]. The comparison of fatigue crack growth data collected in laboratory air versus in ultra-high vacuum demonstrates that hydrogen strongly degrades the fatigue performance of aerospace Al alloys [18]. Lastly,

hydrogen embrittlement is arguably the predominant barrier to the widespread implementation of hydrogen as a fuel source due to the hydrogen-induced degradation of pipeline networks, storage infrastructure, and dispensing equipment, as discussed extensively in the text edited by Gangloff and Somerday [7].

While the above examples by no means represent an exhaustive list, it is clear that hydrogen embrittlement negatively impacts numerous industries at a substantial economic cost. However, efforts to mitigate this deleterious effect are currently hindered by an incomplete understanding of the microscale processes governing hydrogen-induced degradation, which complicates the development of physically-based modeling tools to predict and manage component life. As detailed in extensive reviews by Gerberich [19] and Robertson *et al.* [3], numerous mechanisms seeking to describe the microscale processes of hydrogen embrittlement have been proposed in the literature, including:

- Adsorption-induced dislocation emission (AIDE)
- Hydrogen-enhanced localized plasticity (HELP)
- Hydrogen-enhanced decohesion (HEDE)
- Hydride formation
- Hydrogen-enhanced strain-induced vacancies (HESIV)

Addressing each mechanism in turn, AIDE posits that hydrogen adsorbed at the crack tip weakens interatomic bonds, thereby facilitating dislocation nucleation. Crack growth is then suggested to occur by the combined action of incremental ejection of dislocations on two slip planes and coalescence of this alternate slip with nanovoids formed ahead of the crack [4,5,20]. Alternatively, the HELP paradigm argues that hydrogen congregates in the elastic stress field of dislocations, thereby enhancing dislocation mobility through a reduction in the repulsive stress felt between dislocations [21,22]. Such increases in mobility produce the dual effect of locally enhanced plasticity (which can facilitate enhanced local stress states) and hydrogen concentration. Conversely, HEDE postulates that hydrogen lowers the cohesive strength of interfaces, thereby weakening interatomic bonds and facilitating the onset of brittle fracture at reduced stresses [23,24]. An important distinction between HEDE and HELP is the role of plasticity, with the original articulation of HEDE ignoring plasticity contributions based on observations of low-ductility fractures. Hydride formation and the concomitant brittle fracture along cleavage planes is well-established as a hydrogen degradation mechanism in susceptible systems (Group IVB and VB metals – Ti, Zr, Nb, etc.) [25,26]. Furthermore, hydride formation can occur in other systems if sufficiently elevated hydrogen concentrations are achieved (*i.e.* Ni-Fe alloys [27]). Lastly, Nagumo has proposed that hydrogen enhances vacancy formation and agglomeration during deformation [28] (HESIV) through the defectant concept [29], where hydrogen reduces the energy of vacancy formation. However, how these strain-induced vacancies participate in the embrittlement process remains unclear [30].

Each of these proposed mechanisms claim support from both theoretical and experimental results, but the multi-faceted nature of the hydrogen degradation problem (as well as the likelihood of mechanism synergy) complicates the universal applicability of any one mechanism. However, despite their much-discussed differences, a common theme amongst the mechanisms is the assumption of a localized interaction between hydrogen and microstructural features. This commonality has motivated researchers to investigate these processes through novel, localized experimental and computational techniques, which have collectively highlighted the interactions between hydrogen and deformation as a critical contributor to hydrogen embrittlement susceptibility [21,28,31–33]. One notable example of this localized evaluation is the recent probing of hydrogen-dislocation interactions using a combined transmission electron microscopy (TEM) and focused ion beam (FIB) technique to examine near-crack wake dislocation structure evolution [3]. In this work, Martin et al. examined the dislocation cell structure underneath an intergranular (IG) facet in polycrystalline nickel that had been strained to failure after thermal charging in gaseous hydrogen [34]. Based on the work of Keller et al. [35], who systematically measured the cell diameter of polycrystalline nickel as a function of true strain, Martin et al. argued that hydrogen significantly accelerated cell refinement [34]. Specifically, by extrapolating from the data presented by Keller et al., Martin et al. reasoned that their hydrogenated specimen exhibited cells (which had diameters on the order of 200-400 nm) that were consistent with deformation to a true strain of approximately 0.4 – a value markedly higher than the measured macroscale fracture strain of 0.13. Based on these observations, Martin et al. concluded that IG fracture of hydrogen-charged nickel was attributed to decohesion of the grain boundary due to the attainment of a local hydrogen concentration/stress combination (HEDE) that was principally driven by the interaction of hydrogen and dislocations (HELP) [34]. This assessment was further supported by computational calculations which reasoned that unrealistic hydrogen concentrations would be required to produce grain boundary decohesion in iron by hydrogen alone [36,37], which was taken as evidence that HEDE alone cannot sufficiently explain hydrogen-induced intergranular fracture. However, while these detailed efforts provide critical evidence for a likely role of hydrogen-dislocation interactions, they do not explicitly confirm the dominance of hydrogen-deformation interactions over hydrogen segregated to the grain boundary in determining the conditions for IG cracking. ***Specifically, research conducted to date has convincingly established the synergistic interaction of the two mechanisms, but experiments which isolate the contribution of each mechanism to IG cracking are still needed.***

In addition to further studies on polycrystalline nickel [38], Robertson and coworkers have also examined hydrogen effects on the deformation structure evolution in several other alloys, including polycrystalline iron [39], 300-series stainless steels [40], ferritic-pearlitic steel [41], martensitic steel [42], and equimolar alloys [43,44]. In each case, the authors noted that the deformation structure was more refined in the presence of hydrogen as compared to testing in laboratory air. Similar findings have also been

reported by other authors in polycrystalline Fe [45–47] and Pd [48]. Such observations have subsequently been used as evidence to advance the view that hydrogen-induced degradation is predominantly driven by hydrogen-plasticity interactions. These results were then leveraged to propose a combinatory hydrogen-enhanced, plasticity-mediated decohesion mechanism where intergranular cracking might occur as follows [3]:

1. The interaction between hydrogen and deformation facilitates an increase in the generation of dislocations from sources and enables movement of dislocations at lower stresses. This results in an increase in the number of grain boundary-dislocation interactions.
2. This increase in grain boundary-dislocation interactions yields a concomitant increase in the number of dislocations accommodated within the grain boundary, as well as an increase in the number of dislocations piled up against the boundary. The separation distance between dislocations in the pileup will decrease due to the screening effects of hydrogen. This leads to an increase in the local stress state.
3. As additional hydrogen-carrying dislocations impinge on the grain boundary, the local hydrogen concentration will increase, thereby lowering the cohesive strength of the boundary.
4. As the number of accommodated dislocations grows, the boundary will become increasingly disordered. Eventually, slip transmission will not sufficiently dissipate the accumulated strain and the local stress/hydrogen concentration will satisfy the decohesion criterion for the boundary, resulting in fracture of the interface.

While this proposed mechanism enjoys considerable experimental support from the aforementioned FIB/TEM experiments, several outstanding questions must still be addressed. First, as noted by Keller et al. [35], the measured grain-to-grain variation in both dislocation cell diameter and type is not insignificant. Specifically, standard deviations reaching between 30 and 50% of the mean cell diameter were observed in each specimen/strain level tested (approximately 15 grains were examined at each condition); such behavior suggests that differences in grain orientation can significantly influence the observed dislocation patterning, as has been extensively documented in the literature [49–51]. However, despite this well-known influence, many of the noted studies have not held this variable constant when comparing deformation structures. Such experimental complications may similarly explain why two studies comparing deformation structures in hydrogen-charged versus non-charged Ni *did not* observe any evidence of deformation refinement in the hydrogen condition [52,53]. Second, experiments conducted on fatigue [40] and monotonically [42] loaded specimens did not examine the deformation structure at a constant stress intensity (K). Given that the stress/strain field proximate to the crack is explicitly dependent on the applied stress intensity [54], it is reasonable to expect that such differences could give rise to variations in the observed dislocation

patterning. Third, the inherent limitation of the TEM/FIB approach is the small material area sampled during characterization, which is typically on the order of tens of μm^2 . Given this areal limitation, in addition to the previously noted complications of grain orientation and applied driving force, the use of characterization techniques which can inform deformation behavior at larger length scales may be worthwhile. Towards this end, the calculation of geometrically necessary dislocation (GND) densities proximate to the crack wake using high-resolution electron backscatter diffraction (HR-EBSD) via cross-correlation techniques represents an attractive combination of spatial resolution (>75 nm) and sampling area ($\sim 100\text{s}-1000\text{s}$ of μm^2) [55–57]. However, the use of this technique to assess near-crack deformation is limited, suggesting that validation of results using TEM is still required, though initial results assessing GND distributions after plastic deformation [58,59] and near crack initiation sites [60] are promising. ***In summary, variations in deformation structure with grain orientation and applied crack tip driving force complicate assessment of hydrogen-plasticity contributions to IG cracking and comparison of results across specimens. These complications underscore the limited area of observation inherent to TEM/FIB-based studies, suggesting that characterization techniques with larger sampling areas should be explored. HR-EBSD offers the ability to quantify deformation via the calculation of GND densities at sufficient size scales, but the viability of this technique for assessing near-crack deformation needs to be further explored.***

In addition to the lack of clarity regarding the microscale processes governing hydrogen-assisted cracking, the extension of these mechanisms into more complex, industrially-relevant alloys is complicated by uncertainty regarding the role of microstructural features in the context of such mechanisms. The importance of understanding microstructural influences on hydrogen-induced degradation is underscored by the large measured variations in susceptibility across similar alloy systems, or even amongst different material heats of the same alloy [61]. Though such data indicate that microstructural variables strongly contribute to the intrinsic resistance of an alloy to hydrogen embrittlement, the relative effect of a given microstructural feature on susceptibility remains uncertain. Isolating the contribution of a particular microstructural feature is complicated by the likelihood that several microstructural parameters impact susceptibility. For example, considering possible microstructural influences on the hydrogen-enhanced, plasticity-mediated mechanism, a succinct list of potential contributors includes: impurity segregation to grain boundaries [62], grain size [63], grain boundary character [64,65], interaction of hydrogen and slip with secondary phases (*i.e.* hydrogen trapping [66] and global slip morphology [67]), yield strength [68], and hydrogen-metal interactions (*i.e.* hydrogen uptake [69]). For example, increased sulfur content at the grain boundary is known to lower the grain boundary cohesive strength in Fe and Ni [70,71]; such a modification would decrease the critical localized hydrogen concentration/stress required for decohesion. Previous studies have attempted to systematically identify the role of such features in alloys such as Inconel

718 [72], but the isolation of critical factors is complicated by the presence of multiple secondary phases (depending on applied heat treatment). Such findings suggest that the examination of microstructural effects should be completed in a nominal two-phase alloy system, which would limit the possible degrees of freedom. However, to date, such a systematic study has not been completed. *The microstructural feature(s) which govern IG cracking should be quantitatively determined in the context of hydrogen embrittlement susceptibility for industrially-relevant alloy systems. The subsequent influence of these salient feature(s) on proposed microscale mechanism(s) must be established.*

1.2. Knowledge gaps

The preceding overview has identified the following critical knowledge gaps regarding the influence of microstructural features on hydrogen embrittlement susceptibility:

1. Recent literature posits that hydrogen-induced intergranular fracture can be predominantly attributed to hydrogen-enhanced plasticity processes. However, an experimental study *directly comparing* the influence of hydrogen-deformation interactions and hydrogen segregated to grain boundaries prior to deformation is lacking.
2. Research to date examining the influence of hydrogen on near-crack dislocation structure evolution has not accounted for changes in both the crack tip driving force and local grain orientation. Variations in these parameters complicates comparison amongst experimental results and assessment of hydrogen-enhanced plasticity's contribution to the local failure criterion. Moreover, the limited sampling area of the FIB/TEM technique exacerbates these complications, suggesting that an intermediate length-scale characterization strategy should be employed, such as HR-EBSD.
3. Variations in the embrittlement susceptibility of similar alloys (or even amongst different material heats of the same alloy) suggests that microstructural variables govern the intrinsic resistance of a material to hydrogen (for a given set of loading and environmental parameters). Yet, quantitative understanding of the metallurgical features that control susceptibility remains elusive.

1.3. Research Questions

The background and identified knowledge gaps detailed above demonstrate the need for improved understanding of the microstructure's fundamental role in determining susceptibility to hydrogen-assisted cracking. Towards this end, this dissertation seeks to answer the following questions:

1. Mechanistically, to what extent do hydrogen-deformation interactions govern intergranular cracking?
2. What are the critical microstructural features that govern hydrogen embrittlement susceptibility?

3. How do variations in these critical features affect possible microscale mechanism(s) for hydrogen embrittlement?

1.4. Dissertation overview

The following dissertation is organized into five chapters, which can be divided into two primary thrusts. First, to address Research Question #1, Chapter 2 describes a fundamental study utilizing commercially-pure nickel to systematically evaluate the role of hydrogen-deformation interactions on hydrogen-induced intergranular cracking. By quantitatively evaluating the relative contribution of hydrogen-deformation interactions, this study will better inform the extent to which dislocation-based factors like bulk slip morphology may contribute to embrittlement susceptibility in more complex alloys. The second thrust of the dissertation, presented in Chapters 3-5, describes a series of studies that evaluates the role of microstructure on hydrogen environment-assisted cracking susceptibility (Research Questions #2-3) in a simple, but industrially-relevant, Ni-base alloy Monel K-500 [73]. This material is an ideal ‘model’ system for assessing the effects of microstructural variation on hydrogen embrittlement susceptibility in precipitation-hardened alloys, as it is nominally composed of just two phases: a Ni-Cu solid solution matrix phase (γ) and homogeneously distributed, highly coherent Ni_3Al (γ') strengthening precipitates [74]. Moreover, Monel K-500 is known to be susceptible to hydrogen environment-assisted cracking (HEAC) when stressed in chloride-containing environments (*e.g.* seawater) while under cathodic polarization [61]. Additionally, from an engineering perspective, understanding the influence of microstructural features on HEAC is particularly pertinent to Monel K-500 as intermittent field failures suggest that microstructural variability likely affects susceptibility [13,61]. The dissertation then concludes in Chapter 6 with a brief overview of recent efforts to characterize the near-crack deformation via a multiple length-scale approach. This characterization strategy offers exciting promise regarding the ability to broadly capture the effect on hydrogen on localized deformation, which can then be utilized to develop physically-based failure criteria for incorporation into models of hydrogen embrittlement.

Each chapter begins with a brief summary of chapter, followed a brief background section and the identification of the overarching objectives/research questions which guide the work completed within the chapter. An overview of the experimental methods utilized is also provided within each chapter, followed by the presentation and discussion of pertinent results. Each chapter then concludes with a summary of major conclusions and an outline of possible future research directions.

1.5. References

- [1] R.P. Gangloff, Hydrogen Assisted Cracking of High Strength Alloys, in: I. Milne, R.O. Ritchie, B. Karihaloo (Eds.), *Compr. Struct. Integr.*, Elsevier Science, New York, NY, 2003: pp. 31–101.

- [2] W.H. Johnson, On some remarkable changes produced in iron and steel by the action of hydrogen and acids, *Proc. R. Soc. London.* 23 (1874) 168–179. doi:10.1098/rspl.1874.0024.
- [3] I.M. Robertson, P. Sofronis, A. Nagao, M.L. Martin, S. Wang, D.W. Gross, et al., Hydrogen Embrittlement Understood, *Metall. Mater. Trans. B.* (2015). doi:10.1007/s11663-015-0325-y.
- [4] S.P. Lynch, Mechanisms and Kinetics of Environmentally Assisted Cracking: Current Status, Issues, and Suggestions for Further Work, *Metall. Mater. Trans. A.* 44A (2013) 1209–1229. doi:10.1007/s11661-012-1359-2.
- [5] S. Lynch, Hydrogen embrittlement phenomena and mechanisms, *Corros. Rev.* 30 (2012) 105–123. doi:DOI 10.1515/corrrev-2012-0502.
- [6] R.P. Gangloff, Critical issues in hydrogen assisted cracking of structural alloys, in: S. Shiilov (Ed.), *Environment Induc. Crack. Met.*, 2006: pp. 6337–6349.
- [7] R.P. Gangloff, B.P. Somerday, Gaseous hydrogen embrittlement of materials in energy technologies: mechanisms, modelling, and future developments, Woodhead Publishing Ltd., Cambridge, UK, 2012.
- [8] H.E. Townsend, K.H. Frank, B. Brignano, C. Choi, Hydrogen embrittlement testing and results of full-size ASTM A354 grade BD rods in the SFOBB, *Bridg. Struct.* 11 (2015) 117–130. doi:10.3233/BRS-160096.
- [9] M. Cabanatuan, J. Van Derbeken, Ominous new cracks found on Bay Bridge rods, *SFGate*. (2015). <https://www.sfgate.com/bayarea/article/Ominous-new-cracks-found-on-Bay-Bridge-rods-6345359.php>.
- [10] A. Tovey, Cheesegrater bolt failures to cost Severfield £6m, *Telegr.* (2015). <https://www.telegraph.co.uk/finance/newsbysector/constructionandproperty/11680433/Cheesegrater-bolt-failures-to-cost-Severfield-6m.html>.
- [11] B.C. De Cooman, K. Chin, J. Kim, High Mn TWIP steels for automotive applications, *New Trends Dev. Automot. Syst. Eng.* (2011) 1001–128. doi:Export Date 9 December 2013.
- [12] R.A. Carneiro, R.C. Ratnapuli, V. de Freitas Cunha Lins, The influence of chemical composition and microstructure of API linepipe steels on hydrogen induced cracking and sulfide stress corrosion cracking, *Mater. Sci. Eng. A.* 357 (2003) 104–110. doi:10.1016/S0921-5093(03)00217-X.
- [13] L.H. Wolfe, C.C. Burnette, M.W. Joosten, Hydrogen Embrittlement of Cathodically Protected Subsea Bolting Alloys, *Mater. Perform.* 32 (1993) 14–21.
- [14] K.D. Efir, Failure of Monel Ni-Cu-Al Alloy K-500 Bolts in Seawater, *Mater. Perform.* 24 (1985) 37–40.
- [15] J.R. Scully, M.G. Vassilaros, The Hydrogen Embrittlement Susceptibility of Monel Alloy K-500, *Electrochem. Soc. Fall 1983 Meet.* (1983).
- [16] R.K. Dayal, N. Parvathavarthini, Hydrogen embrittlement in power plant steels, *Sadhana.* 28 (2003) 431–451. doi:10.1007/BF02706442.
- [17] M.B. Djukic, G.M. Bakic, V.S. Zeravcic, A. Sedmak, B. Rajicic, Hydrogen Embrittlement of Industrial Components : Prediction , Prevention , and Models, 72 (2016) 943–961. doi:10.5006/1958.
- [18] J.T. Burns, J.J. Jones, A.D. Thompson, J.S. (Warner. Locke, Fatigue crack propagation of aerospace aluminum alloy 7075-T651 in high altitude environments, *Int. J. Fatigue.* 106 (2018) 196–207. doi:10.1016/j.ijfatigue.2017.09.017.

- [19] W.W. Gerberich, Modelling hydrogen induced damage mechanisms in metals, in: R.P. Gangloff, B.P. Somerday (Eds.), *Gaseous Hydrog. Embrittlement Mater. Energy Technol.*, Woodhead Publishing, 2012: pp. 209–246.
- [20] S.P. Lynch, Environmentally assisted cracking: Overview of evidence for an adsorption-induced localised-slip process, *Acta Metall.* 36 (1988) 2639–2661. doi:10.1016/0001-6160(88)90113-7.
- [21] I.M. Robertson, The effect of hydrogen on dislocation dynamics, *Eng. Fract. Mech.* 65 (2001) 671–692.
- [22] H.K. Birnbaum, P. Sofronis, Hydrogen-enhanced localized plasticity—a mechanism for hydrogen-related fracture, *Mater. Sci. Eng. A.* 176 (1994) 191–202. doi:10.1016/0921-5093(94)90975-X.
- [23] R.A. Oriani, P.H. Josephic, Equilibrium aspects of hydrogen-induced cracking of steels, *Acta Metall.* 22 (1974) 1065–1074. doi:10.1016/0001-6160(74)90061-3.
- [24] R.A. Oriani, A Mechanistic Theory of Hydrogen Embrittlement of Steels, *Berichte Der Bunsen-Gesellschaft Fur Phys. Chemie.* 76 (1972) 848–857.
- [25] D.G. Westlake, A generalized model for hydrogen embrittlement, *Trans. ASM.* 62 (1969) 1000–1006.
- [26] R. Dutton, K. Nuttall, M.P. Puls, L.A. Simpson, Mechanisms of hydrogen induced delayed cracking in hydride forming materials, *Metall. Trans. A.* 8 (1977) 1553–1562. doi:10.1007/BF02644858.
- [27] M.L. Wayman, G.C. Smith, Hydride formation in nickel-iron alloys, *J. Phys. Chem. Solids.* 32 (1971) 103–108. doi:10.1016/S0022-3697(71)80012-4.
- [28] M. Nagumo, Hydrogen related failure of steels – a new aspect, *Mater. Sci. Technol.* 20 (2004) 940–950. doi:10.1179/026708304225019687.
- [29] R. Kirchheim, B. Somerday, P. Sofronis, Chemomechanical effects on the separation of interfaces occurring during fracture with emphasis on the hydrogen-iron and hydrogen-nickel system, *Acta Mater.* 99 (2015) 87–98. doi:10.1016/j.actamat.2015.07.057.
- [30] T. Neeraj, R. Srinivasan, J. Li, Hydrogen embrittlement of ferritic steels: Observations on deformation microstructure, nanoscale dimples and failure by nanovoiding, *Acta Mater.* 60 (2012) 5160–5171. doi:10.1016/j.actamat.2012.06.014.
- [31] S.K. Lawrence, Y. Yagodzinsky, H. Hanninen, E. Korhonen, F. Tuomisto, Z.D. Harris, et al., Effects of Grain Size and Deformation Temperature on Hydrogen-Enhanced Vacancy Formation in Ni Alloys, *Submitt. to Acta Mater.* (2016).
- [32] A. Barnoush, H. Vehoff, Recent developments in the study of hydrogen embrittlement: Hydrogen effect on dislocation nucleation, *Acta Mater.* 58 (2010) 5274–5285. doi:10.1016/j.actamat.2010.05.057.
- [33] P.J. Ferreira, I.M. Robertson, H.K. Birnbaum, Hydrogen effects on the interaction between dislocations, *Acta Mater.* 46 (1998) 1749–1757. doi:10.1016/S1359-6454(97)00349-2.
- [34] M.L. Martin, B.P. Somerday, R.O. Ritchie, P. Sofronis, I.M. Robertson, Hydrogen-induced intergranular failure in nickel revisited, *Acta Mater.* 60 (2012) 2739–2745. doi:10.1016/j.actamat.2012.01.040.
- [35] C. Keller, E. Hug, R. Retoux, X. Feugas, TEM study of dislocation patterns in near-surface and core regions of deformed nickel polycrystals with few grains across the cross section, *Mech. Mater.* 42 (2010) 44–54. doi:10.1016/j.mechmat.2009.09.002.
- [36] M. Dadfarnia, A. Nagao, S. Wang, M.L. Martin, B.P. Somerday, P. Sofronis, Recent advances on

- hydrogen embrittlement of structural materials, *Int. J. Fract.* (2015). doi:10.1007/s10704-015-0068-4.
- [37] S. Wang, M.L. Martin, I.M. Robertson, P. Sofronis, Effect of hydrogen environment on the separation of Fe grain boundaries, *Acta Mater.* 107 (2016) 279–288. doi:10.1016/j.actamat.2016.01.067.
- [38] S. Wang, A. Nagao, K. Edalati, Z. Horita, I.M. Robertson, Influence of hydrogen on dislocation self-organization in Ni, *Acta Mater.* 135 (2017) 96–102. doi:10.1016/j.actamat.2017.05.073.
- [39] S. Wang, M.L. Martin, P. Sofronis, S. Ohnuki, N. Hashimoto, I.M. Robertson, Hydrogen-induced intergranular failure of iron, *Acta Mater.* 69 (2014) 275–282. doi:10.1016/j.actamat.2014.01.060.
- [40] M.L. Martin, P. Sofronis, I.M. Robertson, T. Awane, Y. Murakami, A microstructural based understanding of hydrogen-enhanced fatigue of stainless steels, *Int. J. Fatigue.* 57 (2013) 28–36. doi:10.1016/j.ijfatigue.2012.08.009.
- [41] S. Wang, A. Nagao, P. Sofronis, I.M. Robertson, Hydrogen-modified dislocation structures in a cyclically deformed ferritic-pearlitic low carbon steel, *Acta Mater.* 144 (2018) 164–176. doi:10.1016/j.actamat.2017.10.034.
- [42] A. Nagao, C.D. Smith, M. Dadfarnia, P. Sofronis, I.M. Robertson, The role of hydrogen in hydrogen embrittlement fracture of lath martensitic steel, *Acta Mater.* 60 (2012) 5182–5189. doi:10.1016/j.actamat.2012.06.040.
- [43] K.E. Nygren, K.M. Bertsch, S. Wang, H. Bei, A. Nagao, I.M. Robertson, Hydrogen embrittlement in compositionally complex FeNiCoCrMn FCC solid solution alloy, *Curr. Opin. Solid State Mater. Sci.* 22 (2018) 1–7. doi:10.1016/j.cossms.2017.11.002.
- [44] K.E. Nygren, S. Wang, K.M. Bertsch, H. Bei, A. Nagao, I.M. Robertson, Hydrogen embrittlement of the equi-molar FeNiCoCr alloy, *Acta Mater.* 157 (2018) 218–227. doi:10.1016/j.actamat.2018.07.032.
- [45] Y. Ogawa, D. Birenis, H. Matsunaga, A. Thøgersen, Ø. Prytz, O. Takakuwa, et al., Multi-scale observation of hydrogen-induced, localized plastic deformation in fatigue-crack propagation in a pure iron, *Scr. Mater.* 140 (2017) 13–17. doi:10.1016/j.scriptamat.2017.06.037.
- [46] D. Birenis, Y. Ogawa, H. Matsunaga, O. Takakuwa, J. Yamabe, Ø. Prytz, et al., Interpretation of hydrogen-assisted fatigue crack propagation in BCC iron based on dislocation structure evolution around the crack wake, *Acta Mater.* 156 (2018) 245–253. doi:10.1016/j.actamat.2018.06.041.
- [47] Y. Ogawa, D. Birenis, H. Matsunaga, O. Takakuwa, J. Yamabe, Ø. Prytz, et al., The role of intergranular fracture on hydrogen-assisted fatigue crack propagation in pure iron at a low stress intensity range, *Mater. Sci. Eng. A.* 733 (2018) 316–328. doi:10.1016/j.msea.2018.07.014.
- [48] Y.Z. Chen, H.P. Barth, M. Deutges, C. Borchers, F. Liu, R. Kirchheim, Increase in dislocation density in cold-deformed Pd using H as a temporary alloying addition, *Scr. Mater.* 68 (2013) 743–746. doi:10.1016/j.scriptamat.2013.01.005.
- [49] J.A. Wert, X. Huang, G. Winther, W. Pantleon, H.F. Poulsen, Revealing deformation microstructures, *Mater. Today.* 10 (2007) 24–32. doi:10.1016/S1369-7021(07)70206-7.
- [50] N. Hansen, X. Huang, G. Winther, Grain orientation, deformation microstructure and flow stress, *Mater. Sci. Eng. A.* 494 (2008) 61–67. doi:10.1016/j.msea.2007.10.086.
- [51] X. Huang, N. Hansen, Grain orientation dependence of microstructure in aluminium deformed in tension, *Scr. Mater.* 37 (1997) 1–7. doi:10.1016/S1359-6462(97)00072-9.
- [52] I.M. Robertson, H.K. Birnbaum, Effect of hydrogen on the dislocation structure of deformed

- nickel, *Scr. Metall.* 18 (1984) 269–274. doi:10.1016/0036-9748(84)90521-0.
- [53] W.A. McInteer, A.W. Thompson, I.M. Bernstein, The effect of hydrogen on the slip character of nickel, *Acta Metall.* 28 (1980) 887–894. doi:10.1007/BF02655107.
- [54] T.L. Anderson, *Fracture Mechanics: Fundamentals and Applications*, 3rd ed., Taylor & Francis, 2005.
- [55] A.J. Wilkinson, G. Meaden, D.J. Dingley, High-Resolution Elastic Strain Measurement from Electron Backscatter Diffraction Patterns: New Levels of Sensitivity, *Ultramicroscopy*. 106 (2006) 307–313. doi:http://dx.doi.org/10.1016/j.ultramic.2005.10.001.
- [56] J. Jiang, T.B. Britton, A.J. Wilkinson, Measurement of geometrically necessary dislocation density with high resolution electron backscatter diffraction: Effects of detector binning and step size, *Ultramicroscopy*. 125 (2013) 1–9. doi:10.1016/j.ultramic.2012.11.003.
- [57] T.J. Ruggles, T.M. Rampton, A. Khosravani, D.T. Fullwood, The effect of length scale on the determination of geometrically necessary dislocations via EBSD continuum dislocation microscopy, *Ultramicroscopy*. 164 (2016) 1–10. doi:10.1016/j.ultramic.2016.03.003.
- [58] T. Benjamin Britton, A.J. Wilkinson, Stress fields and geometrically necessary dislocation density distributions near the head of a blocked slip band, *Acta Mater.* 60 (2012) 5773–5782. doi:10.1016/j.actamat.2012.07.004.
- [59] J. Jiang, T.B. Britton, A.J. Wilkinson, Evolution of dislocation density distributions in copper during tensile deformation, *Acta Mater.* 61 (2013) 7227–7239. doi:10.1016/j.actamat.2013.08.027.
- [60] J. Jiang, J. Yang, T. Zhang, J. Zou, Y. Wang, F.P.E. Dunne, et al., Microstructurally sensitive crack nucleation around inclusions in powder metallurgy nickel-based superalloys, *Acta Mater.* 117 (2016) 333–344. doi:10.1016/j.actamat.2016.07.023.
- [61] R.P. Gangloff, H.M. Ha, J.T. Burns, J.R. Scully, Measurement and Modeling of Hydrogen Environment-Assisted Cracking in Monel K-500, *Metall. Mater. Trans. A.* 45 (2014) 3814–3834. doi:10.1007/s11661-014-2324-z.
- [62] D.H. Lassila, H.K. Birnbaum, Intergranular fracture of nickel: the effect of hydrogen-sulfur co-segregation, *Acta Metall.* 35 (1987) 1815–1822. doi:10.1016/0001-6160(87)90127-1.
- [63] A. Oudriss, J. Creus, J. Bouhattate, E. Conforto, C. Berziou, C. Savall, et al., Grain size and grain-boundary effects on diffusion and trapping of hydrogen in pure nickel, *Acta Mater.* 60 (2012) 6814–6828. doi:DOI 10.1016/j.actamat.2012.09.004.
- [64] S. Bechtle, M. Kumar, B.P. Somerday, M.E. Launey, R.O. Ritchie, Grain-boundary engineering markedly reduces susceptibility to intergranular hydrogen embrittlement in metallic materials, *Acta Mater.* 57 (2009) 4148–4157. doi:10.1016/j.actamat.2009.05.012.
- [65] M. Seita, J.P. Hanson, S. Gradečak, M.J. Demkowicz, The dual role of coherent twin boundaries in hydrogen embrittlement, *Nat. Commun.* 6 (2015) 6164. doi:10.1038/ncomms7164.
- [66] N. Winzer, O. Rott, R. Thiessen, I. Thomas, K. Mraczek, T. Höche, et al., Hydrogen diffusion and trapping in Ti-modified advanced high strength steels, *Mater. Des.* 92 (2016) 450–461. doi:10.1016/j.matdes.2015.12.060.
- [67] L. Liu, C. Zhai, C. Lu, W. Ding, A. Hirose, K.F. Kobayashi, Study of the effect of ?? phase on hydrogen embrittlement of Inconel 718 by notch tensile tests, *Corros. Sci.* 47 (2005) 355–367. doi:10.1016/j.corsci.2004.06.008.
- [68] N. Bandyopadhyay, J. Kameda, C.J. McMahon, Hydrogen-Induced Cracking in 4340-Type Steel: Effect of Composition, Yield Strength, and H₂ Pressure, *Metall. Trans. A.* 14A (1983) 881–888.

- [69] B.A. Kehler, J.R. Scully, Predicting the effect of applied potential on crack tip hydrogen concentration in low-alloy martensitic steels (Reprinted from Proceedings of the CORROSION/2007 research topical symposium “Advances in Environmentally Assisted Cracking”, 2007), *Corrosion*. 64 (2008) 465–477.
- [70] M. Yamaguchi, M. Shiga, H. Kaburaki, Grain Boundary Decohesion by Impurity Segregation in a Nickel-Sulfur System, *Science* (80-.). 307 (2005) 393–398.
- [71] M. Yamaguchi, M. Shiga, H. Kaburaki, Grain Boundary Decohesion by Sulfur Segregation in Ferromagnetic Iron and Nickel —A First-Principles Study, *Mater. Trans.* 47 (2006) 2682–2689. doi:10.2320/matertrans.47.2682.
- [72] B. Kagay, K. Findley, S. Coryell, A.B. Nissan, Effects of alloy 718 microstructure on hydrogen embrittlement susceptibility for oil and gas environments, *Mater. Sci. Technol.* 32 (2016) 697–707. doi:10.1080/02670836.2016.1139225.
- [73] G.K. Dey, P. Mukhopadhyay, Precipitation in the Ni-Cu-base alloy Monel K-500, *Mater. Sci. Eng.* 84 (1986) 177–189. doi:10.1016/0025-5416(86)90236-3.
- [74] G.K. Dey, R. Tewari, P. Rao, S.L. Wadekar, P. Mukhopadhyay, Precipitation hardening in nickel-copper base alloy monel K 500, *Metall. Trans. A.* 24 (1993) 2709–2719. doi:10.1007/BF02659495.
- [75] D.H. Lassila, H.K. Birnbaum, The effect of diffusive hydrogen segregation on fracture of polycrystalline nickel, *Acta Metall.* 34 (1986) 1237–1243. doi:10.1016/0001-6160(86)90010-6.
- [76] A.H. Windle, G.C. Smith, The Effect of Hydrogen on the Deformation and Fracture of Polycrystalline Nickel, *Met. Sci. J.* 4 (1970) 136–144. doi:10.1179/msc.1970.4.1.136.
- [77] T. Boniszewski, G. Smith, The influence of hydrogen on the plastic deformation ductility, and fracture of nickel in tension, *Acta Metall.* (1963).

Chapter 2. Mechanistic assessment of hydrogen-induced cracking in Ni

2.1. Overview

Uniaxial mechanical testing conducted at room temperature (RT) and 77 K on hydrogen-exposed polycrystalline nickel was coupled with targeted microscopy to evaluate the influence of deformation temperature, and therefore mobile hydrogen (H)-deformation interactions, on hydrogen-induced intergranular cracking. Results from interrupted tensile tests conducted at cryogenic temperatures (77 K), where mobile H-deformation interactions are effectively precluded, and RT, where mobile H-deformation interactions are active, indicate that mobile H-deformation interactions are not an intrinsic requirement for hydrogen-induced intergranular fracture. Moreover, an evaluation of the true strain for intergranular microcrack initiation for testing conducted at RT and 77 K suggests that H which is segregated to grain boundaries prior to the onset of straining dominates the H-induced fracture process for the prescribed H concentration of 4000 appm. Finally, recent experiments suggesting that H-induced fracture is predominately driven by mobile H-deformation interactions, as well as the increased susceptibility of coherent twin boundaries to H-induced crack initiation, are re-examined in light of these new results.

Note: One (1) peer-reviewed journal article has been published based on the work presented in this chapter, which can be accessed using the details below:

1. **Z.D. Harris**, S.K. Lawrence, D.L. Medlin, G. Guetard, J.T. Burns, and B.P. Somerday, “Elucidating the contribution of mobile hydrogen-deformation interactions to hydrogen-induced intergranular cracking in polycrystalline nickel”, *Acta Materialia*, vol. 158, pp. 180-192, 2018.
 - a. Harris contribution: primary performer; conducted tensile experiments, analyzed data, performed specimen characterization, wrote manuscript.

2.2. Introduction

As reviewed in Chapter 1, numerous mechanisms for hydrogen embrittlement have been proposed in the literature, with the most commonly invoked being: H-enhanced localized plasticity (HELP) [1], H-enhanced decohesion (HEDE) [2,3], adsorption-induced dislocation emission (AIDE) [4], H-enhanced, strain-induced vacancy mechanism (HESIV) [5], and hydride formation [6]. Each of these proposed mechanisms claim support from both theoretical and experimental results, but the multi-faceted nature of H-induced degradation, as well as the likelihood of mechanism synergy [7], complicates the universal application of any one paradigm. However, a consistent theme amongst the proposed mechanisms is the assumption that H-induced degradation is principally driven by a localized H-microstructure interaction. In particular, recent research has collectively highlighted the interaction between mobile H and deformation as a possible contributor to H-induced intergranular fracture. For example, H has been found to lower the barrier for homogeneous dislocation nucleation [8], increase dislocation mobility [9], decrease the energy required for vacancy and vacancy cluster formation [10], and suppress dislocation cross-slip [7,11]. Mechanistically, one notable example of this focus on H-enhanced degradation is the recent evaluation of near-fracture surface dislocation structures in H-charged iron and nickel *via* a combinatory transmission electron microscopy (TEM)/focused ion beam (FIB) technique [12–14]. In these studies, the authors conclude that H-induced intergranular fracture ultimately proceeds *via* decohesion of grain boundaries due to the attainment of a critical localized stress and H concentration combination (*i.e.* HEDE), which is primarily driven by the interaction between H and dislocations (*i.e.* HELP) [13]. This conclusion was reached based on observations of a systematic refinement in the dislocation cell structure of H-charged specimens relative to similarly strained non-charged specimens. Such a refinement has also been reported in other TEM-based studies on Ni, Pd, and Al alloys [15–18], and is directionally consistent with x-ray diffraction (XRD)-based peak broadening measurements in Pd [17,18]. However, while these experiments have provided critical new insights into H-dislocation interactions and their possible contribution to H-induced intergranular fracture, they do not quantitatively establish the dominance of mobile H-deformation interactions in determining the conditions required for intergranular fracture. Specifically, the contribution of the initial grain boundary H concentration (*i.e.* the H present on the grain boundary *prior* to the onset of deformation) relative to the role of mobile H-deformation interactions in conditioning the grain boundaries for intergranular cracking remains unclear.

Quantifying the contribution of the initial grain boundary H concentration versus that of mobile H-deformation interactions is complicated by their concurrent (and likely synergistic) nature. However, literature results suggest that mobile H-deformation interactions can be suppressed at cryogenic

temperatures [1,19,20]. For example, serrated yielding of nickel attributed to H was found to diminish with decreasing temperature; specifically, serrations were not observed below 150 K for an applied strain rate of $3.33 \times 10^{-4} \text{ s}^{-1}$ [19]. This absence was attributed to the inability of H to redistribute to defects due to the significant decrease in H diffusivity at cryogenic temperatures ($D_{\text{H}} \sim 10^{-31} \text{ cm}^2/\text{s}$ at 77 K vs. $10^{-11} \text{ cm}^2/\text{s}$ at 300 K in Ni [21]). The suppression of mobile H-deformation interactions at such low temperatures is also consistent with the expectations of the original HELP formulation, which states that H shielding of dislocations is not expected to be active below 200 K in Ni alloys [1]. Therefore, it is hypothesized that the contribution of mobile H-deformation interactions to H-induced intergranular fracture relative to that of H segregated to the grain boundary prior to straining can be evaluated *via* targeted testing of pre-charged samples at two conditions: (1) room temperature, where mobile H-deformation interactions are active, and (2) cryogenic temperatures, where mobile H-deformation interactions are suppressed.

2.2.1. Chapter objective and research questions

The objective of this chapter is to systematically evaluate the influence of deformation temperature, and therefore the contribution of mobile H-deformation interactions, on H-induced intergranular fracture in nickel. Towards this end, this chapter seeks to answer the following research questions:

1. What is the relative contribution of mobile H-deformation interactions versus hydrogen segregated to the grain boundary prior to deformation to the conditions required for intergranular crack initiation?
2. What is the relative contribution of mobile H-deformation interactions versus hydrogen segregated to the grain boundary prior to deformation to intergranular crack evolution?

2.3. Experimental methods and material

2.3.1. Material

All experiments were conducted on commercially-pure, polycrystalline nickel (Ni-201) obtained from ThyssenKrupp VDM USA, Inc. in the form of a 13.2 mm-thick plate. The grain structure was nominally equiaxed with an average grain size of 35 μm and the impurity content was measured *via* glow discharge mass spectrometry as (in wt. %) 0.0048 Cu, 0.062 Fe, 0.09 Mn, 0.00016 P, 0.00013 S, and 0.046 Si.

2.3.2. Mechanical Testing

Uniaxial tensile tests were performed on an MTS 810 servohydraulic load frame operated under actuator displacement control at a constant displacement rate of 0.0078 mm/s, yielding a strain rate of $4 \times 10^{-4} \text{ s}^{-1}$ (calculated by dividing the displacement rate by the specimen gage length). Cylindrical tensile

specimens were machined with a gage length of 19 mm; gage diameters of 4.0 and 3.6 mm were used for testing at 77 K and RT, respectively. Prior to straining, H-charged specimens that had been cryogenically stored were held at room temperature (RT, ~298 K) for one hour, so as to allow H to redistribute and reach the equilibrium grain boundary hydrogen concentration for this temperature [22]. This RT aging step also ensured that an equivalent grain boundary H concentration was established in each specimen prior to the onset of straining at either testing temperature. As every specimen was H charged, cryogenically stored, and RT aged in an identical manner, the important assumption of an equivalent *initial* grain boundary H concentration (*i.e.* at the onset of testing) from specimen-to-specimen is justified from both a thermodynamic and kinetic perspective [22–24].

Testing at 77 K was completed with the aid of an immersion chamber, which was filled with liquid nitrogen (LN₂) and did not impede the load train. After the one hour hold at RT, specimens designated for testing at 77 K were fully immersed in LN₂ for approximately ten minutes prior to the onset of testing – this corresponded to the time at which the specimen and LN₂ were thermally equilibrated (*i.e.* minimal boiling). Each uniaxial tensile test was designed to either be interrupted at a prescribed strain or strained to failure. Tests to failure proceeded until final fracture, whereas interrupted testing was halted at a targeted strain value estimated *via* the actuator displacement for testing at 77 K or an attached extensometer for testing at RT. At the employed displacement rate, testing to failure was completed in less than 15 and 30 minutes for experiments at RT and 77 K, respectively. Interrupted specimens were slowly unloaded upon test completion (~2 kN/minute) to minimize the possibility of compressive loading. The applied strain was evaluated post-test through the calculation of the true plastic strain (ϵ_T) *via* the reduction in area (RA); the use of the true plastic strain allows for direct comparison between specimens, including those specimens which exhibited necking. ϵ_T is calculated as follows:

$$\epsilon_T = -\ln(1 - RA) \quad (2.1)$$

where RA is the reduction in area, defined by:

$$RA = \frac{d_i^2 - d_f^2}{d_i^2} \quad (2.2)$$

where d_f and d_i are the final and initial diameters of the gage section, respectively. Diameter measurements were taken at the center of the specimen gage section using either a laser micrometer or digital calipers with knife edges. If a specimen necked, the diameter measurement was taken as the minimum diameter in the necked region as measured *via* laser micrometer.

2.3.3. Hydrogen Charging

Atomic H was introduced into the tensile specimens *via* thermal charging; a detailed overview of this charging procedure is reported elsewhere [23,25]. Briefly, specimens were placed inside an autoclave mounted within a furnace, which was heated to 573 K and then filled with 99.9999% pure hydrogen gas until the target charging pressure of 96.5 MPa was reached. The system was then held at these conditions for approximately 144 hours to allow sufficient time for the development of a uniform H concentration across the specimen diameter [23]. The anticipated lattice H concentration under these charging conditions is approximately 4000 atomic parts per million (appm) [23]. Upon removal from the furnace, specimens were immediately stored in a cryogenic freezer maintained at 223 K; minimal H egress is expected under these conditions given the slow H diffusivity ($\sim 2 \times 10^{-12}$ cm²/s [26]).

To confirm the targeted theoretical concentration was achieved, the H concentrations of two small pieces sectioned from the gage length of a non-strained specimen were evaluated using an inert gas fusion analyzer. Hydrogen concentrations of 78 and 81 weight parts per million (wppm) were measured in these specimens, corresponding to an average hydrogen concentration of approximately 4660 appm. This deviation between the theoretical and measured hydrogen concentration is consistent with previously measured differences for thermally-charged Ni-201 [23]. As the referenced theoretical calculations only estimate the equilibrium concentration of hydrogen in the lattice, the measured hydrogen concentration is expected to differ from calculated values due to hydrogen trapped at grain boundaries, dislocations, and other defects [23].

2.3.4. Microscopy

Interrupted specimens were sectioned at the gage diameter midpoint along the longitudinal axis using electrical discharge machining. Sectioned specimens were then mounted in epoxy and mechanically polished, finishing with 0.05 μ m colloidal silica. Scanning electron microscopy (SEM) was used to identify and measure the number and length of intergranular microcracks in the interrupted specimens as well as to examine the fracture morphology of specimens strained to failure. Microcracks were classified as intergranular based on two criteria: (1) the microcrack clearly propagated along the grain boundary and (2) the aspect ratio (length to width) was greater than five. The aspect ratio requirement was implemented to ensure extraneous features, such as pores which appeared randomly on grain boundaries, were excluded from the analysis. Examples of such features are shown in Figure 1a (white arrows) for a non-strained, H-charged specimen prepared in an identical manner to the interrupted specimens. The approximate length of each observed microcrack was measured along the centerline of the crack, with the line of measurement following the general shape of the microcrack. For all but the highest strain values, an area of 14.11 mm² was systematically searched (with the center of the specimen gage section or necked region as the area

centroid) at a magnification of 355x using both backscatter and secondary electron imaging modes. Backscattered electrons provide grain contrast, which can be used to identify the location of grain boundaries, as shown in Figure 1a. For specimens with extensive straining and associated degree of microcracking, the observation area was reduced from 14.11 mm² due to the large number of observed microcracks. As such, reported crack lengths and number of microcracks are normalized by the observed area to remove any effect from differences in evaluated area. Orientation imaging microscopy (OIM) (Figure 1b) was completed *via* electron backscatter diffraction (EBSD) using an accelerating voltage of 20 kV, a step size of 1 μm, and a probe current of 7 nA. OIM maps were evaluated using the Tango (Oxford Instruments) post-processing software to ascertain grain size and confirm the accuracy of the grain boundary identification procedure detailed above.

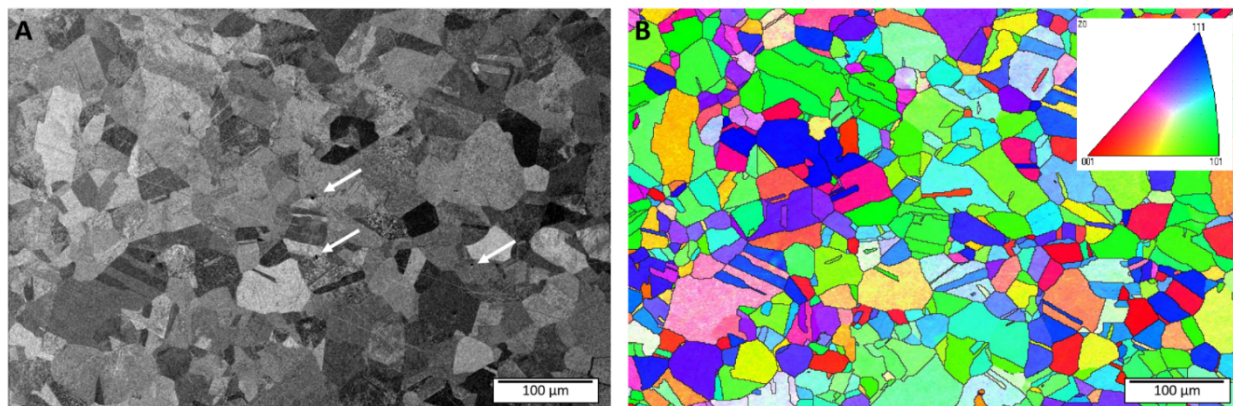


Figure 1 – Comparison between (a) scanning electron micrograph and (b) inverse pole figure (IPF) map via EBSD of a non-strained tensile specimen of Ni-201 charged with hydrogen. Note the presence and location of the pore-like features (white arrows), particularly with respect to grain boundaries.

A transmission electron microscopy study was also conducted to evaluate the influence of deformation temperature on the dislocation substructure. Tensile specimens for this study were charged to a H concentration of 3000 appm (144 hours at a pressure of 62 MPa and temperature of 573 K) and deformed to a true strain of 0.10 at RT and 77K (one specimen at each temperature). Electron-transparent TEM foils were prepared by electropolishing slices taken from the gage section of the tensile specimens (the foils were oriented normal to the longitudinal axis). Electropolishing was performed at a potential of 11 V using a solution of 20 vol. % perchloric acid/80 vol. % acetic acid cooled in the range of 5°C to 0°C. Observations were conducted using an FEI Titan TEM operated at 200 keV using the diffraction contrast scanning transmission electron microscopy (DC-STEM) method [27]. Images were obtained in an on-zone condition with the selected grains oriented primarily along either a $\langle 110 \rangle$ or $\langle 112 \rangle$ zone axis (one data set

was collected along $\langle 310 \rangle$ and another along $\langle 114 \rangle$). The advantages of this imaging technique are discussed in detail in Chapter 6.

To compare the length-scale distributions of the dislocation cells observed in the DC-STEM images, a random linear intercept method was implemented using Matlab. The first step in this procedure was to binarize the images. Long-range variations in image intensity were flattened by convolving each image with a disc blurring function (164 nm diameter) and then subtracting this background intensity from the original image. The background subtracted images were then thresholded to generate binarized images (typical threshold levels were between 5% and 15% of the average background intensity). A 3x3 pixel-wide median filter was then applied to clean up single-pixel noise. For the intercept analysis, 10 lines were constructed at random over each image and the length distribution of line segments falling within the cell-wall interiors were tabulated. A total of eight micrographs (area of $44.9 \mu\text{m}^2$ for each image, sampled at 3.27 nm/pixel) were analyzed for each specimen (across 4 grains at RT and 6 grains at 77 K), yielding approximately 4000 intercept measurements per specimen.

2.4. Results

2.4.1 Testing to Failure

Four specimens, representing the H-charged/RT (H/RT), non-charged/RT (no H/RT), H-charged/77 K (H/77K), and non-charged/77 K (no H/77 K) conditions, were strained to failure to determine tensile properties and predominant fracture morphology under each H/temperature combination. The engineering stress-strain and calculated true stress-strain curves for each testing condition are shown in Figure 2a and Figure 2b, respectively. Pertinent tensile properties are reported in Table 1. As expected from previous literature results [19,20,23], a substantial decrease in RA was measured between the H-charged and non-charged specimens. Specifically, the RA value for H/RT was approximately 18% of the RA measured for no H/RT, while the RA for H/77K was 50% of no H/77K. Using these measured RA values and Equation 1, a strain-to-failure was calculated for both H-charged conditions. This true fracture strain is 0.176 for H/RT and 0.535 for H/77 K (see Table 1); these values represent the maximum targeted strains for subsequent interrupted testing.

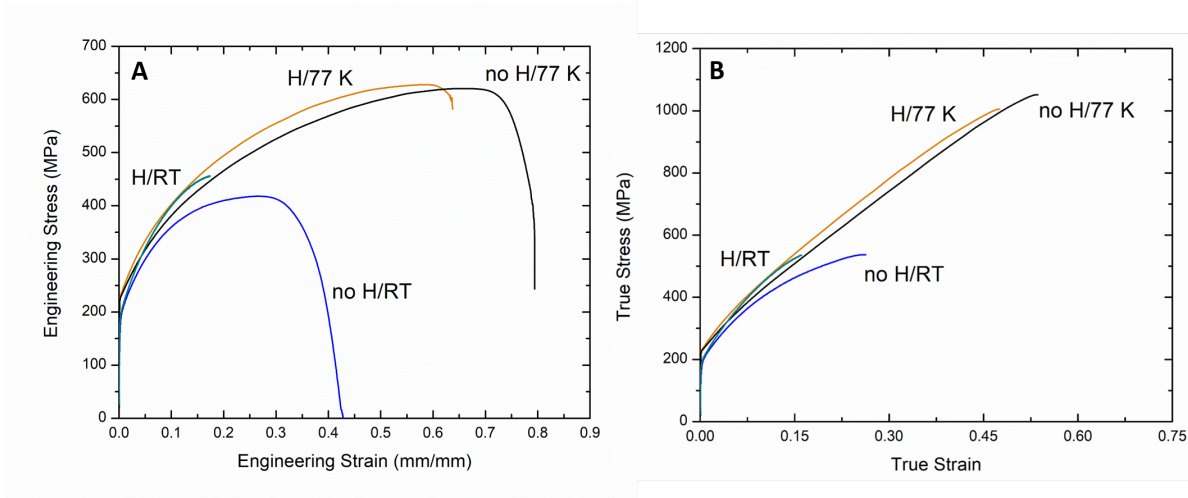


Figure 2 - (a) Engineering and (b) calculated true stress-strain curves for both H-charged and non-charged Ni-201 specimens strained to failure at room temperature (RT) and 77 K using an applied strain rate of $4 \times 10^{-4} \text{ s}^{-1}$. Note that the curves for testing at 77 K are estimated using the actuator displacement and that the true stress-strain curves are truncated at the stress corresponding to the onset of necking.

Fractography of the four tested conditions, shown in Figure 3 for testing at RT and in Figure 4 for testing at 77 K, corroborates the observed differences in ductility. No H/RT (Figure 3a-b) displayed extensive evidence of ductile failure *via* microvoid coalescence, while H/RT (Figure 3c-d) clearly exhibited intergranular fracture. However, fine slip traces (not shown) were observed on the intergranular facets of H/RT, suggesting some plastic deformation occurred prior to failure, consistent with other results for hydrogen-charged nickel [13,23]. No H/77 K (Figure 4a-b) had a similar morphology as no H/RT, though the dimples found at 77 K were generally smaller than those observed at RT. Interestingly, H/77 K (Figure 4c-d) exhibited facets resulting from intergranular fracture as well as evidence of ductile fracture, consistent with the higher degree of plastic deformation sustained prior to fracture (Figure 2).

Table 1 – Mechanical properties from testing to failure

Testing Condition	Yield Strength (MPa)	Ultimate Tensile Strength (MPa)	Work Hardening Rate at 6% Strain (MPa)	Reduction of Area (%)	True Fracture Strain
No H/77 K	222	620	1418	82.5	1.75
H/77 K	233	627	1548	41.4	0.535
No H/RT	182	418	1430	89.7	2.27
H/RT	192	456	1705	16.2	0.176

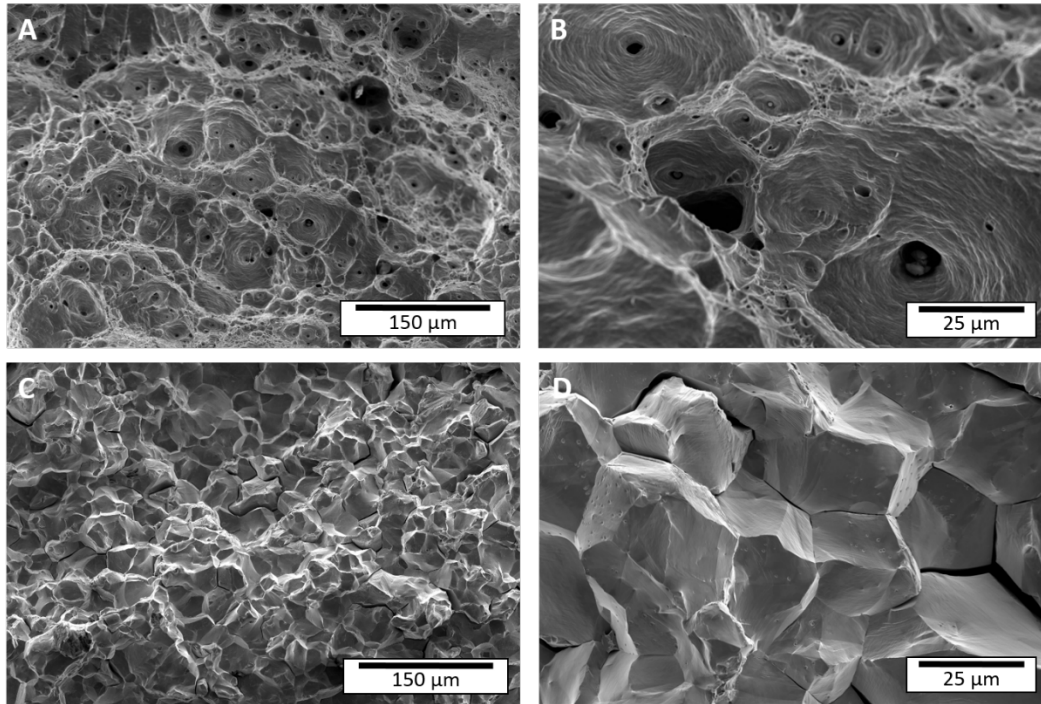


Figure 3 – Low and high magnification fractographs of the non-charged (a,b) and H-charged (c,d) Ni-201 specimens tested to failure at RT.

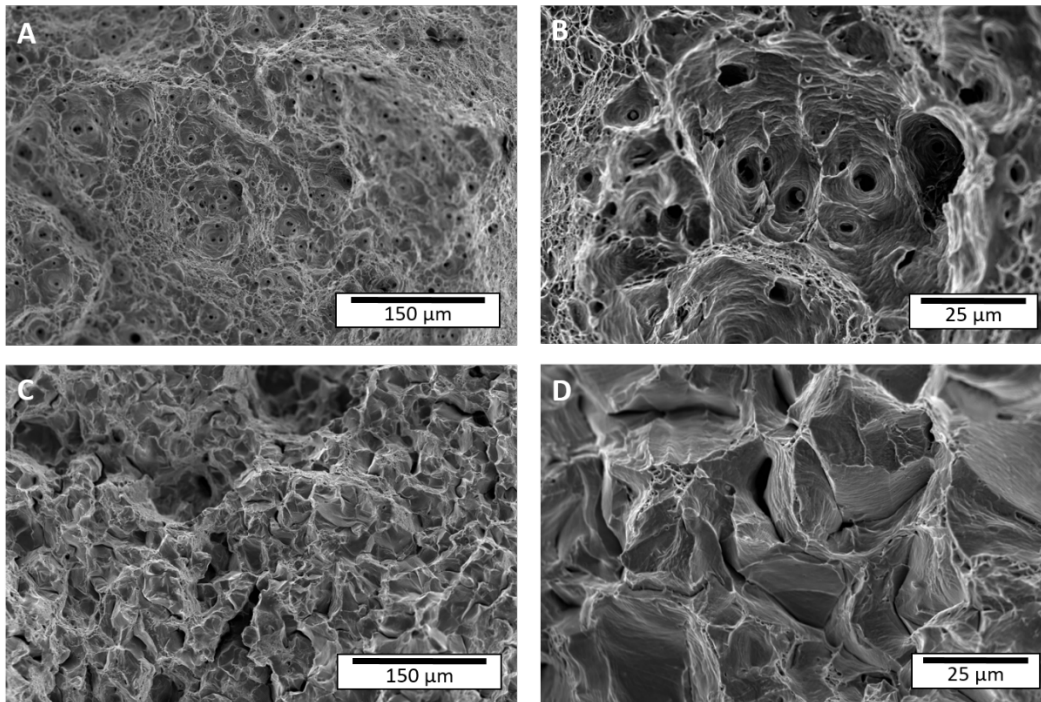


Figure 4 – Low and high magnification fractographs of the non-charged (a,b) and H-charged (c,d) Ni-201 specimens tested to failure at 77 K.

2.4.2. Evaluation of Intergranular Microcracks in Interrupted Specimens

The RA, calculated true plastic strain, observed area, number of intergranular microcracks, average and standard deviation in measured crack lengths, and cumulative crack length measured for each interrupted test at RT and 77 K are presented in Table 2, along with the normalized cracks per area (CPA) and total crack length per area (CLPA) values. Testing to true plastic strains of 0.1 and 0.15 was conducted at both 77 K and RT to enable a comparison at equivalent strain values. Representative micrographs of microcracks observed in specimens strained to 0.15 at RT and 77 K are shown in Figure 5a-d. Higher magnification images (Figure 5c and Figure 5d) demonstrate that the microcracks do propagate along grain boundaries at both RT and 77 K. Critically, despite nominally equivalent true plastic strain levels and a six-fold increase in evaluated area at 77 K (RT: 2.28 mm², 77 K: 14.11 mm²), significantly more intergranular microcracks were observed in the RT specimen as compared to the 77 K specimen (77 vs. 3, respectively).

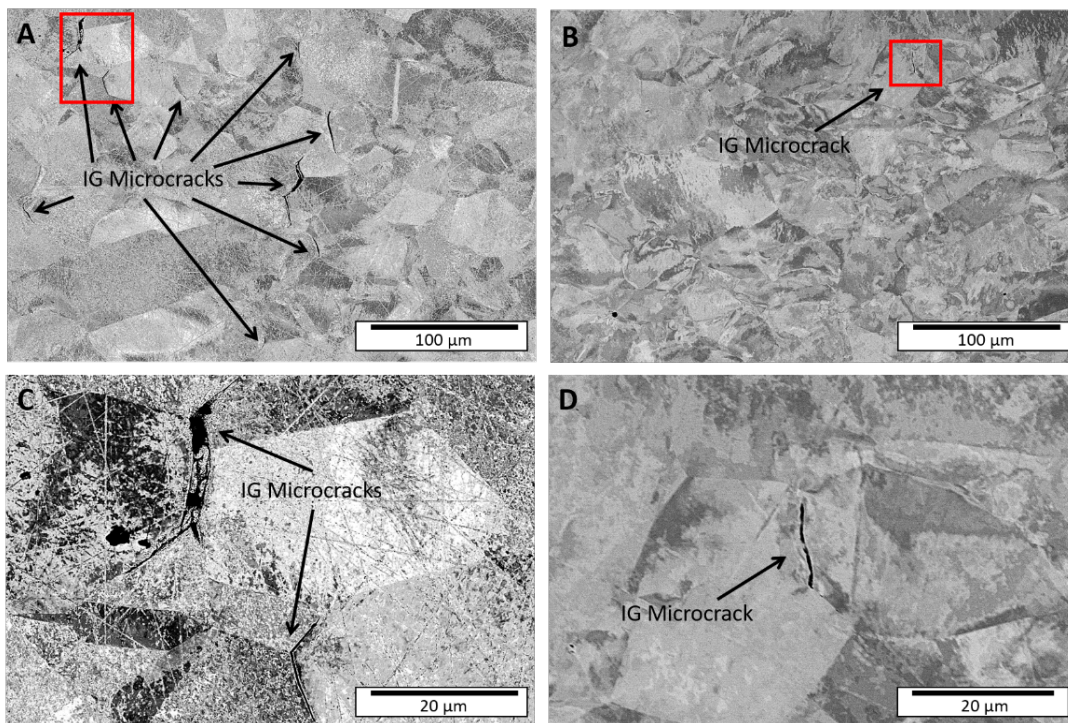


Figure 5 – Representative backscattered electron SEM micrographs demonstrating intergranular (IG) microcrack locations for H-charged specimens strained to a true strain of 0.15 at (a) RT and (b) 77 K. High magnification images of the areas in (a) and (b) outlined by the red boxes are shown in (c) and (d), respectively.

To better understand the influence of deformation temperature on intergranular microcrack initiation and evolution¹, the CPA, CLPA, and average crack length for each interrupted test are plotted as a function of true plastic strain in Figure 6a-c, respectively. Three distinct trends can be observed from these data. First, testing at both 77 K and RT exhibited a characteristic “initiation” strain at which both the number and cumulative length of microcracks per area began to rapidly increase. If the true plastic strain for microcrack initiation (ϵ_i) is defined as the point at which CPA is greater than unity, ϵ_i can be approximated as 0.12 and 0.2 for testing conducted at RT and 77 K, respectively. Second, a clear difference in the evolution of intergranular microcracks is observed between the two testing temperatures. Specifically, the difference between the true fracture strain (Table 1) and the initiation strain is quite small at RT ($\Delta\epsilon \approx 0.056$) as compared to 77 K ($\Delta\epsilon \approx 0.335$). Stated otherwise, testing at RT rapidly proceeds to failure after the initiation of microcracks, while testing at 77 K exhibits a more gradual evolution of intergranular microcracking leading to final fracture. Third, despite these differences in initiation/evolution, the average crack length (Figure 6c; symbols) is effectively constant as a function of both true plastic strain and deformation temperature, though the standard deviation (error bars) does increase with true plastic strain for both deformation temperatures.

2.4.3. *Quantifying the Variability of Intergranular Microcrack Metrics*

Accurate interpretation of the measured CPA inherently requires this metric to have been evaluated over a sufficiently large area such that calculated values are: (1) repeatable and (2) accurately reflect global behavior. Statistical frameworks provide the means by which to quantitatively determine the expected variability in CPA if the measurements were repeated using a different observation area. Using the statistics of a binomial distribution, the expected variation in CPA can be evaluated using the area of observation, the number of cracked grain boundaries, and the total number of grain boundaries observed for each interrupted test [28]. In this analysis, grain boundaries, as opposed to the number of microcracks, are employed due to the inherent assumptions of a binomial distribution, *i.e.* only two discrete outcomes are allowed (boundaries can either be cracked or not cracked). Moreover, grain boundaries are considered a reasonable proxy for the number of microcracks, as at least one grain boundary must have fractured for every observed microcrack.

¹Microcrack evolution refers to the increase in the **number** and **total length** of intergranular microcracks per area with increasing true plastic strain. Moreover, it should be noted that this approach does not follow the progression of a single microcrack, but instead compares the observed population of microcracks across separate specimens.

Table 2 - Results of interrupted testing

Reduction of Area (%)	True Plastic Strain	Number of IG Cracks	Total Crack Length (μm)	Average Crack Length (μm)	Standard Deviation of Crack Length (μm)	Area Observed (mm^2)	Cracks Per Area ($\#/\text{mm}^2$)	Total Crack Length Per Area ($\mu\text{m}/\text{mm}^2$)
Testing at 77 K								
9.9	0.104	1	12.0	12.0	0	14.11	0.07	0.85
12.3	0.131	1	1.2	1.2	0	14.11	0.07	0.09
13.9	0.15	3	5.6	1.9	5.85	14.11	0.21	0.40
18.1	0.2	13	145.8	11.2	7.48	14.11	0.92	10.3
20.6	0.231	53	474.5	8.9	7.71	14.11	3.76	33.6
24.9	0.286	33	450.2	13.6	8.42	3.005	11.0	150
27.9	0.328	21	266.0	12.7	11.28	0.56	37.5	475
30.7	0.367	52	842.2	16.2	15.7	0.56	93.0	1504
42	0.545	71	1261.4	17.8	36.8	0.56	126	2252
Testing at RT								
3.6	0.036	1	25.2	25.2	0	14.11	0.07	1.79
5.6	0.058	3	31.9	10.6	3.18	14.11	0.21	2.26
9.8	0.103	4	47.0	11.8	7.3	14.11	0.28	3.33
11.2	0.119	8	108.2	13.5	8.74	14.11	0.56	7.67
13.8	0.148	77	904.7	11.8	5.93	2.277	33.8	397

Table 3 – Analysis of variation in microcrack metrics for interrupted testing

True Plastic Strain	Number of Cracked Grain Boundaries	Total Number of Grain Boundaries Observed	Cracked Fraction of Grain Boundaries	Calculated Variation (# of GBs)	Number of Cracked Grain Boundaries Per Area (#/mm ²)	Variation in Number of Cracked Grain Boundaries Per Area (#/mm ²)
Testing at 77 K						
0.104	2	30690	6.5x10 ⁻⁵	1.4	0.14	0.1
0.131	1	30690	3.3x10 ⁻⁵	1	0.07	0.07
0.15	5	30690	1.6x10 ⁻⁴	2.2	0.35	0.16
0.2	20	30690	6.5x10 ⁻⁴	4.5	1.42	0.32
0.231	88	30690	2.8x10 ⁻³	9.4	6.24	0.67
0.286	55	6537	8.4x10 ⁻³	7.4	18.3	2.46
0.328	44	1218	0.036	6.5	78.6	11.6
0.367	112	1218	0.092	10.1	200	18.0
0.545	167	1218	0.137	12	298	21.4
Testing at RT						
0.036	2	30690	6.5x10 ⁻⁵	1.4	0.17	0.10
0.058	3	30690	9.8x10 ⁻⁵	1.7	0.21	0.12
0.103	7	30690	2.3x10 ⁻⁴	2.6	0.50	0.18
0.119	10	30690	3.3x10 ⁻⁴	3.2	0.71	0.23
0.148	127	4953	0.026	11.1	55.8	4.87

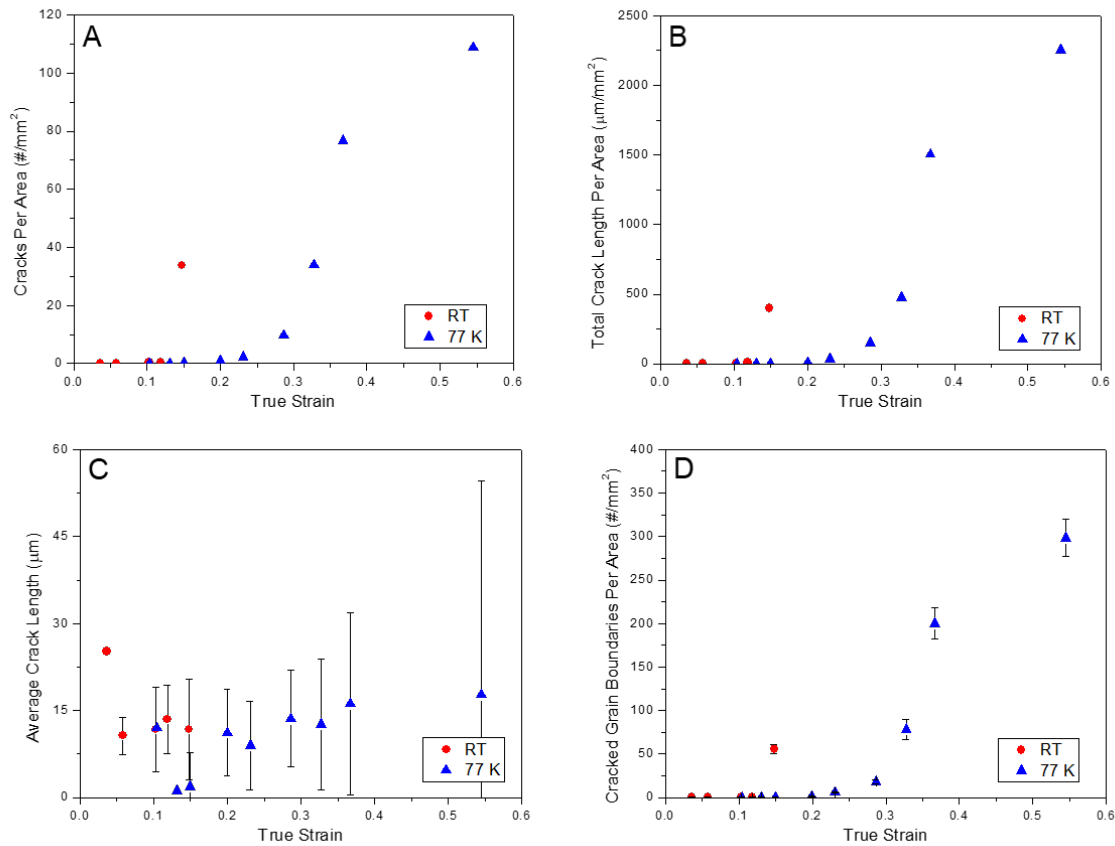


Figure 6 – Plots of (a) CPA, (b) CLPA, (c) average crack length, and (d) cracked grain boundaries per area versus true strain for interrupted testing conducted on H-charged specimens at RT and 77 K.

The measured number of cracked grain boundaries as a function of deformation temperature and true plastic strain are listed in Table 3. Differences in observation area are accounted for by the total number of grain boundaries observed, also shown in Table 3, which is calculated as follows. Assuming a hexagonal shape for each grain, the number of grain boundaries can be approximated as three times the number of observed grains (since two grains share each individual boundary). High strains will modify the microstructure and complicate quantification of the observed grains from OIM results. As such, the number of observed grains in each specimen was estimated *via* the product of the observed area and a grains-per-area multiplier (725 grains/mm²) obtained from an OIM map of a non-strained, H-charged specimen (Figure 1b). This calibration specimen was charged with a H content of 3000 appm (62 MPa H₂ gas, 573 K, 144 hours) and then sectioned in a similar manner as the interrupted specimens; the grain size is not expected to differ between this sample and the 4000 appm specimens as the charging time and temperature are

identical. It should be noted that this analysis inherently assumes that each grain boundary has an equal probability of cracking. While physically unrealistic, this assumption is a reasonable simplification as $\Sigma 3$ boundaries (which are argued to be less susceptible than random high-angle boundaries [23]) were excluded from the grain size calculation used to determine the grains per area multiplier. As such, the number of observed grain boundaries shown in Table 3 is (1) a lower-bound for the total number of grain boundaries and (2) nominally composed of only susceptible “high-angle” grain boundaries.

From the data in Table 3, the fraction of cracked grain boundaries (p_c) can be obtained as follows:

$$p_c = \frac{y_c}{N_c} \quad (2.3)$$

where y_c and N_c are the number of cracked grain boundaries observed and the total number of observed grain boundaries, respectively. This value is then used to calculate the expected variation in the number of cracked grain boundaries (σ_c):

$$\sigma_c = \sqrt{N_c p_c (1 - p_c)} \quad (2.4)$$

Values of σ_c and p_c for each interrupted test are listed in Table 3, along with their respective observation area-normalized value for σ_c . As shown in Figure 6d, the calculated variation in cracked grain boundaries per area (shown by the error bars) does increase with increasing true plastic strain. It is hypothesized that this increase is primarily due to the decreased observation area in these high strain specimens. Regardless, as shown in Table 3, this statistical analysis indicates that the expected variation is generally well below 1% of the total number of observed grain boundaries. These results quantitatively demonstrate that the measured CPA values are statistically significant and representative of the global specimen behavior, thereby justifying the use of this metric to evaluate the initiation and evolution of H-induced intergranular microcracks.

2.4.4. Evaluation of Deformation Microstructure and Dislocation-Grain Boundary Interactions at RT and 77 K

In order to isolate the effect of deformation temperature on hydrogen redistribution and its relationship to intergranular microcrack evolution, it is pertinent to evaluate whether deformation temperature modifies other factors that could strongly influence intergranular microcrack evolution, such as dislocation-grain boundary interactions and deformation substructure refinement in H-charged Ni. This confirmation is critical as the presence of significant temperature-related microstructural stresses would complicate the use of temperature as a means by which to examine the role of mobile H-deformation

interactions to intergranular cracking. Towards this end, the dislocation substructures for specimens deformed at 77K and RT were investigated using DC-STEM. As noted in Section 2.3.4., the specimens for the TEM study were charged to a hydrogen content of 3000 appm (62 MPa H₂ gas, 573 K, 144 hours) and deformed to a true plastic strain of 0.10. This difference in lattice H concentration (3000 appm vs 4000 appm) is not expected to systematically alter the effect of deformation temperature on dislocation microstructure. Moreover, given the similarity in flow curves between the specimens tested at 4000 appm herein and those strained at 3000 appm [10], the deformation substructure is not expected to vary significantly between the two H concentrations for a given applied strain and temperature.

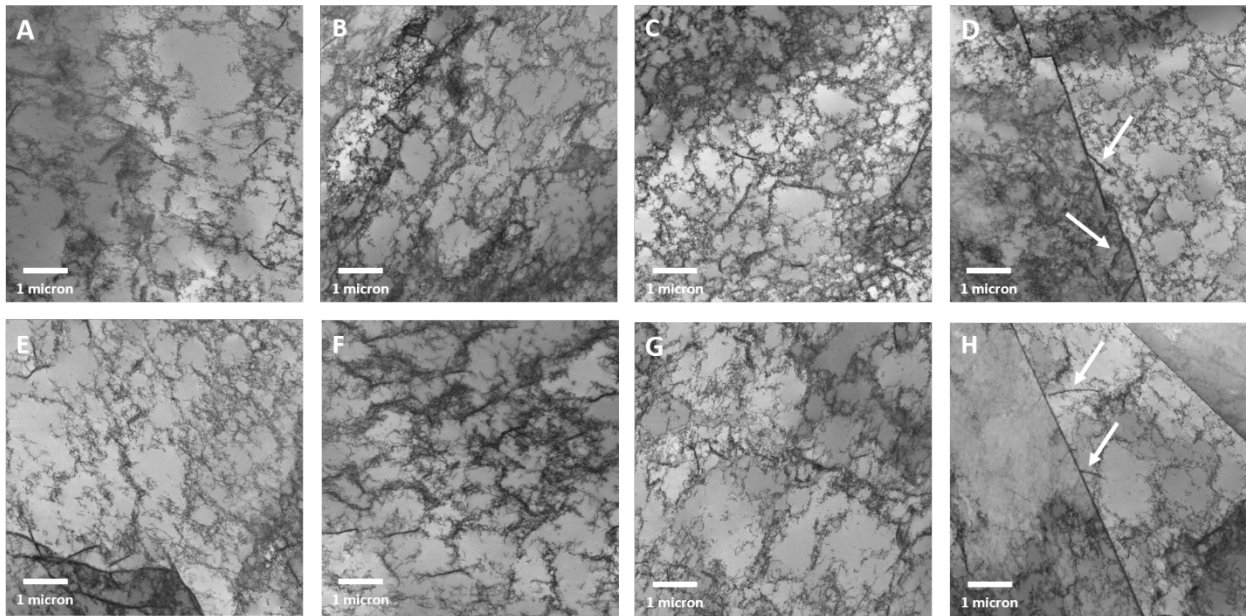


Figure 7 – DC-STEM electron micrographs of deformation structures observed in specimens charged with H to 3000 appm and deformed to a true strain of 0.10 at 77K (a-d) and RT (e-h). Image contrast is inverted for clarity. Examples of the dislocation “packet” morphologies at grain boundaries are highlighted by white arrows in (d) 77 K and (h) RT.

Micrographs taken from the interior of three different grains are shown in Figure 7a-c for 77 K and Figure 7e-g for RT. Additionally, micrographs of grain boundaries from specimens deformed at 77 K and RT are shown in Figure 7d and Figure 7h, respectively. To quantitatively compare the dislocation substructure at the two deformation temperatures, we applied a random linear intercept analysis to DC-STEM images, as described in the experimental methods section. Figure 8 plots the cumulative distributions of the intercept lengths characterizing the interior of the dislocation cells. Empirically, we found that the distribution of intercept lengths was well described by an inverse Gaussian probability density function [29]:

$$f(x; \mu, \lambda) = \left[\frac{\lambda}{2\pi x^3} \right]^{1/2} \exp \left\{ \frac{-\lambda(x - \mu)^2}{2\mu^2 x} \right\} \quad (5)$$

where μ is the mean, λ is the shape parameter, and x is the line segment length between cell walls. The parameter fits for the analyzed images are summarized in Table 4. Eight images of independent areas were analyzed for each temperature; these sampled 4 different grains for the RT deformed sample and 6 different grains for the 77 K deformed sample. Qualitatively, the distribution plots for the two sets of temperature conditions appear indistinguishable. This conclusion is supported by the parameter fits in Table 4, for which the differences for μ and λ between the two temperatures are small compared with the spread in the data.

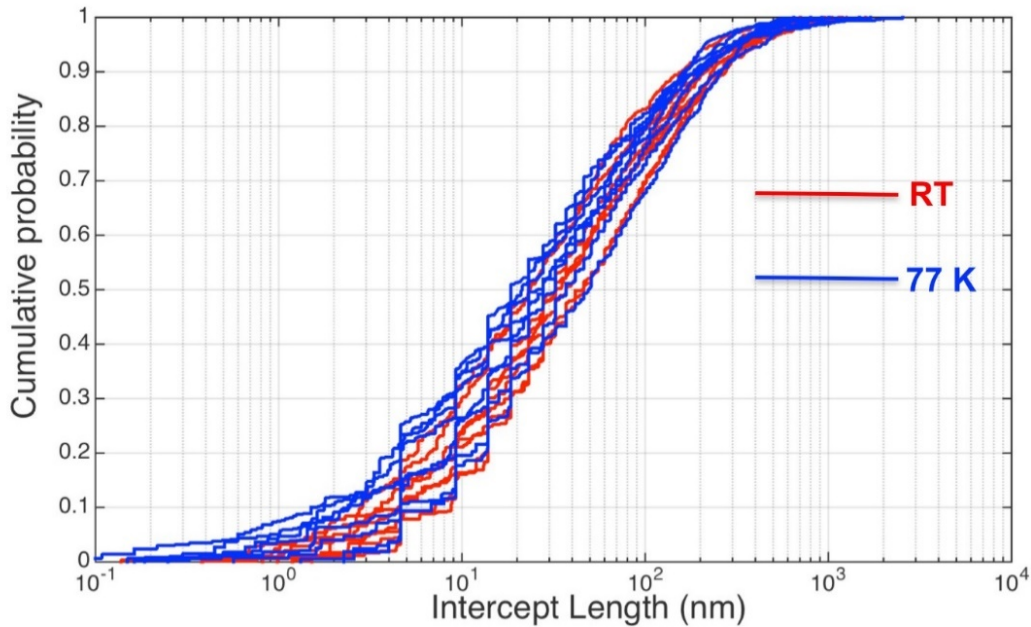


Figure 8 – Cumulative probability distributions for intercept lengths characterizing the dislocation cell configurations. 8 images were analyzed for each temperature (red: deformed at room temperature; blue: deformed at 77K). The distributions follow an inverse Gaussian function, with parameter fits given in Table 4. The distributions for the two deformation temperatures as essentially indistinguishable.

Two observations can be made from these micrographs and the analysis of the dislocation substructure distributions. First, considering grain boundary-dislocation interactions, dislocation “packets” (delineated by the white arrows in Figure 7d and Figure 7h), which intersect the grain boundary and appear to be aligned along a crystallographic plane, were observed on numerous grain boundaries at both RT and 77 K. While a detailed examination of these features is outside the scope of the current effort, it is notable that these structures occurred with similar frequency at both deformation temperatures. This similarity in

both appearance and frequency, in addition to an absence of other prominent features, suggests that grain boundary-dislocation interactions are not systematically altered at 77 K relative to RT. Second, although there is certainly image-to-image variation in the dislocation patterning, which is likely attributable to local heterogeneities in plastic strain [30], there does not appear to be a distinguishable difference in the dislocation cell distributions between the two temperatures.

2.5. Discussion

The presented flow curves (Figure 2) and fractography (Figure 3 and Figure 4) demonstrate that the true fracture strain (Table 1) of Ni-201 decreases in the presence of hydrogen at both RT and 77 K. Interrupted testing revealed differences in the normalized number and length of intergranular microcracks as a function of true strain (Figure 6) for each testing temperature. At RT, intergranular microcracks were found to initiate at a true strain of 0.12, followed by a rapid transition to failure. Conversely, specimens strained at 77 K exhibited intergranular microcrack initiation at a true strain of 0.2, with a more gradual transition to failure. Separately, Ni-201 specimens strained to 0.10 at both deformation temperatures revealed deformation microstructures that were virtually indistinguishable when examined *via* DC-STEM (Figure 7). Based on these results, the following discussion will: (1) justify the critical assumptions applied in this work, (2) quantitatively evaluate the relative contribution of mobile H-deformation interactions to HE, and (3) comment on the mechanistic implications of the current results.

2.5.1. Justification of Critical Assumptions

There are three critical assumptions in this work: (1) an equal grain boundary concentration of H was achieved prior to the onset of straining at both temperatures, (2) mobile H-deformation interactions are effectively suppressed during straining at 77 K, and (3) microstructure-level stresses promoted by deformation processes, as well as the applied macroscale remote stress, are essentially the same magnitude at 77 K and RT for a given applied strain. As discussed in Section 2.3.3., the first assumption is strongly justified from both thermodynamic and kinetic perspectives. Significant efforts were made to ensure the tensile specimens (1) originated from the same material heat, (2) were thermally charged with H concurrently, (3) were cryogenically stored under identical conditions, and (4) were aged at RT for the same amount of time prior to straining. As such, it is reasonable to conclude that the initial grain boundary H concentration was equivalent from specimen-to-specimen at the onset of straining. The second assumption is based on the findings of previous studies [1,19,21,31]. Arguments for the exclusion of mobile H-deformation interactions are based on the significant decrease in the diffusivity of H in nickel from $\sim 10^{-11}$ cm²/s at RT to $\sim 10^{-31}$ cm²/s at 77 K [21]. This sharp reduction in H diffusivity effectively prevents any deformation-related redistribution of hydrogen. As such, the processes assumed to be suppressed at 77 K are any interactions that explicitly require mobile H to operate. For example, the effect of hydrogen on

dislocation-dislocation interactions under the HELP paradigm [1], particularly the screening effect that produces enhanced dislocation mobility and increased dislocation pileups [7,11], is not active at 77 K. Similarly, the recently proposed mechanism centered on H segregation to deformation-modified defect structures at grain boundaries is also precluded [7]. However, it should be noted that this immobilization *does not* preclude all H-deformation interactions [10]. For example, as shown in Table 1 and Figure 2, differences in yield strength and work hardening rate, though modest, were observed between no H/77 K and H/77 K. While a mechanistic interpretation for these differences in mechanical properties is outside the scope of the current study, detailed insights on possible mechanisms by which hydrogen modifies the stress-strain curves at RT and 77 K are presented in Reference [10].

Finally, in reference to the third critical assumption, models for void nucleation *via* particle-matrix debonding suggest that the driving force for interface decohesion can be considered a function of both the applied remote stress and the local microstructure-level stresses (*i.e.* those due to the local defect structure) [32]. Assuming a similar paradigm is operative for grain boundary decohesion, it is therefore important to determine whether testing at 77 K causes an increase in either stress contribution as a function of applied strain for H-charged Ni-201 (relative to testing at RT). Critically, if such increases were to occur, the strain associated with the initiation of intergranular microcracks would be biased towards lower values for testing conducted at 77 K. Since this testing condition is intended to suppress deformation-induced H redistribution and therefore isolate the population of H previously segregated to the grain boundary, higher microstructure-level stresses at 77 K would artificially inflate the inferred contribution of H segregated to the grain boundary prior to straining on intergranular microcracking. Considering microstructure-level stresses, a significant influence of deformation temperature appears unlikely based on the results of the DC-STEM characterization presented in Section 2.4.4., which revealed only subtle differences in deformation structure and grain boundary-deformation interactions between the two testing temperatures. From a remote stress perspective, examination of the flow curves presented in Figure 2 for H/RT and H/77 K suggest only minor differences in work hardening behavior and flow stress as a function of strain. Specifically, the applied true stress was found to vary by less than 10% for comparable strains (Figure 2b). As such, it is unlikely that testing at 77 K led to significant variations in the driving force for intergranular microcrack initiation relative to testing at RT, suggesting that the third assumption stated above is justified. Finally, the authors acknowledge that decohesion is generally considered to be a stress-controlled phenomenon [33]. However, the use of strain as a driving force metric in this work is justified based on: (1) the true strain can be physically measured post-test with minimal ambiguity, (2) as stated above, the operative stress is composed of *both* the remote stress and the microstructure-level stresses; the latter is difficult to measure with a high degree of certainty, and (3) both the remote stress and the microstructure-level stress are generally considered to be proportional to the applied strain [32].

Table 4 - Summary of fit parameters for the inverse Gaussian distribution describing the intercept distributions measured from DC-STEM images of the dislocation substructure. The error columns tabulate the standard error in the fit for the parameter estimate.

Testing at 77 K					Testing at RT				
Image	μ (nm)	error (nm)	λ (nm)	error (nm)	Image	μ (nm)	error (nm)	λ (nm)	error (nm)
1	67.52	9.22	5.51	0.30	1	76.73	9.20	10.05	0.62
2	66.30	8.44	6.35	0.35	2	84.45	8.58	15.12	0.92
3	75.10	12.82	4.36	0.25	3	96.02	8.80	19.58	1.15
4	83.19	12.81	7.25	0.47	4	76.22	10.45	6.96	0.41
5	104.91	10.29	20.51	1.26	5	95.94	10.01	16.88	1.05
6	97.89	9.26	20.60	1.26	6	84.29	10.37	11.52	0.74
7	59.98	11.91	2.30	0.13	7	61.39	7.01	7.66	0.44
8	65.14	5.78	12.29	0.67	8	98.01	8.36	22.54	1.30
average:	77.38		9.90		average:	84.13		13.79	
st. dev.	16.59		7.17		st. dev.	12.58		5.67	

2.5.2. Quantifying the Relative Contribution of Mobile Hydrogen-Deformation Interactions to Intergranular Cracking

The relative contribution of mobile H-deformation interactions to intergranular microcrack initiation (schematically shown in Figure 9) can be quantitatively assessed as follows. First, recall that the non-charged specimen tested to failure at 77 K clearly fractured *via* ductile microvoid coalescence (Figure 4). Realizing that fracture is a competitive process, it is clear for the case of no H/77 K that the criteria (*i.e.* critical strain and/or stress) for fracture *via* microvoid coalescence were satisfied *before* the criteria for intergranular cracking were attained. Alternatively, given that brittle fracture is generally considered to be stress-controlled [33], it can be assumed that the stress required to initiate an intergranular microcrack was not achieved at the measured true fracture strain of 1.75 (Table 1). As such, assuming a constant strain across the necked region where the reduction of area was measured, the true fracture strain of 1.75 for no H/77 K can be interpreted as a lower-bound proxy for the true strain at intergranular microcrack initiation in the absence of H. Now, considering that H diffusion, and thus mobile H-deformation interactions, are precluded during testing at 77 K, the measured true strain for microcrack initiation of 0.2 for H/77 K is solely attributable to H which was trapped on the grain boundary prior to the onset of straining. Therefore, the decrease in microcrack initiation strain from 1.75 for no H/77 K to 0.2 for H/77K only results from this previously segregated H. Finally, at RT, the H segregated to grain boundaries prior to the onset of straining may be augmented by H that redistributes as a result of mobile H-deformation interactions, which yields a further decrease in initiation strain from 0.2 to 0.12. Taken together, this analysis demonstrates that mobile H-deformation interactions do tangibly contribute to H-induced intergranular fracture (thereby providing support for HE mechanism synergy [7]), but at the current H concentration, this contribution is strongly outweighed by the governing role of H segregated to the grain boundary prior to straining (*i.e.* purely HEDE). Such results represent direct experimental evidence for the relative importance of previously segregated hydrogen vs. mobile H-deformation interactions in conditioning the grain boundaries for intergranular fracture. Note that no specific mechanism related to mobile H-deformation interactions is invoked for the enhanced intergranular cracking at RT. Such mechanisms cited in the literature include the H-screening effect (*i.e.* HELP paradigm [1]) that leads to enhanced dislocation mobility [7,11] as well as the recently proposed mechanism centered on H segregation to deformation-modified defect structures at grain boundaries [7].

Considering microcrack evolution, Table 1 demonstrates that H/RT specimens fracture at lower true strains than H/77 K specimens. This observation is consistent with the rapid increase in CPA and CLPA (Figure 6) for RT as compared to 77 K. Specifically, the intergranular microcracking process from initiation to specimen failure at RT evolved over the strain range from 0.12 to 0.176 ($\Delta\varepsilon = 0.056$), whereas specimens

tested at 77 K sustained a strain range of $\Delta\epsilon = 0.335$ between microcrack initiation and failure. However, attributing this accelerated microcrack evolution at RT solely to mobile H-deformation interactions is complicated by the ability of H to redistribute about stress centers as strain increases. For example, the current testing approach cannot determine whether this rapid evolution to failure for the H/RT condition is governed by mobile H-deformation interactions or the redistribution of H to the stress fields of nucleated microcracks. In the latter scenario, H that redistributes to nascent microcracks stimulates their growth, *e.g.* by increasing the H concentration on grain boundaries ahead of the microcrack tips. Additional insight into the microcrack evolution process can also be gleaned from the results presented in Figure 6c. Specifically, despite a significant increase in the number of observed microcracks as the strain is increased for both deformation temperatures (Table 2), the average crack length was found to remain relatively constant (Figure 6c). These data suggest that the observed increase in total crack length with strain (Figure 6b) can be largely attributed to the initiation of *new* microcracks as opposed to the propagation of *existing* microcracks, though some microcracks must be elongating based on the increase in standard deviation with applied strain (Figure 6c). As discussed in the next section, this inference has important experimental ramifications with regards to identifying susceptible grain boundaries based on a post-mortem analysis of fractured specimens.

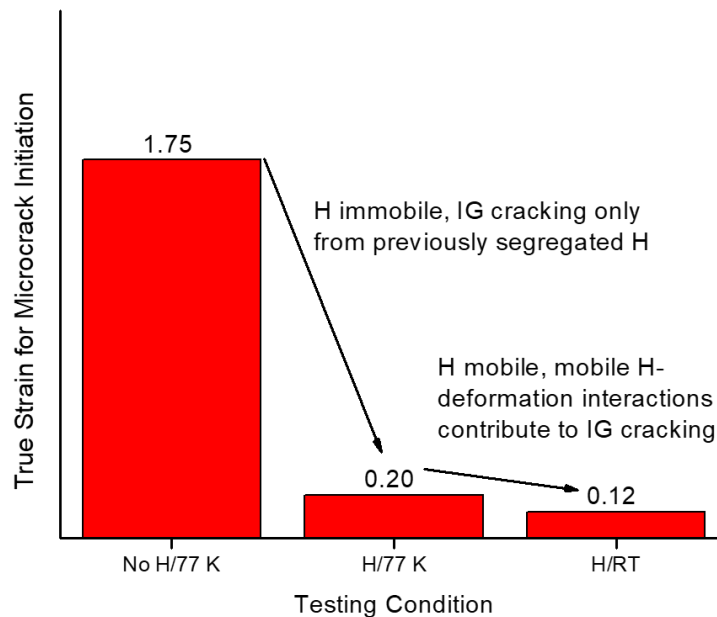


Figure 9 - Effect of testing condition on true strain for H-induced intergranular (IG) microcrack initiation.

2.5.3. Mechanistic Interpretations and Comments on Current Literature

The experimental findings presented herein provide an opportunity to comment on recent mechanistic developments in the HE community and suggest possible experiments and modeling to clarify remaining knowledge gaps. First, it has been recently proposed that H-induced intergranular fracture is primarily driven by H-enhanced dislocation processes (*e.g.* accelerated deformation structure refinement, increased dislocation mobility, etc.) [12–14]. This view is based on extensive TEM-based characterization of near-fracture surface deformation structures, which were shown to be systematically more refined in H-charged specimens relative to non-charged specimens. However, the current results demonstrate that: (1) H-induced intergranular cracking is possible under conditions where such mobile H-deformation interactions are precluded (*i.e.* 77 K) and (2) H-induced intergranular microcrack initiation is predominantly driven by H segregated to grain boundaries prior to the onset of straining. As such, for a H concentration of 4000 appm, mobile H-deformation interactions do not govern the initiation of H-induced intergranular fracture, but instead provide a more secondary contribution to conditioning the grain boundaries for failure. Moreover, given the observed similarities in deformation structure and grain boundary-deformation interaction features at RT and 77 K (Figure 7 and Figure 8), the current results suggest that the HELP mechanism is not active up to a true strain of 0.10 under the current experimental conditions.

Second, the current study conclusively establishes that H-induced intergranular microcracks initiate well before final fracture. Additionally, an examination of the average crack length as a function of applied true strain (Table 2) suggests that increases in the total crack length (Figure 6b) are principally attributed to the initiation of new intergranular microcracks, indicating that new microcracks can also initiate at high strains. Taken together, these data demonstrate that attempts to evaluate H-induced crack initiation characteristics using specimens tested to failure should be avoided given the difficulty in establishing precisely when a specific grain boundary actually fractured. Such experimental difficulties are likely responsible for the inconsistent results regarding the resistance of ‘special’ grain boundaries (*e.g.* Σ 3-type boundaries) to H-induced intergranular cracking. Specifically, recent work by Bechtle et al. showed that Ni-201 processed to contain an increased fraction of special boundaries was less susceptible to H-induced intergranular cracking than as-received Ni-201 [23]. This observation is supported by recent computational models for hydrogen trapping at grain boundaries, which showed that hydrogen does not prefer to segregate to such ‘special’ boundaries [34–37]. Yet, these results were seemingly contradicted by a recent report indicating that such special boundaries may actually serve as initiation sites for H-induced intergranular fracture [38]. However, these latter observations of preferential microcrack formation on special boundaries were made based on an examination of specimens strained to failure, which does not allow an assessment of intergranular cracking as a function of strain. More directly, it is possible that the observed microcracks

on special boundaries could have initiated toward the end of the experiment (*i.e.* at higher strains), which would instead imply that they are *highly resistant* to HE.

2.6. Conclusions

The influence of deformation temperature, and therefore mobile H-deformation interactions, on H-induced intergranular cracking in polycrystalline nickel was systematically evaluated through mechanical testing at ambient and cryogenic temperatures. Microscopy-based analysis of separate specimens tested to increasing strain levels at both deformation temperatures revealed several important insights into H-induced intergranular cracking in nickel:

1. The initiation of intergranular microcracks in H-charged Ni-201 at the current H concentration of 4000 appm is predominantly attributed to the initial grain boundary H concentration (*i.e.* concentration prior to deformation); mobile H-deformation interactions provided only a secondary contribution to intergranular microcrack initiation.
2. Intergranular microcrack evolution is enhanced at RT relative to 77 K, but a mechanistic interpretation of this finding is complicated by the likely concurrent influences of mobile H-deformation interactions and H redistribution to the stress centers created by microcracks.
3. Transmission electron microscopy of H-charged specimens subjected to approximately 10% strain at both RT and 77 K did not reveal a systematic difference in either dislocation cell size or dislocation-grain boundary interactions.

2.7. Suggested Future Research Directions

There are three suggested future research directions based on the work presented in this chapter. First, it is likely that the relative contributions of the initial grain boundary H concentration and mobile H-deformation interactions to intergranular cracking may depend on the lattice H concentration, *e.g.* H-deformation interactions may predominate at lower lattice H concentrations, since this leads to lower initial grain boundary H concentrations. As such, additional experiments leveraging interrupted testing at 77 K and RT at lower H concentrations are needed to continue exploring the relative contribution of mobile H-deformation interactions to H-induced intergranular fracture. In particular, replicating the current experiments at lattice concentrations of 2000 and 3000 appm would be of interest. Second, the flow curves presented in Figure 2 reveal an interesting effect of H on work hardening behavior. Specifically, small differences in work hardening behavior were observed between the H-charged specimens tested at 77 K and RT as well as between the non-charged and H-charged conditions at 77 K, while a strong difference was observed between the non-charged and H-charged conditions at RT. Taken together with the similarities in deformation structure presented in Figure 7, these data suggest that the effect of H on work

hardening is independent of its ability to diffuse, at least for the current lattice concentration. Additional TEM of specimens strained at RT and 77 K with lower H concentrations may provide interesting insights into this peculiar behavior. In particular, if similar work hardening behavior and deformation structure are observed at 77 K and RT with lower H concentrations, such findings would support the assessment that mobile H-deformation interactions do not govern intergranular cracking. Finally, given the ambiguity in interpretation of recent work evaluating H-induced crack initiation at coherent twin boundaries, additional experiments leveraging tensile tests interrupted at strain levels spanning microcrack initiation to specimen failure, coupled with the detailed characterization and modeling utilized by Seita and coworkers [38,39], would more convincingly determine whether or not special boundaries serve as microcrack initiation sites at lower strains. Such insights could have important ramifications for grain boundary engineering as a mitigation strategy for HE.

2.8. Acknowledgements

The assistance of Jeff Campbell (hydrogen charging), Ken Lee (mechanical testing), Nancy Yang (sample preparation), and Mark Homer (TEM sample preparation) at Sandia National Laboratories are sincerely appreciated. Helpful discussions with Prof. Richard Gangloff, Prof. John Scully, Prof. Sean Agnew, and Jayendran Srinivasan at the University of Virginia are also gratefully acknowledged.

2.9. References

- [1] H.K. Birnbaum, P. Sofronis, Hydrogen-enhanced localized plasticity—a mechanism for hydrogen-related fracture, *Mater. Sci. Eng. A.* 176 (1994) 191–202. doi:10.1016/0921-5093(94)90975-X.
- [2] R.A. Oriani, A Mechanistic Theory of Hydrogen Embrittlement of Steels, *Berichte Der Bunsen-Gesellschaft Fur Phys. Chemie.* 76 (1972) 848–857.
- [3] A.R. Troiano, The Role of Hydrogen and Other Interstitials in the Mechanical Behavior of Metals: (1959 Edward De Mille Campbell Memorial Lecture), *Metallogr. Microstruct. Anal.* 5 (2016) 557–569. doi:10.1007/s13632-016-0319-4.
- [4] S.P. Lynch, Environmentally assisted cracking: Overview of evidence for an adsorption-induced localised-slip process, *Acta Metall.* 36 (1988) 2639–2661. doi:10.1016/0001-6160(88)90113-7.
- [5] M. Nagumo, Hydrogen related failure of steels – a new aspect, *Mater. Sci. Technol.* 20 (2004) 940–950. doi:10.1179/026708304225019687.
- [6] R. Dutton, K. Nuttall, M.P. Puls, L.A. Simpson, Mechanisms of hydrogen induced delayed cracking in hydride forming materials, *Metall. Trans. A.* 8 (1977) 1553–1562. doi:10.1007/BF02644858.
- [7] I.M. Robertson, P. Sofronis, A. Nagao, M.L. Martin, S. Wang, D.W. Gross, et al., Hydrogen Embrittlement Understood, *Metall. Mater. Trans. B.* (2015). doi:10.1007/s11663-015-0325-y.
- [8] A. Barnoush, H. Vehoff, Recent developments in the study of hydrogen embrittlement: Hydrogen effect on dislocation nucleation, *Acta Mater.* 58 (2010) 5274–5285.

doi:10.1016/j.actamat.2010.05.057.

- [9] P.J. Ferreira, I.M. Robertson, H.K. Birnbaum, Hydrogen effects on the interaction between dislocations, *Acta Mater.* 46 (1998) 1749–1757. doi:10.1016/S1359-6454(97)00349-2.
- [10] S.K. Lawrence, Y. Yagodzinsky, H. Hanninen, E. Korhonen, F. Tuomisto, Z.D. Harris, et al., Effects of grain size and deformation temperature on hydrogen-enhanced vacancy formation in Ni alloys, *Acta Mater.* 128 (2017) 218–226. doi:10.1016/j.actamat.2017.02.016.
- [11] I.M. Robertson, The effect of hydrogen on dislocation dynamics, *Eng. Fract. Mech.* 65 (2001) 671–692.
- [12] S. Wang, M.L. Martin, P. Sofronis, S. Ohnuki, N. Hashimoto, I.M. Robertson, Hydrogen-induced intergranular failure of iron, *Acta Mater.* 69 (2014) 275–282. doi:10.1016/j.actamat.2014.01.060.
- [13] M.L. Martin, B.P. Somerday, R.O. Ritchie, P. Sofronis, I.M. Robertson, Hydrogen-induced intergranular failure in nickel revisited, *Acta Mater.* 60 (2012) 2739–2745. doi:10.1016/j.actamat.2012.01.040.
- [14] S. Wang, A. Nagao, K. Edalati, Z. Horita, I.M. Robertson, Influence of hydrogen on dislocation self-organization in Ni, *Acta Mater.* 135 (2017) 96–102. doi:10.1016/j.actamat.2017.05.073.
- [15] G. Girardin, C. Huvier, D. Delafosse, X. Feugas, Correlation between dislocation organization and slip bands: TEM and AFM investigations in hydrogen-containing nickel and nickel-chromium, *Acta Mater.* 91 (2015) 141–151. doi:10.1016/j.actamat.2015.03.016.
- [16] Y.J. Ro, S.R. Agnew, R.P. Gangloff, Effect of Environment on Fatigue Crack Wake Dislocation Structure in Al-Cu-Mg, *Metall. Mater. Trans. A.* 43A (2012) 2275–2292. doi:DOI 10.1007/s11661-012-1089-5.
- [17] M. Deutges, H.P. Barth, Y. Chen, C. Borchers, R. Kirchheim, Hydrogen diffusivities as a measure of relative dislocation densities in palladium and increase of the density by plastic deformation in the presence of dissolved hydrogen, *Acta Mater.* 82 (2015) 266–274. doi:10.1016/j.actamat.2014.09.013.
- [18] Y.Z. Chen, H.P. Barth, M. Deutges, C. Borchers, F. Liu, R. Kirchheim, Increase in dislocation density in cold-deformed Pd using H as a temporary alloying addition, *Scr. Mater.* 68 (2013) 743–746. doi:10.1016/j.scriptamat.2013.01.005.
- [19] T. Boniszewski, G. Smith, The influence of hydrogen on the plastic deformation ductility, and fracture of nickel in tension, *Acta Metall.* (1963).
- [20] A.H. Windle, G.C. Smith, The Effect of Hydrogen on the Deformation and Fracture of Polycrystalline Nickel, *Met. Sci. J.* 4 (1970) 136–144. doi:10.1179/msc.1970.4.1.136.
- [21] D.H. Lassila, H.K. Birnbaum, Intergranular fracture of nickel: the effect of hydrogen-sulfur co-segregation, *Acta Metall.* 35 (1987) 1815–1822. doi:10.1016/0001-6160(87)90127-1.
- [22] D.H. Lassila, H.K. Birnbaum, The effect of diffusive hydrogen segregation on fracture of polycrystalline nickel, *Acta Metall.* 34 (1986) 1237–1243. doi:10.1016/0001-6160(86)90010-6.
- [23] S. Bechtle, M. Kumar, B.P. Somerday, M.E. Launey, R.O. Ritchie, Grain-boundary engineering markedly reduces susceptibility to intergranular hydrogen embrittlement in metallic materials, *Acta Mater.* 57 (2009) 4148–4157. doi:10.1016/j.actamat.2009.05.012.

- [24] D.H. Lassila, H.K. Birnbaum, The effect of diffusive segregation on the fracture of hydrogen charged nickel, *Acta Metall.* 36 (1988) 2821–2825. doi:10.1016/0001-6160(88)90128-9.
- [25] B.P. Somerday, J.A. Campbell, K.L. Lee, J.A. Ronevich, C. San Marchi, Enhancing safety of hydrogen containment components through materials testing under in-service conditions, *Int. J. Hydrogen Energy.* (2016) 4–11. doi:10.1016/j.ijhydene.2016.04.189.
- [26] K.A. Lee, R.B. McLellan, The diffusivity of hydrogen in nickel at low temperatures, *Scr. Metall.* 18 (1984) 859–861.
- [27] P.J. Phillips, M.C. Brandes, M.J. Mills, M. de Graef, Diffraction contrast STEM of dislocations: Imaging and simulations, *Ultramicroscopy.* 111 (2011) 1483–1487. doi:10.1016/j.ultramic.2011.07.001.
- [28] B. Alexandreanu, G.S. Was, A priori determination of the sampling size for grain-boundary character distribution and grain-boundary degradation analysis, *Philos. Mag. A Phys. Condens. Matter, Struct. Defects Mech. Prop.* 81 (2001) 1951–1965. doi:10.1080/01418610010019143.
- [29] A.W. Marshall, I. Olkin, *Life Distributions*, Springer, New York, 2007.
- [30] B. Bay, N. Hansen, D.A. Hughes, D. Kuhlmann-Wilsdorf, Evolution of f.c.c. deformation structures in polyslip, *Acta Metall. Mater.* 40 (1992) 205–219. doi:10.1016/0956-7151(92)90296-Q.
- [31] B.A. Wilcox, G.C. Smith, The Portevin-Le Chatelier Effect in Hydrogen Charged Nickel, *Acta Metall.* 12 (1964) 371–376.
- [32] S.H. Goods, L.M. Brown, The nucleation of cavities by plastic deformation, *Acta Metall.* 27 (1979) 1–15. doi:10.1016/0001-6160(79)90051-8.
- [33] A.W. Thompson, J.F. Knott, Micromechanisms of brittle fracture, *Metall. Trans. A.* 24 (1993) 523–534. doi:10.1007/BF02656622.
- [34] D. Di Stefano, M. Mrovec, C. Elsasser, First-principles investigation of hydrogen trapping and diffusion at grain boundaries in nickel, *Acta Mater.* 98 (2015) 306–312. doi:10.1016/j.actamat.2015.07.031.
- [35] A. Alvaro, I. Thue Jensen, N. Kheradmand, O.M. Løvvik, V. Olden, Hydrogen embrittlement in nickel, visited by first principles modeling, cohesive zone simulation and nanomechanical testing, *Int. J. Hydrogen Energy.* 40 (2015) 16892–16900. doi:10.1016/j.ijhydene.2015.06.069.
- [36] X. Zhou, D. Marchand, D.L. McDowell, T. Zhu, J. Song, Chemomechanical Origin of Hydrogen Trapping at Grain Boundaries in fcc Metals, *Phys. Rev. Lett.* 116 (2016) 1–5.
- [37] J. Chen, A.M. Dongare, Role of grain boundary character on oxygen and hydrogen segregation-induced embrittlement in polycrystalline Ni, *J. Mater. Sci.* 52 (2017) 30–45. doi:10.1007/s10853-016-0389-3.
- [38] M. Seita, J.P. Hanson, S. Gradečak, M.J. Demkowicz, The dual role of coherent twin boundaries in hydrogen embrittlement, *Nat. Commun.* 6 (2015) 6164. doi:10.1038/ncomms7164.
- [39] M. Seita, J.P. Hanson, S. Gradečak, M.J. Demkowicz, Probabilistic failure criteria for individual microstructural elements: an application to hydrogen-assisted crack initiation in alloy 725, *J. Mater. Sci.* 52 (2017) 2763–2779. doi:10.1007/s10853-016-0568-2.

Chapter 3. Effect of microstructural variation on HEAC of Monel K-500

3.1. Overview

The influence of microstructural variation on hydrogen environment-assisted cracking (HEAC) of Monel K-500 was evaluated using five nominally peak-aged heats of material tested under slow-rising stress intensity (K) loading while immersed in NaCl solution under cathodic polarizations. Minimal variation in HEAC susceptibility amongst the material heats was observed for an applied potential of -950 mV_{SCE} (vs. saturated calomel), suggesting that relatively severe H environments produce sufficient crack-tip H to minimize the impact of metallurgical differences. Conversely, observed heat-to-heat variability in the fracture morphology indicates a significant difference in the HEAC resistance at the less negative potential of -850 mV_{SCE}. These results are corroborated by sensitivity analyses of proposed decohesion-based models, which suggest that significant variations in HEAC resistance are possible for realistic changes in grain boundary toughness, hydrogen uptake behavior, and yield strength. Observed variations in grain size, impurity segregation, grain boundary character/connectivity, crack path tortuosity, and yield strength/strain hardening parameters amongst the tested material heats are considered in the context of the measured HEAC susceptibility. Despite this systematic evaluation, no clear trend between specific microstructural features and HEAC susceptibility was identified, suggesting that a critical interplay amongst microstructural parameters may govern HEAC susceptibility. The study concludes with an evaluation of the K_{TH} decohesion-based model's ability to capture the observed heat-to-heat variations in HEAC susceptibility; a modification to the model is then proposed to account for the effect of grain boundary impurities.

Note: Two (2) peer-reviewed journal articles have been published based on the work presented in this chapter, which can be accessed using the details below:

2. **Z.D. Harris**, J.D. Dolph, G.L. Pioszak, B.C. Rincon Troconis, J.R. Scully, and J.T. Burns, "The Effect of Microstructure Variation on the Hydrogen Environment-Assisted Cracking of Monel K-500", *Metallurgical and Material Transactions A*, vol. 47, pp. 3488-3510, 2016.
 - a. Harris contribution: co-primary performer; analyzed and interpreted fracture mechanics test data, co-performed material characterization/imaging and subsequent analysis, and co-wrote manuscript.
3. B.C. Rincon Troconis, **Z.D. Harris**, H.M. Ha, J.T. Burns, and J.R. Scully, "The Effect of Heat-to-Heat Variations in Metallurgy and Hydrogen-Metal Interactions on Hydrogen Embrittlement of Monel K-500", *Materials Science and Engineering: A*, vol. 703, pp. 533-550, 2017.
 - a. Harris contribution: secondary performer; assisted with SSRT testing, performed analysis of mechanical test data, assisted with materials characterization/imaging, and co-wrote manuscript.

3.2. Introduction

Monel K-500 is a Ni-Cu superalloy commonly utilized in marine applications due to its excellent combination of corrosion resistance, strength, and fracture toughness. For such applications, environment-assisted cracking (EAC) is historically evaluated via a wide-range of testing strategies (e.g. NACE MR0175 and ASTM G30, G39, G129, E1681, and F1624 [1–6]). Material selection engineers will often use data from such tests in a “go/no-go” paradigm where the long-term EAC resistance is inferred based on empirical material testing. Specifically, if testing indicates that the service environment and loading conditions are below a threshold level of severity, it is then assumed that cracking will not occur over the lifetime of the component. Such an approach is codified in NACE MR0175 [1], which outlines guidelines for the selection of “cracking resistant materials” in H₂S environments (of note is that this specification does state that materials meeting this standard are “not necessarily” immune under all service conditions). The inadequacy of this “go/no-go” approach is demonstrated by isolated, long-time (~10 year) service failures of Monel K-500 components on North Sea oil and gas platforms, deep gas wells, and marine craft [7–13]. In each of these cases, the Monel K-500 components were immersed in seawater and cathodically polarized to protect adjacent carbon and low alloy steel structures. This service environment, combined with the observation of fracture surfaces that exhibited intergranular (IG) with small amounts of transgranular (TG) crack growth [7,8,11–13], suggests that the failure of these components can be attributed to EAC – an assessment corroborated by laboratory testing of Ni-based superalloys [14–18].

These service failures expose critical, non-conservative flaws in the existing approach to EAC management for current- and next-generation materials. Specifically, current EAC characterization techniques, material selection criteria, and structural integrity prognosis approaches fail to fully account for conditions where slow sub-critical crack propagation occurs over a significant portion of component life. This deficiency demonstrates the need for high-fidelity linear elastic fracture mechanics-based (LEFM) material characterization of both the threshold stress intensity for EAC (K_{TH}) and the steady state (Stage II) sub-critical crack growth kinetics (da/dt_{II}) for the pertinent service environment [19]. Additionally, if slow crack propagation dominates the total service life of the component, then sub-critical crack growth kinetics can be coupled with LEFM-based life prediction methods (e.g. *SCCrack*, recently developed for EAC modeling [20]) to provide a powerful tool for structural design, material/coating/cathodic protection selection, and/or structural life management. An analogous approach is well established in the fatigue community where LEFM-based programs are commonly used to aid structural life management [21–23]. Ultimately, the rigor of the LEFM approach is critically dependent on the applicability of the crack growth kinetics data to the relevant environment, loading conditions, and material of interest. ***An initial study evaluated the influence of the former two variables on EAC behavior in Monel K-500 [18], but the effect***

of heat-to-heat metallurgical variation on HEAC susceptibility is not known.

Crack growth kinetics for environment/cathodic polarization combinations pertinent to marine service conditions were established in prior work using the direct current potential difference (dcPD) technique [24] to monitor crack progression during slow-rising stress intensity (K) testing of single-edge notched (SEN) specimens from a single heat of Monel K-500 [18]. The resulting data quantitatively demonstrated that decreasing the applied potential from $-750 \text{ mV}_{\text{SCE}}$ to $-1100 \text{ mV}_{\text{SCE}}$ in 0.6 M NaCl solution will decrease the EAC threshold (K_{TH}) and increase the Stage II crack growth rate (da/dt_{II}). In addition to their engineering relevance, these data provided the basis for the modeling of potential-dependent EAC in the context of a decohesion-based hydrogen (H) embrittlement mechanism. Estimates of the overpotential for H production at the crack-tip were established as a function of bulk applied potential via rescaled crevice experiments [18]. These data were coupled with effective H solubility measurements versus H overpotential to establish that the crack-tip diffusible H concentration ($C_{\text{H-Diff}}$) rises with decreasing applied potential from -750 to $-1100 \text{ mV}_{\text{SCE}}$ [25]. As the level of cathodic polarization increases, the increase in EAC susceptibility directly scales with increasing crack-tip diffusible H concentration, thereby suggesting that hydrogen environment-assisted cracking (HEAC) is the governing mechanism for sub-critical cracking in Monel K-500. This finding is consistent with a wide literature that supports the H-embrittlement phenomenon in Ni-based alloys [26–31]

While several viable mechanisms for hydrogen embrittlement in Ni-based alloys exist [32–34], hydrogen-enhanced decohesion-based (HEDE) models provide a means to quantitatively relate the stress-enhanced H concentration ($C_{\text{H-}\sigma}$) in the fracture process zone (FPZ) to the relevant HEAC metrics (K_{TH} and da/dt_{II}) [35–38]. Critically, $C_{\text{H-}\sigma}$ can be calculated from the empirically determined $C_{\text{H-Diff}}$, thereby establishing $C_{\text{H-}\sigma}$ as the key environmental variable in the HEDE models for K_{TH} and da/dt_{II} . Prior work argued that this relationship (Eqn 3.1) can be described with Fermi-Dirac statistics by reasonably assuming a single dominant reversible trap site and low lattice H concentrations [18].

$$C_{\text{H-}\sigma} = C_{\text{H-Diff}} \exp \left[\frac{\sigma_{\text{H}} V_{\text{H}}}{R T} \right] \quad (\text{Eqn 3.1})$$

where V_{H} is the partial molar volume of hydrogen in a nickel lattice ($1.73 \text{ cm}^3/\text{mol H}$) [18], R is the gas constant, T is temperature, and σ_{H} is the hydrostatic stress. Depending on the approach (discrete dislocation models, blunted crack finite element models, or strain gradient plasticity models), crack-tip mechanics estimates of σ_{H} vary from 3 to 20 times the yield strength of the alloy [39].

K_{TH} for HEAC is predicted using the decohesion-based model proposed by Gerberich *et al.*

[32,35,38] (Eqn 3.2) to describe the near crack-tip stress state:

$$K_{TH} = \frac{1}{\beta'} \exp \left[\frac{(k_{IG} - \alpha C_{H\sigma})^2}{\alpha'' \sigma_{YS}} \right] \quad (\text{Eqn 3.2})$$

where β' ($(\text{MPa}\sqrt{\text{m}})^{-1}$) and α'' ($\text{MPa}\cdot\text{m}$) are constants from modeling the dislocation shielding of the crack-tip elastic stress, k_{IG} ($\text{MPa}\sqrt{\text{m}}$) is the intrinsic Griffith toughness of the grain boundary, α ($\text{MPa}\sqrt{\text{m}}(\text{atom fraction of hydrogen})^{-1}$) is a weighting factor which defines the decrease in k_{IG} per unit H concentration, and σ_{YS} (MPa) is the yield strength [18,32,35]. The steady-state (Stage II) sub-critical HEAC growth behavior is limited by the diffusion of H from the crack-tip surface to the location of maximum stress within the FPZ [18,37]. As such, a HEDE-based model for H-diffusion ahead of a discontinuously propagating crack results in the relationship given in Eqn 3.3:

$$\left(\frac{da}{dt} \right)_{II} = \frac{4 D_{\text{eff}}}{x_{\text{crit}}} \left(\text{erf}^{-1} \left(1 - \frac{C_{H\sigma\text{-crit}}}{C_{H\sigma}} \right) \right)^2 \quad (\text{Eqn 3.3})$$

where D_{eff} is the effective diffusivity of hydrogen which accounts for the presence of trap sites in the alloy (reported values are bounded by $5.0 \times 10^{-11} \text{ cm}^2/\text{s}$ and $1.3 \times 10^{-10} \text{ cm}^2/\text{s}$ for Monel K-500 [25]), x_{crit} is the critical distance ahead of the crack-tip where discontinuous H-assisted crack advance nucleates, and $C_{H\sigma\text{-crit}}$ is the critical concentration of hydrogen necessary to activate decohesion at x_{crit} [18]. The parameter x_{crit} is on the order of 1 μm for many high strength alloys and is related to the position of maximum hydrostatic stress in front of the crack tip [40]. Prior work demonstrated that using a single experimentally calibrated parameter and the empirically derived applied potential versus $C_{H\text{-Diff}}$ relationship gave predictions from Eqn 3.2 and 3.3 that showed excellent agreement with measured HEAC parameters for applied potentials ranging from -700 to -1100 mV_{SCE} in a single heat of Monel K-500 [18]. The success of these HEDE-based modeling paradigms, along with the high fidelity of the dcPD technique for measuring crack growth, justify the extension of these approaches to understand the effect of metallurgical variation on HEAC behavior.

Understanding the effect of heat-to-heat variations in metallurgy on HEAC susceptibility is especially relevant for Monel K-500, where metallurgical differences are a potential controlling factor for intermittent service failures. The specification governing material procurement (Federal Specification QQ-N-286G) is a property-driven document that specifies benchmarks for composition, mechanical properties, IG susceptibility, and grain size uniformity [41]. However, while there are suggested heat treatments, the specification allows for age hardening to "be accomplished by any process proved adequate to meet the mechanical property requirements" [41]. This flexibility in production can lead to significant variations in

strength and metallurgical features and their effects are unlikely to be captured by the rudimentary testing mandated by QQ-N-286G for determining IG failure susceptibility. In particular, the grain size, distribution of grain boundary misorientation angles, bulk impurity concentration, degree of impurity segregation to grain boundaries, precipitate morphology, and post-processing dislocation density can all appreciably vary with changes in material lot/processing route. Critically, these changes can influence the HEAC behavior by modifying the material strength, slip behavior, grain boundary cohesion characteristics, crack path connectivity/tortuosity, and/or H-metal interactions. The micromechanical models detailed in Eqn. 3.2 and 3.3 provide a quantitative framework to link these metallurgy variations with the HEAC behavior by speculating how heat-to-heat differences vary the pertinent input parameters (k_{IG} , α , σ_{YS} , x_{crit} , $C_{H,Diff}$, $C_{H-\sigma}$, D_{eff} , and $C_{H\sigma-crit}$). ***However, a systematic characterization and analysis of the relative influence of changes in these metallurgical features on the HEAC behavior is lacking for Monel K-500.***

3.2.1. Chapter objectives and research questions

The objective of this chapter is to (1) systematically evaluate the extent to which HEAC behavior varies across five Monel K-500 material heats that each satisfy the governing QQ-N-286G material specification and (2) correlate these differences in HEAC susceptibility with measured microstructural parameters to identify the critical metallurgical factors which govern embrittlement resistance. Towards this end, this chapter seeks to answer the following specific research questions:

3. How does the HEAC susceptibility, as measured by K_{TH} and da/dt_{II} , vary amongst the five tested materials heats?
4. Does the observed variability in HEAC susceptibility correlate with measured differences in metallurgical parameters?
5. Can the previously-validated decohesion-based models explain the observed variations in HEAC susceptibility amongst the material heats?
6. Can the decohesion-based model for K_{TH} effectively capture the observed variations in HEAC susceptibility amongst the tested material heats? If not, what modifications (or alternative approaches) may improve the model's ability to capture microstructural effects on HEAC susceptibility?

3.3. Experimental methods and material

3.3.1. Material

Monel K-500 is composed of a Ni-Cu solid solution matrix (γ) that is precipitation-hardened by the intermetallic γ' ($Ni_3(Al,Ti)$) phase. The γ' precipitates are homogeneously distributed and highly coherent (<0.1% misfit strain) with an ordered $L1_2$ structure composed of Ni atoms at the faces and Al (or Ti) atoms

on the corners of the unit cell [42–44]. Due to this low misfit, these precipitates form as spherical particles – a morphology that is maintained even after prolonged aging [43]. Dislocation interactions with γ' are generally controlled by the size of the γ' precipitates, with a noted shift from dislocation cutting to Orowan looping for larger particle radii [43,44]. A heterogeneous distribution of MC-type carbides (typically TiC) are also found in this alloy, but literature suggests that this distribution will not appreciably change under typical aging conditions for Monel K-500 [45] and that their contribution to the strength of Monel K-500 is minimal [43].

Five heats of Monel K-500 were evaluated in this work. The first heat was obtained from ATI Allvac (termed Allvac) as a 15.9 mm diameter bar that was hot worked and then age hardened as follows: 16 h at 866 K (593°C), cooled at 14 K/h to 755 K (482°C), and then air cooled to ambient temperature. Three heats of Monel K-500 were harvested from retired engineering components (intact components that were roughly 305 x 51 x 38 mm in size). The exact service conditions for the components are not known, but are estimated as roughly 10-15 years of full immersion in seawater with exposure to applied potentials likely ranging from –1000 to –750 mV_{SCE}. These heats are termed Component 1 (TR 1), Component 2 (TR 2), and Component 3 (TR 3) and have an unknown processing history.² The final heat of Monel K-500 was received from the U.S. Naval Research Laboratory (NRL) with thermal processing designed to capture the upper-bound strength requirement of QQ-N-286. This material (termed NRL-High Strength (NRL HS)), was processed from a 114 mm diameter bar procured from Special Metals that was direct-aged at 866 K (593°C) for 16 h, furnace cooled at 14 K/h to 811 K (538°C), held for 1 h, furnace cooled at 14 K/h to 755 K (482°C), held for 1 h, and air cooled to ambient temperature. Table 5 presents both the QQ-N-286 composition requirements and the measured bulk chemical compositions for each heat; concentrations of trace elements S, P, Sn, Zr, Mg, Hf, and Pb were determined using glow discharge mass spectrometry. Measured mechanical properties are reported in Table 6; the yield strength and Ramberg-Osgood flow rule constants (n and α) were determined by fitting the Ramberg-Osgood relationship to stress-strain data obtained from cylindrical specimens compressively loaded to 2% total strain:

$$\epsilon = \frac{\sigma}{E} + \alpha \frac{\sigma_0}{E} \left(\frac{\sigma}{\sigma_0} \right)^n \quad (\text{Eqn 3.4})$$

² HEAC testing of the component specimens were performed in the as-received conditions. A companion study suggests that H-charging that occurred during field service may lead to a total internal H-concentration, $C_{H\text{-total}}$, on the order of 5 wppm which is similar to the 6 wppm at the crack tip at -850 mV_{SCE} for the Allvac material heat [18]. The effects of the precharged hydrogen is discussed in more detail elsewhere [121]. However, HEAC testing of the component specimens in an inert environment did not show H-enhanced IG cracking due to the precharged H-content.

Where ϵ is the total strain, σ is the applied stress, E is the elastic modulus, σ_0 is a reference stress (generally taken to be the 0.2% offset yield strength), n is the strain hardening exponent, and α is a fitting parameter.

3.3.2. Fracture mechanics-based environmental testing

3.3.2.1. Mechanical testing and crack length monitoring approach

Single edge notch tensile (SEN(T)) specimens were machined from each of the material lots with gauge sections of 12.5 mm (10.6 mm for Allvac) in width (W), and 2.68 mm in thickness (B). Specimens were loaded parallel to the bar/component longitudinal axis with the Mode I crack growth occurring in the radial direction. An initial $200 \pm 10 \mu\text{m}$ notch was placed in the center of the gauge section using electrical discharge machining (EDM). Specimens were fatigue precracked in laboratory air using the following protocol: (1) constant maximum load (12.5 kN) at $R = 0.1$ from the initial notch to a crack length of ~ 0.4 mm (ending $K_{\text{max}} \approx 15 \text{ MPa}\sqrt{\text{m}}$) and (2) constant $R = 0.1$ with K_{max} decreasing from 15 $\text{MPa}\sqrt{\text{m}}$ to a final value of 13 $\text{MPa}\sqrt{\text{m}}$ at a crack length of approximately 1 mm. All specimens were loaded in clevis grips to allow for free rotation in compliance with K-solution boundary conditions [46].

Fracture mechanics testing at a constantly increasing elastic K (dK/dt) was achieved by coupling active crack length feedback *via* dcPD with software-controlled, servo-hydraulic actuator displacement. Testing in NaCl solution was conducted at a constant $dK/dt = 0.33 \text{ MPa}\sqrt{\text{m/hr}}$, which corresponds to an approximate grip velocity of $2 \times 10^{-6} \text{ mm/s}$, while inert environment testing was completed at a constant dK/dt of either 0.33 or 1 $\text{MPa}\sqrt{\text{m/hr}}$ to limit test duration. Crack progression was monitored via the direct current potential difference method (dcPD) and the grip velocity was adjusted every 5 seconds to maintain the desired dK/dt . This procedure included current-polarity reversal to eliminate thermally-induced voltages, crack potential difference normalization by a remote reference, and active-normalized potential values averaged in groups of 50. Each potential measurement was converted to a crack length via Johnson's equation [47], where the potential associated with the initial notch depth (a_0) is the adjustable constant (V_0) [48]. The resolvable average crack extension, Δa , for this technique is $\sim 0.5 \mu\text{m}$, based on the ability to resolve 0.1 μV changes in measured potential for a constant applied current of $4.000 \pm 0.005 \text{ A}$. Post-test initial crack length measured via electron microscopy typically varied $<5\%$ from the dcPD-based calculated value. If necessary, the initial crack length was corrected to match the measured value from fractography and all subsequent crack measurements were recalculated using the measured voltage at each time step. The crack growth rate (da/dt) at each crack length and time combination was determined using the incremental ($n=3$) polynomial method described in ASTM E647-13 Appendix X1 [49]. High-resolution crack growth monitoring for environment-material combinations that are resistant to HEAC is complicated by plasticity-based resistivity increases, which establish a functional resolution limit of 0.2 to 1 nm/s, depending on the applied K and dK/dt [18]. False da/dt were observed at low K due to crack surface

electrical contact enabled by the cathodic polarization-induced destabilization of the surface oxide film; a post-test analysis protocol (as detailed elsewhere [18]) was used for data correction. The effects of specimen plasticity are accounted for using established J-integral solutions to calculate a total stress intensity (K_J) [50]. Remaining ligament plasticity was evaluated via analytical solutions for a stationary crack in a material that deforms according to the Ramberg-Osgood flow rule and the effective crack length (a_{eff} , taken as the physical crack length plus the plain strain plastic zone correction). Full details of this approach are presented elsewhere [50]. Testing and material response complexities can cause deviations from the classic da/dt vs. K behavior, *i.e.* an initial absence of crack growth below K_{TH} that is followed by a steep rise in da/dt with increasing K , ultimately reaching a K -independent (Stage II) growth rate (da/dt_{II}). As such, it is necessary to assign conditions for determining K_{TH} and da/dt_{II} . For the current study, K_{TH} is defined as the K at which the growth rate exceeds the plasticity-based resolution limit of the dcPD system (as discussed in [18]) and the Stage II crack growth rate is defined as the da/dt at $K = 60 \text{ MPa}\sqrt{\text{m}}$.

3.3.2.2. Testing environments

Three test environments were investigated at 298 K (25°C): full immersion in an aqueous chloride electrolyte with an applied potential of either -950 or $-850 \text{ mV}_{\text{SCE}}$ and dry N_2 gas ($\text{RH} < 5\%$). Prior efforts suggest that the HEAC susceptibility of Monel K-500 in these environments is aggressive, mild, and inert, respectively [18]. To isolate the specimen in the environment of interest, the gage section of the SEN(T) specimen was placed inside a 340 mL cylindrical Plexiglass cell. Immersion testing was completed by circulating 0.6 M non-deaerated NaCl solution from a 4L reservoir at $\sim 20 \text{ mL}/\text{min}$ in ambient conditions. Testing was completed at constant applied potentials of -850 and -950 mV , referenced to a standard calomel electrode (SCE) controlled by a potentiostat operated in floating mode (to avoid a ground loop). The SEN(T) specimen was grounded through grip attachment to the testing machine. A platinum-coated Nb mesh counter-electrode and the SCE were placed in the cell, with the counter-electrode surrounding the specimen. Prior to onset of mechanical testing, the open circuit potential of the specimen was monitored for 1 hour, followed by the specimen being polarized to the selected test potential. The bulk solution pH was found to rise from ~ 6.0 to between 6.2-6.5 during an experiment. Only a 1 mm window surrounding the Mode I crack path from the notch to an a/W of ~ 0.75 was exposed to solution; all other surfaces within the cell were masked with 3M Electroplating Tape 470 and a butyl rubber-based lacquer (Tolber Micro XP-2000 Stop-off Lacquer). Inert environment testing was completed by flowing N_2 into the environmental cell at a rate that maintained a measured relative humidity of less than 5% for the duration of loading. It is acknowledged that appreciable hydrogen will still be present during testing in dry N_2 gas, but prior work demonstrated that the hydrogen fugacity under such conditions was insufficient to cause HEAC in Monel K-500 [18].

Table 5 - Chemical composition of Monel K-500 heats (wt. %, except S, P, Sn, Pb, Mg, Zr, Hf, B are wppm)

Material Heat	Ni	Cu	Al	Fe	Mn	Si	Ti	C	Co	S	P	Sn	Pb	Mg	Zr	Hf	B
Allvac	66.12	28.57	2.89	0.80	0.81	0.08	0.45	0.17	0.01	1.60	92	2.4	2.1	39	370	2.6	3.8
NRL HS	63.44	30.74	3.20	0.91	0.85	0.10	0.57	0.14	0.02	17.00	40	2.2	3.5	40	650	0.8	2.0
TR1	65.55	29.18	2.86	0.93	0.67	0.04	0.47	0.22	0.01	3.10	55	1.2	2.4	170	230	4.6	0.3
TR2	64.66	30.15	2.73	0.69	0.73	0.09	0.45	0.20	0.04	11.00	71	6.9	2.5	130	330	5.6	1.5
TR3	64.17	30.34	3.21	0.71	0.81	0.09	0.45	0.13	0.04	12.00	74	6.8	2.4	130	320	5.4	1.5
QQ-N-286	>63.0	27-33	2.3-3.15	<2.0	<1.5	<0.50	0.35-0.85	<0.18	<0.25	<60	<200	<60	<60	N/A	N/A	N/A	N/A

Table 6 - Mechanical properties of Monel K-500 heats

Material Heat	σ_{ys} (MPa)	E (GPa)	n	α
Allvac	786	180	20	0.39
NRL HS	910	191	18	0.405
TR1	898	183	18	0.39
TR2	795	202	20	0.39
TR3	792	194	20	0.39

3.3.3. Characterization

Scanning electron microscopy (SEM) was performed to identify the final precrack length and to examine the fracture morphology. Orientation imaging microscopy (OIM) was completed for each heat using electron backscatter diffraction (EBSD) with a 30 kV accelerating voltage and a 7.6 nA probe current. EBSD samples were extracted from the non-gauge portion of the SEN(T) specimens, mechanically polished to 0.10 μm , and then vibratory polished using 0.05 μm alumina suspension. A 0.5 μm step size was employed to ensure >10 steps for the smallest grains observed. The resulting OIM maps were then analyzed using the Tango post-processing software (Oxford Instruments) to evaluate grain boundary misorientation character and average grain size.

Auger electron spectroscopy (AES) was conducted using a Physical Electronics PHI 710 Scanning Auger Nanoprobe operated at 10 keV with a probe current of 10 nA and a beam probe diameter of 20 nm. AES specimens were machined in the form of 19-mm long, 6.25-mm diameter cylindrical pins that contained a 90° notch located 11.5 mm from the end of the specimen (minor diameter of notch was 2.2 mm). Due to equipment availability limitations, AES was only conducted on TR1, TR2, Allvac, and NRL HS. To ensure an intergranular fracture morphology for assessing grain boundary sulfur content, all AES specimens were charged with hydrogen for 60 days via immersion in 0.6 M NaCl at an applied potential of -1200 mV_{SCE}. Upon removal from the charging station, specimens were kept under cryogenic temperatures (using either liquid nitrogen or dry ice) at all times prior to loading in the AES system so as to minimize hydrogen egress. Attempts to fracture the specimens under vacuum using a custom impact fracture rig in the AES system were unsuccessful, therefore all specimens were fractured via bending just prior to being placed in the AES system. Elemental profiles as a function of depth were collected via sputter depth profiling of intergranular facets, with multiple facets (~5 per specimen) being analyzed/sputtered simultaneously. Incremental sputtering was completed to a depth of ~50 nm (step size \approx 1 nm) using an Ar ion beam at an accelerating voltage of 2 keV and an impingement angle of 52°; these conditions yield an approximate sputtering rate that is equivalent to 2 nm/min in SiO₂ [51].

3.4. Results

3.4.1. Inert (dry N₂) environment testing

The da/dt versus K_I results for Allvac, TR1, TR2, TR3, and duplicate NRL HS tests in a dry nitrogen gas environment (RH < 5%) are shown in Figure 1. Consistent with prior results for Allvac material [18], each heat demonstrated two regimes of behavior. First, da/dt was found to increase linearly with increasing K_I over a range of low K_I (10 < K_I < 35 MPa^{1/2}/m). This behavior has been attributed to a crack

tip plasticity-induced change in resistivity that scales with applied K and increases the dcPD-measured potential [18]. Thus, it is possible to establish a false da/dt “resolution limit”, as discussed elsewhere [18], which is described by the following relationship for Allvac tested at a dK/dt of $1 \text{ MPa}\sqrt{\text{m/hr}}$ (solid line in Figure 1): $\log[da/dt_{\text{FALSE}} \text{ (mm/s)}] = -6.3009 + 0.0127 K_I \text{ (MPa}\sqrt{\text{m}})$. Since the plastic zone size depends on both K and yield strength [52], it is expected that the magnitude of false dcPD rise due to crack tip plasticity effects will be independent of the applied loading rate. Therefore, the resolution limit should scale linearly with applied dK/dt , with the resolution limit for dK/dt of $0.33 \text{ MPa}\sqrt{\text{m/hr}}$ simply being a three-fold reduction of the $1 \text{ MPa}\sqrt{\text{m/hr}}$ resolution limit. Despite heat-to-heat differences in yield strength, this is shown to be reasonably accurate by comparing tests conducted at a constant dK/dt of $0.33 \text{ MPa}\sqrt{\text{m/hr}}$ in dry nitrogen with the predicted $0.33 \text{ MPa}\sqrt{\text{m/hr}}$ resolution limit (dashed line in Figure 10). Subsequent plots will report the resolution limit specific to the dK/dt used for data generation.

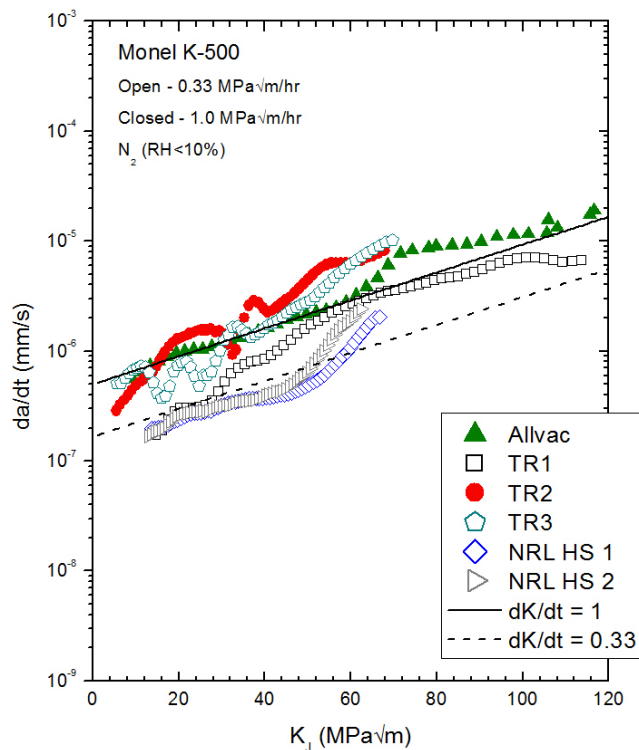


Figure 10 – Crack growth rate versus total K for five lots of peak-aged Monel K-500 stressed under two different dK/dt protocols in a dry nitrogen ($\text{RH} < 5\%$) environment. Closed symbols represent specimens tested at $dK/dt = 1 \text{ MPa}\sqrt{\text{m/hr}}$, while open symbols were tested at $dK/dt = 0.33 \text{ MPa}\sqrt{\text{m/hr}}$. Expected false da/dt produced by crack tip plastic deformation for each dK/dt are represented by the solid ($1 \text{ MPa}\sqrt{\text{m/hr}}$) and dashed ($0.33 \text{ MPa}\sqrt{\text{m/hr}}$) lines.

The second regime of behavior is typified by apparent crack growth above the plasticity-induced resolution limit at K_I values greater than $35\text{-}42 \text{ MPa}\sqrt{\text{m}}$, as shown by the NRL HS duplicates in Figure 1. SEM fractography conducted across all tested material heats revealed a triangular-shaped zone of transgranular/ductile fracture morphologies isolated to the center, high-constraint portion of the specimens,

as shown for inert environment-tested TR2 in Figure 11. Moreover, the dimpled, ductile crack progression in the center of the specimen (Figure 11b, right) was distinct from the morphology in the precrack region (left). Prior work postulated that this observed region was evidence of real sub-critical ductile crack advance, which may be governed by a thermally-activated dislocation glide mechanism [53] in the γ' -precipitate free zones known to form about TiC particles [43]. This hypothesis was based on the analysis of a deformation-mechanism map for pure Ni, which suggested that, at ambient temperature (i.e. 296 K (23°C)) and high stresses (as pertinent to a crack tip), enhanced dislocation glide (which is not true time-dependent creep behavior) will be active [54]. It was also suggested that this mechanism may be augmented by an H-contribution from either residual internal H or low levels of crack tip production due to residual moisture in the dry N₂ and/or H production at mild cathodic polarizations [53].

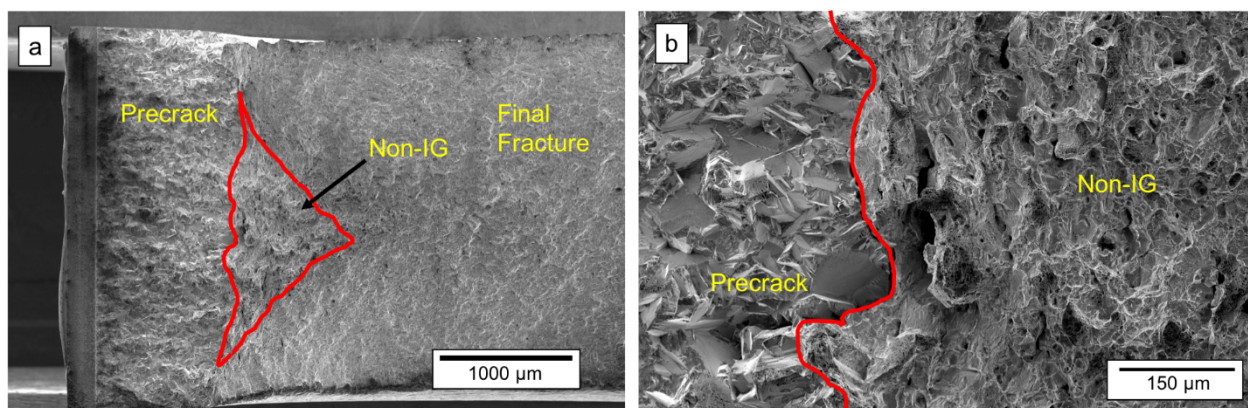


Figure 11 – Fractographs illustrating the (a) dimpled, ductile fracture morphology observed in the center (b) of inert environment-tested specimens.

However, recent work by Popernack demonstrates that this region is an artifact of the final fracture process [55]. Specifically, after conducting an inert environment test on the NRL HS heat, Popernack performed a ‘post-test’ fatigue protocol to induce a transgranular fracture morphology similar to the precrack in Figure 11b. Given the differences in fracture morphology, demonstrated in Figure 11b, this post-test fatigue would therefore enable a clear identification of any observed ductile crack growth. The solid and dashed white lines in Figure 12 mark the end of the fatigue precrack and dCPD-indicated crack length after the completion of the inert environment rising-K testing, respectively; the post-test fatigue region is then bounded by the white dashed line and black line in the micrograph. From this image, it is clear that the triangular region appears after the post-test fatigue region, which strongly suggests that sub-critical ductile crack advance did not occur during the slow rising-K portion of the experiment and that the observed triangular region occurs during final failure.

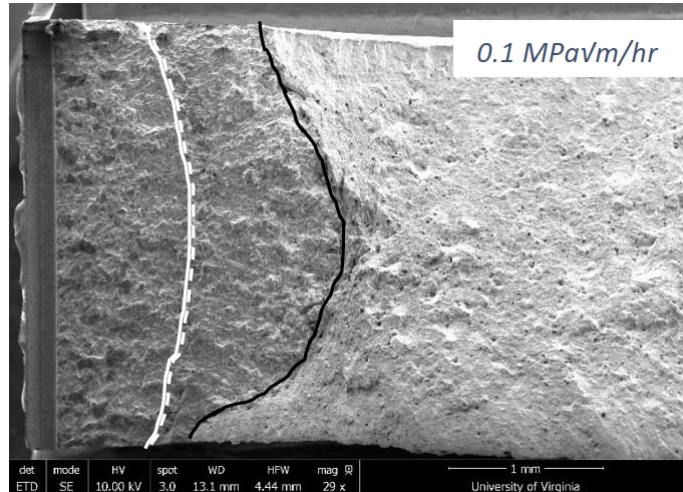


Figure 12 – Fractograph of an NRL HS specimen tested in dry N₂ at $dK/dt = 0.1 \text{ MPa}\sqrt{\text{m/hr}}$. The white solid line and dashed line represent the end of the fatigue precrack and the dcPD-indicated crack length after slow rising-K testing, respectively, while the black line represents the end of the post-test fatigue region. Adapted from [55].

While this finding clarifies the fractographic features observed in the inert environment-tested specimens, it does not explain the apparent crack growth above the resolution limit shown in Figure 1. To elucidate the origins of this crack growth, Popernack measured the voltage output from a dcPD-instrumented NRL HS dog-bone tensile specimen that was strained to failure [55]. As shown in Figure 13, three regions of behavior were identified during this testing. First, the voltage was found to linearly increase with increasing load, which is likely attributable to geometric effects on the electrical resistance as dictated by Poisson’s ratio (*e.g.* the specimen cross-section will shrink as the gage length is increased). However, upon reaching a load that aligns well with the proportional (elastic) limit of the alloy (denoted as (a) in Figure 13), the voltage begins to increase in a non-linear manner with additional strain. Finally, once the specimen has surpassed the force necessary for yielding (denoted as (b) in Figure 13), the voltage returns to a linear increase with load, but at a significantly steeper slope than was observed in the elastic region. Based on these results, Popernack calculated that the proportional limit would be exceeded (assuming no true crack growth occurred) in the NRL HS specimens shown in Figure 10 at $K \approx 40 \text{ MPa}\sqrt{\text{m}}$ [55], which was found to correlate well with the beginning of the inflection point shown in Figure 10. Taken together, these results strongly suggest that the crack growth above the resolution limit observed in Figure 10 can be attributed to bulk plasticity effects on the dcPD system. Such an effect has important ramifications on the testing of high toughness, moderate yield strength alloys (such as Monel K-500), as it effectively limits the K range over which the dcPD system will be accurate, and will be discussed further in Chapter 4.

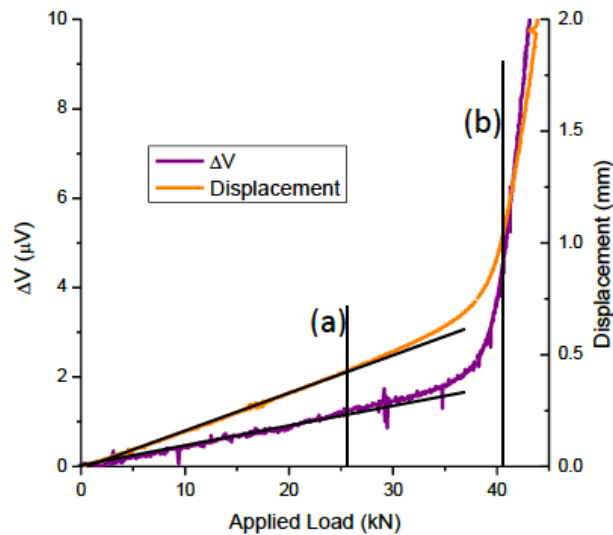


Figure 13 – Comparison of the change in dcPD-measured voltage and actuator displacement with applied force for a smooth dog-bone tensile specimen of NRL HS, with the force corresponded to the alloy proportional limit and yield stress denoted by (a) and (b), respectively. Adapted from [55].

3.4.2. Aqueous chloride electrolyte testing

3.4.2.1. Applied potential of -950 mV_{SCE}

The da/dt versus K_I data for Allvac, TR1, TR2, TR3, and duplicate NRL HS tests in 0.6 M NaCl at an applied potential of -950 mV_{SCE} are presented in Figure 14. The Allvac, TR 1, TR 2, TR 3, and NRL HS material lots show measured K_{TH} values of 29, 14, 18, 19, and 15/17 $\text{MPa}\sqrt{\text{m}}$, respectively. All K_{TH} values are closely clustered together for this testing condition, with the exception of Allvac, whose higher threshold value suggests an increased resistance to HEAC. This threshold stress intensity is similar to a previous reported value of 30 $\text{MPa}\sqrt{\text{m}}$ for the Allvac heat at -934 mV_{SCE} [18]. Stage II crack growth rates (at $K = 60\text{ MPa}\sqrt{\text{m}}$) of 7.2×10^{-6} , 3.8×10^{-6} , 2.7×10^{-6} , 4.6×10^{-6} , and $2.6 \times 10^{-6}/2.8 \times 10^{-6}\text{ mm/s}$ were observed for Allvac, TR 1, TR 2, TR 3, and NRL HS, respectively. The variation by a factor of 3 between lots is within the expected growth rate scatter established via five replicate tests of a single heat of Monel K-500 in 0.6 M NaCl at -1000 mV ; specifically, a 4-fold variation in da/dt_{II} was observed [56]. The current growth rates are lower than the previously reported da/dt_{II} of 1.9 to $2.3 \times 10^{-5}\text{ mm/s}$ at -1000 mV_{SCE} and $1.1 \times 10^{-5}\text{ mm/s}$ at -900 mV_{SCE} for Allvac [18]. However, the current da/dt_{II} data is reported at K_I of $60\text{ MPa}\sqrt{\text{m}}$ for a dK/dt of $0.33\text{ MPa}\sqrt{\text{m/hr}}$, whereas prior work reported values for K_I of $50\text{ MPa}\sqrt{\text{m}}$ for a dK/dt of $1.1\text{ MPa}\sqrt{\text{m/hr}}$ [18]. While observed slower growth rates for Allvac in the current work may be attributed to test-to-test scatter, they are directionally consistent with prior results in H-producing environments that show increasing dK/dt can enhance HEAC susceptibility in Ni-based alloys [18], steels [57], and Ti-6Al-4V [58].

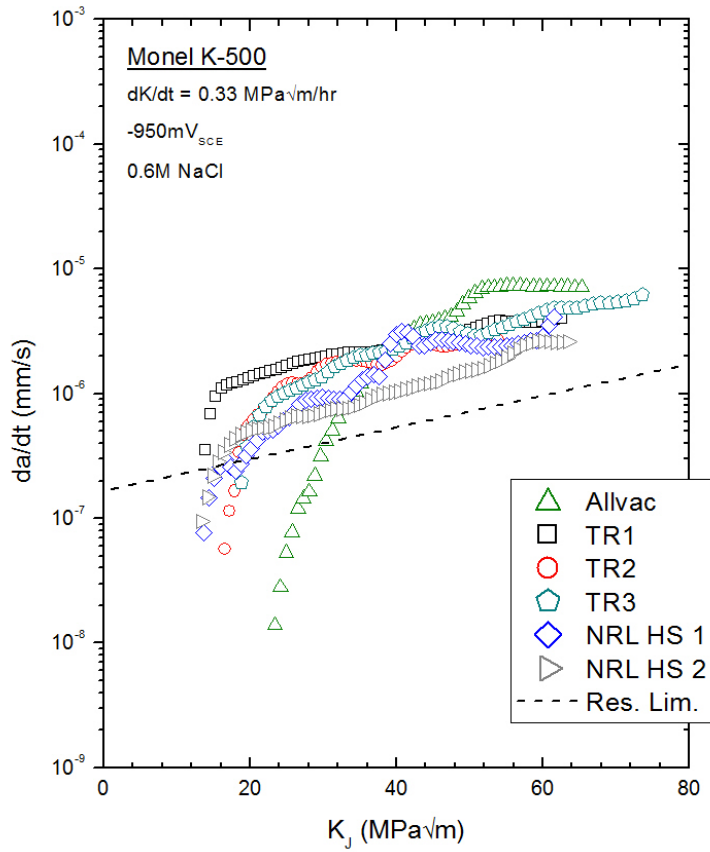


Figure 14 – Crack growth rate versus total K for five lots of peak-aged Monel K-500 stressed in NaCl solution at a constant applied potential of $-950\text{mV}_{\text{SCE}}$. The dashed line represents the expected false da/dt produced by crack tip plastic deformation for $dK/dt = 0.33 \text{ MPa}\sqrt{\text{m/hr}}$.

Fractography (each at roughly a K of $40 \text{ MPa}\sqrt{\text{m}}$) shown in Figure 15 demonstrates that IG cracking is the dominant fracture morphology for each material heat during slow-rising displacement testing in 0.6M NaCl at an applied potential of $-950 \text{ mV}_{\text{SCE}}$. However, NRL HS also showed distinct transgranular (TG) features (Figure 15e-f). Each image was taken at the same magnification, therefore different feature sizes reflect differences in grain size between material heats. High magnification images (Figure 16) reveal slip traces on the fracture surface IG features for each material. A detailed study of the density, spacing, and surface step height was not performed for each specimen, but a coarse observation suggests that the features were generally similar between the tested heats. Prior efforts have shown a correlation between the spacing of the slip traces on the IG fracture feature with TEM characterization of the dislocation cell structure underneath the fracture surface, suggesting a potentially critical effect of bulk slip behavior on the controlling HEAC damage mechanism [31,59]. The slip behavior for Monel K-500 (and the resulting strength and hardening behavior) is predominantly governed by the morphology of the homogeneously-distributed γ' precipitates, which is critically dependent on the processing history [43,44]. Given the differences in the yield strength reported in Table 6, it is likely that differences in γ' precipitate morphology

exist amongst the five heats of material, which could result in variations in the bulk slip morphology (*i.e.* the relative amount of shearing and looping) [44]. An initial study examining the variation in bulk slip morphology amongst these material heats was inconclusive and not reported here, but additional efforts are ongoing.

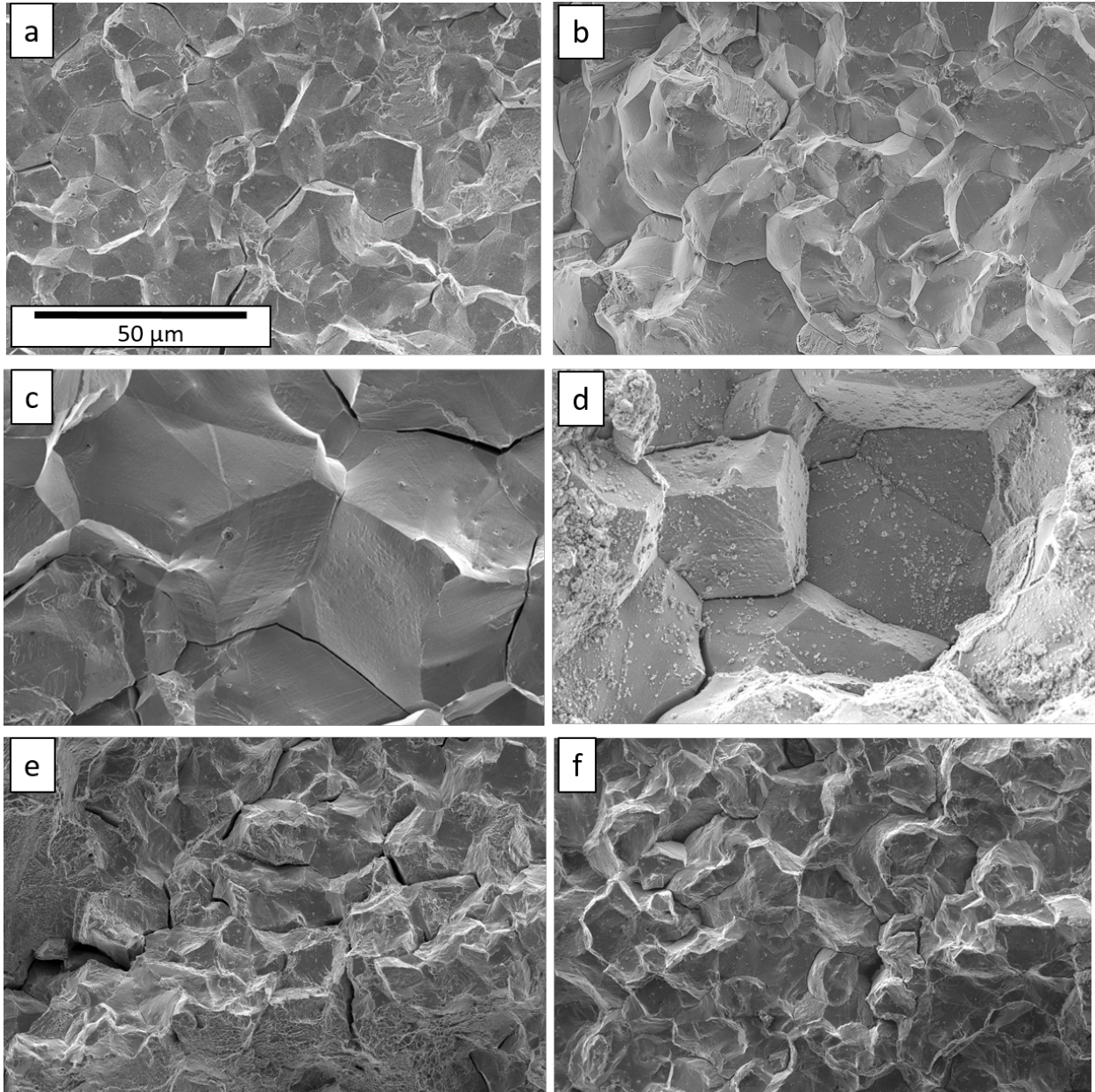


Figure 15 – Fractography of the intergranular (IG) fracture morphology observed for (a) Allvac, (b) TR1, (c) TR2, (d) TR3, and (e-f) NRL HS when tested in 0.6M NaCl solution with an applied potential of -950mVSCE. In addition to the IG morphology, NRL HS (e-f) also exhibited some transgranular features.

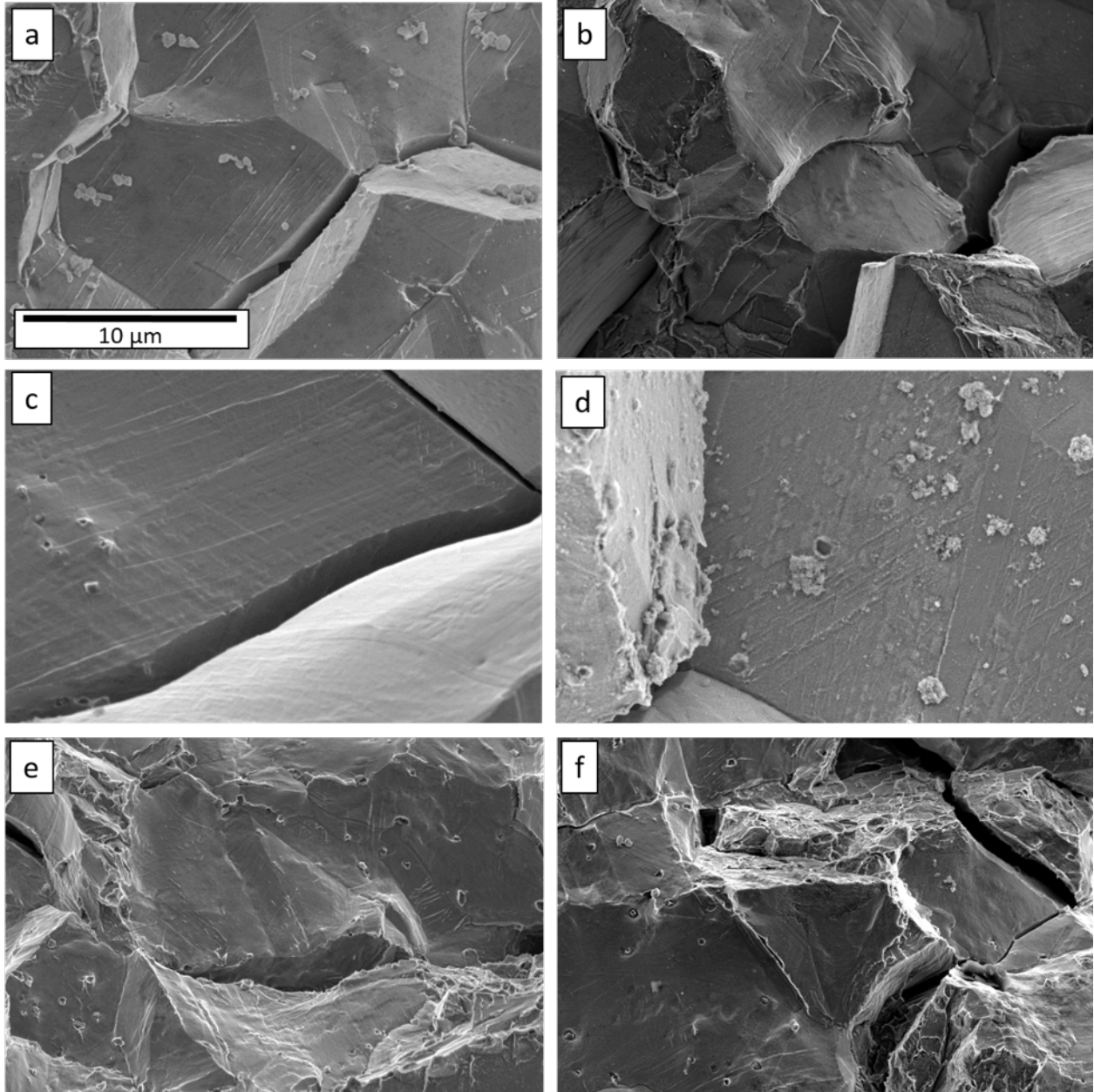


Figure 16 – Fractographs of facet slip traces for (a) Allvac, (b) TR1, (c) TR2, (d) TR3, and (e-f) NRL HS when tested in 0.6M NaCl solution with an applied potential of -950mV_{SCE}.

3.4.2.2. Applied potential of -850 mV_{SCE}

Severe H-producing environments will give rise to sufficiently high crack tip H-concentrations ($C_{H,c}$) such that any effect of heat-to-heat variation in metallurgy on HEAC susceptibility may be masked by the strong propensity for HEAC. Therefore, it is advantageous to investigate the effect of metallurgy-based variations in the HEAC behavior by testing at applied potentials that produce a lower level of C_{H-Diff} . Prior work established an empirical relationship between diffusible hydrogen concentration and the applied potential for Monel K-500 by utilizing artificial crevice geometries pertinent to current LFM experiments.

These experiments demonstrated that, for an applied potential of $-850 \text{ mV}_{\text{SCE}}$, the value of $C_{\text{H-Diff}}$ generated in the crack tip environment is $<10 \text{ wppm}$ [18,25]. As such, the HEAC kinetics were established at this less negative potential ($-850 \text{ mV}_{\text{SCE}}$) in 0.6 M NaCl for each material lot.

The da/dt versus K_I data for duplicate Allvac, TR1, TR2, TR3, and duplicate NRL HS tests in 0.6 M NaCl at an applied potential of $-850 \text{ mV}_{\text{SCE}}$ are presented in Figure 17. The TR1, TR 2, and TR 3 material lots all had similar da/dt_{II} crack growth rates of $2.2 \times 10^{-6} \text{ mm/s}$, $4.0 \times 10^{-6} \text{ mm/s}$, and $3.8 \times 10^{-6} \text{ mm/s}$ at a K_I of $60 \text{ MPa}\sqrt{\text{m}}$ with K_{TH} values of 17, 42, and $24 \text{ MPa}\sqrt{\text{m}}$, respectively. Macroscale fractography of TR 2 shows the smooth EDM notch (Figure 18a, far left), the in-air fatigue precrack region that consisted of TG-slip based cracking ending at the dotted line, transitioning to mixed IG/TG crack progression along the entire crack front during the slow-rising displacement testing to the solid line, followed by final ductile failure. The mixed IG/TG morphology observed during loading at an applied potential of $-850 \text{ mV}_{\text{SCE}}$ in 0.6 M NaCl is shown at a K_I of roughly $40 \text{ MPa}\sqrt{\text{m}}$ in Figure 18b-d for TR1, TR 2, and TR 3, respectively. This morphology is consistent with slow-rising displacement testing of Monel K-500 where mild cathodic polarizations resulted in HEAC with identical IG/TG crack growth [18].

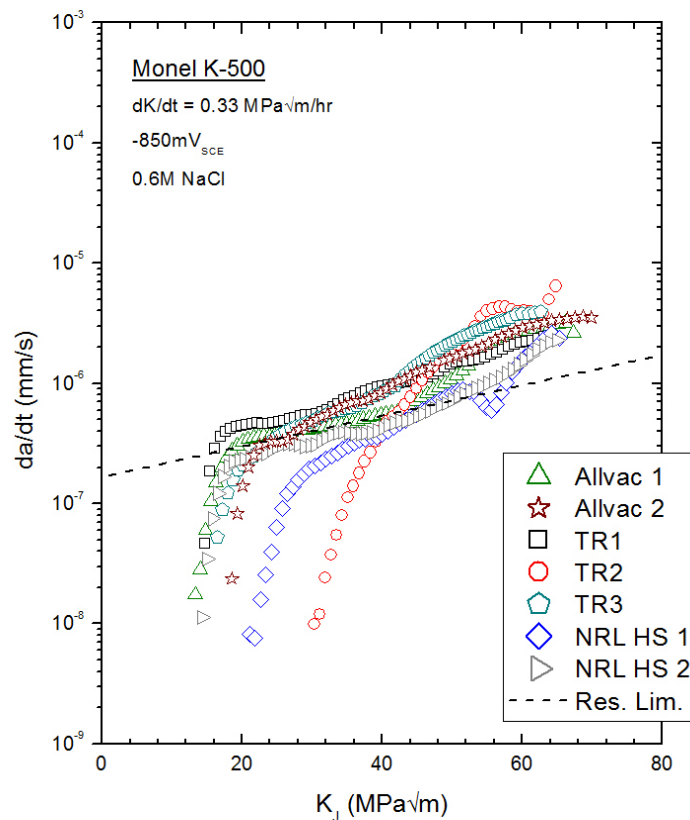


Figure 17 – Crack growth rate versus total K_I for five lots of peak-aged Monel K-500 stressed in NaCl solution at a constant applied potential of $-850 \text{ mV}_{\text{SCE}}$. The dashed line represents the expected false da/dt produced by crack tip plastic deformation for $dK/dt = 0.33 \text{ MPa}\sqrt{\text{m/hr}}$.

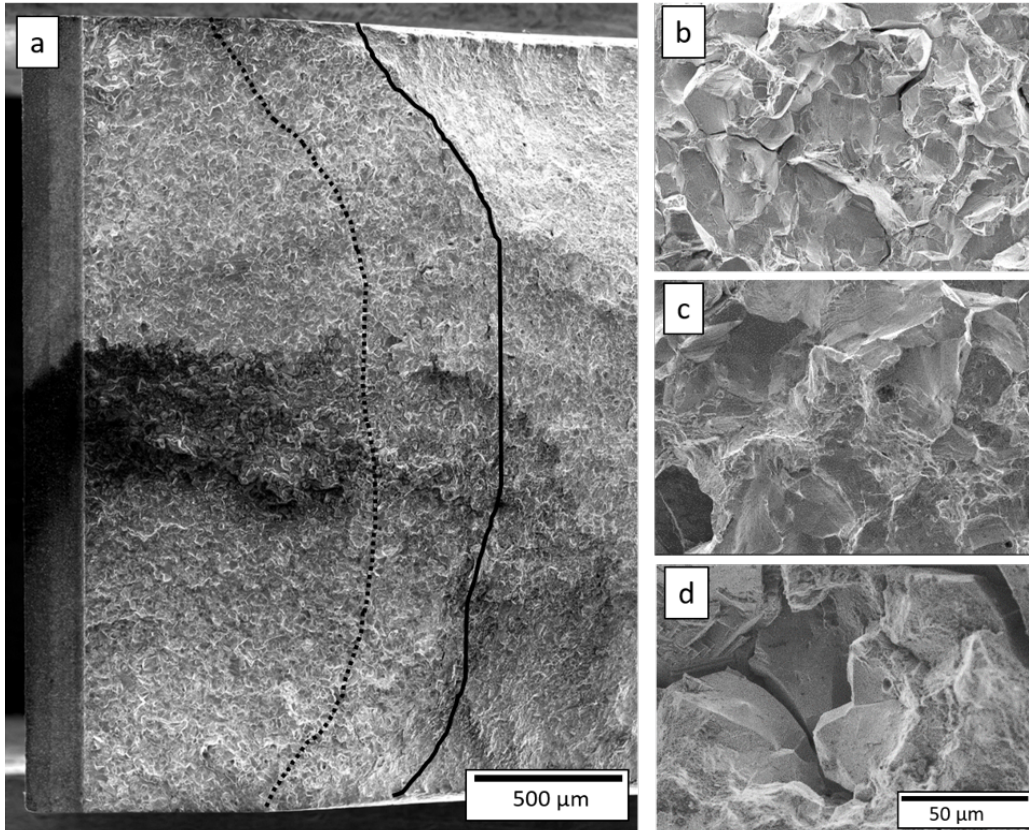


Figure 18 – Fractography of samples tested at an applied potential of -850 mVSCE in 0.6M NaCl: (a) overview of TR2 fracture surface and the fracture morphology observed at the crack length where $K = 40 \text{ MPa}\sqrt{\text{m}}$ for (b) TR1, (c) TR2, and (d) TR3. The black dashed line and solid line indicate the end of the fatigue precrack and slow rising-K test, respectively.

As shown in Figure 17, the da/dt versus K_I data are quite similar amongst the five material heats. These similarities in the apparent growth rates between the non-susceptible and susceptible material heats underscore the challenge of testing proximate to the immunity potential (e.g. the potential above which (or more positive than) HEAC does not occur). However, fractography of the NRL HS and Allvac specimens tested at -850 mVSCE (e.g. Figure 19b) shows ductile morphology typical of inert dry N_2 testing (e.g. Figure 11a), suggesting HEAC did not occur in these material heats. The enhanced HEAC resistance of NRL HS and Allvac is further supported by the similarity in da/dt vs. K data at -850 mVSCE for Allvac (replicate tests) and NRL HS (replicate tests) specimens with inert dry N_2 growth rates, as demonstrated in Figure 19a for NRL HS³. Taken together, these findings suggest that no HEAC occurred in these specimens; therefore, K_{TH} and da/dt_H are not reported for the Allvac and NRL HS lots. This observed variations in HEAC susceptibility amongst the materials heats is corroborated by recent slow-strain rate tensile testing

³ The similarities in fracture morphology for NRL HS tested at -850 mVSCE and in dry N_2 also suggest that bulk plasticity effects on the measured dcPD voltage are responsible for the observed crack growth rates above the resolution limit (shown in Figure 17 and Figure 19a).

of Allvac and TR2 materials pre-charged with H, which demonstrated enhanced susceptibility to IG fracture for TR2 [60].

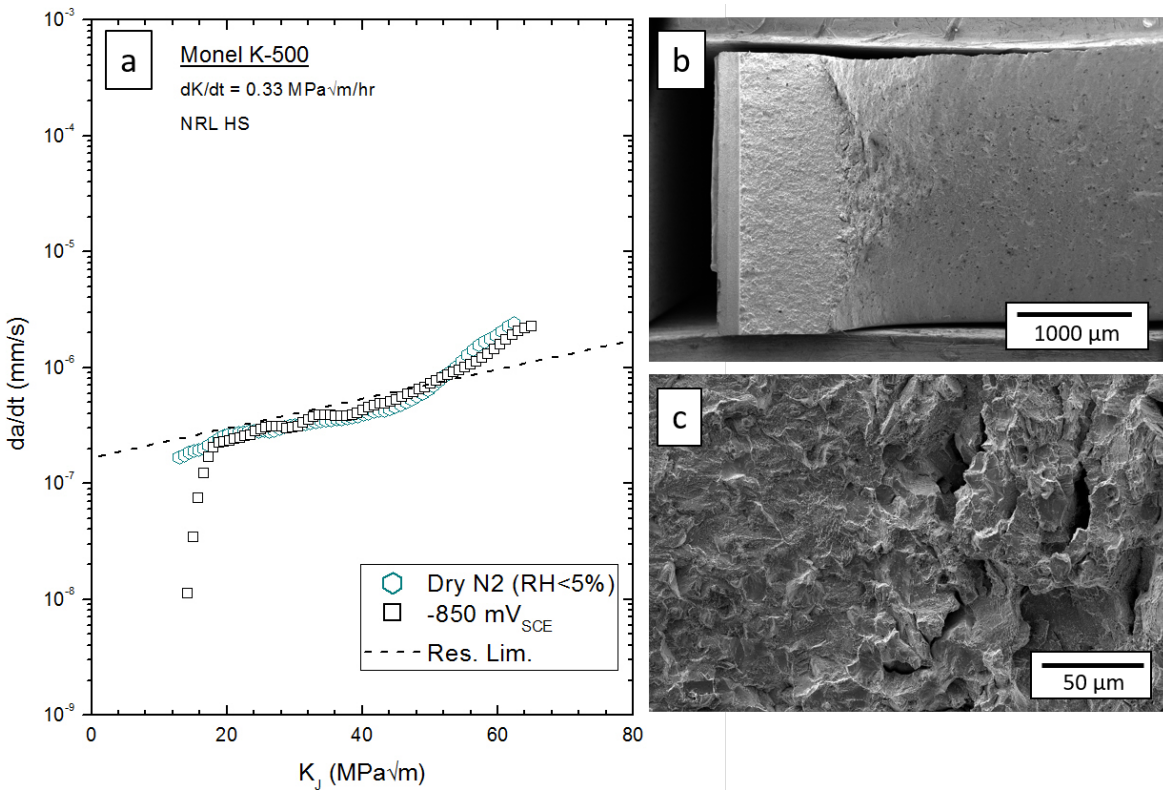


Figure 19 – Comparison of (a) crack growth kinetics data for NRL HS tested in dry N2 and 0.6M NaCl at -850 mVSCE and fractographs of the (b) dimpled, ductile fracture morphology observed in the center (c) of the 0.6M NaCl at -850 mVSCE specimen.

In summary, despite the nominally similar growth rates shown in Figure 17, the fractography in Figure 18 and Figure 19 clearly demonstrates a difference in fracture morphology between the TR materials and the Allvac/NRL HS materials. Specifically, the observed ductile failure morphology suggests that the Allvac/NRL HS lots are more resistant to HEAC at -850 mV_{SCE} than the TR lots, which contained the mixed IG/TG morphology typical of HEAC. This inconsistency in the HEAC susceptibility amongst material heats can be interpreted as either (1) variability that is inherent to testing in a potential regime where minor changes in local crack environment result in orders of magnitude changes in HEAC susceptibility [18], or (2) metallurgy-specific characteristics that shift the critical potential where HEAC susceptibility initiates and modify HEAC growth rates. Additional studies (discussed in Section 3.7) are needed to probe the former, while the latter will be discussed in detail in the following sections.

3.4.3. Characterization of grain size and grain boundary character distribution

For polycrystalline materials, it has been suggested that the HEAC behavior may be influenced by the prevalence of certain ‘special’ boundaries (low angle and coincident site lattice boundaries (CSL)) as well as the degree of high angle boundary connectivity (*i.e.* the possibility that ‘special’ boundaries disrupt connected pathways of ‘susceptible’ boundaries) [61–63]. As such, it is worthwhile to characterize the grain size and grain boundary character distribution of the tested material heats to determine whether variations in these parameters correlate with susceptibility. Towards this end, orientation maps colored to reflect grain orientations relative to the Z-axis (IPF-Z, Z is oriented out of the page) are presented for each material in Figure 20a-e, with grain boundaries highlighted as black lines. The results of an ASTM E112-113 grain size analysis are reported in Table 7, along with the calculated grain boundary surface area to volume ratio (S_v ; mm^2/mm^3) [64,65]. The OIM of a representative 0.05 mm^2 area of each material is used to quantify the distribution of high angle ($>15^\circ$), low angle ($>5^\circ$ and $\leq 15^\circ$), and CSL boundaries. The resolution of the analysis enabled characterization of orientation variations within grains (attributed to sub-grain crystal distortions and possibly dislocation structures [66]), though for clarity in the intergrain misorientation analysis and grain size calculations, the orientation of each grain was averaged using the Tango software and misorientation angles below 5° were not included in the analysis. The fraction of (1) the total number of boundaries and (2) the total S_v that are low energy (including random boundaries $<15^\circ$ and CSL boundaries) range from 53-61% and 53-64%, respectively (Table 7), with the majority of low energy boundaries being $\Sigma 3$ boundaries. Despite this seemingly small range, the differences in grain size give rise to non-negligible variations in the total S_v of low energy boundaries between material lots, which may be important in the context of the susceptible path connectivity [61,62]. For example, 43 and 44% of the S_v are high energy boundaries in Allvac and TR 2, but grain size differences (13.8 and $35.3 \mu\text{m}$, respectively) result in the total S_v of high energy boundaries being $162 \text{ mm}^2/\text{mm}^3$ for Allvac and $70 \text{ mm}^2/\text{mm}^3$ for TR2.

Table 7 - Grain size and grain boundary characteristics of Monel K-500 heats

Material Heat	d (μm)	Total S_v (mm^2/mm^3)	Low Angle/CSL Boundary Fraction (%)	High Angle Boundary S_v (mm^2/mm^3)	Low Angle/CSL Boundary S_v (mm^2/mm^3)
Allvac	13.8	341	57	146.6	194.4
NRL-HS	11.2	407	62	154.7	252.3
TR1	25.8	252	60	100.8	151.2
TR2	35.3	149	56	65.6	83.4
TR3	31.8	160	53	75.2	84.8

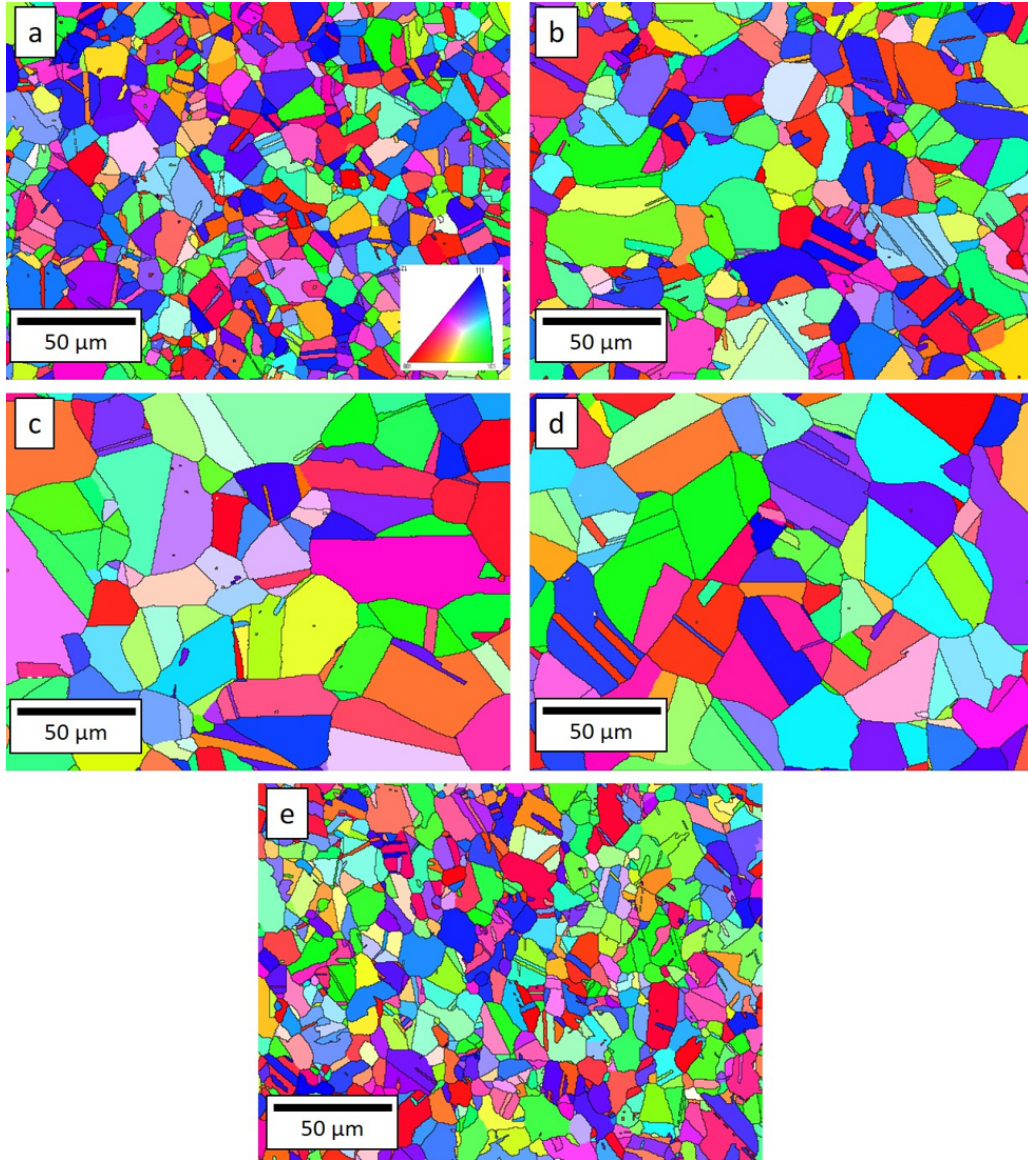


Figure 20 – Orientation maps for (a) Allvac, (b) TR1, (c) TR2, (d) TR3, and (e) NRL HS collected using electron backscatter diffraction. Grain boundaries (black lines) were defined by misorientations greater than 15°.

3.4.4. Characterization of hydrogen-metal interactions

For transparency, the experiments/results/interpretations described in the following section (as well as Section 3.5.2.3.) should not be credited to the author, though this work is presented within two manuscripts (see Section 3.1 for details) to which the author has contributed. This work was completed by Prof. Brendy Rincon Troconis and Prof. John Scully, but the findings are highly relevant to the current chapter and so have been included for context. For more details on the methodology employed, the reader is referred to Reference [60].

Evaluating the effect of hydrogen interactions requires the examination of many parameters. These

include hydrogen evolution kinetics to address differences in H production and adsorption, hydrogen concentration, hydrogen diffusion rates, and trap binding energies. The segregation of trace elements to the grain boundary is also of interest due to their potential to promote increased hydrogen activity and/or lower $C_{H,crit}$ [67], as well as lower intrinsic fracture toughness (k_{IG}) [25,68,69]. The kinetics of the hydrogen evolution reaction were studied by measuring the Tafel slope and exchange current densities for water reduction (hydrogen evolution) in 0.6 M NaCl at pH 8.0. Hydrogen production rates were found to be similar amongst the different materials, indicating that heat-to-heat variation does not affect this parameter. Figure 21 displays the effect of hydrogen overpotential on both the total ($C_{H,Total}$) and diffusible ($C_{H,Diff}$) hydrogen concentration where both concentration parameters were found to increase with increasing hydrogen overpotential. As expected, the total hydrogen concentration $C_{H,Total}$ was larger than $C_{H,Diff}$ [25]. In terms of heat-to-heat variation, there was limited difference between both $C_{H,Total}$ and $C_{H,Diff}$, except for the Allvac material, which consistently exhibited hydrogen concentration near the lower bound of all other heats or statistically lower hydrogen levels based on repeat measurements at some potentials.

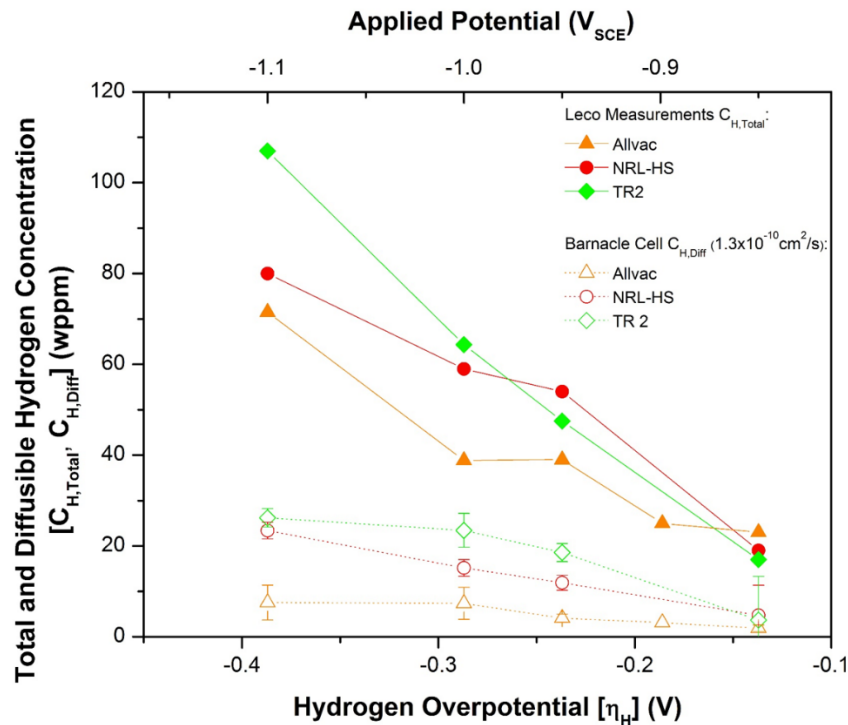


Figure 21 – Effect of hydrogen overpotential on total and diffusible hydrogen concentrations for the Allvac, TR2, and NRL-HS. Error bars represent 95% confidence interval.

Variations in diffusible hydrogen concentration could arise from hydrogen interacting with low and high binding energy traps, such as: dislocations[70,71], grain boundaries, carbides[72], microvoids, age

hardening precipitates (e.g. γ') [25,70,73], among others. Two trap binding states were found in all the heats tested; these results are in agreement with previous information reported on solution heat treated (SHT), aged and SHT, cold worked, aged Monel K-500 materials [25]. The average values for the binding energies for γ' were found in the range 7.8 to 17.7 kJ/mol in the following ascending order: NRL-HS < TR 2 < Allvac. Changes in trap binding energy would result in heat-to-heat differences in the hydrogen diffusion coefficient, which would critically affect the proposed HEAC behavior (as quantified in Eqn 3.3). However, prior analysis found similar hydrogen diffusion coefficients (in the range $0.9\text{-}3.9 \times 10^{-14} \text{ m}^2/\text{s}$) for all materials, suggesting a secondary role of trapping/diffusion on heat-dependent HEAC behavior [25,74].

3.5. Discussion

The crack growth kinetics (Figure 1, Figure 14, and Figure 17) and cracking morphologies (Figure 15 and Figure 19) demonstrate that, in both inert (dry N_2 gas) and aggressive (0.6 M NaCl polarized to $-950 \text{ mV}_{\text{SCE}}$) environments, the sub-critical cracking behavior shows little variation in HEAC susceptibility between different heats of Monel K-500. However, at mildly aggressive environments (0.6 M NaCl polarized to $-850 \text{ mV}_{\text{SCE}}$) where low crack tip H-uptake is expected [18], a noticeable variation in fracture morphology is observed amongst the material heats. Specifically, the Allvac and NRL HS heats exhibit no fractographic evidence of HEAC and have crack growth kinetics that are essentially identical to those ‘measured’ in inert environments, while TR1, TR2, and TR2 show both a mixed TG/IG morphology and crack growth kinetics consistent with a HEAC-based mechanism. This disparity in fracture morphology, despite similar measured crack growth kinetics, underscores the challenge of measuring HEAC kinetics in modest susceptibility environments. Taken together, these data demonstrate that heat-to-heat microstructural variation can tangibly influence HEAC susceptibility in Monel K-500, even if all tested heats satisfy the current procurement specification [41].

The following discussion elucidate the microstructural features governing HEAC susceptibility in Monel K-500 by correlating the fracture mechanics testing results with materials characterization data and mechanism-based modeling. First, decohesion-based models of HEAC are exercised to mechanistically inform how potential variations in microstructure could impact HEAC susceptibility metrics. Then, measured variations in microstructural features are evaluated against the observed HEAC metrics to enable the identification of salient parameters. Microstructural features evaluated in the current work include: grain size, grain boundary character/connectivity, bulk and grain boundary composition, H-metal interactions, and yield strength/strain hardening. Finally, a potential modification to the K_{TH} model to better account for microstructural influences is evaluated.

3.5.1. Effect of microstructure variations on HEAC at mild and aggressive applied potentials

Decohesion-based models (Eqn. 3.2 and 3.3) provide a quantitative framework for understanding the extent to which variations in material properties will influence HEAC metrics (K_{TH} and da/dt_H) at different applied potentials. Specifically, this framework can be utilized to inform why all material heats demonstrate similar HEAC susceptibility at -950 mV_{SCE}, while significant differences are observed for materials tested at -850 mV_{SCE}. The justification and validation of the decohesion-based modeling approach was established in prior work [18] and has been recently refined [53]. For the current sensitivity analysis, the input parameters for K_{TH} modeling are $\sigma_{YS} = 786$ MPa (Allvac), $\alpha'' = 0.0002$ MPa \sqrt{m} , and $\beta' = 0.20$ (MPa \sqrt{m})⁻¹ (based on dislocation-shielding simulations of the near crack tip stress field [32,75] and validated by experimental data on IN718 [37,53]). $C_{H-\sigma}$ is calculated from Eqn. 3.11, where $\sigma_H = 9\sigma_{YS}$ and an empirical relationship relates the applied potential to C_{H-Diff} for the Allvac material [18]. k_{IG} is the Griffith toughness of the IG interface, calculated to be 0.88 MPa \sqrt{m} using the Griffith relation and theoretical values of the surface energy of Ni[53]. α represents the potency of the local H in decreasing k_{IG} and is set to 4.078 (MPa \sqrt{m} per atom fraction H) to fit the model to the average of three Allvac K_{TH} values (established from previous work as 18 MPa \sqrt{m} [18]) at an applied potential of -1000 mV_{SCE}. From these parameters, the baseline predicted effect of applied potential on the K_{TH} of Allvac is reported in Figure 22a-c (solid black line).

The sensitivity of HEAC to microstructural variation at different applied potentials can be evaluated by systematically varying model input parameters that are likely to exhibit heat-to-heat differences. As such, three modeling parameters are varied in the current K_{TH} modeling. First, the sensitivity of the models to variations in H uptake behavior is evaluated by multiplying and dividing the calculated C_{H-Diff} by 2.5 (corresponding to a 250% increase and a 60% decrease). This 250% increase in uptake behavior is physically realistic for Monel K-500 [18] and is supported by the analysis conducted by Rincon Troconis and Scully (Figure 21), which indicates lower C_{H-Diff} in Allvac for a given applied potential. Figure 22a clearly demonstrates that increasing/decreasing C_{H-Diff} results in a more pronounced variation in K_{TH} as the applied potential is increased from -950 to -850 mV_{SCE}. For example, increasing C_{H-Diff} by 250% (Figure 22a, thick solid blue line) results in a decrease of K_{TH} by 61 MPa \sqrt{m} at -850 mV_{SCE} whereas a decrease of only 15 MPa \sqrt{m} is calculated for -950 mV_{SCE}. Similarly, the changes in K_{TH} are again more severe at -850 mV_{SCE} when the intrinsic grain boundary toughness (k_{IG}) is varied $\pm 25\%$ with all other inputs at the baseline levels, as shown in Figure 22b. Physically, such variations in grain boundary toughness could result from differences in the fraction of high energy boundaries or boundaries containing significant concentration of deleterious impurity atoms. Considering the latter possibility, atomistic modeling has shown that a grain boundary sulfur concentration of 5 at. % can reduce the grain boundary strength by $\sim 20\%$ [76]. Decreasing

k_{IG} from 0.88 to 0.66 $\text{MPa}\sqrt{\text{m}}$ (Figure 22b, thick solid blue line) results in a K_{TH} decrease of 62 and 14 $\text{MPa}\sqrt{\text{m}}$ for -850 and -950 mV_{SCE} , respectively. Note that modifications to k_{IG} will have a similar effect as varying the $\alpha C_{H-\sigma}$ term since the two terms are subtracted in Equation 3.2. Finally, the -850 mV_{SCE} condition is significantly more sensitive to a $\pm 15\%$ change in σ_{YS} (Figure 22c, thick solid blue line); an increase in σ_{YS} from 786 to 904 MPa results in a 65 and 16 MPa change in K_{TH} for -850 and -950 mV_{SCE} , respectively. Critically, this variation in yield strength represents the range of values observed for the current materials, as shown in Table 6, illustrating the large change in HEAC resistance that could be expected across the tested material heats.

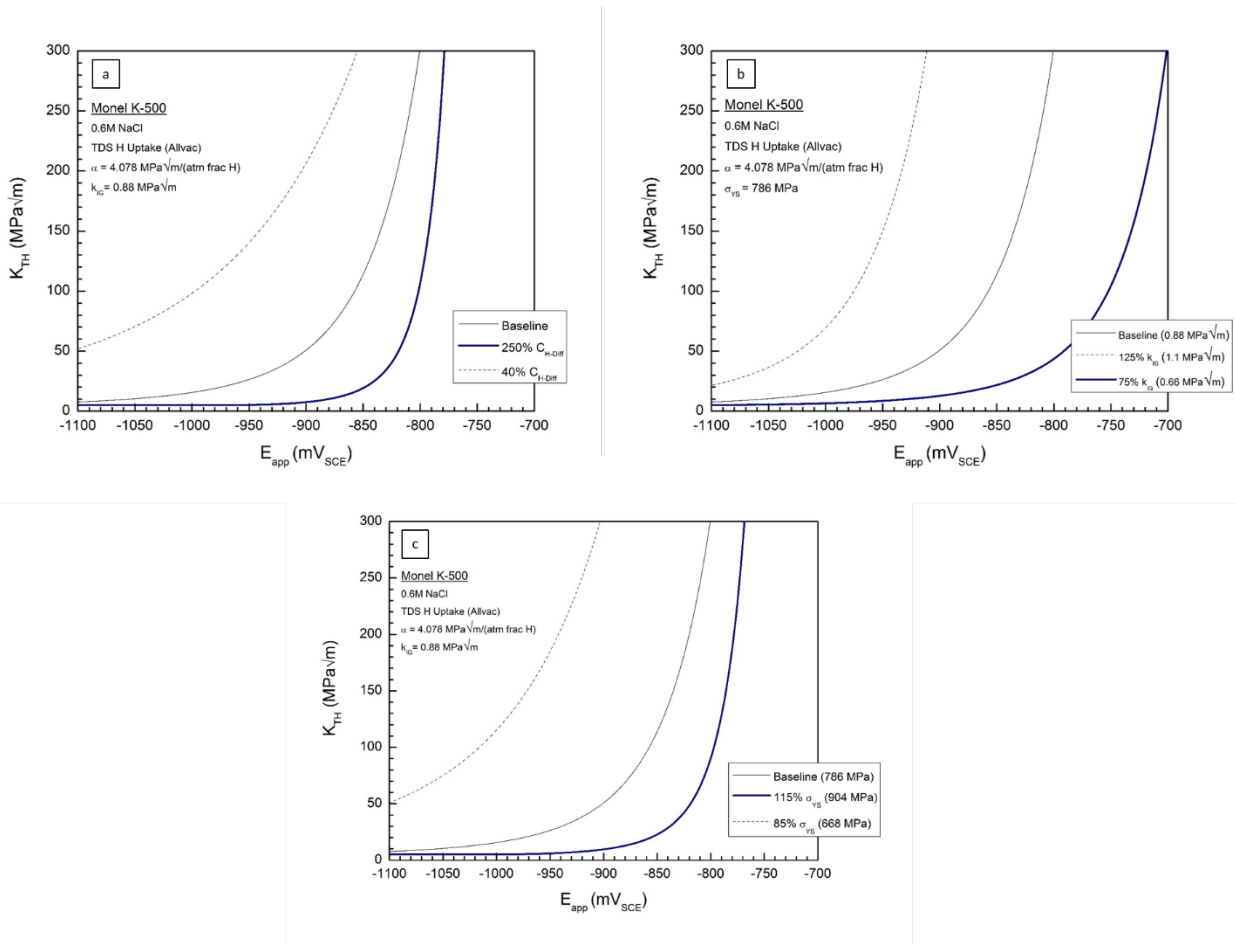


Figure 22 – Sensitivity analysis conducted on the modeling to determine the effect of (a) a $\pm 250\%$ change in diffusible hydrogen concentration relative to the baseline value found for Allvac, (b) a $\pm 25\%$ change in the Griffith toughness of the grain boundary (k_{IG}) relative to the baseline value of $0.88 \text{ MPa}\sqrt{\text{m}}$, and (c) a $\pm 15\%$ change in the yield strength from the Allvac yield strength (786 MPa) on the calculated threshold stress intensity.

A similar sensitivity analysis was performed to understand how changes in microstructure may influence da/dt_{II} at different applied potentials, shown in Figure 23. The baseline parameters for current modeling mimic those in prior work [18,53], where $D_{eff} = 1 \times 10^{-10} \text{ cm}^2/\text{s}$, $x_{crit} = 1 \text{ }\mu\text{m}$, $C_{H-\sigma}$ is calculated in

the same manner as in the K_{TH} modeling, and C_{H-crit} is set to 647 wppm [53]. The baseline calculation (Figure 23a-b; black solid line) demonstrates HEAC growth rates increase several orders of magnitude as the potential is decreased from approximately -840 to 900 mV_{SCE}; however, further reduction of the potential from -900 to -1100 mV_{SCE} results in a minimal increase in da/dt. The sensitivity of this behavior to varying metallurgical features can be quantitatively evaluated by varying the hydrogen uptake behavior and yield strength inputs in Eqn 3.3; the D_{eff} and x_{crit} parameters are considered invariant with regards to microstructure [18,25]. To evaluate the sensitivity of the model to variations in hydrogen uptake, the diffusible hydrogen concentration was again increased 250% and decreased 60% (Figure 23a-b, thick solid blue line and dashed line, respectively). As demonstrated by Figure 23a, the difference in da/dt_{II} significantly increases amongst the three calculated curves when moving from -950 to -850 mV_{SCE}, suggesting that the effect of metallurgical variations is more discernible at higher potentials. This same behavior is noted when varying the yield strength $\pm 15\%$; specifically, the effect of yield strength variation on da/dt_{II} is more pronounced at less negative applied potentials (Figure 23b). These observations can be rationalized in the context of strong cathodic polarizations leading to a level of crack-tip H that greatly exceeds the critical value required for cracking (i.e. $C_{H\sigma-crit}$). Therefore, it can be expected that variations in material HEAC resistance will only marginally influence the cracking behavior at -950 mV_{SCE}, while HEAC susceptibility becomes more material-dependent as the applied potential increases to -850 mV_{SCE}.

In summary, a sensitivity analysis using previously validated models for K_{TH} and da/dt_{II} (Eqn 2 and 3, respectively) clearly establishes that microstructure-based changes in material properties are expected to have an increasing effect on HEAC susceptibility at applied potentials that produce lower crack-tip H concentrations. These results are consistent with experimental observations of minimal heat-to-heat variation in the HEAC behavior at -950 mV_{SCE} (Figure 14) and significant heat-dependent HEAC behavior at -850 mV_{SCE} (Figure 18 and Figure 19). Taken together, these experimental and decohesion-based modeling results demonstrate that microstructural influences can alter HEAC susceptibility with the caveat that these deviations are attenuated as environmental conditions increase in severity. Furthermore, these findings reinforce the need to accurately capture environmental conditions when performing engineering-scale modeling so as to ensure reliable predictions.

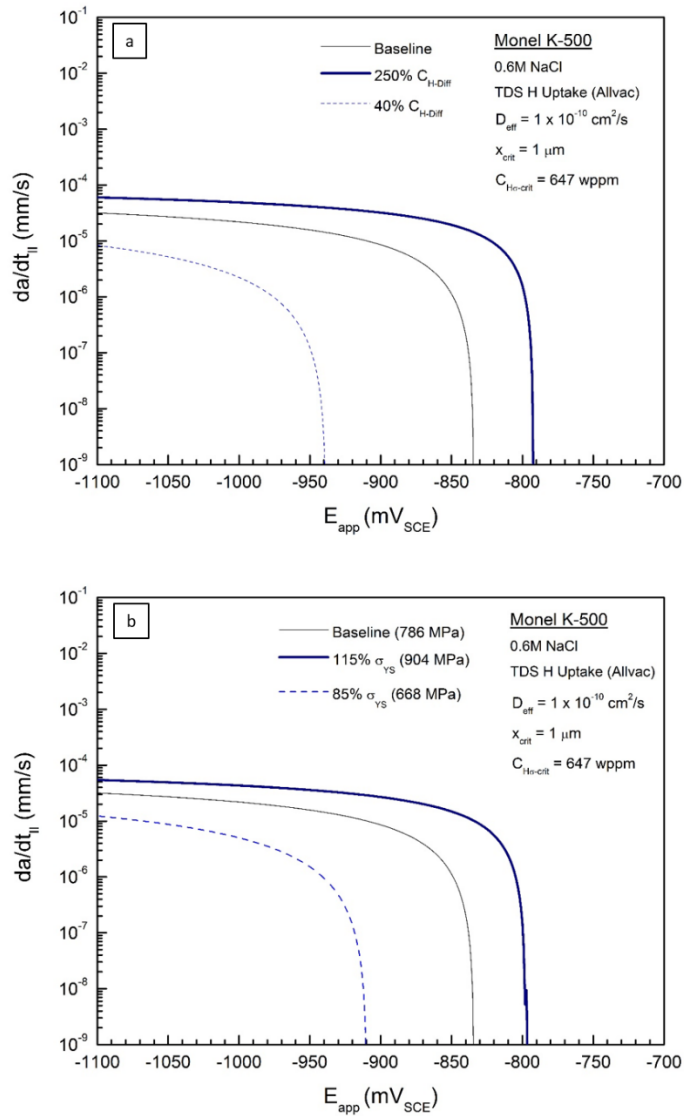


Figure 23 – Sensitivity analysis conducted on the modeling to determine the effect of (a) a $\pm 250\%$ change in diffusible hydrogen concentration relative to the baseline value found for Allvac and (b) a $\pm 15\%$ change in the yield strength from the Allvac yield strength (786 MPa) on the calculated H-diffusion limited crack growth rate, da/dt_{II} .

3.5.2. Correlating the variation in microstructural features with HEAC susceptibility

3.5.2.1. Material Composition

The basic composition of Monel K-500 consists of roughly 66 wt% Ni and 30 wt% Cu, augmented by the addition of ~ 3 wt% Al and 0.6 wt% Ti to enable further strengthening via precipitation of the γ^2 -phase [77]. Trace impurity elements can have significant effects on creep resistance, weldability, corrosion resistance, and mechanical properties in Ni-based alloys and must be controlled to optimize material performance [78–80]. Specifically, impurity elements (e.g. O, H, N, Ar, He, S, P, Pb, Bi, Sb, As, Se, Ag,

Cu, Tl, Te) have been broadly characterized as deleterious to the material properties of Ni and/or Ni-based alloys [78,81]. As shown in Table 5, no clear trend of trace S, P, Pb, Ag, or Sb content and HEAC resistance was observed, though higher levels of As (and marginally Bi and Te) were found in the more susceptible TR 1, TR2, and TR3 materials. These subtle differences are likely not sufficient to deleteriously influence properties, especially considering the minute bulk impurity levels [78,81]. However, there is a broad literature which demonstrates that elements such as Bi, Te, Pb, S, B, C, Zr, Hf, P, Mg, and Ta have an affinity for segregating to grain boundaries (GBs), giving rise to local concentrations well above what is observed in the bulk [79,82,83]; this segregation can magnify the influence of variations in the trace element content. The degree of segregation is dependent on the element and the grain boundary misorientation [62,84,85], as well as the concentration of intentionally added getter elements (e.g. Mg, Zr, Hf, C) which retard the segregation of deleterious elements to the GB. Of critical importance to the HEAC behavior is the (direct or indirect) effect of these impurity and trace elements on the grain boundary susceptibility to (chemo-)mechanical failure.

While elemental C segregation to GBs has been shown to be innocuous [86] or even beneficial [87] in Ni alloys, Natishan *et al.* have suggested that a semi-continuous, thin film of unalloyed C may contribute to the IG failure of Monel K-500 in hydrogen [88,89]. This film was sporadically observed along grain boundaries and is likely in the form of graphite, similar to what has been reported for Nickel 200 after prolonged exposures to 698-923 K (425-650°C) [90]. In the context of present results, Table 5 demonstrates that the more susceptible TR1 and TR2 have increased levels of C, but this is conflicted by HEAC-susceptible TR3 having less C content than the immune Allvac lot. However, prior researchers found that the prevalence of the film does not scale with the bulk carbon content, but instead is dependent on applied thermal processing [89]. In this paradigm, a composition/processing variation that failed to produce a graphite film would then be responsible for the lack of IG cracking in Allvac and NRL HS, while the mixed IG/TG features observed for TR1, TR2, and TR3 (Figure 18) at $-850 \text{ mV}_{\text{SCE}}$ would be due to graphite film-induced IG failure as opposed to HEAC. However, this conjecture is not consistent with the absence of crack growth for all alloys in the dry N_2 environment or during prior low H environment testing for the Allvac heat [53]. Moreover, according to Natishan *et al.*, the graphite film-enhanced IG susceptibility of Monel K-500 was most pronounced at low H conditions, while inhibiting HEAC susceptibility at higher H concentrations [88,89], which directly contradicts the current experimental results (Figure 14 and Figure 15). Finally, during the initial assessment of bulk slip morphology *via* TEM, no grain boundary graphite film was observed in any of the tested material heats. As such, this graphite film-based mechanism is not considered to be a source of the current heat-to-heat variation.

Sulfur (where segregation can give rise to GB concentrations over 2000-fold higher than bulk levels [78,91,92]) is widely considered to be the dominant deleterious segregant for Ni-based alloys [63,78,93]. Similar deleterious behavior has been postulated for P, which also strongly segregates to GBs [78], however experimental [94] and theoretical [86] results have suggested that P is either inert or even beneficial in Ni-based alloys [79]. Using either quantum mechanical cluster calculations [86,95] or a local spin density atomic cluster model [96], researchers have postulated that the electronegativity of S changes the local chemical bonding structure to decrease the GB cohesive properties [63]. Additionally, the embrittling effect of sulfur has been found to be synergistic with that of H [67,87,93,97], which suggests that heat-to-heat variations in sulfur segregation/gettering may impact HEAC susceptibility. There is a modest correlation between increased bulk S content (Table 5) and HEAC susceptibility at -850 mV_{SCE} (Figure 17), though it is complicated by the HEAC-resistant NRL HS material having 5 times the S content (17 wppm) of the susceptible TR1 material (3.1 wppm). However, the rigor of correlating bulk S content to the GB cracking susceptibility is compromised by: (1) the presence of getter elements that will strongly influence the concentration of S available for segregation, (2) the grain boundary surface area available for segregation, and (3) the presence of trace elements that are known to increase the cohesive strength of the GB interface. Such complications motivate the use of Auger electron spectroscopy, which enables the direct assessment of the GB chemistry when utilized on freshly exposed intergranular facets. Critically, by directly sampling the GB chemistry, the extraneous influences of gettering elements and grain size are inherently accounted for. A second advantage of the AES approach is that hydrogen is utilized to induce brittle fracture, which results in H-susceptible GBs being exposed for analysis. As such, measured impurity contents will be representative of the chemistry participating in HEAC. However, AES is not without complications. First, it is well known that GB character can strongly influence GB chemistry due to variations in free volume [98]. As such, it is critical that multiple GB facets be sampled in order to effectively capture the average GB chemistry. Second, contaminant elements from the atmosphere (principally C and O) can obfuscate AES due to the buildup on the specimen surface. As such, significant efforts must be made to reduce surface contamination, whether that be through the use of *in-vacuo* fracture stages or keeping the specimen under cryogenic conditions to minimize buildup.

The average maximum sulfur concentration of ~5 GB facets (3 for TR2) from the NRL HS, Allvac, TR1, and TR2 material heats measured using AES is shown in Figure 24. Three observations are apparent from these data. First, the average GB sulfur concentrations in the four tested material heats are ~300-1000 times greater than the measured bulk sulfur contents listed in Table 5, confirming that substantial increases in the impurity concentration relative to the bulk content are possible at GBs. Second, despite conducting measurements across multiple GB facets, the standard deviation (represented by the error bars in Figure 24) is ~33-50% of the measured average in all cases, with the exception of TR2. While this large spread in the

data is likely attributable to the inherent GB-to-GB variation in impurity concentration, it further underscores the importance of statistics when characterizing GB chemistry. Lastly, substantial overlap in measured GB sulfur concentration exists amongst the four tested material heats. Moreover, the HEAC-resistant NRL HS heat was found to have the highest average GB sulfur concentration, while the HEAC-susceptible TR2 (albeit less susceptible than TR1 per measured K_{TH} ; Figure 17) had the lowest average GB sulfur concentration. ***Given this similarity in GB sulfur content, as well as the poor correlation with measured HEAC susceptibility, it is unlikely that GB sulfur concentration governs HEAC susceptibility in Monel K-500.***

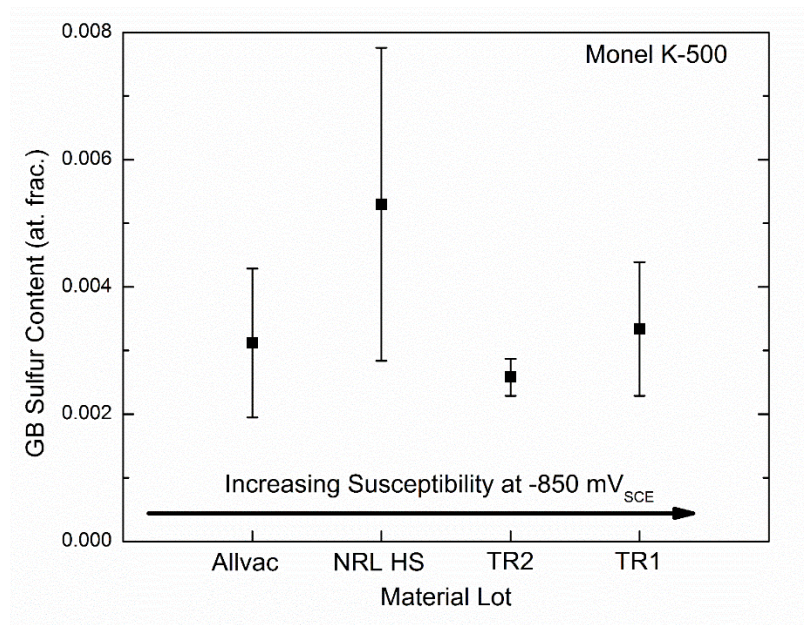


Figure 24 - Average maximum grain boundary sulfur concentration (in atomic fraction) for four different heats of Monel K-500. Error bars represent the standard deviation from 5-6 facets (3 for TR2).

GB segregants can also have the beneficial effect of raising HEAC resistance. In particular, B has been experimentally [99] and theoretically [63,82,86,96,100] shown to increase the cohesive strength of the GB. It has also been postulated that Zr will have a beneficial intrinsic effect on GB cohesion [101], however such a beneficial effect (above the gettering efficiency of Zr) is not widely accepted [78,79]. Attempts to assess the GB B concentrations using AES on intergranular facets did not detect B above background levels. As such, the bulk B data is utilized to estimate of the impact of B on HEAC. The materials that have the highest bulk B levels (Allvac; 3.8 wppm, NRL HS; 2.0 wppm) in Table 5 correlate with higher observed HEAC resistance (Figure 17). However, no correlation is found with observed HEAC resistance when the bulk B concentration is normalized by S_v , as the susceptible TR2 and TR3 lots have a higher value than that observed for NRL HS. The unknown potency and the relative concentration of B that

segregates to the GB (rather than forming borides [99]) precludes conclusive and quantitative understanding of the extent to which such small changes (0.5-1.5 wppm) in bulk B content will impact the HEAC resistance.

In summary, the current results indicate that impurity concentration (either in the bulk or at the grain boundary) does not explain the observed variations in HEAC susceptibility between the tested material heats. However, based on a robust literature database describing the effect of grain boundary impurities in Ni-base alloys on mechanical properties [78,84,91,102], particularly S, it is reasonable to suggest that grain boundary impurities will contribute to HEAC susceptibility, but not differentiate different heats. For example, this influence may not be sufficient to induce variations in performance alone, but when coupled with other factors, such as the propensity for slip planarity, the effect may become acute.

3.5.2.2. Grain size and grain boundary character

Literature results regarding the effect of grain size on HEAC behavior are inconsistent; increasing grain size has been reported to decrease susceptibility [103,104], while others report HEAC behavior is independent of size variation [105]. Regarding the current study, Table 7 demonstrates that material heats with larger grain sizes (TR heats) are consistently more susceptible to HEAC than those with smaller grains (NRL HS and Allvac). However, the isolation of the intrinsic effect of grain size is complicated by its influence on other metallurgical properties. For example, yield strength, H-trapping behavior (through a modification of the trap number density) [77,113], GB impurity segregation [106], and crack path-induced variations in driving force (through crack deflection) [114] may all be influenced by variations in grain size. Considering the last effect, stress intensity reductions due to increasing crack deflection away from the Mode I path with increasing grain size have been shown to increase fatigue cracking thresholds and decrease crack growth rates in the slow cracking region (less than 10^{-6} mm/cycle) [107–109]. Based on this observation, the following 2-dimensional relationship was proposed to describe the effective stress intensity of a deflected crack (K_{def}):

$$K_{def} = K \frac{D \cos^2\left(\frac{\theta_D}{2}\right) + S}{D + S} \quad (\text{Eqn 3.5})$$

where D is the distance over which the tilted crack advances, S is the span of the non-deflected Mode I crack, and θ is the angle of deflection [107]. From this equation, it is clear that larger grain sizes would lead to increased D and S values, resulting in a K_{def}/K ratio of less than 1 (*i.e.* a reduction in driving force), indicating that the large grain materials would be less susceptible to HEAC if this factor is governing intergranular HEAC. However, as discussed above, the larger grain materials (TR heats) were more susceptible than the smaller grain heats (Allvac and NRL HS), which strongly suggests that **crack**

deflection-induced differences in stress intensity are not the dominant source of heat-to-heat variation in HEAC susceptibility.

Recent literature suggests that grain boundary character (misorientation, interfacial energy, and structure) may influence IG cracking susceptibility in Ni-base alloys due to the presence of ‘special’ boundaries that are argued to have (1) less favorable segregation energies for hydrogen and (2) higher strength relative to random high angle boundaries. Boundaries which are hypothesized to fall under this less-susceptible category include grain boundaries of low misorientation (15° or less) and coincident site lattice (CSL) boundaries of $1 < \Sigma < 29$ [110,111]. Considering the current results in Table 7, both the number and S_V fraction of low energy (CSL and low angle $< 15^\circ$) GBs are similar for all materials, ranging from 53-62% with no discernable trend regarding HEAC. However, while the fraction of grain boundaries is a useful parameter, intergranular cracking occurs over numerous boundaries, which suggests that characterization of the grain boundary “network” would provide more physically meaningful insights. In particular, it is worthwhile to explore whether or not an uninterrupted pathway of ‘susceptible’ boundaries would be expected to exist across the tested material heats.

There are two common pathways for assessing the ‘connectivity’ of the grain boundary network: fractal analysis and percolation theory. Considering the former, a fractal analysis of connectivity seeks to evaluate the availability of a susceptible crack path by quantifying the fractal dimension (D_R) of the maximum connectivity network (MCN) using a box-counting method [111]. To complete this analysis, the boundary misorientation angles are characterized via OIM analysis in each material (Figure 20); these data are then used to trace the maximum connectivity network (MCN) of random, susceptible, high angle boundaries, as illustrated for the Allvac material in Figure 25. Figure 25a presents the OIM map (with averaged grain orientations) and the respective inverse pole figure. From these data, traces of the random (black; misorientation angle $> 15^\circ$) and CSL (various colors) are then identified (Figure 25b). The high angle boundaries ($> 15^\circ$) are then extracted (Figure 25c) and a computer program is used to identify the MCN (red lines in Figure 25d) for each material lot. For this MCN analysis, two data points were considered connected if they were adjacent or < 2 pixels apart (thus $< 1 \mu\text{m}$), so that short non-indexed paths along the grain boundary do not affect the connectivity analysis. This $1 \mu\text{m}$ threshold is employed to overcome possible errors induced by step size artifacts (e.g. ‘kinks’ in the boundary) or small, likely-anomalous segments of CSL boundaries located within a high-angle boundary segment. The MCN is then overlaid with a square grid, each box of side length η ($= 12.5, 25, \text{ or } 50 \mu\text{m}$). For each box size (η), the number of boxes containing part of the MCN ($N(\eta)$) is determined and D_R is then evaluated as follows [111]:

$$D_R = - \frac{\log [N(\eta)]}{\log [\eta]} \quad (\text{Eqn 3.6})$$

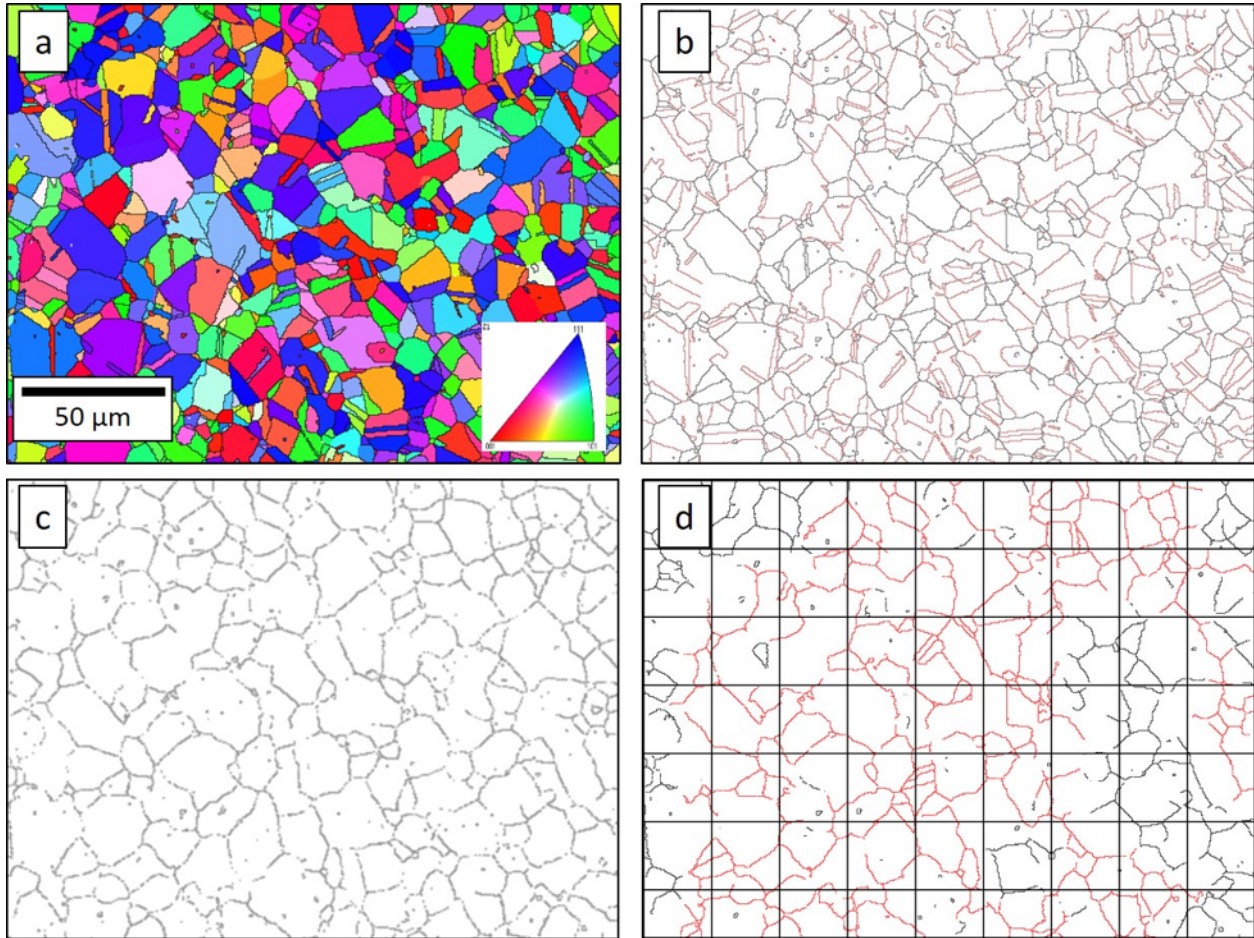


Figure 25 – The process for establishing the fractal dimension included: (a) obtaining an orientation map via electron backscatter diffraction, (b) identification of high (black lines) angle grain boundaries and low (red lines) angle grain boundaries, (c) isolating high angle grain boundaries by removing all low angle grain boundaries, (d) measuring the maximum connected network (highlighted red lines) and overlaying a square grid with a known side length.

As discussed by Kobayashi [111], values of D_R greater than 1.15 have a sufficient connectivity of high-angle boundaries to undergo IG failure (based on their linking of this D_R value to a percolation threshold), which can be physically interpreted as the fraction of non-susceptible boundaries not being sufficiently elevated as to disrupt a crack growing along high angle boundaries. Considering the current material heats, the D_R was found to be 1.59 (Allvac), 1.49 (NRL HS), 1.53 (TR1), 1.38 (TR2), and 1.35 (TR3). Clearly, all tested material heats are above the threshold D_R for intergranular cracking, suggesting that any variations in non-susceptible boundary fraction are insufficient to affect HEAC susceptibility due to the presence of a contiguous path of susceptible boundaries. This high degree of susceptible boundary

connectivity is also consistent with the expectations from percolation theory. Specifically, as documented by Frary and Schuh [112], a minimum non-susceptible boundary fraction of ~ 0.65 (for a 2-D analysis as presented herein) is required to ensure disruption of the susceptible path; none of the tested material heats surpass this criterion. Finally, it has been argued that intragranular $\Sigma 3$ boundaries should not be included in connectivity analyses as they are physically unable to disrupt the high angle boundary pathway [113]. While these values were included in this current study, their removal would only further strengthen the conclusion since the fraction and S_V of low angle/CSL boundaries would be further decreased (and therefore lower than the threshold necessary for susceptible pathway disruption). ***In conclusion, differences in grain boundary character/connectivity are likely not responsible for the observed variation in HEAC behavior.***

3.5.2.3. Hydrogen-metal interactions

There are four specific hydrogen-metal interactions that may vary across the material heats, thereby affecting HEAC susceptibility: hydrogen production, uptake, diffusion, and trapping. As discussed in Section 3.4.3., minimal differences in hydrogen production, diffusion, and trapping were observed amongst the tested material heats (NRL HS, Allvac, and TR2) [60]. Considering hydrogen uptake, previous work found different diffusible hydrogen concentrations as a function of applied potential in two Monel K-500 lots, thereby suggesting that the relationship between the diffusible hydrogen concentration and applied potential may vary amongst the material lots [18]. This variation is confirmed by the differences in measured C_{H-Diff} found for three lots (Allvac, NRL-HS, and TR2) at hydrogen overpotentials ranging from -0.85 to $-1.1 V_{SCE}$ (Figure 21). As described in Eqn 3.1, a lower value of C_{H-Diff} will lead to a concomitant reduction of $C_{H-\sigma}$ for a given hydrogen overpotential, which would increase HEAC resistance by reducing the H concentration available to nucleate crack growth, $C_{H\sigma-crit}$. Moreover, the hydrogen coverage at grain boundaries in the fracture process zone for a heat-invariant grain boundary trap binding energy would be reduced by the lower C_{H-Diff} , though it should be noted that grain boundary trap states are difficult to distinguish from the γ' trap state due to similarities in trap binding energy [60]. Additionally, this change in H-material interaction could interact with the previously discussed heat-to-heat differences (e.g. S segregation and/or grain boundary character distribution/connectivity, thereby altering the k_{IG} and $C_{H\sigma-crit}$ in Eqns 3.2 and 3.3) to influence the material-specific HEAC behavior. ***However, strong similarities in $C_{H-Total}$ and C_{H-Diff} at $-850 mV_{SCE}$ exist amongst the tested material heats, suggesting that differences in hydrogen-metal interactions cannot explain the observed HEAC behavior.*** At more aggressive potentials, statistical significant differences in C_{H-Diff} arise amongst the material heats, which may explain the variation in K_{TH} and growth rates at $-950 mV_{SCE}$. However, this assessment is complicated by the Allvac exhibiting the highest da/dt_{II} at $-950 mV_{SCE}$, in addition to the similarity in da/dt_{II} between NRL HS and TR2.

3.5.2.4. Yield strength and strain hardening

Variations in yield strength can have important consequences for HEAC susceptibility due to its influence on the crack tip stress field, where increased yield strength enable the development of higher stresses *via* constraint effects [17]. This constraint arises from the inability of the material volume proximate to the crack tip, where the stresses are beyond the yield strength, to plastically deform due to the surrounding material experiencing stresses below the yield strength. Hence, the surrounding material *constrains* the near-crack tip material volume from deforming, resulting in further increases in stress proximate to the crack tip. Increases in yield strength then affect HEAC by enabling higher hydrostatic stresses in the crack tip region, which facilitates the development of larger local hydrogen concentrations since the hydrogen concentration is exponentially dependent on the hydrostatic stress (Eqn 3.1). While the exact ratio between yield strength and hydrostatic stress varies depending on the applied formulation (*i.e.* Hutchinson-Rice-Rosengren (HRR) [114, 115], strain gradient plasticity [39], etc.), the yield strength represents a reasonable proxy of the local stress field when evaluating possible heat-to-heat differences. Such an approach is consistent with the consistent implementation of a *maximum* yield strength design criteria in hydrogen embrittlement-related standards, such as in NACE MR0175 [1].

Considering the yield strength of the material heats in this work (Table 6), increased yield strength does not correlate with lower K_{TH} at -850 mV_{SCE} . Specifically, both NRL HS and Allvac were found to be non-susceptible to HEAC at -850 mV_{SCE} , despite having the highest and lowest yield strengths of the tested heats, respectively. One possible explanation for this lack of trend could be differences in strain hardening (quantified by n in Table 6), which is known to strongly influence the local stress fields within the crack tip plastic zone. While the n values are quite similar, suggesting that such an influence is unlikely to govern the observed behavior, it is worthwhile to explore this possibility since it can be readily estimated using the well-known HRR solutions for the plastic crack tip stress field [115], for which the governing equation is:

$$\frac{\sigma_{ij}}{\sigma_0} = \left(\frac{EJ}{\alpha\sigma_0^2 I_n r} \right)^{\frac{1}{n+1}} \tilde{\sigma}_{ij}(n, \theta) \quad (\text{Eqn 3.7})$$

where σ_0 is a reference stress (often taken as the yield strength [116]), I_n is a dimensionless constant and $\tilde{\sigma}_{ij}(n, \theta)$ are dimensionless angular distributions that both depend on the strain hardening exponent (n), E is the elastic modulus, J is a description of the crack tip driving force that is equal to K^2/E' if small-scale yielding is assumed where $E' = E$ for plane stress and $E/(1-\nu^2)$ for plane strain, and r is the distance from the crack tip. Empirical functions for $\tilde{\sigma}_{ij}(n, \theta)$ are available in the literature [116], while I_n can be fit using

tabulated data [115]. For this analysis, a plane strain stress state is assumed and the following dependences on n will be utilized for $\theta = 0$:

$$I_n = 3.952 * \left(1 + \frac{1.588}{n} - \frac{1.218}{n^2} \right) \quad (\text{Eqn 3.8})$$

$$\tilde{\sigma}_H = 2.5 - e^{-0.1n} \quad (\text{Eqn 3.9})$$

where $\tilde{\sigma}_H$ represents the non-dimensional angular function for the maximum hydrostatic stress. Note that the functional form of I_n is fit over a strain hardening interval of $15 \geq n \geq 3$, but can be reasonably extended to $n = 20$ due to the asymptotic nature of the I_n versus n relationship [116].

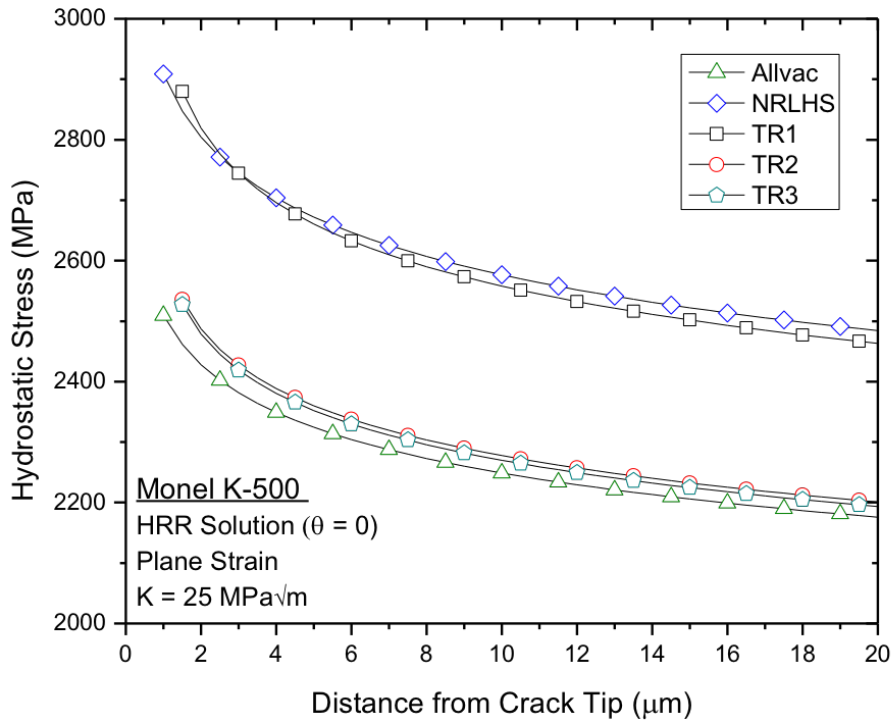


Figure 26 – Variation in hydrostatic stress with distance from the crack tip for the tested Monel K-500 heats calculated using the HRR solutions assuming plane strain conditions.

Using Eqns 3.7 and 3.8, as well as the material properties documented in Table 6, the calculated σ_H with distance from the crack tip amongst the tested material heats is shown in Figure 26. A modest $K = 25 \text{ MPa}\sqrt{\text{m}}$ is employed in these calculations; this K is relevant based on the threshold stress intensities observed at $-850 \text{ mV}_{\text{SCE}}$. Two observations can be gleaned from these data. First, the aforementioned strong dependence of the crack tip stress field on the yield strength is readily apparent as NRL HS and TR1, which have yield strengths of 910 and 898 MPa, exhibit consistently higher hydrostatic stress values (by an order

400 MPa) than Allvac, TR2, and TR 3 (yield strengths between 786 and 795 MPa) for all considered distances from the crack tip. Second, the stress data for a distance of interest are bounded by Allvac and NRL HS, which were both found to be non-susceptible at $-850 \text{ mV}_{\text{SCE}}$, **indicating that HEAC susceptibility does not solely scale with the enhanced stress values proximate to the crack tip**. It should be noted that other theories for the crack tip stress field have been proposed, *e.g.* strain gradient plasticity [117]; evaluation of the stress field using these higher-order theories may modify the ordering found by the HRR solution utilized herein, but such an analysis is outside the scope of the current study.

3.5.3. Modeling K_{TH} for heat-to-heat variations in yield strength and composition

The results of the sensitivity analysis shown in Figure 22a-c demonstrate that significant variations in K_{TH} can arise from realistic heat-to-heat changes in yield strength, grain boundary toughness, and hydrogen uptake behavior. Moreover, the discussion presented herein demonstrates that a single microstructural feature (at least amongst those examined) does not correlate with HEAC susceptibility, suggesting that the microstructural influence on HEAC is a combinatory and/or synergistic effect. While the detailed examination of this coupled effect is precluded by the lack of systematic microstructural controls in the current study, the previously presented decohesion-based models offer an analytical tool to assess this possible influence. In the following section, the K_{TH} model (Eqn. 3.2) is leveraged to predict the HEAC behavior of the five material lots using the previously developed modeling parameters [18], along with material heat specific inputs. A modification to the K_{TH} model that incorporates the effects of impurity segregation to GBs is then implemented and compared to experimental results.

Predicted K_{TH} versus E_{app} results for Allvac, TR1, TR2, TR3, and NRL HS are shown in Figure 27 using previously validated parameters for the Allvac material ($\alpha'' = 0.0002 \text{ MPa}\sqrt{\text{m}}$, $\beta' = 0.20 \text{ (MPa}\sqrt{\text{m}})^{-1}$, $k_{\text{IG}} = 0.88 \text{ MPa}\sqrt{\text{m}}$, and $\alpha = 4.078 \text{ MPa}\sqrt{\text{m}}/(\text{atm frac H})$ [18,53]) and each material's respective yield strength (Table 6). As expected, the variation in yield strength amongst the material lots (and its effect on the local hydrostatic stress) gives rise to drastic differences in calculated threshold values as the applied potential is increased. However, as shown by the experimental results plotted alongside the predicted curves, the previously validated modeling parameters are not able to fully capture the effect of microstructure changes on HEAC susceptibility. In particular, the NRL HS is predicted to be the most susceptible of the five lots (blue dashed line), but was found to be immune to HEAC when experimentally tested at $-850 \text{ mV}_{\text{SCE}}$, as shown by the black arrow extending upward. This deviation from experimental results may be rooted in the influence of sulfur and boron on the grain boundary toughness, k_{IG} ; especially with regards to NRL HS, which has the highest bulk sulfur content. To further explore the effect of impurity segregation, we make two assumptions: (1) any effect of impurity elements on k_{IG} occurs prior to H exposure and (2) sulfur and boron are the only two elements influencing the GB toughness. This leads to

the following modification of Eqn. 2, which is similar in form to the modification invoked by Gerberich and coworkers [32]:

$$K_{TH} = \frac{1}{\beta'} \exp \left[\frac{((k_{IG} - \beta C_S + \gamma C_B) - \alpha C_{HG})^2}{\alpha'' \sigma_{YS}} \right] \quad (\text{Eqn 3.10})$$

Where β (MPa $\sqrt{m}/(\text{atm frac S})$) and γ (MPa $\sqrt{m}/(\text{atm frac B})$) are the weighting factors that define how effectively sulfur and boron alter k_{IG} , C_S and C_B are the concentrations of sulfur and boron at the grain boundary, and all other variables are defined as in Eqn 2. Given that AES data is not available for all tested material heats, the average concentration of boron and sulfur at an arbitrary grain boundary were estimated by leveraging the systematic AES analysis of Ladna and Birnbaum to generate factors for amplifying the bulk concentration [99]. These amplification factors (48,000x and ~1,270x for S and B, respectively) were then linearly scaled to reflect differences in grain size between the original and current study, resulting in final amplifications of approximately 180x and 3x in NRL HS (for S and B, respectively). Notably, this 180x enhancement (~0.0031 atomic fraction S) is within the error bars reported for NRL HS in Figure 24, suggesting that the employed estimation protocol is accurate to the first-order. Based on this approach, C_S and C_B were calculated for each material lot, along with the previously calculated C_{HG} , and then α , β , and γ were fit to minimize the square of the difference between the calculated K_{TH} and the experimentally measured K_{TH} for each heat at -950 mV $_{SCE}$, where heat-to-heat variations in metallurgy should have minimal effect. From this analysis, $\alpha = 4.167$ (MPa $\sqrt{m}/(\text{atm frac H})$), $\beta = 2.753$ (MPa $\sqrt{m}/(\text{atm frac S})$), and $\gamma = 4.12 \times 10^{-4}$ (MPa $\sqrt{m}/(\text{atm frac B})$), which suggests that boron has minimal effect on grain boundary toughness.

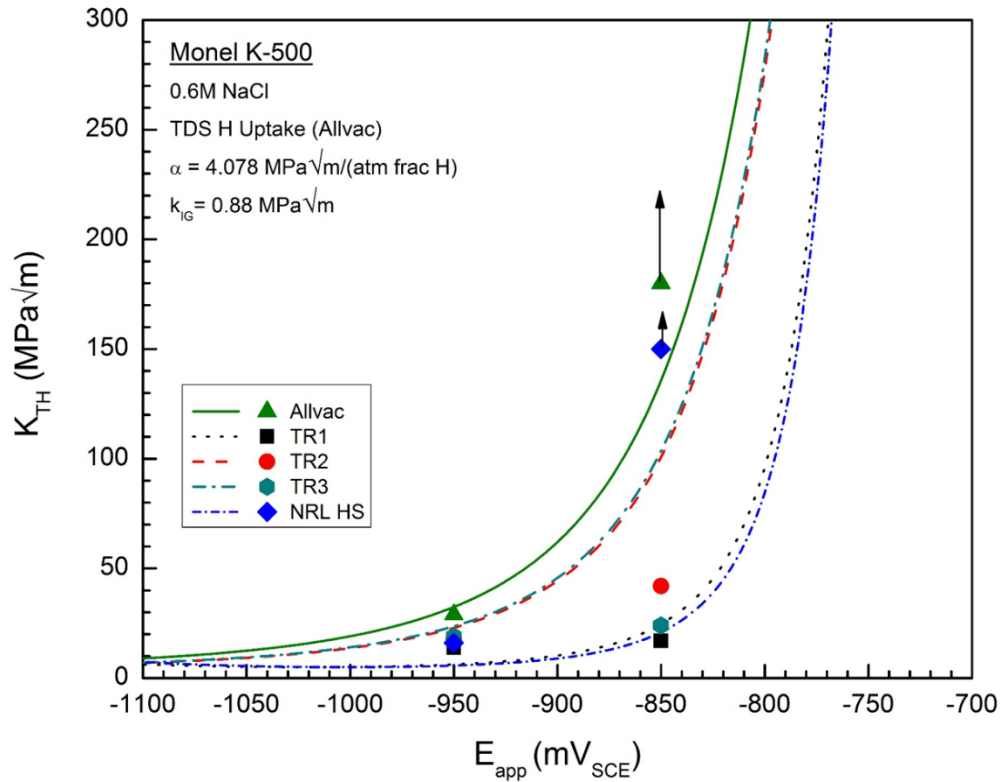


Figure 27 – Plot of the calculated threshold stress intensity versus applied potential curves for each heat of Monel K-500 using previously validated parameters with experimental data points included for -950 and -850 mV_{SCE}. Black arrows extending upward represent experimental observations of HEAC immunity at the tested potential.

Calculated K_{TH} versus E_{app} using the newly fit parameters are shown in Figure 28 for Allvac, TR1, TR2, TR3, and NRL HS, along with experimental results for -950 and -850 mV_{SCE}. Despite a noticeable shift in the predictions compared to Figure 27, especially at less cathodic potentials, a significant difference in theoretical and experimental results still exists. This inability to accurately replicate the experimental data underscores the challenge of predicting the influence of subtle, and likely synergistic, microstructural influences. Such difficulties are magnified by known limitations in the decohesion-based models. For example, Eqn 3.2 was derived such that hydrogen effects on plasticity were ignored [118]; these effects may alter the modeling coefficients (α' and β') predicted from the dislocation shielding calculations. Second, a variation in modeling parameter dependencies, especially regarding the dependence on yield strength, has been found for different materials. Specifically, a less severe dependence of K_{TH} on yield strength was found for Mo ($\exp(\sigma^{-1/2})$) as compared to the original Fe-3%Si solution ($\exp(\sigma^{-1})$) [75]. The yield strength dependence has not been explored for Ni-based alloys and merits further investigation if the models continue to be leveraged. Lastly, it has been proposed that the plastic work of fracture is more sensitive to hydrogen than the elastic work of fracture [119], raising the question as to whether or not both parameters should be included in the threshold model. However, if such factors must be included to

accurately capture behavior, then the development of a new modeling paradigm, such as one derived from the stress-based approach proposed by Oriani [120], may prove more tractable.

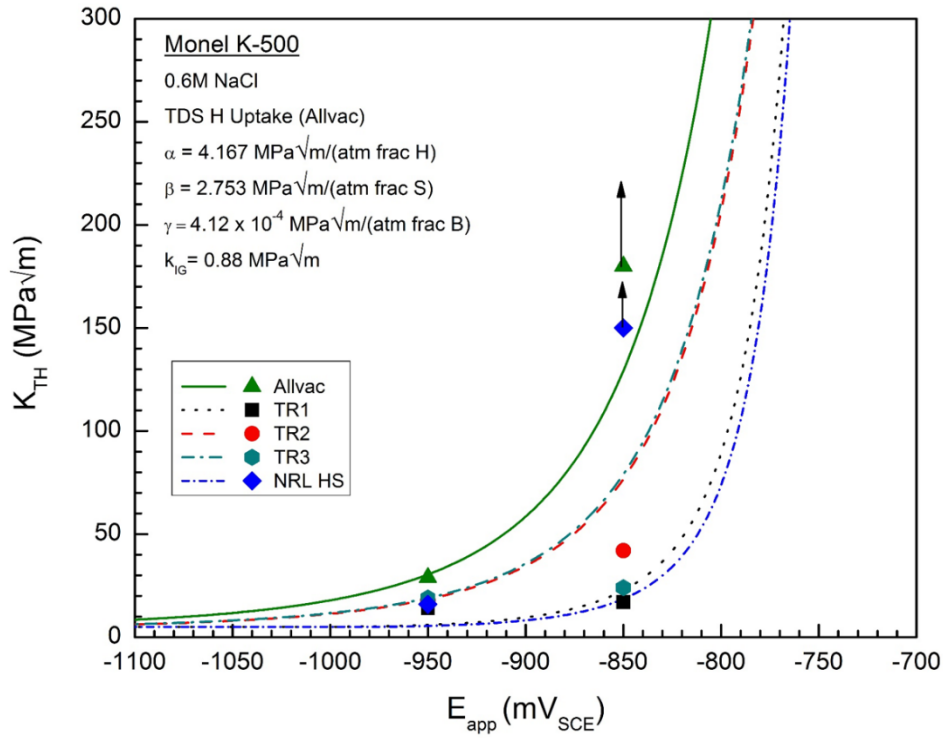


Figure 28 – Plot of the calculated threshold stress intensity versus applied potential curves for each heat of Monel K-500 using new parameters with experimental data points included for -950 and -850 mV_{SCE}. New parameters include the effects of grain boundary impurity segregation of sulfur (β) and boron (γ). Black arrows extending upward represent experimental observations of HEAC immunity at the tested potential.

3.6. Conclusions

The influence of microstructure variation on hydrogen environment-assisted cracking of Monel K-500 are evaluated using five nominally peak-aged lots of material (all of which satisfy the QQ-N-286 specification) tested under slow-rising stress intensity loading while immersed in NaCl solution under cathodic polarizations. Quantitative HEAC parameters were established using fracture mechanics testing and were coupled with a detailed characterization of the microstructure (e.g. composition, grain character analysis, and H-metal interaction parameters.) The results of these analyses are coupled with micromechanical models to quantitatively evaluate how observed changes in the microstructure relate to the resulting HEAC behavior. The following conclusions are established.

1. Limited heat-to-heat variation in HEAC susceptibility was observed in five peak-aged Monel K-500 lots when immersed in 0.6M NaCl under an applied potential of -950 mV_{SCE} during slow-rising K testing, suggesting minimal influence of metallurgical variation in severe H-producing environments.

2. Extensive heat-to-heat variation in both HEAC metrics (K_{TH} and da/dt_{II}) and fractography was observed amongst the material lots when immersed in 0.6 M NaCl under an applied potential of -850 mV_{SCE} during slow-rising K testing.
3. The influence of metallurgical features, including grain size, impurity segregation, grain boundary character and connectivity, hydrogen-metal interactions, crack path deflection due to grain size, yield strength, and strain hardening was evaluated. No specific trend between these individual metallurgical parameters and HEAC susceptibility metrics was identified, suggesting a combinatory and/or synergistic influence of multiple metallurgical features.
4. Sensitivity analysis of the decohesion-based, micromechanical models suggests that physically realistic variations in hydrogen uptake behavior, yield strength, and intrinsic grain boundary toughness give rise to large changes in HEAC susceptibility.
5. Predicted values of K_{TH} did not align with experimental results when previously validated modeling parameters were employed, suggesting that the current models need to be extended, or more new modeling approaches developed, to more accurately capture the effect of heat-to-heat variations in microstructure.
6. A modification to K_{TH} model was proposed to incorporate the effect of impurity segregants, resulting in new modeling parameters, but was unable to accurately predict experimental results, underscoring the need for additional model development.

3.7. Suggested Future Research Directions

There are four research pathways based on the work presented in the preceding chapter that merit further exploration. First, a detailed comparison of the bulk slip morphology (i.e. wavy versus planar slip) is needed to determine whether this parameter scales with HEAC susceptibility. A large literature database establishes that planar slip alloys are more susceptible to embrittlement than wavy slip alloys, but it is unclear whether this trend holds for the tested material heats. Based on the observed variations in yield strength, it is likely that differences in precipitate morphology exist amongst the material heats, but whether or not this difference is sufficient to affect the slip morphology is unknown. Efforts are currently on-going in this area. Second, additional testing at potentials of -800 mV_{SCE} and -900 mV_{SCE} would provide data that may improve the fitting of modeling parameters. At a minimum, this additional data would enable the calculation of an individual α parameter for each material heat. Third, given the measured variations in HEAC, it would be interesting to evaluate the mechanical properties after precharging with gaseous hydrogen. In particular, examination of the deformation structure after straining to incrementally higher stresses, with and without hydrogen, may provide insights into the processes governing HEAC. Lastly, the development of physically-based models for predicting/managing hydrogen embrittlement remains a

critical goal of the hydrogen community. While the decohesion-based models are attractive due to their (1) closed-form and (2) physical basis, the extension of these models to other alloy systems is complicated by a lack of representative modeling parameters and an inability to capture the important effects of subtle microstructural variations. This leads to two possible pathways for future research: (1) extension of the current modeling paradigms or (2) development of new models. Regarding the former, neglecting any effect of hydrogen on plasticity processes remains a criticism of the decohesion [118] – initial efforts for improvement should start with this addition. For the latter, the physical basis of a local stress-based model for hydrogen cracking is sound [120], but correctly accounting for the pertinent localized stresses in a model that can be used for engineering purposes is non-trivial. However, one potential pathway that should be explored is the incorporation of hydrogen effects into crystal plasticity models – such an approach would enable the assessment of stresses at a scale relevant to engineering, with a clear pathway for integration into structural integrity tools.

3.8. Acknowledgements/Statement of Contribution

The assistance of Mr. Denny Paul and Dr. John Hammond at Physical Electronics, USA with conducting the Auger electron spectroscopy experiments is gratefully acknowledged. Fracture mechanics experiments were conducted by Mr. Justin Dolph and Ms. Christina Kaminsky. OIM and connectivity analysis were completed by Dr. Greger Pioszak and Mr. Justin Dolph. Prof. Brendy Rincon Troconis performed the hydrogen-metal interaction experiments/analysis and assisted with writing of the published manuscript (see Appendix II). Ms. Allison Popernack conducted the experiment from which the voltage-load data was obtained. Given the extensive efforts of others on this task, the contributions of the author should be specified. The author was responsible for analysis and interpretation of fracture mechanics experiments, conducted scanning electron microscopy of fracture surfaces, interpreted characterization data in the context of HEAC susceptibility, identified and evaluated the influence of mechanical properties on the dcPD voltage, conducted the AES experiments, and wrote the manuscript in which these results were published.

3.9. References

- [1] NACE, Sulfide Stress Cracking Resistant Metallic Material for Oil Field Equipment, (1998).
- [2] ASTM Standard G30, 1997 (2009), Stand. Pract. Mak. Using U-Bend Stress. Test Specimens. (n.d.). doi:10.1520/g0030-97r09.
- [3] ASTM Standard G39, 1999 (2011), Stand. Pract. Prep. Use Bent-Beam Stress. Test Specimens. (n.d.). doi:10.1520/g0039-99r11.
- [4] ASTM Standard G129, 2000 (2013), Stand. Pract. Slow Strain Rate Test. to Eval. Susceptibility Met. Mater. to Environ. Assist. Crack. (n.d.). doi:10.1520/g0129-00r13.

- [5] ASTM International, Standard Test Method for Determining Threshold Stress Intensity Factor for Environment-Assisted Cracking of Metallic Materials, (2003) 1–13. doi:10.1520/E1681-03R14.2.
- [6] ASTM Standard F1624, 2012, Stand. Test Method Meas. Hydrog. Embrittlement Threshold Steel by Increm. Step Load. Tech. (n.d.). doi:10.1520/f1624-12.
- [7] R.E. Butler, Hydrogen embrittlement of high-strength alloys in marine environments, in: Eng. with Copper-Nickel Alloy., Metals Society, London, U.K., 1988: pp. 79–84.
- [8] C.A. Clark, S. Driscoll, P. Guha, Development of a New Fastener Alloy Resistant to Hydrogen Embrittlement, *Br. Corros. J.* 27 (1992) 157–160.
- [9] G.A. Scott, Studbolting Experience in the Underwater Environment of the North Sea, Occidental Petroleum Ltd. , 1985.
- [10] R.N. Tuttle, J.W. Kochera, Control of Hydrogen Embrittlement in Deep Gas Wells, in: A.W. Thompson, I.M. Bernstein (Eds.), *Eff. Hydrog. Behav. Mater.*, Metallurgical Society of AIME, Moran, WY, 1976: pp. 531–541.
- [11] L.H. Wolfe, M.W. Joosten, Failures of Nickel/Copper Bolts in Subsea Applications, *SPE Prod. Eng.* 3 (1988) 382–386. doi:10.2118/16632-PA.
- [12] J.R. Scully, M.G. Vassilaros, The Hydrogen Embrittlement Susceptibility of Monel Alloy K-500, *Electrochem. Soc. Fall 1983 Meet.* (1983).
- [13] R.D. Bayles, T. Lemieux, F. Martin, D. Lysogorski, T. Newbauer, W. Hyland, et al., Monel K-500 Hydrogen Embrittlement, in: *Nav. Surf. Treatment Cent. MR2010 Proc. Present.*, 2010. <http://nstcenter.com/docs/PDFs/MR2010/Thurs-1-Presentations/10-Bayles.PDF>.
- [14] L.H. Wolfe, C.C. Burnette, M.W. Joosten, Hydrogen Embrittlement of Cathodically Protected Subsea Bolting Alloys, *Mater. Perform.* 32 (1993) 14–21.
- [15] J.A. Lillard, Environment Assisted Cracking of a Nickel-Based Superalloy in Hydrogen-Producing Solutions, University of Virginia, 1998.
- [16] W.K. Boyd, W.E. Berry, Stress Corrosion Cracking Behavior of Nickel and Nickel Alloys, in: *Stress Corros. Crack. Met. - A State Art*, ASTM STP 518, American Society for Testing and Materials, 1972: pp. 58–78.
- [17] R.P. Gangloff, Hydrogen Assisted Cracking of High Strength Alloys, in: I. Milne, R.O. Ritchie, B. Karihaloo (Eds.), *Compr. Struct. Integr.*, Elsevier Science, New York, NY, 2003: pp. 31–101.
- [18] R.P. Gangloff, H.M. Ha, J.T. Burns, J.R. Scully, Measurement and Modeling of Hydrogen Environment-Assisted Cracking in Monel K-500, *Metall. Mater. Trans. A.* 45 (2014) 3814–3834. doi:10.1007/s11661-014-2324-z.
- [19] R.P. Gangloff, Critical issues in hydrogen assisted cracking of structural alloys, in: S. Shiilov (Ed.), *Environment Induc. Crack. Met.*, 2006: pp. 6337–6349.
- [20] R.P. Gangloff, Probabilistic Fracture Mechanics Simulation of Stress Corrosion Cracking Using Accelerated Laboratory Testing and Multi-Scale Modeling, *Corrosion.* (2016).
- [21] J.A. Harter, AFGROW Program Version 4.0012.15, <Http://Www.Afgrow.Net/Downloads/Pdownload.aspx>. (2007).

<http://www.afgrow.net/downloads/pdownload.aspx>.

- [22] W.A. Grell, P.J. Laz, Probabilistic fatigue life prediction using AFGROW and accounting for material variability, *Int. J. Fatigue*. 32 (2010) 1042–1049. doi:10.1016/j.ijfatigue.2009.12.001.
- [23] J.A. Harter, Comparison of contemporary FCG life prediction tools, *Int. J. Fatigue*. 21 (1999) 181–185. doi:10.1016/S0142-1123(99)00070-5.
- [24] R.P. Gangloff, D.C. Slavik, R.S. Piascik, R.H. Van Stone, *Direct Current Electrical Potential Measurement of the Growth of Small Cracks*, Philadelphia, 1992.
- [25] J. Ai, H.M. Ha, R.P. Gangloff, J.R. Scully, Hydrogen diffusion and trapping in a precipitation-hardened nickel–copper–aluminum alloy Monel K-500 (UNS N05500), *Acta Mater.* 61 (2013) 3186–3199. doi:10.1016/j.actamat.2013.02.007.
- [26] T. Boniszewski, G. Smith, The influence of hydrogen on the plastic deformation ductility, and fracture of nickel in tension, *Acta Metall.* (1963).
- [27] A.H. Windle, G.C. Smith, The Effect of Hydrogen on the Deformation and Fracture of Polycrystalline Nickel, *Met. Sci. J.* 4 (1970) 136–144. doi:10.1179/msc.1970.4.1.136.
- [28] D.H. Lassila, H.K. Birnbaum, The effect of diffusive hydrogen segregation on fracture of polycrystalline nickel, *Acta Metall.* 34 (1986) 1237–1243. doi:10.1016/0001-6160(86)90010-6.
- [29] D.M. Symons, A comparison of internal hydrogen embrittlement and hydrogen environment embrittlement of X-750, *Eng. Fract. Mech.* 68 (2001) 751–771. doi:[http://dx.doi.org/10.1016/S0013-7944\(00\)00123-5](http://dx.doi.org/10.1016/S0013-7944(00)00123-5).
- [30] S. Bechtle, M. Kumar, B.P. Somerday, M.E. Launey, R.O. Ritchie, Grain-boundary engineering markedly reduces susceptibility to intergranular hydrogen embrittlement in metallic materials, *Acta Mater.* 57 (2009) 4148–4157. doi:10.1016/j.actamat.2009.05.012.
- [31] M.L. Martin, B.P. Somerday, R.O. Ritchie, P. Sofronis, I.M. Robertson, Hydrogen-induced intergranular failure in nickel revisited, *Acta Mater.* 60 (2012) 2739–2745. doi:10.1016/j.actamat.2012.01.040.
- [32] W.W. Gerberich, Modelling hydrogen induced damage mechanisms in metals, in: R.P. Gangloff, B.P. Somerday (Eds.), *Gaseous Hydrog. Embrittlement Mater. Energy Technol.*, Woodhead Publishing, 2012: pp. 209–246.
- [33] S.P. Lynch, Mechanisms and Kinetics of Environmentally Assisted Cracking: Current Status, Issues, and Suggestions for Further Work, *Metall. Mater. Trans. A.* 44A (2013) 1209–1229. doi:10.1007/s11661-012-1359-2.
- [34] S.P. Lynch, Hydrogen Embrittlement Phenomena and Mechanisms, *Corros. Rev.* 30 (2012) 105–123.
- [35] Y. Katz, N. Tymiak, W.W. Gerberich, Nanomechanical probes as new approaches to hydrogen/deformation interaction studies, *Eng. Fract. Mech.* 68 (2001) 619–646. doi:10.1016/S0013-7944(00)00119-3.
- [36] Y. Lee, R.P. Gangloff, Measurement and modeling of hydrogen environment-assisted cracking of ultra-high-strength steel, *Metall. Mater. Trans. A Phys. Metall. Mater. Sci.* 38 A (2007) 2174–2190. doi:10.1007/s11661-006-9051-z.

- [37] R.P. Gangloff, Science-Based Prognosis to Manage Structural Alloy Performance in Hydrogen, in: B.P. Somerday, P. Sofronis, R.H. Jones (Eds.), *Eff. Hydrog. Mater.*, ASM International, Materials Park, OH, 2009: pp. 1–21.
- [38] W.W. Gerberich, R.A. Oriani, M. Lii, X. Chen, T. Foecke, The necessity of both plasticity and brittleness in the fracture thresholds of iron, *Philos. Mag. A.* 63 (1991) 363–376.
- [39] U. Komaragiri, S.R. Agnew, R.P. Gangloff, M.R. Begley, The role of macroscopic hardening and individual length-scales on crack tip stress elevation from phenomenological strain gradient plasticity, *J. Mech. Phys. Solids.* 56 (2008) 3527–3540. doi:10.1016/j.jmps.2008.08.007.
- [40] R.P. Gangloff, Diffusion Control of Hydrogen Environment Embrittlement in High Strength Alloys, in: N.R. Moody, A.W. Thompson (Eds.), *Hydrog. Eff. Mater.*, The Minerals, Metals & Materials Society, Warrendale, PA, 2002.
- [41] QQ-N-286G: Nickel-Copper-Aluminum Alloy, Wrought (UNS N05500), (2000).
- [42] J.R. Davis, ed., *Nickel, Cobalt, and Their Alloys: ASM Specialty Handbook*, in: 2000: pp. 167–188.
- [43] G.K. Dey, P. Mukhopadhyay, Precipitation in the Ni-Cu-base alloy Monel K-500, *Mater. Sci. Eng.* 84 (1986) 177–189. doi:10.1016/0025-5416(86)90236-3.
- [44] G.K. Dey, R. Tewari, P. Rao, S.L. Wadekar, P. Mukhopadhyay, Precipitation hardening in nickel-copper base alloy monel K 500, *Metall. Trans. A.* 24 (1993) 2709–2719. doi:10.1007/BF02659495.
- [45] Å. Gustafson, Coarsening of TiC in austenitic stainless steel - Experiments and simulations in comparison, *Mater. Sci. Eng. A.* 287 (2000) 52–58. doi:10.1016/S0921-5093(00)00827-3.
- [46] H. Tada P.C. Paris, and G.R. Irwin, *The Stress Analysis of Cracks Handbook*, Paris Productions Incorporated, St. Louis, MO, 1985.
- [47] H.H. Johnson, Calibrating the Electric Potential Method for Studying Slow Crack Growth, *Mater. Res. Stand.* 5 (1965) 442–445.
- [48] K.-H. Schwalbe, D. Hellmann, Application of the Electrical Potential Method to Crack Length Measurements Using Johnson’s Formula, *J. Test. Eval.* 9 (1981) 218–221.
- [49] ASTM Standard E647-13: Standard Test Method for Measurement of Fatigue Crack Growth Rates, (2013). doi:10.1520/E0647-13E01.2.
- [50] V. Kumar, M.D. German, C.F. Shih, *An Engineering Approach for Elastic-Plastic Fracture Analysis*, Electric Power Research Institute, Palo Alto, CA, 1981.
- [51] Z.D. Harris, Private communication with Denny Paul, (2017).
- [52] T.L. Anderson, *Fracture Mechanics: Fundamentals and Applications*, 3rd ed., Taylor & Francis, 2005.
- [53] J.T. Burns, Z.D. Harris, J.D. Dolph, R.P. Gangloff, Measurement and Modeling of Hydrogen Environment Assisted Cracking in a Ni-Cu-Al-Ti Superalloy, *Metall. Mater. Trans. A.* 47 (2016) 990–997. doi:10.1007/s11661-015-3315-4.

- [54] H.J. Frost, M.F. Ashby, *Deformation-mechanism maps : the plasticity and creep of metals and ceramics*, 1st ed., Pergamon Press, Oxford Oxfordshire ; New York, 1982.
- [55] A.S. Popernack, *Loading Rate Effects on Hydrogen-Enhanced Cracking Behavior of Ni- and Co-Based Superalloys for Marine Applications*, University of Virginia, 2017.
- [56] J.T. Burns, R.P. Gangloff, W.E. Waldman, *Development of Corrosion-Hydrogen Crack Resistant Aircraft Alloys from Mechanistic Understanding*, 2014.
- [57] K.A. Nibur, B.P. Somerday, C. San Marchi, J.W. Foulk, M. Dadfarnia, P. Sofronis, The relationship between crack-tip strain and subcritical cracking thresholds for steels in high pressure hydrogen gas, *Metall. Mater. Trans. A*. DOI: 10.10 (2013).
- [58] E. Richey, R.P. Gangloff, Strain rate dependent environment assisted cracking of alpha/beta-Ti alloys in chloride solution, in: R.D. Kane (Ed.), *Environ. Assist. Crack. Predictive Methods Risk Assess. Eval. Mater. Equipment, Struct. ASTM STP 1401*, ASTM, West Conshohocken, PA, 2000: pp. 104–127.
- [59] M.L. Martin, I.M. Robertson, P. Sofronis, Interpreting hydrogen-induced fracture surfaces in terms of deformation processes: A new approach, *Acta Mater.* 59 (2011) 3680–3687. doi:10.1016/j.scriptamat.2011.06.016.
- [60] B.C.R. Troconis, Z.D. Harris, H. Ha, J.T. Burns, J.R. Scully, The effect of heat-to-heat variations in metallurgy and hydrogen-metal interactions on the hydrogen embrittlement of Monel K-500, *Mater. Sci. Eng. A*. 703 (2017) 533–550. doi:10.1016/j.msea.2017.07.019.
- [61] J.R. Scully, Environment-Assisted Intergranular Cracking: Factors that Promote Crack Path Connectivity, in: R.D. Kane (Ed.), *Environ. Assist. CrackMng Predict. Methods Risk Assess. Eval. Mater. Equipment, Struct. ASTM STP 1401*, American Society for Testing and Materials, West Conshohocken, PA, 2000: pp. 40–69.
- [62] T. Watanabe, Grain boundary engineering: historical perspective and future prospects, *J. Mater. Sci.* 46 (2011) 4095–4115. doi:DOI 10.1007/s10853-011-5393-z.
- [63] P. Lejcek, Chapter 7: grain boundary segregation and related phenomena, in: P. Lejcek (Ed.), *Grain Bound. Segreg. Met.*, Springer, Berlin, 2010.
- [64] A. E112, No Title, (n.d.).
- [65] E.E. Underwood, *Quantitative stereology*, Addison-Wesley Pub. Co., Reading, Mass., 1970.
- [66] A.J. Wilkinson, G. Meaden, D.J. Dingley, High-Resolution Elastic Strain Measurement from Electron Backscatter Diffraction Patterns: New Levels of Sensitivity, *Ultramicroscopy*. 106 (2006) 307–313. doi:http://dx.doi.org/10.1016/j.ultramicro.2005.10.001.
- [67] C.D. Taylor, M. Neurock, J.R. Scully, A First-Principles Model for Hydrogen Uptake Promoted by Sulfur on Ni(111), *J. Electrochem. Soc.* 158 (2011) F36–F44. doi:10.1149/1.3536470.
- [68] C.L. Briant, H.C. Feng, C.J. McMahon, Embrittlement of a 5 Pct Nickel High Strength Steel by Impurities and Their Effects on Hydrogen-Induced Cracking, *Metall. Trans. A*. 9 (1978) 625–633. doi:10.1007/BF02659919.
- [69] G.M. Pressouyre, Trap theory of hydrogen embrittlement, *Acta Met.* 28 (1980) 895–911.

- [70] A. Turnbull, R.G. Ballinger, I.S. Hwang, M.M. Morra, Hydrogen Transport in Nickel-Base Alloys, *Metall. Mater. Trans. A.* 23 (1992).
- [71] J.P. Hirth, Effects of Hydrogen on the Properties of Iron and Steel, *Metall. Mater. Trans. A.* 11 (1980) 861–890.
- [72] D. Li, R.P. Gangloff, J.R. Scully, Hydrogen trap states in ultrahigh-strength AERMET 100 steel, *Metall. Mater. Trans. A.* 35 (2004) 849–864. doi:10.1007/s11661-004-0011-1.
- [73] J.E. Angelo, N.R. Moody, M.I. Baskes, Trapping of hydrogen to lattice defects in nickel, *Model. Simul. Mater. Sci. Eng.* 3 (1995) 289–307. doi:10.1088/0965-0393/5/6/007.
- [74] B.C. Rincon-Troconis, Z.D. Harris, J.T. Burns, J.R. Scully, No Title, *Corrosion.* (n.d.).
- [75] H. Huang, W.W. Gerberich, Quasi-equilibrium modeling of the toughness transition during semibrittle cleavage, *Acta Metall. Mater.* 42 (1994) 639–647. doi:10.1016/0956-7151(94)90260-7.
- [76] M. Yamaguchi, M. Shiga, H. Kaburaki, Grain Boundary Decohesion by Sulfur Segregation in Ferromagnetic Iron and Nickel —A First-Principles Study, *Mater. Trans.* 47 (2006) 2682–2689. doi:10.2320/matertrans.47.2682.
- [77] W.F. Smith, *Structure and properties of engineering alloys*, 2nd ed., McGraw-Hill, New York, 1993. <http://www.loc.gov/catdir/description/mh022/92006795.html>.
- [78] R.T. Holt, W. Wallace, Impurities and trace elements in nickel-base superalloys, *Int. Met. Rev.* (1976) 1–24.
- [79] B. Geddes, Chapter 5: Compositional Effects, in: B. Geddes, H. Leon, H. Huang (Eds.), *Superalloys Alloy. Perform.*, ASTM International, West Conshohocken, PA, 2010: pp. 59–109.
- [80] J.N. DuPont, J.C. Lippold, S.D. Kiser, *Welding metallurgy and weldability of nickel-base alloys*, John Wiley & Sons, Hoboken, N.J., 2009.
- [81] W.B. Kent, Trace-Element Effects in Vacuum-Melted Superalloys, *J. Vac. Sci. Technol.* 11 (1974) 1038–1046. doi:Doi 10.1116/1.1318677.
- [82] E.S. Huron, K.R. Bain, D.P. Mourer, J.J. Schirra, P.L. Reynolds, E.E. Montero, The influence of grain boundary elements on properties and microstructures of P/M nickel based superalloys, in: K.A. Green, T.M. Pollock, H. Harada, T.E. Howson, R.C. Reed, J.J. Shirra, et al. (Eds.), *Superalloys 2004*, TMS, 2004.
- [83] J.M. Walshe, K.P. Gumz, N.P. Anderson, In situ auger electron spectroscopy tensile fracture study of nickel alloys, in: N.S. McIntyre (Ed.), *Quant. Surf. Anal. Mater. ASTM STP 643*, ASTM, 1978: pp. 72–82.
- [84] W. Swiatnicki, S. Lartigue, M. Biscondi, D. Bouchet, Intergranular sulfur and grain boundary plane in a nickel bicrystal, *J. Phys. Colloq.* 51 (1990) 341–346.
- [85] D. Raabe, M. Herbig, S. Sandlobes, Y. Li, D. Tytko, M. Kuzmina, et al., Grain boundary segregation engineering in metallic alloys: A pathway to the design of interfaces, *Curr. Opin. Solid State Mater. Sci.* 18 (2014) 253–261. doi:DOI 10.1016/j.cossms.2014.06.002.
- [86] R.P. Messmer, C.L. Briant, The Role of Chemical Bonding in Grain-Boundary Embrittlement, *Acta Metall.* 30 (1982) 457–467. doi:Doi 10.1016/0001-6160(82)90226-7.

- [87] A. Kimura, H.K. Birnbaum, Hydrogen Induced Grain-Boundary Fracture in High-Purity Nickel and Its Alloys - Enhanced Hydrogen Diffusion Along Grain-Boundaries, *Acta Metall.* 36 (1988) 757–766. doi:Doi 10.1016/0001-6160(88)90109-5.
- [88] M.E. Natishan, M. Wagenhofer, Conditions causing intergranular cracking in high strength nickel-copper alloys, in: T.L. Panontin, S.D. Sheppard (Eds.), *Fatigue Fract. Mech. Twenty-Ninth Vol.* ASTM STP 1332, ASTM, West Conshohocken, PA, 1999: pp. 384–392.
- [89] M.E. Natishan, W.C. Porr, The effect of grain boundary carbon on the hydrogen-assisted intergranular failure of nickel-copper alloy K-500 fastener material, in: P.M. Toor (Ed.), *Struct. Integr. Fasten.* ASTM STP 1236, ASTM, Philadelphia, PA, 1995: pp. 81–92.
- [90] T.S.F. Lee, R.M. Latanision, Effects of Grain-Boundary Segregation and Precipitation on the Hydrogen Susceptibility of Nickel, *Metall. Trans. A.* 18 (1987) 1653–1662. doi:Doi 10.1007/Bf02646149.
- [91] W.C. Johnson, J.E. Doherty, B.H. Kear, A.F. Giamei, Confirmation of sulfur embrittlement in nickel alloys, *Scr. Metall.* 8 (1974) 971–974. doi:http://dx.doi.org/10.1016/0036-9748(74)90394-9.
- [92] T. Miyahara, K. Stolt, D.A. Reed, H.K. Birnbaum, Sulfur Segregation on Nickel, *Scr. Metall.* 19 (1985) 117–121. doi:Doi 10.1016/0036-9748(85)90276-5.
- [93] R.H. Jones, A review of combined impurity segregation-hydrogen embrittlement processes, in: R.M. Latanision, T.E. Fischer (Eds.), *Adv. Mech. Phys. Surfaces*, Hardwood Academic Publishers, Chur, Switzerland, 1986: pp. 1–70.
- [94] X. Xie, X.F. Liu, J. Dong, Y. Hu, Z. Xu, Segregation behavior of phosphorus and its effect on microstructure and mechanical properties in alloy system Ni-Cr-Fe-Mo-Nb-Ti-Al, in: E.A. Loria (Ed.), *Superalloys 718, 625, 706 Var. Deriv.*, TMS, 1997: pp. 531–542.
- [95] C.L. Briant, R.P. Messmer, The Effect of Impurity Elements on Chemical Bonding at Grain-Boundaries, *J. Phys.* 43 (1982) 255–269. doi:DOI 10.1051/jphyscol:1982623.
- [96] G.S. Painter, F.W. Averill, Effects of Segregation on Grain-Boundary Cohesion - a Density-Functional Cluster Model of Boron and Sulfur in Nickel, *Phys. Rev. Lett.* 58 (1987) 234–237. doi:DOI 10.1103/PhysRevLett.58.234.
- [97] D.H. Lassila, H.K. Birnbaum, Intergranular fracture of nickel: the effect of hydrogen-sulfur co-segregation, *Acta Metall.* 35 (1987) 1815–1822. doi:10.1016/0001-6160(87)90127-1.
- [98] P. Lejček, M. Šob, V. Paidar, Interfacial segregation and grain boundary embrittlement: An overview and critical assessment of experimental data and calculated results, *Prog. Mater. Sci.* 87 (2017) 83–139. doi:10.1016/j.pmatsci.2016.11.001.
- [99] B. Ladna, H.K. Birnbaum, Surface and Grain-Boundary Segregation of Sulfur and Boron in Nickel, *Acta Metall.* 36 (1988) 745–755. doi:Doi 10.1016/0001-6160(88)90108-3.
- [100] H.H. Kart, T. Cagin, The effects of boron impurity atoms on nickel E5 (012) grain boundary by first principles calculations, *J. Achievements Mater. Manuf. Eng.* 30 (2008) 177–181.
- [101] H.E. Huang, C.H. Koo, Effect of zirconium on microstructure and mechanical properties of cast fine-grain CM 247 LC superalloy, *Mater. Trans.* 45 (2004) 554–561. doi:DOI 10.2320/matertrans.45.554.

- [102] M. Yamaguchi, M. Shiga, H. Kaburaki, Grain Boundary Decohesion by Impurity Segregation in a Nickel-Sulfur System, *Science* (80-.). 307 (2005) 393–398.
- [103] N.R. Moody, R.E. Stoltz, M.W. Perra, The relationship of grain size to critical distance and hydrogen-induced crack growth thresholds, *Scr. Metall.* 20 (1986) 119–123. doi:http://dx.doi.org/10.1016/0036-9748(86)90224-3.
- [104] A. Oudriss, J. Bouhattate, C. Savall, J. Creus, X. Feugas, F. Martin, et al., On the implications of hydrogen on inter-granular fracture, *Procedia Mater. Sci.* 3 (2014) 2030–2034.
- [105] J.F. Lessar, W.W. Gerberich, Grain size effects in hydrogen-assisted cracking, *Metall. Trans. A.* 7 (1976) 953–960. doi:10.1007/BF02644060.
- [106] R.M. Latanision, H. Opperhauser, The intergranular embrittlement of nickel by hydrogen: The effect of grain boundary segregation, *Metall. Trans.* 5 (1974) 483–492. doi:10.1007/BF02644118.
- [107] S. Suresh, Crack Deflection - Implications for the Growth of Long and Short Fatigue Cracks, *Metall. Trans. A.* 14 (1983) 2375–2385. doi:Doi 10.1007/Bf02663313.
- [108] R.O. Ritchie, S. Suresh, Some Considerations on Fatigue Crack Closure at near-Threshold Stress Intensities Due to Fracture Surface-Morphology, *Metall. Trans. a-Physical Metall. Mater. Sci.* 13 (1982) 937–940. doi:Doi 10.1007/Bf02642409.
- [109] J.E. King, Effects of grain size and microstructure on threshold values and near threshold crack growth in powder-formed Ni-base superalloy, *Met. Sci.* 16 (1982) 345–355. doi:doi:10.1179/030634582790427479.
- [110] M. Seita, J.P. Hanson, S. Gradečak, M.J. Demkowicz, The dual role of coherent twin boundaries in hydrogen embrittlement, *Nat. Commun.* 6 (2015) 6164. doi:10.1038/ncomms7164.
- [111] S. Kobayashi, T. Maruyama, S. Tsunekawa, T. Watanabe, Grain boundary engineering based on fractal analysis for control of segregation-induced intergranular brittle fracture in polycrystalline nickel, *Acta Mater.* 60 (2012) 6200–6212. doi:http://dx.doi.org/10.1016/j.actamat.2012.07.065.
- [112] M. Frary, C.A. Schuh, Connectivity and percolation behaviour of grain boundary networks in three dimensions, *Philos. Mag.* 85 (2005) 1123–1143. doi:10.1080/14786430412331323564.
- [113] C.A. Schuh, R.W. Minich, M. Kumar, Connectivity and percolation in simulated grain-boundary networks, *Philos. Mag.* 83 (2003) 711–726. doi:Doi 10.1080/0141861021000056681.
- [114] J.R. Rice, G.F. Rosengren, Plane strain deformation near a crack tip in a power-law hardening materials, *J. Mech. Phys. Solids.* 16 (1968) 1–12.
- [115] J.W. Hutchinson, Singular behaviour at the end of a tensile crack in a hardening material, *J. Mech. Phys. Solids.* 16 (1968) 13–31.
- [116] M.R. Begley, J.A. Begley, C.M. Landis, Continuum mechanics modeling of hydrogen embrittlement, in: R.P. Gangloff, B.P. Somerday (Eds.), *Gaseous Hydrog. Embrittlement Mater. Energy Technol.*, Woodhead Publishing, 2012: pp. 286–325.
- [117] E. Martínez-Pañeda, C.F. Niordson, On fracture in finite strain gradient plasticity, *Int. J. Plast.* 80 (2016) 154–167. doi:10.1016/j.ijplas.2015.09.009.
- [118] I.M. Robertson, P. Sofronis, A. Nagao, M.L. Martin, S. Wang, D.W. Gross, et al., Hydrogen

- Embrittlement Understood, *Metall. Mater. Trans. B.* (2015). doi:10.1007/s11663-015-0325-y.
- [119] M.L. Jokl, V. Vitek, C.J. McMahon, Microscopic Theory of Brittle Fracture in Deformable Solids: a Relation Between Ideal Work To Fracture and Plastic Work., *Acta Metall.* 28 (1980) 1479–1488. doi:10.1016/0001-6160(80)90048-6.
- [120] R.A. Oriani, A Mechanistic Theory of Hydrogen Embrittlement of Steels, *Berichte Der Bunsen-Gesellschaft Fur Phys. Chemie.* 76 (1972) 848–857.
- [121] J. Dolph, The Effect of Microstructure on the HEAC Behavior of Monel K-500, University of Virginia, 2015.

Chapter 4. Effect of heat treatment variation on HEAC in Monel K-500

4.1. Overview

The effect of isothermal heat treatment on hydrogen environment-assisted cracking (HEAC) susceptibility in a single heat of Monel K-500 was evaluated via slow-rising stress intensity (K) testing while immersed in 0.6 M NaCl solution and exposed to an applied potentials ranging from -1000 to -1200 mV_{SCE} (vs. saturated calomel electrode). Four heat treatments, corresponding to the non-aged, under-aged, peak-aged, and over-aged conditions, conducted at a constant aging temperature of 923 K, were examined in this study. Crack growth kinetics and fractography demonstrate that alloys heat-treated to the under-aged and peak-aged conditions exhibit increased susceptibility to HEAC relative to alloys treated to the non-aged and over-aged conditions, respectively. Microstructural variables which are expected to vary under this isothermal heat treatment protocol are grain size, grain boundary character, grain boundary impurity concentration, yield strength, strain hardening, and precipitate morphology. A detailed assessment of grain size, grain boundary character, and grain boundary impurity concentration evolution with aging time suggests these variables do not govern the HEAC susceptibility of Monel K-500. Differences in crack tip stresses induced by variations in yield strength and strain hardening were directionally consistent with the observed HEAC susceptibility, but could not explain the enhanced susceptibility of the under-aged heat treatment relative to the peak-aged condition. However, transmission electron microscopy of each heat treatment revealed the presence of planar slip in the under-aged and peak-aged specimens, as compared to wavy slip in the non-aged and over-aged specimens, suggesting that the propensity for strain localization correlates well with HEAC susceptibility.

Note: One (1) peer-reviewed conference proceedings has been published based on the work presented in this chapter, which can be accessed using the details below:

4. **Z.D. Harris** and J.T. Burns, “The Effect of Heat Treatment on Hydrogen Environment-Assisted Cracking of Monel K-500”, in *Material Performance in Hydrogen Environments: Proceedings of the 2016 International Hydrogen Conference*, B.P. Somerday and P. Sofronis, eds., pp. 367-376.
 - a. Harris contribution: primary performer; conducted heat treatments, fracture mechanics testing, materials characterization, analysis and interpretation of data, and wrote manuscript.

4.2. Introduction

As described in detail in Chapter 3, several recent studies have sought to identify the causal factors which govern the susceptibility of Monel K-500 to HEAC, with particular emphasis on the effect of applied potential [1], mechanical loading [2], and metallurgy [3,4]. Considering the former, slow-rising stress intensity (K) testing demonstrated a clear enhancement in HEAC susceptibility with increasingly negative applied potential [1]. However, for a constant applied potential, the HEAC susceptibility was found to vary extensively across two material heats [1]. This observation suggests that HEAC in Monel K-500 is sensitive to variations in metallurgy, with the effect being magnified at near-threshold levels of hydrogen overpotential. As documented in Chapter 3, slow-rising K testing of five different material heats of peak-aged Monel K-500 (all of which satisfied the QQ-N-286G federal procurement standard for Monel K-500 [5]) immersed in 0.6 M NaCl solution at $-850 \text{ mV}_{\text{SCE}}$ confirmed this important role of metallurgical variability [3]. Specifically, two material heats did not display any evidence indicating the onset of HEAC, whereas three other heats exhibited varying degrees of susceptibility based on measured threshold stress intensities (K_{TH}) ranging from ~ 5 to 14% of the plane strain fracture toughness (K_{IC}). This study attempted to correlate the observed variation in susceptibility to differences in microstructural features, with examined parameters including: yield strength, grain size, impurity and gettering element content, and grain boundary character/connectivity. However, little correlation between individual microstructural variations and HEAC susceptibility was identified [3]. A companion study examining the influence of variations in H-metal interactions (*i.e.* hydrogen uptake, hydrogen trapping, hydrogen diffusivity, and hydrogen evolution rate) also noted only a minimal correlation between these parameters and HEAC susceptibility [4].

These previous attempts [3,4] to evaluate the relationship between metallurgy and HEAC susceptibility in Monel K-500 in Chapter 3 were limited by the lack of experimental controls inherent to utilizing “engineering” heats procured from separate vendors. Specifically, the simultaneous variation in multiple properties (1) obfuscates the assessment of the influence of any one metallurgical parameter and (2) complicates the evaluation of coupled microstructural effects (*e.g.* the influence of both grain size and gettering element concentrations on grain boundary impurity content). The contribution of metallurgical features to the microscale mechanism(s) which govern HEAC susceptibility must be understood in order to inform material procurement standards, design hydrogen-resistant alloys, and develop hydrogen-sensitive structural integrity models. This knowledge gap motivates further examination of the role of metallurgical variations in determining the HEAC susceptibility of Monel K-500, with particular emphasis on systematically controlling the variation in microstructure through targeted heat treatments on a single heat of Monel K-500.

4.2.1. Chapter objective and research questions

The objective of this paper is to elucidate the metallurgical variables governing the HEAC susceptibility of Monel K-500 by systematically altering a small number of variables through targeted isothermal heat treatments on a single material heat and then correlating these data with measured HEAC susceptibility metrics (K_{TH} and da/dt_{II}). To accomplish this objective, this chapter will seek to answer the following specific research questions:

1. How does HEAC susceptibility in Monel K-500 vary with different isothermal aging times?
2. How does variations in isothermal aging time affect the metallurgical parameters pertinent to HEAC susceptibility?
3. Do these measured variations in metallurgy with heat treatment correlate with HEAC susceptibility?

4.3. Experimental methods and material

4.3.1. Material and heat treatment protocol

All experiments were conducted on a single heat of Monel K-500 procured in form of a 6-m long, 16-mm diameter bar heat-treated to the solution-annealed condition. The as-received grain structure was nominally equiaxed with a supplier-reported average grain size of $\sim 10 \mu\text{m}$. Bulk composition was evaluated using inductively coupled plasma optical emission spectroscopy (ICP-OES), while glow discharge mass spectroscopy (GDMS) was utilized for trace elemental analysis; the measured composition is shown in Table 8.

Table 8 – Composition of the tested Monel K-500 heat (wt. % except Si, Zr, P, S, and B are in wppm)

Ni	Cu	Al	Ti	Mn	Fe	Si	Zr	P	S	B
62.3	31.8	2.96	0.59	0.7	0.78	850	310	69	31	1.2

The evolution of yield strength as a function of aging time was evaluated by heat-treating 38-mm long, 12.7-mm diameter cylindrical blanks in a tube furnace using the following protocol: (1) solution-treatment at 1223 K for one hour followed by immediate water quench and (2) aging at 923 K for times ranging from 0.5 to 100 hours followed by immediate water quench. Prior work demonstrated that the solution-annealing temperature of 1223 K was above the γ' solvus and that the quench sensitivity of the alloy was sufficiently modest to enable the use of water quenching [6,7]. All cylindrical specimens were then compressively loaded to 2% total strain to determine yield strength (calculated from the 0.2% offset) and Ramberg-Osgood coefficients. These data were then employed to select aging conditions which corresponded to the non-aged (NA), under-aged (UA), peak-aged (PA), and over-aged (OA) conditions.

4.3.2. Fracture mechanics testing

100-mm long, 16-mm diameter cylindrical blanks were heat treated to the selected aging conditions using the preceding protocol; aged blanks were then machined into single edge notch tensile (SEN(T)) specimens with gage sections of 12.5 ± 0.02 mm in width (W) and 2.68 ± 0.02 mm in thickness (B). A starter notch was then placed at the midpoint of the gage section using electrical discharge machining. The notch depth was varied across heat treatments such that a K of ~ 35 MPa $\sqrt{\text{m}}$ and a $K > 40$ MPa $\sqrt{\text{m}}$ could be obtained for the non-aged and all other aging conditions, respectively, before the elastic limit of the net section was exceeded, assuming no crack extension. Prior work demonstrated that false dcPD-measured crack growth attributed to bulk-scale plasticity occurs upon exceeding the elastic limit in the remaining ligament [2]. The stress corresponding to the elastic limit was identified using the results of the 2% compression testing previously described and is reported for each condition in Table 9. Based on this design requirement, notch depths of 5.625 ± 0.01 mm and 2.775 ± 0.01 mm were machined for the non-aged condition and all other heat treatments, respectively. Notch depths were measured prior to testing with a calibrated Hirox RH-8800 digital microscope; three measurements were taken on either side of the specimen and then averaged to obtain the final notch depth value.

Specimens were oriented such that the loading axis was parallel to the longitudinal direction of the bar stock, with Mode I crack growth occurring in the radial direction; all specimens were loaded in clevis grips to allow for free rotation in accordance with K-solution boundary conditions [8]. Prior to HEAC testing, specimens were fatigue precracked in laboratory air at a constant $K_{\text{max}} = 11$ MPa $\sqrt{\text{m}}$ at $R = 0.1$ and $f = 3$ to 5 Hz from the initial notch depth to a notch plus crack length of 5.95 mm for the non-aged condition and 3.0 mm for all other heat treatments. These short precrack distance were utilized to mitigate crack closure-induced shorting of the dcPD voltage, which is speculatively attributed to the intergranular fracture morphology observed during fatigue loading in the current material heat. Critically, these distances were also selected to ensure that the crack had propagated sufficiently far from the notch such that the crack-tip stress field was not influenced by the stress field associated with the notch [9,10].

Fracture mechanics testing at a constantly increasing elastic K (dK/dt) was achieved by coupling active crack length feedback via dcPD with software-controlled, servo-hydraulic actuator displacement. All testing was completed at a constant $dK/dt = 0.33$ MPa $\sqrt{\text{m/hr}}$, which corresponded to an approximate grip velocity of 2×10^{-6} mm/s. Crack extension was continuously monitored using the direct current potential difference (dcPD) technique [11] and the grip displacement was adjusted every 15 seconds to maintain the specified dK/dt . Crack lengths were calculated from measured potentials using Johnson's equation [12], where the adjustable constant (V_0) is the potential associated with the initial notch depth (a_0) [13]. Each potential measurement was corrected for thermally-induced voltages using current-polarity reversal. Post-test initial crack length measured via electron microscopy typically varied $<2\%$ from the dcPD-based

calculated value. If necessary, the initial crack length was corrected to match the measured value from fractography and all subsequent crack measurements were recalculated using the measured voltage at each time step. The crack growth rate (da/dt) was then calculated using the increment ($n = 3$) polynomial method presented in ASTM E647-13 Appendix XI [14]. A post-test correction for false crack growth due to crack surface electrical contact enabled by cathodic polarization-induced destabilization of the crack wake surface oxide film was performed as has been previously described [1]. The effects of plasticity on the fracture driving force were accounted for through the calculation of the total stress intensity (K_J) *via* established J-intergral procedures. Specifically, remaining ligament plasticity was evaluated through analytical solutions for a stationary crack in a material deforming according to the Ramberg-Osgood flow rule and the plastic zone-corrected effective crack length. Additional details of the analysis procedure are presented elsewhere [15]. HEAC metrics were defined as follows: K_{TH} is defined as the K at which the crack growth rate exceeds the plasticity-based resolution limit (defined from inert environment testing [1]) of the dcPD system and $da/dt_{K=45}$, which is the measured crack growth rate at $K = 45 \text{ MPa}\sqrt{\text{m}}$. This crack growth parameter was selected based on the lowest final K measured during HEAC testing (UA -1100 mV_{SCE} ; $45 \text{ MPa}\sqrt{\text{m}}$) and does not have the same physical basis as the diffusion-limited Stage II crack growth rate (da/dt_{II}) discussed in Chapter 3 [1].

Four environments were investigated in this work, each at ambient temperature ($\sim 298 \text{ K}$): dry N_2 gas ($\text{RH} < 5\%$) and full immersion in aqueous chloride electrolyte at an applied potentials of -1000, -1100, and -1200 mV_{SCE} . Prior investigations of HEAC in Monel K-500 found these potentials to correspond to inert, aggressive, severe, and extreme, respectively. These more aggressive potentials were utilized based on the absence of HEAC at -1000 mV_{SCE} for all aging conditions except the under-aged alloy, as documented below. To isolate the testing environment, the gage section of the SEN(T) specimen was placed inside a sealed 240 mL cylindrical Plexiglass cell which did not impede the load train. Immersion testing was completed using 0.6 M NaCl solution circulated from a 2L reservoir at $\sim 20 \text{ mL/min}$, while testing in dry N_2 was conducted by flowing nitrogen into the cell at a rate such that the relative humidity was maintained below 5% for the duration of loading. Testing in 0.6 M NaCl was completed at a constant applied potential, referenced to a saturated calomel electrode, controlled by a potentiostat operating in ‘floating mode’ to avoid a ground loop. A platinum-coated Nb mesh was used as a counter electrode and was positioned such that it encircled the specimen in the environmental cell. Testing was stopped upon exceeding the net section elastic limit based on the nominal stress applied over the remaining specimen ligament; this criteria mitigates extraneous dcPD voltages induced by bulk-scale plastic deformation [2]. Upon test completion, the specimen was rinsed with deionized water and allowed to dry. After a 48-hour hold at ambient conditions to allow hydrogen egress, each specimen underwent “post-test” fatigue to better delineate the extent of intergranular cracking. This fatigue protocol was conducted as follows: the specimen

was cyclically loaded in laboratory air using a rising K_{\max} from 30 to 60 MPa $\sqrt{\text{m}}$ at $R = 0.5$ starting from the final IG crack depth measured by dcPD to a total crack length of 10.0 mm. After reaching 10 mm, the specimen was rapidly loaded to failure using displacement control. Upon final fracture, the specimen was rinsed with deionized water, sonicated in acetone and methanol for 15-20 minutes each, and then dried with compressed air.

4.3.3. Characterization

4.3.3.1. Microscopy

Orientation imaging microscopy (OIM) was completed via electron backscatter diffraction (EBSD) on a FEI Helios DB FIB/SEM using an accelerating voltage of 30 keV, a step size of 0.75 μm , and a probe current of 3.2 nA. EBSD samples were extracted from the non-gauge portion of the SEN(T) specimens and iteratively polished using SiC grinding papers and diamond slurries to a final finish with 0.05 μm colloidal silica. OIM maps were evaluated using the Tango (Oxford Instruments) post-processing software to determine the grain size as a function of aging time. Approximately 1000 individual grains were sampled to determine the average grain size in each condition. Grain boundary character length fractions were analyzed from the collected OIM maps using the Matlab-based MTEX package.

Foil specimens for transmission electron microscopy (TEM) were prepared from the cylindrical specimens compressed to approximately 2% total strain using the following procedure. First, ~2.5-mm thick discs were sectioned from the compression specimens using a low-speed cut-off saw; electron backscatter diffraction confirmed that the saw damage depth was less than 300 μm . The discs were then progressively thinned using SiC papers, finishing at 1200 grit, to a final thickness of 80-110 μm . Care was taken to minimize extraneous damage to the foils by removing (1) at least 600 μm from each side of the disc to avoid possible saw damage effects and (2) at least 3x the average particle size of the preceding SiC grinding paper before advancing to next grit size to minimize polishing-induced damage from lower grit sizes. For example, since the supplier-reported average particle size for the 400-grit SiC paper is ~22 μm , a minimum of 66 μm (typically 70 μm) was removed using the 600-grit SiC paper before advancing to the 800-grit SiC paper. After the grinding step, 3-mm diameter foils were punched from the thin disc using a Gatan disc puncher and then electrochemically polished in a Fischione 110 twin jet polisher. A solution of 60% H_2SO_4 and 40% H_2O (by volume) was used at ambient temperature (296 to 298 K) with an applied voltage of 5 V, which corresponded to a current of ~35 mA. A FEI Titan equipped with a double-tilt specimen holder and operated at 300 keV was utilized to evaluate the variation in the γ' and bulk slip morphology with aging time. The γ' size distribution was evaluated for each aging condition using ~500 precipitates taken from a minimum of five different regions spread across two separate TEM foils. Similarly, the bulk slip morphology was globally assessed via imaging of dislocations across 3-5 regions on two different foils for

each aging condition. The two-beam condition utilized for examining the bulk slip morphology is noted on each respective micrograph.

4.3.3.2. Auger electron spectroscopy

Auger electron spectroscopy (AES) was completed on each aging condition using a Physical Electronics PHI 710 Scanning Auger Nanoprobe operated at 10 keV with a probe current of 10 nA and a beam probe diameter of 20 nm. AES specimens were machined in the form of 19-mm long, 6.25-mm diameter cylindrical pins that contained a 90° notch located 11.5 mm from the end of the specimen (minor diameter of notch was 2.2 mm). To ensure an intergranular fracture morphology for assessing grain boundary sulfur content, all AES specimens were charged with hydrogen for 60 days via immersion in 0.6 M NaCl at an applied potential of -1200 mV_{SCE}. Upon removal from the charging station, specimens were kept under cryogenic temperatures (using either liquid nitrogen or dry ice) at all times prior to loading in the AES system so as to minimize hydrogen egress and reduce surface contamination. Attempts to fracture the specimens under vacuum using a custom impact fracture rig in the AES system were unsuccessful, therefore all specimens were fractured via bending prior to being sent to Physical Electronics for AES analysis. Elemental profiles as a function of depth were collected via sputter depth profiling of intergranular facets, with multiple facets (~2-3 per specimen) being analyzed/sputtered simultaneously. Incremental sputtering was completed to a depth of ~50 nm (step size ≈ 1 nm) using an Ar ion beam at an accelerating voltage of 2 keV and an impingement angle of 52°; these conditions yield an approximate sputtering rate that is equivalent to 2 nm/min in SiO₂ [16].

4.4. Results

4.4.1 Variation in yield strength with isothermal aging time

The measured yield strength as a function of aging time at 923 K for the tested heat of Monel K-500 is shown in Figure 29. Duplicate specimens for aging times of 0 and 2 hours had similar yield strengths (0 hr: 296 and 298 MPa, 2 hr: 556 and 558 MPa), thereby establishing the repeatability of the heat treatment procedure. As expected from the work of Dey et al. [6], the yield strength rapidly increases from the non-aged condition with increasing aging time, reaching a peak value after approximately 5 hours, followed by a gradual decrease in yield strength with additional aging. From these experiments, four aging times were selected for further study via fracture mechanics testing, representing the non-aged (0 hours), under-aged (0.5 hours), peak-aged (5 hours), and over-aged (50 hours) conditions, respectively. The yield strength and Ramsberg-Osgood coefficients (n and α ; defined in Section 3.3.1.) measured via compression testing for each aging condition are shown in Table 9 (note that values for the non-aged condition represent the average of the duplicate tests).

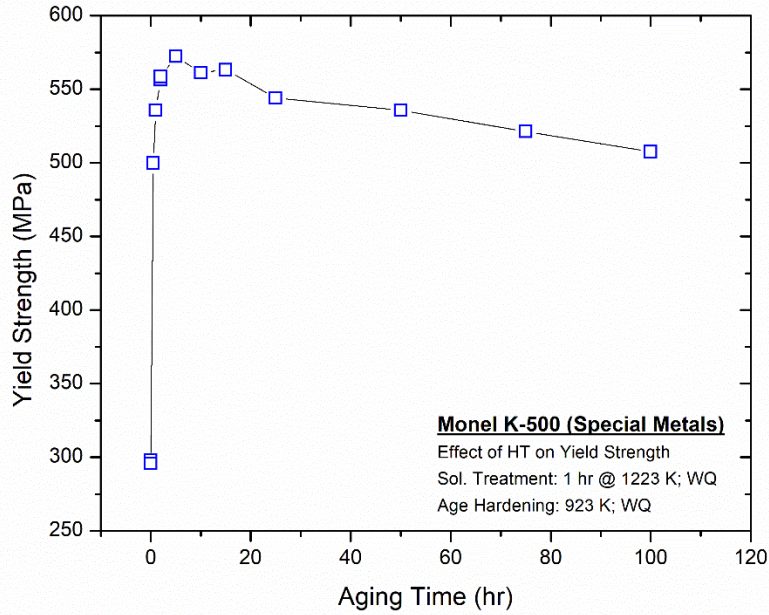


Figure 29 – Variation in yield strength of Monel K-500 as a function of aging time at 923 K.

Table 9 – Measured mechanical properties for the selected aging conditions

Aging Condition	Aging Time (hr)	Elastic Limit (MPa)	Yield Strength (MPa)	E (GPa)	n	α
Non-aged	0	185	297	181.9	6.54	1.98
Under-aged	0.5	380	500	184.2	12	0.68
Peak-aged	5	425	572	183.5	13.5	0.48
Over-aged	50	405	536	186.4	19.6	0.62

4.4.2. Quantifying HEAC kinetics as a function of isothermal aging time

4.4.2.1. Non-aged condition

The measured da/dt versus total stress intensity (K_I) results for the NA condition tested in 0.6 M NaCl at applied potentials of -1100 and -1200 mV_{SCE} are presented in Figure 30. First, these kinetics data indicate that the measured crack growth rate for NA -1100 mV_{SCE} is consistently faster compared to testing at -1200 mV_{SCE}. However, the observed disparity (on average ~1.4x) in crack growth rates is well within the 4x scatter previously measured for a single heat of Monel K-500 in 0.6 M NaCl at -1000 mV_{SCE} [1], suggesting that these differences are likely attributable to test-to-test variability. Second, the measured da/dt at both applied potentials appears to increase linearly (on a logarithmic scale) with increasing K_I instead of exhibiting the characteristic rapid acceleration in da/dt typical of Stage I crack growth [17]. As discussed in depth in Chapter 3, such linear increases in $\log(da/dt)$ with increasing K_I are generally not attributable to

real crack growth, but are rather due to localized plasticity-induced changes in resistivity that increase the dcPD-measured potential, thereby resulting in ‘false’ crack growth [1]. As such, given the similarities in crack growth kinetics between the two applied potentials and the apparent linear dependence on K_I , it is unlikely that HEAC occurred in the NA specimens prior to exceeding the net section elastic limit at a K_I of $\sim 43 \text{ MPa}\sqrt{\text{m}}$ (the condition for ending the experiment due to dcPD-related artifacts [2]; see Section 4.3.2. for more details)⁴.

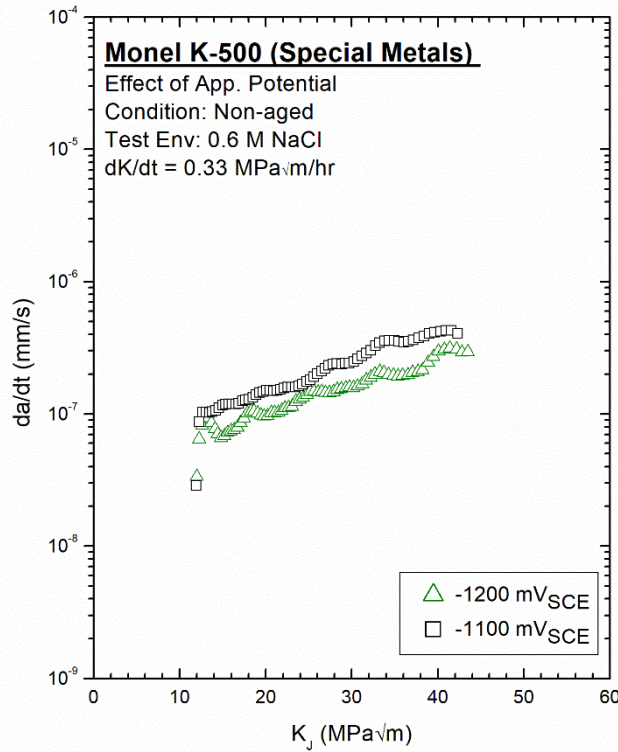


Figure 30 – Crack growth rate versus total K for specimens heat-treated to the non-aged condition tested under slow-rising K in 0.6 M NaCl at -1100 and -1200 mV_{SCE} using a constant $dK/dt = 0.33 \text{ MPa}\sqrt{\text{m/hr}}$.

Examination of the fractography in Figure 31 corroborates this assessment as, despite exposure to severe hydrogen-producing environments for Monel K-500 [1], the NA alloy does not exhibit any evidence of intergranular (IG)-HEAC at either -1100 mV or -1200 mV_{SCE} . Specifically, as highlighted by the white arrows in Figure 31a-b for NA -1200 mV_{SCE} , fractographic features consistent with those expected from crack-tip blunting (*i.e.* “stretch zones”) were observed across the specimen width at a distance from the EDM notch (white dashed line in Figure 31a-b, left side) similar to the targeted fatigue precrack depth

⁴ It is important to recognize that the current results do not preclude the possibility of HEAC occurring at higher K_I values for the NA specimen. However, given that K_{TH} values lower than $43 \text{ MPa}\sqrt{\text{m}}$ were observed in the other heat treatments (shown below) at -1100 and -1200 mV_{SCE} , testing to this K_I was sufficient for ranking HEAC susceptibility as a function of heat treatment (Section 4.5.).

(~300 μm). Higher magnification imaging of the region proximate to these features (Figure 31c; “stretch zones” indicated by white arrows) confirms the absence of IG-HEAC in NA -1200 mV_{SCE} . Similar fractographic features were also observed in NA -1100 mV_{SCE} , as highlighted by the white arrows in Figure 31d. Interestingly, beyond these blunting features in the post-test fatigue region of NA -1100 mV_{SCE} (noted as PTF in Figure 31), a mixed IG/transgranular (TG) fatigue fracture morphology was observed. This morphology has been previously reported for Monel K-500 cyclically loaded in laboratory air [18] and, as will be shown in subsequent sections, is found across all tested conditions in the current material heat (though only in the PTF region for the tested NA specimens). Critically, this fracture morphology is not considered evidence for HEAC given that it clearly occurs after (1) the blunting features and (2) features consistent with transgranular fatigue crack growth (as indicated by the yellow arrow in Figure 31d). Therefore, given (1) the lack of fractographic evidence for IG-HEAC and (2) the measured linear increase in da/dt with K_I consistent with local plasticity-induced increases in dcPD-measured voltage, it is concluded that the NA heat treatment is not susceptible to HEAC (over the tested K_I intervals) for applied potentials more positive than -1200 mV_{SCE} . As such, values for K_{TH} and $da/dt_{K=45}$ are not reported for the NA condition.

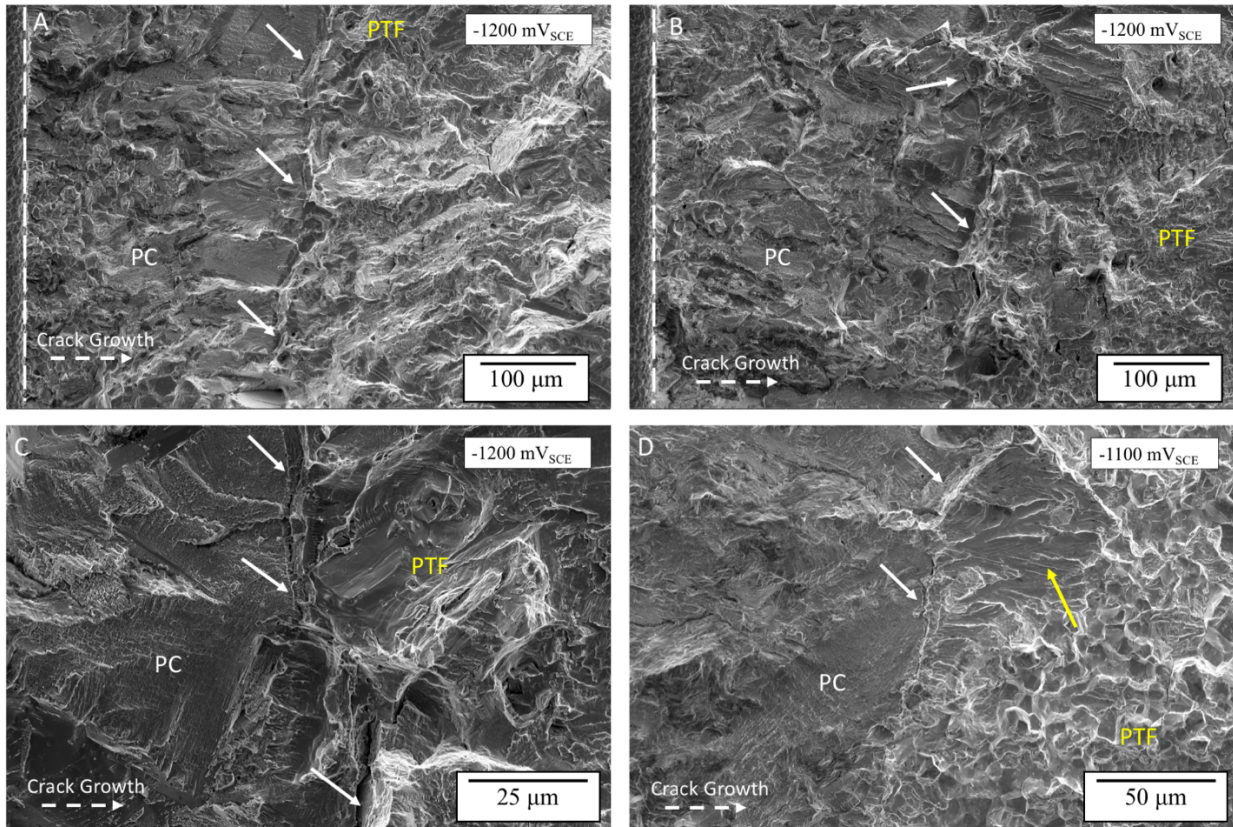


Figure 31 – Micrographs of the fracture morphologies observed in non-aged specimens tested at -1200 (a-c) and -1100 mV_{SCE} (d) in 0.6 M NaCl. The white arrows in (a-d) denote fractographic features consistent with crack-tip blunting,

which occurred at a distance similar to the targeted precrack (PC) depth from the EDM notch (white dashed line in (a-b), left). The yellow arrow in (d) indicates a transgranular (TG) feature in the post-test fatigue (PTF) region that separates the blunting features and the IG/TG fatigue fracture morphology. Crack growth occurs from left to right in all images, as shown by the dashed white arrow.

4.4.2.2. Under-aged condition

The da/dt versus K_I relationships measured for the UA heat treatment in dry N_2 (RH <5%) and in 0.6 M NaCl at -1000, -1100, and -1200 mV_{SCE} are shown in Figure 32. The dashed line represents the linear fit to the false crack growth rates measured during inert environment testing in dry N_2 (termed ‘resolution limit’) and is described by the following relationship: $\log[da/dt_{FALSE} \text{ (mm/s)}] = -7.7968 + 0.0279K_I$. Examination of the kinetics data clearly demonstrates that the measured crack growth rates for all tested applied potentials exceeded the growth rates attributable to localized plasticity, suggesting the onset of HEAC in each respective experiment. As such, K_{TH} was measured as 12, 21, and 25 MPa \sqrt{m} , while $da/dt_{K=45}$ was 3.8×10^{-6} , 2.2×10^{-6} , and 1.4×10^{-6} mm/s, for testing at -1200, -1100, and -1000 mV_{SCE}, respectively. The increase in measured crack growth rates and decrease in K_{TH} with increasingly negative applied potentials is consistent with the findings in Chapter 3 and other prior work on Monel K-500 [1]. One notable feature in Figure 32 is the apparent divergence of the three tested applied potentials at $K_I \approx 40$ MPa \sqrt{m} , respectively. Mechanistically, this divergence is likely linked to a hydrogen diffusion-limited crack growth rate [19], which is principally a function of the effective hydrogen diffusivity (D_{eff}) and the diffusible hydrogen concentration ($C_{H,Diff}$). Under this mechanistic paradigm, the presence of additional diffusible hydrogen at more negative applied potentials enables crack growth at increased velocities, since for a given time increment, more hydrogen is able to diffuse into the fracture process zone (for a constant D_{eff}). As such, while a sufficiently large K interval was not measured in the current study to explicitly determine this Stage II crack growth rate, the observed divergence (particularly for UA -1000 mV_{SCE}) is directionally consistent with a hydrogen diffusion limitation.

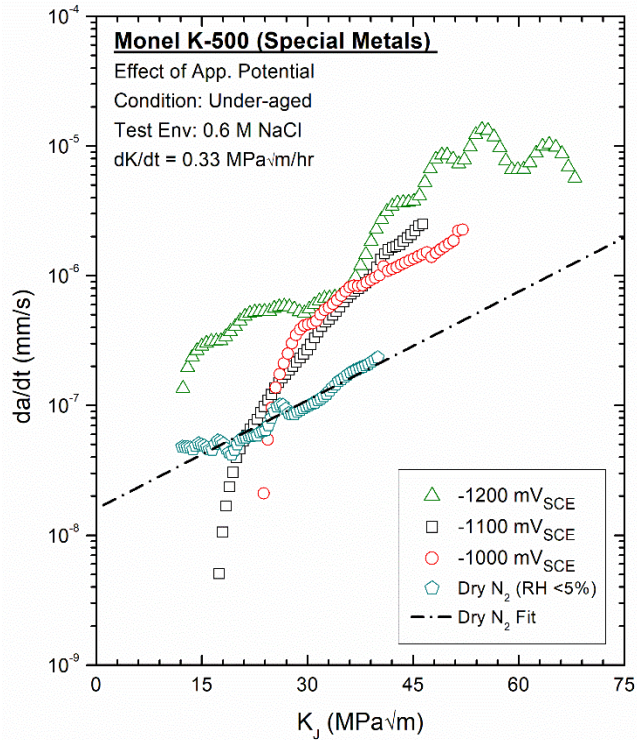


Figure 32 – Crack growth rate versus total K for specimens heat-treated to the under-aged condition tested under slow-rising K in dry N_2 ($RH < 5\%$) and in 0.6 M NaCl at -1000, -1100, and -1200 mV_{SCE} using a constant $dK/dt = 0.33 \text{ MPa}\sqrt{m}/\text{hr}$. The dashed line corresponds to the linear fit of the $\log(da/dt)$ vs. K_I data measured during dry N_2 testing.

Fractography of the UA specimens tested in 0.6 M NaCl at applied potentials of -1000, -1100, and -1200 mV_{SCE} , shown in Figure 33, confirm the onset of IG-HEAC across all tested applied potentials. Considering UA -1200 mV_{SCE} , Figure 33a demonstrates that extensive intergranular cracking was observed (on the order of millimeters; noted as HEAC) during testing. Though not as extensive, clear evidence of HEAC was also observed in UA -1100 mV_{SCE} and UA -1000 mV_{SCE} , as shown by the stark transition in fracture morphology between the IG/TG fatigue precrack (noted as PC in the micrographs) and the HEAC region in Figure 33b-c (transition marked by red dashed line). Finally, as was observed in Chapter 3, the fracture morphology in the HEAC region (Figure 33d) predominantly consisted of IG facets, with some distinct TG features (examples denoted by white arrows).

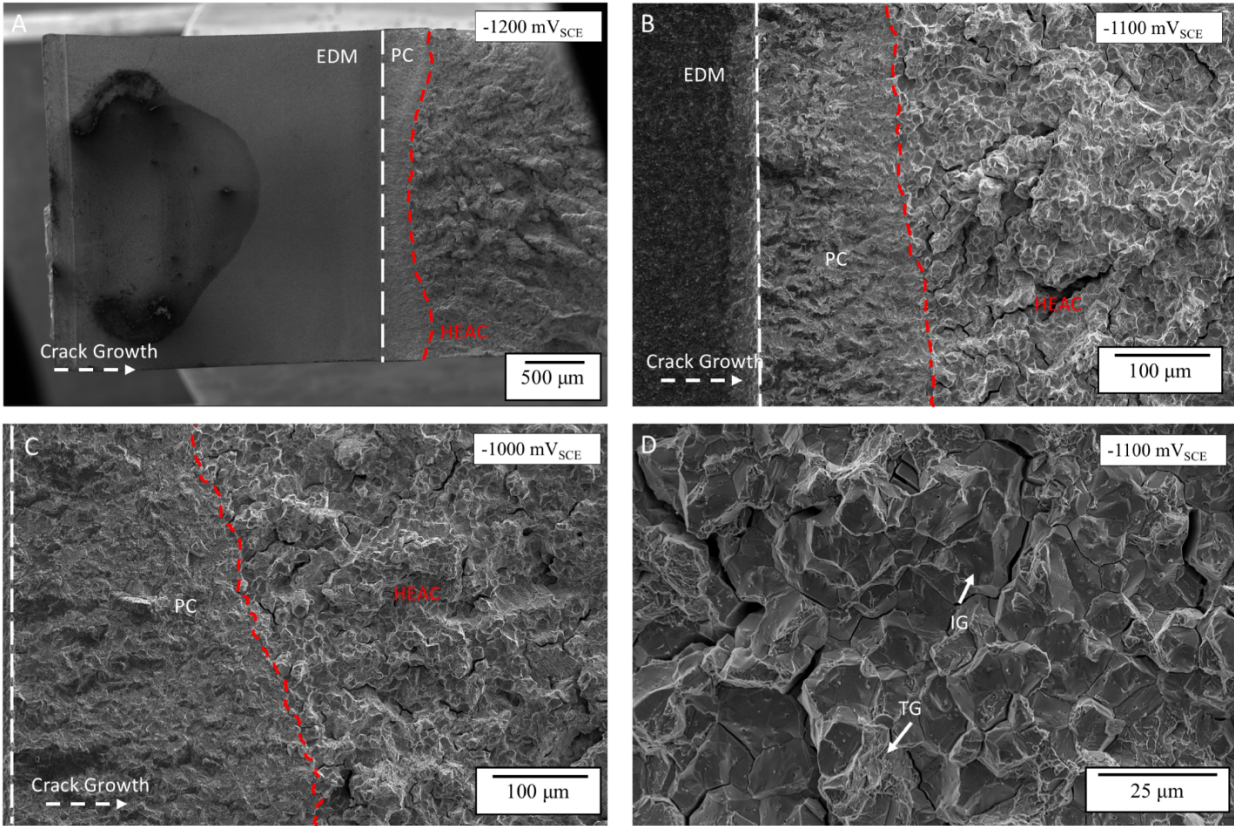


Figure 33 – Overview micrographs of the fracture morphologies observed in under-aged specimens tested at (a) -1200, (b) -1100, and (c) -1100 mV_{SCE} in 0.6 M NaCl. The white dashed line in (a-c) denotes the location of the EDM notch, while the red dashed line in (a-c) indicates the transition from the fatigue precrack (PC) to HEAC. A representative high magnification micrograph of the fracture morphology in the HEAC region is shown in (d), with example intergranular (IG) and transgranular (TG) features noted by the white arrows. Crack growth occurs from left to right in all images, as shown by the dashed white arrow.

4.4.2.3. Peak-aged condition

The measured da/dt vs. K_I data for the peak-aged heat treatment in dry N₂ (RH <5%) and in 0.6 M NaCl at -1000, -1100, and -1200 mV_{SCE} are presented in Figure 34. As in Figure 32, the dashed line represents the linear fit to the false crack growth rates measured during inert environment testing in dry N₂ and is defined by the following equation: $\log[da/dt_{FALSE} \text{ (mm/s)}] = -7.6208 + 0.0198K_I$. Considering the results at -1000 mV_{SCE}, the measured crack growth kinetics were found to linearly increase (on a logarithmic scale) with increasing K_I in a manner consistent with the dry N₂ results. This similarity with the inert environment data indicates an absence of HEAC at this applied potential for the PA condition, up to $K_I \approx 39 \text{ MPa}\sqrt{\text{m}}$ where testing was concluded. Conversely, slow-rising K testing of PA specimens in 0.6 M NaCl at -1100 and -1200 mV_{SCE} resulted in crack growth rates that were elevated compared to the dry N₂-based resolution limit, suggesting the onset of HEAC. As such, K_{TH} and $da/dt_{K=45}$ were measured from the kinetics

data in Figure 34 as $13 \text{ MPa}\sqrt{\text{m}}$ and $4.8 \times 10^{-6} \text{ mm/s}$ for $-1200 \text{ mV}_{\text{SCE}}$ and $18 \text{ MPa}\sqrt{\text{m}}$ and $1.1 \times 10^{-6} \text{ mm/s}$ for $-1100 \text{ mV}_{\text{SCE}}$, respectively, while K_{TH} and $da/dt_{K=45}$ were not reported for $-1000 \text{ mV}_{\text{SCE}}$.

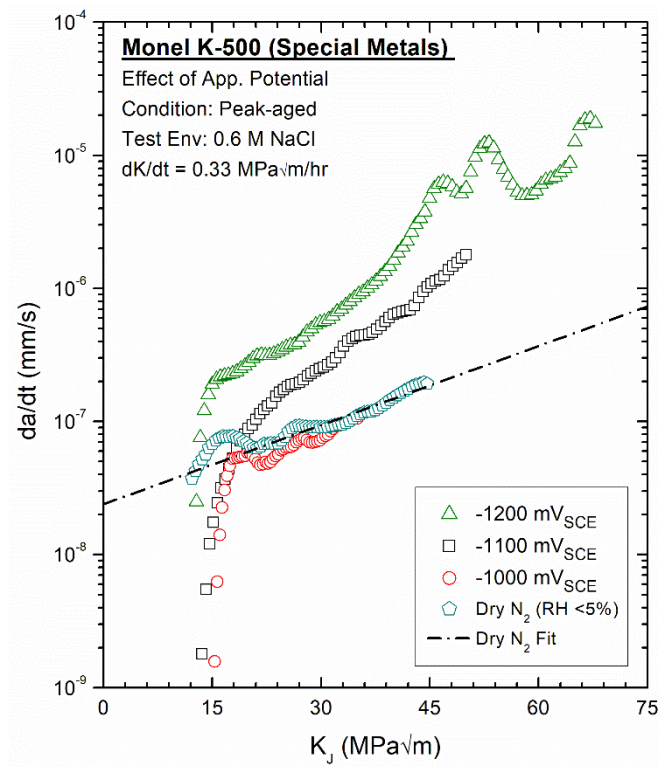


Figure 34 – Crack growth rate versus total K for specimens heat-treated to the peak-aged condition tested under slow-rising K in dry N_2 ($\text{RH} < 5\%$) and in 0.6 M NaCl at -1000 , -1100 , and $-1200 \text{ mV}_{\text{SCE}}$ using a constant $dK/dt = 0.33 \text{ MPa}\sqrt{\text{m/hr}}$. The dashed line corresponds to the linear fit of the $\log(da/dt)$ vs. K_I data measured during dry N_2 testing.

Micrographs of the PA specimens tested in 0.6 M NaCl at -1000 , -1100 , and $-1200 \text{ mV}_{\text{SCE}}$, shown in Figure 35, corroborate the kinetics-based interpretation. First, Figure 35a demonstrates that extensive intergranular cracking attributable to HEAC occurred in PA $-1200 \text{ mV}_{\text{SCE}}$, with IG crack growth extending on the order of millimeters similar to that observed in the UA condition tested at $-1200 \text{ mV}_{\text{SCE}}$ (Figure 33a; marked as HEAC). Second, Figure 35b confirms the presence of HEAC at $-1100 \text{ mV}_{\text{SCE}}$ for the PA heat treatment, with a clear transition in fracture morphology occurring between the precrack (noted as PC) and HEAC regions, as shown in Figure 35d. Similar to the results presented in Figure 33d, the HEAC region for the PA heat treatment consisted predominantly of IG facets, with some discernable TG features. Additionally, as was discussed in Section 4.2.2.1., an IG/TG fracture morphology was observed in the precrack region for this heat treatment condition; an example of an IG facet located in the precrack region of PA $-1100 \text{ mV}_{\text{SCE}}$ is noted by the white arrow in Figure 35d. Finally, considering the PA specimen tested at $-1000 \text{ mV}_{\text{SCE}}$, two observations can be made from the fractography in Figure 35c and Figure 35e. First, as indicated by the white arrows in Figure 35c, this specimen evidence signs of ductile tearing (noted by white arrows), which was caused by a load spike from an unexpected power outage (ending the experiment

at $K_J \approx 39 \text{ MPa}\sqrt{\text{m}}$). Second, close examination of the interface between the precrack and ductile failure regions (Figure 35e) confirms an absence of HEAC for the PA condition at $-1000 \text{ mV}_{\text{SCE}}$ based on the lack of IG features, in agreement with the crack growth kinetics presented in Figure 34.

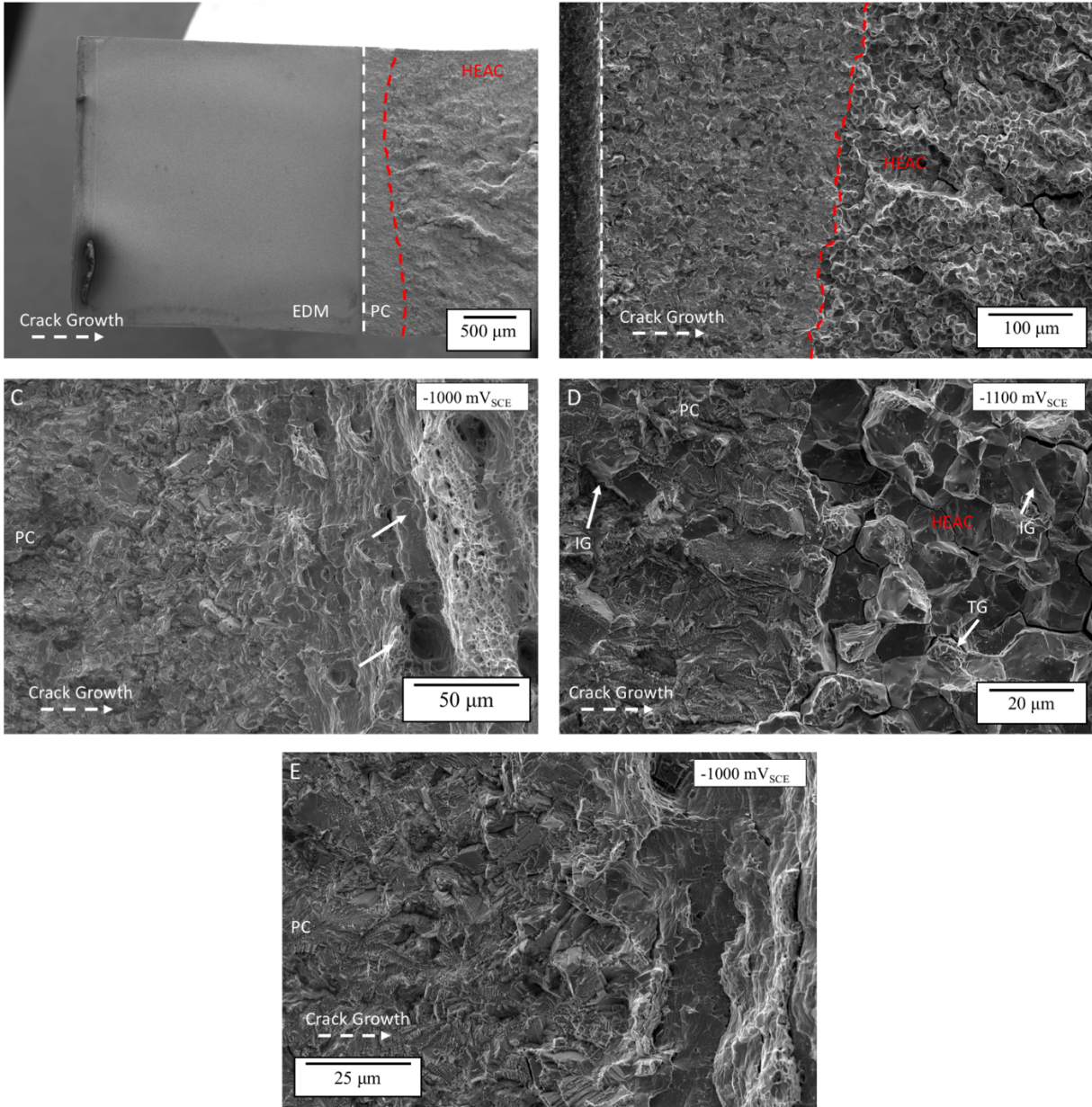


Figure 35 – Overview micrographs of the fracture morphologies observed in under-aged specimens tested at (a) -1200 , (b) -1100 , and (c) $-1100 \text{ mV}_{\text{SCE}}$ in 0.6 M NaCl . The white dashed line in (a-b) denotes the location of the EDM notch, while the red dashed line in (a-b) indicates the transition from the fatigue precrack (PC) to HEAC. Evidence of ductile fracture due to an overload induced by an unexpected power outage is highlighted by the white arrows. A representative high magnification micrograph of the fracture morphology at the transition between the PC and HEAC regions for $-1100 \text{ mV}_{\text{SCE}}$ is shown in (d), with an example intergranular (IG) facet in the PC region noted by the white arrow. A high magnification micrograph of the transition from the precrack to the ductile overload region at $-1000 \text{ mV}_{\text{SCE}}$ is shown in (e). Crack growth occurs from left to right in all images, as shown by the dashed white arrow.

4.4.2.4. Over-aged condition

The da/dt versus K_I relationships measured for the OA condition tested in dry N_2 (RH <5%) and in 0.6 M NaCl at applied potentials of -1100 and -1200 mV_{SCE} are shown in Figure 36. The dashed line represents a linear fit to the false crack growth rates measured during inert environment testing in dry N_2 , which is defined by the following relationship: $\log[da/dt_{FALSE} \text{ (mm/s)}] = -7.6189 + 0.0248K_I$. Regarding the OA dry N_2 data, shorting of the dcPD system (speculatively attributed to crack wake roughness from the aforementioned IG/TG precrack fracture morphology) resulted in poor dcPD measurement quality up until a $K \approx 30 \text{ MPa}\sqrt{\text{m}}$, where the expected linear increase in $\log(da/dt)$ was observed with increasing K_I (Figure 36). As such, data for $K < 30 \text{ MPa}\sqrt{\text{m}}$ were excluded and the linear fit was completed from $K_I = 30$ to $50 \text{ MPa}\sqrt{\text{m}}$. The validity of this modified approach can be assessed by comparing the OA linear fit with the resolution limits from the UA and PA heat treatments. Specifically, given the similarities in yield strength between the UA, PA, and OA conditions (Table 9), the resolution limit (which is nominally dependent on the applied K and yield strength; discussed in Section 3.4.1.) determined for the OA heat treatment should be similar to those determined for the UA and PA heat treatments. A qualitative comparison of the resolution limits for the UA, PA, and OA data sets (Figure 32, Figure 34, and Figure 36, respectively) suggests that the OA resolution limit is reasonably well-aligned with those from the PA and UA results, indicating that the exclusion of data below $30 \text{ MPa}\sqrt{\text{m}}$ did not induce systematic artifacts in the fit. Second, considering the OA experiments in 0.6 M NaCl, the crack growth rates measured at an applied potential of -1100 mV_{SCE} are nominally identical to the resolution limit determined from inert environment testing, indicating an absence of HEAC at -1100 mV_{SCE} for the OA condition up to a $K_I \approx 37 \text{ MPa}\sqrt{\text{m}}$, where testing was ended. Conversely, the kinetics for OA -1200 mV_{SCE} are consistently faster than the resolution limit, suggesting the onset of HEAC. Based on these observations, K_{TH} and $da/dt_{K=45}$ of $14 \text{ MPa}\sqrt{\text{m}}$ and $7.6 \times 10^{-7} \text{ mm/s}$ were measured for OA -1200 mV_{SCE}, while K_{TH} and $da/dt_{K=45}$ were not reported for OA -1100 mV_{SCE}.

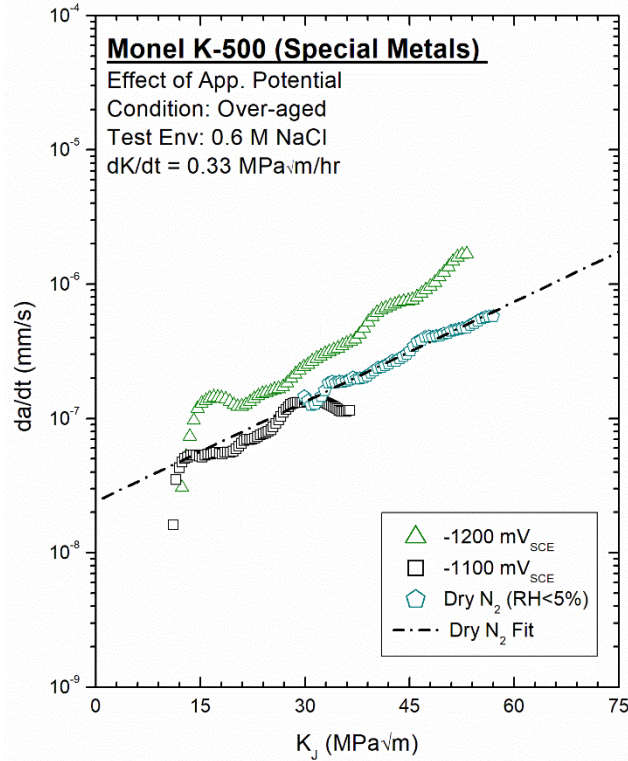


Figure 36 – Crack growth rate versus total K for specimens heat-treated to the over-aged condition tested under slow-rising K in dry N_2 ($RH < 5\%$) and in 0.6 M NaCl at -1100 and -1200 mV_{SCE} using a constant $dK/dt = 0.33 \text{ MPa}\sqrt{m}/\text{hr}$. The dashed line corresponds to the linear fit of the $\log(da/dt)$ vs. K_J data measured during dry N_2 testing.

Fractographs of the OA specimens tested in 0.6 M NaCl at -1100 and -1200 mV_{SCE} are presented in Figure 37. As demonstrated by Figure 37a, the OA -1200 mV_{SCE} specimen exhibited a mixed IG/TG fracture morphology in the precrack region (noted as PC), which transitioned to a predominantly IG with intermixed TG morphology in the HEAC region (shown at a higher magnification in Figure 37d), followed by a return to the mixed IG/TG morphology in the post-test fatigue region (noted as PTF). Conversely, the fractography of OA -1100 mV_{SCE} shown in Figure 37b confirms an absence of HEAC up to a $K_J \approx 37 \text{ MPa}\sqrt{m}$. First, examination of the overview micrograph presented in Figure 37b does not include any characteristics of HEAC, but instead shows evidence of ductile damage (noted by the white arrows in Figure 37b). As was the case for the PA -1000 mV_{SCE} experiment, an unexpected power outage ended the OA -1100 mV_{SCE} experiment at a $K_J \approx 37 \text{ MPa}\sqrt{m}$ and is likely responsible for the apparent ductile damage. Second, this global observation is corroborated by higher magnification microscopy, shown in Figure 37c. Specifically, as noted by the white arrows in Figure 37c, fractographic features consistent with crack-tip blunting were observed at a distance similar to the targeted precrack depth ($\sim 250\text{-}300 \mu\text{m}$). As such, based on the similarities in crack growth kinetics between OA -1100 mV_{SCE} and the resolution limit, along with the lack of fracture features consistent with HEAC, it is concluded that the OA condition is not susceptible to HEAC for applied potentials more positive than -1100 mV_{SCE} (up to a $K_J \approx 37 \text{ MPa}\sqrt{m}$).

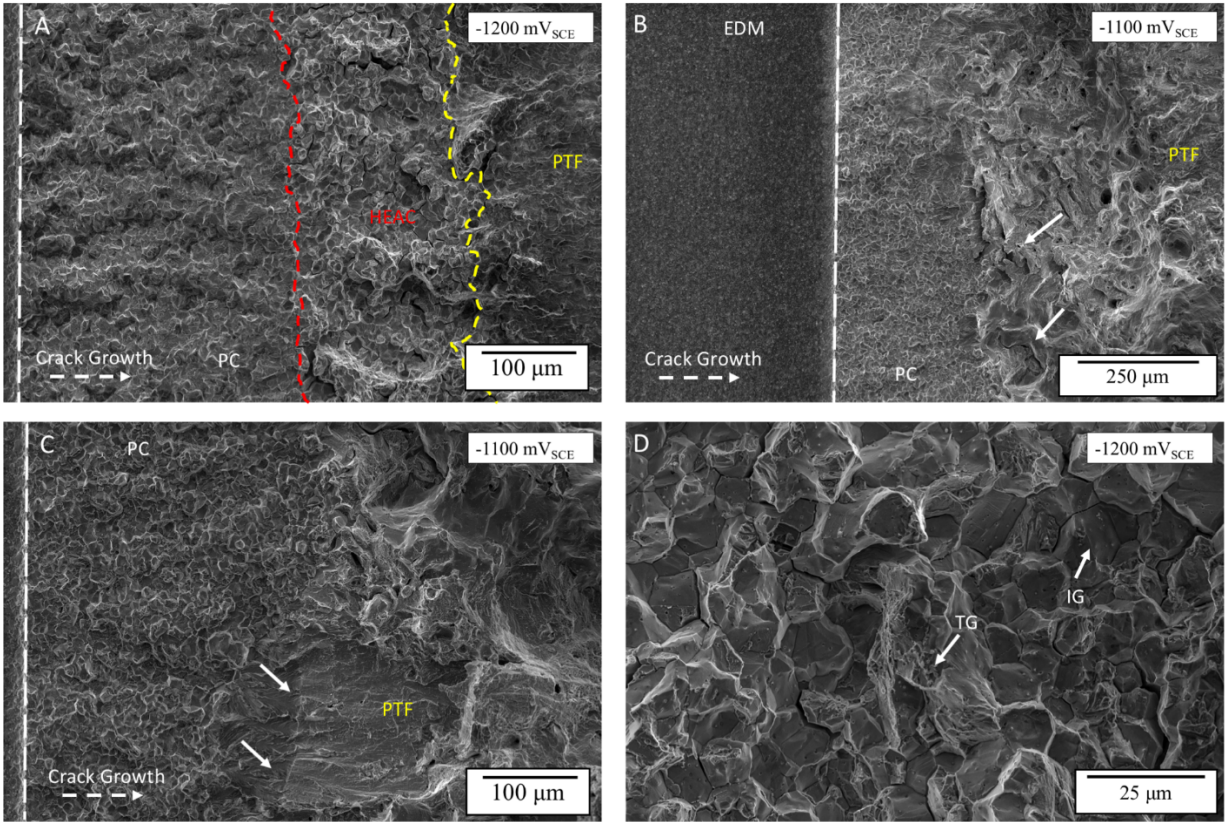


Figure 37 – Overview micrographs of the fracture morphologies observed in over-aged specimens tested at (a) -1200, (b) -1100 mV_{SCE} in 0.6 M NaCl. The white dashed line in (a-c) denotes the location of the EDM notch, while the red and yellow dashed lines in (a) indicates the transition from the fatigue precrack (PC) to HEAC and HEAC to post-test fatigue (PTF), respectively. Ductile damage induced during an unexpected power outage is noted by the white arrows in (b). A higher magnification micrograph of the -1100 mV_{SCE} is shown in (c), with the white arrows noting a fractographic feature consistent with crack-tip blunting, while (d) shows a representative high magnification micrograph of the fracture morphology in the HEAC region for OA -1200 mV_{SCE}. Crack growth occurs from left to right in all images, as shown by the dashed white arrow.

4.5. Discussion

The presented crack growth kinetics (Figure 30, Figure 32, Figure 34, and Figure 36) and fractography (Figure 31, Figure 33, Figure 35, and Figure 37) demonstrates that significant variations in HEAC susceptibility exist amongst the tested heat treatments, with susceptibility ranked (from highest to least) as follows: UA > PA > OA > NA. This ranking of susceptibility is based on (1) the measured HEAC kinetics (K_{TH} and $da/dt_{K=45}$, which are summarized in Figure 38a-b as a function of applied potential) and (2) the immunity potential at which HEAC no longer occurs. Given that all testing was conducted using a single material heat, it is likely the observed differences in HEAC susceptibility are attributable to metallurgical parameters that are sensitivity to heat treatment, which include: (1) grain size, (2) grain boundary character, (3) grain boundary impurity concentration, (4) yield strength/strain hardening, and (5) γ' precipitate morphology. In the following discussion, each of these metallurgical variables is

systematically characterized as a function of aging time at 923 K to determine the expected variation across the tested heat treatment conditions. These measured variations in metallurgy are then evaluated in the context of the measured HEAC susceptibility, thereby allowing for the relative influence of each variable on HEAC in Monel K-500 to be established.

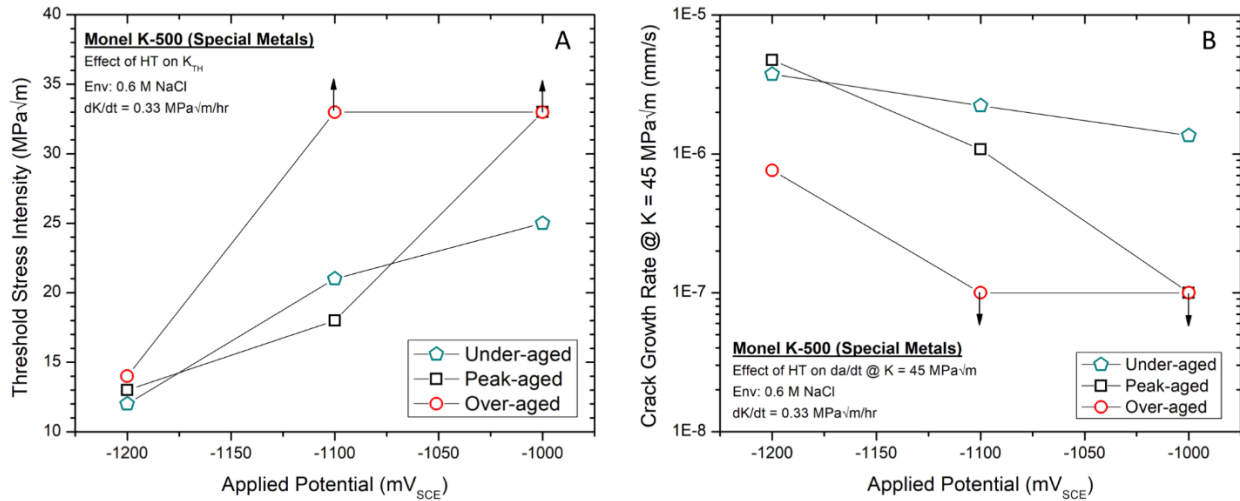


Figure 38 – The measured variation in (a) K_{TH} and (b) $da/dt_{K=45}$ as a function of applied potential for the under-aged, peak-aged, and over-aged heat treatments. Non-aged is excluded due to a lack of HEAC susceptibility across all tested potentials. Arrows point either upward (a) or downward (b) indicates that HEAC was not observed at the respective applied potential.

4.5.1. Grain size and grain boundary character

4.5.1.1. Grain size

As each heat treatment protocol began with the same 1-hour solution anneal at 1223 K, followed by an immediate water quench, any difference in grain size amongst the tested heat treatment conditions would have to arise during the age hardening step at 923 K. While grain growth data as a function of time at 923 K are not available in the literature for Monel K-500, a comparison with pure nickel suggests that appreciable grain growth should not be expected for this temperature. Recall that grain growth kinetics are dependent on both temperature and time [20], as described by Eqn 4.1⁵:

$$D^2 - D_0^2 = Kt = K_0 t * \exp\left(-\frac{Q}{RT}\right) \quad (4.1)$$

⁵ It is acknowledged that multiple forms of the grain growth kinetics have been proposed, such as the common power law description where $D = (Kt)^n$, due to improved fitting with non-pure materials [20]. However, the current form is chosen based on (1) the example data are from a “high-purity” material, which is well-described by Eqn 4.1 and (2) the effect of solute elements and secondary phases will be directionally consistent regardless of the grain growth kinetics equation employed, as shown in for pure vs. impure Ni in [55].

Where D and D_0 are the final and initial grain sizes (in μm), K_0 is a constant (in $\mu\text{m/s}$), t is time (in seconds), Q is the activation energy for grain boundary migration (in J/mol), R is the ideal gas constant (in $\text{J/mol}\cdot\text{K}$), and T is the temperature (in K). Fitting this equation to data published for 99.9945% nickel by Rothova and coworkers [21] yields $K_0 = 1.805 \times 10^9 \mu\text{m/s}$ and $Q = 223 \text{ kJ/mol}$. Assuming these parameters and an initial grain size of $10 \mu\text{m}$, the calculated grain size from Eqn 4.1 after 50 hours at 923 K is $\sim 13 \mu\text{m}$. It is well known that solute atoms, secondary phases, and variations in grain boundary character can all strongly affect grain boundary mobility [20]. As such, given the presence of extensive solute additions ($\sim 30\% \text{ Cu}$) and the formation of strengthening precipitates, it is expected that the Q parameter in Eqn 4.1 for Monel K-500 will be increased relative to the cited pure Ni data. As a comparison, the same authors investigated grain growth in less pure (99.5%) Ni, which yielded $Q \approx 280 \text{ kJ/mol}$. If K is held constant from the pure Ni calculation (it would likely also decrease, but is held constant to assess the most aggressive scenario; *i.e.* fastest grain growth), the predicted grain growth is decreased to on the order of 1-2 nm for 50 hours at 923 K .

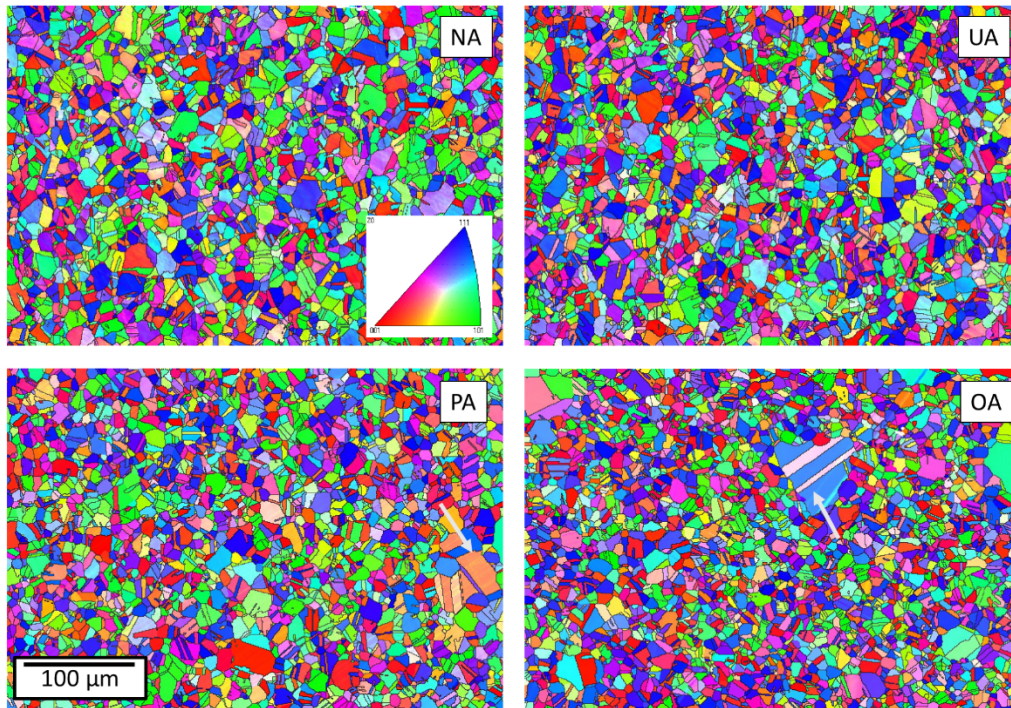


Figure 39 – OIM maps for the non-aged, under-aged, peak-aged, and over-aged conditions. The white arrows indicate examples of grains in the peak-aged and over-aged condition which have undergone abnormal grain growth.

Representative OIM maps from each heat treatment are presented in Figure 39, with the average and standard deviation (denoted by error bars) of the grain size measured from ~ 1000 grains for each heat treatment shown in Figure 40. First, as demonstrated by Figure 40, the average grain size is effectively invariant across the tested heat treatments, with any observed differences being well with the reported

standard deviation, in agreement with preceding analysis using Ni. Second, as shown in Figure 39, some evidence for abnormal grain growth (AGG), where isolated grains will rapidly grow relative to the average grain [22], was noted in the PA and OA conditions (examples highlighted by the white arrows). Such AGG is commonly observed in Ni alloys, particularly between homologous temperatures (T/T_m ; where T_m is the melting temperature) between 0.45 and 0.95 [22], and can deleteriously affect mechanical properties. Given that the aging temperature (923 K) is within the susceptible range for Ni (and therefore Monel K-500), limited AGG should be expected during age hardening in the current study. Considering the influence on mechanical properties, studies have primarily focused on the effect of AGG on fatigue behavior (with emphasis on turbine blade alloys [23]), with reports suggesting that the presence of such grains lowered fatigue life. However, it should be noted that the fraction of grains exhibiting AGG was much higher in this study, with the grain size being reported as a bimodal distribution [23], while the current study exhibited AGG in <0.5% of grains for the OA condition. Moreover, if considered in the context of the measured HEAC susceptibility, the PA and OA conditions were found to be less susceptible to HEAC than the UA condition, which did not exhibit AGG, thereby suggesting that any effects from AGG on the measured HEAC susceptibility are likely negligible. ***In conclusion, based on the likelihood of minimal variation in grain size across the tested heat treatments, which was confirmed via the evaluation of ~1000 grains per heat treatment, it is unlikely that grain size is responsible for the observed variation in HEAC susceptibility.***

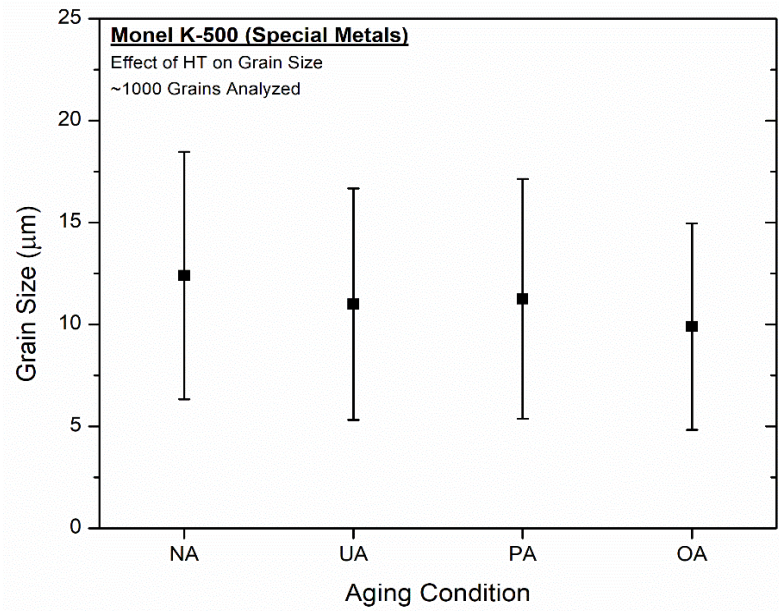


Figure 40 – Measured average and standard deviation (noted by error bars) in grain size for the non-aged, under-aged, peak-aged, and over-aged conditions, calculated from ~1000 grains in OIM maps collected using EBSD.

4.5.1.2. Grain boundary character

Differences in grain boundary character in Ni and Ni-base alloys can arise through variations in applied heat treatment, though these changes are generally induced via coupled thermo-mechanical processing [24]. Such processes are typically composed of incremental mechanical deformation (*e.g.* rolling) to modest cold work levels, immediately followed by thermal annealing, with the deformation-annealing sequence often repeated until the desired properties are achieved. For example, Bechtel et al. performed three cycles of cold rolling (~5% reduction in thickness) and a 15 minute anneal at 1173 K to increase the length fraction of coincident site lattice (CSL) boundaries to 75% in commercially-pure nickel [25]. Considering the current study, (1) mechanical deformation was not employed during heat treatment and (2) the only variation in heat treatment was the time at the age hardening temperature. As such, given the lack of applied mechanical deformation, it is unlikely that appreciable variations in grain boundary character will exist amongst the tested heat treatment conditions.

To confirm the absence of grain boundary character variation, two metrics were evaluated as a function of heat treatment using data generated from multiple OIM maps (examples shown in Figure 39). First, Figure 41 presents the cumulative distribution of grain boundary fraction as a function of grain boundary misorientation angle, based on the evaluation of ~10000 grain boundaries. Second, the length fractions of two CSL boundary types ($\Sigma 3$ and $\Sigma 9$, since these boundary types represented >99% of the CSL length fraction) as a function of heat treatment are shown in Figure 42, based on an analysis of ~42.5 mm of grain boundary length per heat treatment. Examination of both figures reveals striking similarities between the tested heat treatments, with the distribution as a function of grain boundary misorientation angle, the length fraction of $\Sigma 3$ boundaries, and the length fraction of $\Sigma 9$ boundaries all being effectively invariant with heat treatment. ***As such, given the lack of difference in grain boundary character metrics amongst the tested heat treatments, as well the statistical improbability of a disrupted susceptible path, it is concluded that variations in grain boundary character cannot explain the observed differences in HEAC susceptibility.*** Of note is that this finding is consistent with the expectations from percolation theory, which requires a minimum non-susceptible boundary fraction (*i.e.* CSL and boundaries with misorientations <15°) of ~0.65 (for a 2-D analysis as presented herein) to ensure disruption of the susceptible path (*i.e.* high angle grain boundaries) [26]. As the length fraction of these non-susceptible boundaries is ~0.5 for each condition, the probability that the susceptible pathway was disrupted in any of the heat treatments is effectively zero, further suggesting that grain boundary character will not govern HEAC susceptibility in the current study.

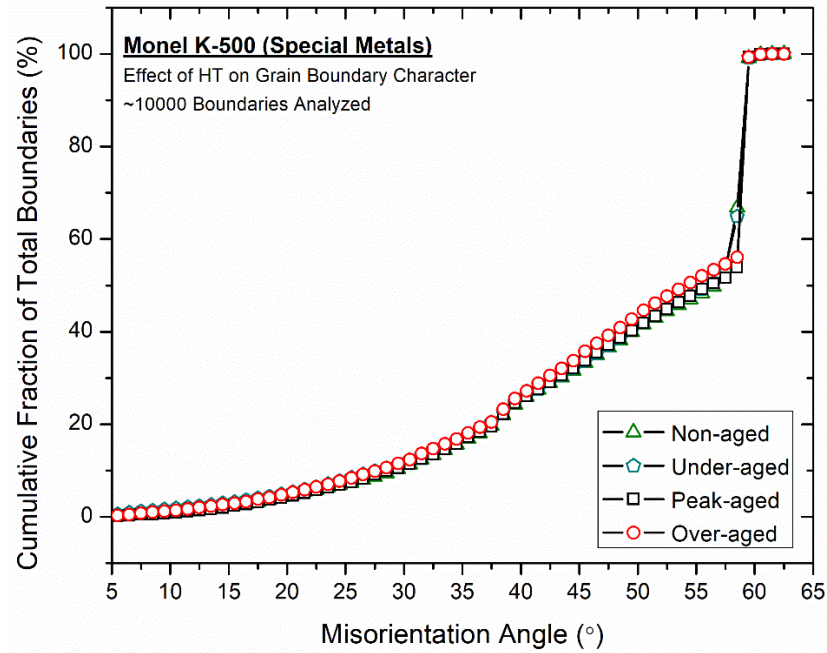


Figure 41 – Cumulative distribution of grain boundary fraction as a function of grain boundary misorientation angle based on the evaluation of ~10,000 grain boundaries from OIM maps collected using EBSD.

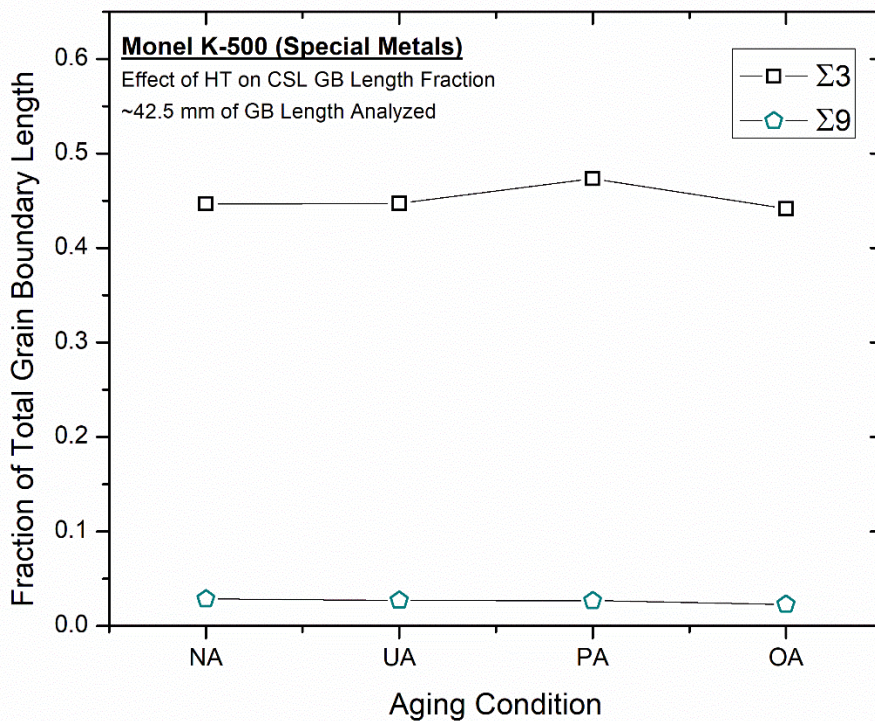


Figure 42 – Length fraction of $\Sigma 3$ and $\Sigma 9$ CSL boundaries as a function of heat treatment. Data is calculated from the observation of ~42.5 mm of grain boundary length from OIM maps collected using EBSD.

4.5.2. Grain boundary impurity segregation

The deleterious effect of sulfur in Ni-based alloys and its dependence on applied heat treatment is well-documented in the literature [27–32]. Mechanistically, this increase in grain boundary sulfur is argued to affect HEAC susceptibility by (1) degrading the intrinsic grain boundary toughness [32–34], resulting in a lowered resistance to intergranular decohesion for a constant grain boundary hydrogen concentration, and/or (2) increase the activity of hydrogen, thereby enhancing the embrittling potency of a given hydrogen concentration [35]. In addition to deleterious elements, some trace elements have been argued to increase the cohesive strength of grain boundaries. For example, the addition of boron was shown to improve the resistance to intergranular fracture in both Ni [30] and Ni₃Al [36]. Considering the current study, it is expected that the OA condition would exhibit the highest grain boundary impurity content (both beneficial and deleterious) due to having the longest exposure to elevated temperatures. For example, Mulford demonstrated that for a Ni-10Cu alloy: (1) sulfur readily diffuses to the grain boundary at 923 K and (2) the grain boundary sulfur concentration after 50 hours at 923 K is approximately double the concentration after 5 hours [29]. Preliminary Auger electron spectroscopy (AES) shown in Figure 43 confirm this systematic enhancement in grain boundary sulfur concentration with increased aging time for the tested heat treatment conditions, with the exception of an increased sulfur concentration in the non-aged condition. This unexpected behavior is likely due to the limited number of grain boundary facets examined, which motivates additional AES experiments to ensure the statistical accuracy of the present results.

Based on the data presented in Figure 43, which is consistent with the previous work of Mulford [29], it is reasonable to suggest that the OA condition contains the highest average grain boundary sulfur concentration. As such, if grain boundary sulfur were to dominate HEAC susceptibility, then susceptibility should increase with longer aging times. However, this paradigm is directionally inconsistent with the fracture mechanics testing results presented in Figure 38, which indicates that HEAC susceptibility decreases with increasing aging time. As such, given the robust literature database surrounding the effects of sulfur in nickel alloys [27–32], grain boundary sulfur content may contribute to HEAC susceptibility via reductions in cohesive strength [33] and/or synergistic interactions with hydrogen [35], but the current results suggest that this contribution is not controlling the variation in HEAC susceptibility with heat-treatment in Monel K-500. The dominance of other proposed deleterious impurity elements such as Sn, Sb, or Pb [27,32] can also be rejected based on similar arguments. Considering the effect of boron, quantitative assessment was precluded by the inability to detect boron on the grain boundary facets in all four heat treatments. However, given that the grain boundary boron concentrations increase from NA to OA, the reduced HEAC susceptibility of the NA heat treatment relative to the OA condition suggests that boron content does not dominate the HEAC susceptibility in Monel K-500. *In conclusion, based on the*

characterization of the local grain boundary concentrations via AES, it is unlikely that the observed variations in HEAC susceptibility can be explained by differences in grain boundary impurity concentration.

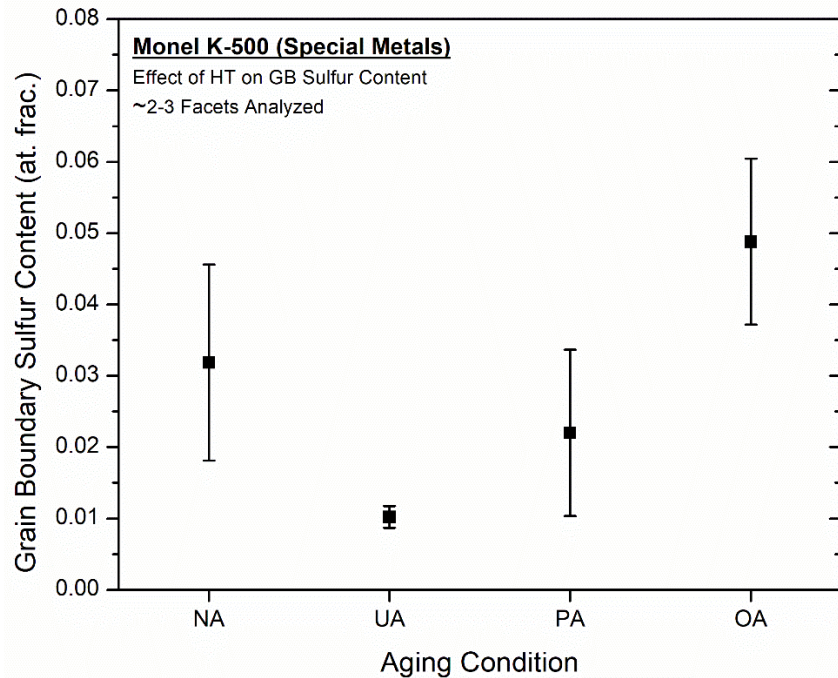


Figure 43 – Measured average and standard deviation (noted by error bars) of the maximum sulfur concentration measured via Auger electron spectroscopy on 2-3 intergranular facets as a function of heat treatment.

4.5.3. Yield strength and strain hardening

As discussed in Chapter 3, the physical basis of the HEAC dependence on yield strength lies in higher yield strengths enabling the development of increased hydrostatic stresses in the crack tip region, which then facilitates the development of larger local hydrogen concentrations since the hydrogen concentration is exponentially dependent on the hydrostatic stress (as shown in Eqn 3.1). However, the current study underscores the limitations of this design criteria, as despite having only ~36 MPa difference in yield strength (Table 9), the UA heat treatment exhibits significantly increased HEAC susceptibility relative to the OA condition (Figure 38). In addition to yield strength, variations in strain hardening can have strong effects on crack tip stresses [37,38]; examination of Table 9 demonstrates that significant differences in strain hardening exponent (n) exist amongst the tested heat treatments (ranging from $n = 6.5$ for NA to $n = 19.6$ for OA). As such, it is useful to utilize the closed-form Hutchinson-Rice-Rosengren (HRR) plane strain solutions to assess possible differences in crack tip stresses, thereby informing whether the noted differences in hardening behavior can explain the observed variations in HEAC susceptibility.

The hydrostatic stress field for $K = 25 \text{ MPa}\sqrt{\text{m}}$ as a function of distance from the crack at $\theta = 0^\circ$ (directly in front of the crack tip) was calculated for each heat treatment using the mechanical properties listed in Table 9 and the equations introduced in Section 3.5.2.4. (Eqn. 3.7-3.9), with the results of these calculations plotted in Figure 44. Several important observations can be made from these data. First, the NA heat treatment clearly exhibits the lowest hydrostatic stress, which may explain its reduced HEAC susceptibility relative to the age-hardened conditions. Second, ranking of the UA, PA, and OA hydrostatic stress at a distance of $1 \text{ }\mu\text{m}$ from the crack tip confirms the important role of strain hardening on the crack tip stress field⁶. Specifically, though the PA condition has only a 36 MPa higher yield strength than the OA heat treatment, the difference in hardening exponent (Table 9; PA: 13.6, OA: 19.6) results in a $\sim 300 \text{ MPa}$ difference in hydrostatic stress. Similarly, the UA condition exhibits an $\sim 100 \text{ MPa}$ increase in hydrostatic stress proximate to the crack tip relative to the OA heat treatment, despite having a 36 MPa *lower* yield strength.

Comparing these results to the measured HEAC susceptibility metrics in Figure 38 indicates that differences in the crack tip hydrostatic stress field induced by variations in yield strength and strain hardening exponent somewhat correlate with the observed variations in HEAC susceptibility. Specifically, the relative ordering of HEAC susceptibility (UA > PA > OA > NA) is directionally consistent with the crack tip stress calculations (PA > UA > OA > NA). However, this calculation does not explain the increased susceptibility of the UA heat treatment relative to the PA condition, as the hydrostatic stress is $\sim 200 \text{ MPa}$ higher for PA at a distance of $1 \text{ }\mu\text{m}$ from the crack tip. It is possible (though not explicitly assessed in the current work; see Section 4.7) that the hydrostatic stress of the UA condition may surpass the PA heat treatment at distance $< 1 \text{ }\mu\text{m}$ from the crack tip, as may be predicted from strain gradient plasticity (SGP) theories [39,40]. Speculatively, if a similar length scale parameter were applicable for the PA and UA heat treatments condition, which may be justified given that the same length parameter ($l = 5 \text{ }\mu\text{m}$) generated for pure Ni was previously utilized for SGP calculations on Monel K-500 [41], then the SGP calculations may predict the same general trends as the HRR calculations. ***As such, while differences in strain hardening and yield strength likely contribute to the observed variations in HEAC susceptibility, this contribution does not fully explain all observed HEAC behavior, suggesting other factors are governing.***

⁶ For the HRR solution, lower strain hardening exponents (n) result in elevated crack tip stresses.

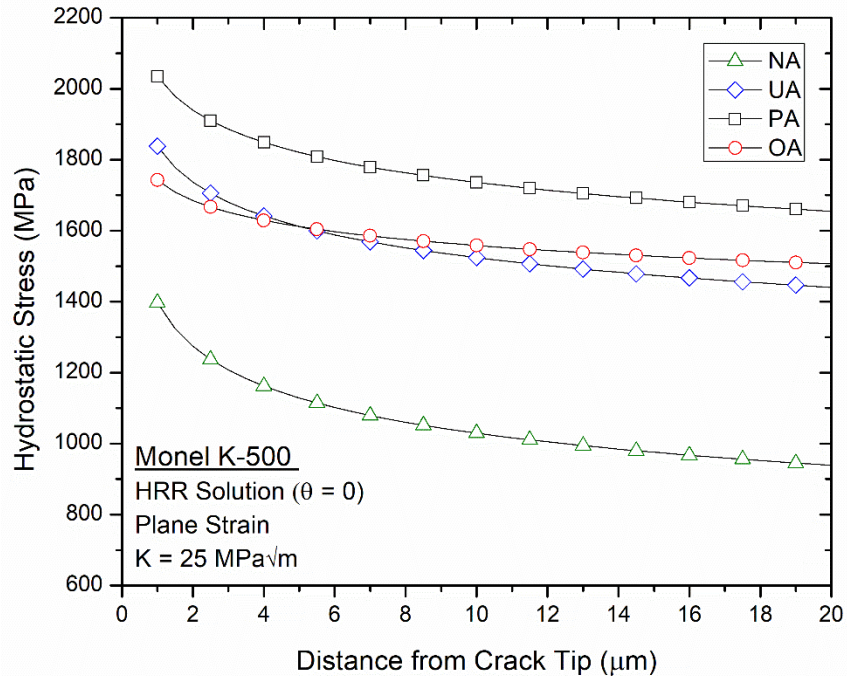


Figure 44 – Variation in hydrostatic stress with distance from the crack tip for the tested heat treatments calculated using the HRR solutions assuming plane strain conditions.

4.5.4. Precipitate morphology

Based on the work of Dey et al. [6,7], homogeneously distributed and highly coherent (<0.1% misfit strain) γ' (Ni_3Al) precipitates are expected to nucleate and then coarsen with increased aging time in Monel K-500. Due to this low misfit strain, the precipitates form as spherical particles; this morphology and low misfit strain are reported to persist even after prolonged aging [7]. In agreement with the prior work of Dey [7], the γ' size was found to appreciably increased across the tested heat treatment conditions, as shown by the γ' size distributions for the three age-hardened conditions presented in Figure 45a and the representative micrographs of the γ' precipitate morphology for the UA, PA, and OA conditions in Figure 45b-d, respectively. The average and standard deviation of the precipitate radius from the measurements in Figure 45a are shown in Table 10. Considering the NA condition, examination of multiple regions across several TEM specimens failed to identify any evidence of γ' (either from imaging contrast or superlattice reflections in diffraction mode), indicating that the immediate water quench was sufficient to prevent γ' precipitation after solution treatment at 1223 K. As such, γ' radius and misfit data for the NA heat treatment are not reported in Table 10.

The γ' misfit parameter (δ) can be calculated from diffraction patterns utilizing the following equation [7]:

$$\delta = \frac{2(a' - a)}{a' + a} \quad (4.2)$$

where a' and a are the lattice parameters measured for γ' precipitate and γ matrix, respectively. Based on the average of 10 measurements for the $(01\bar{1})$ reflection for the γ' precipitate and $(02\bar{2})$ reflection for the γ matrix in the OA condition, the lattice parameter was estimated as 0.3525 nm and 0.3522 nm for γ' and γ , respectively. Based on these values, δ is calculated as 0.00091, which is in good agreement with the 0.0056 observed by Dey et al. [7] (for comparison, the misfit parameter for TiC in Monel K-500 is 0.194), thereby demonstrating that the γ' precipitates remain highly coherent with the γ matrix, even after 50 hours of aging.

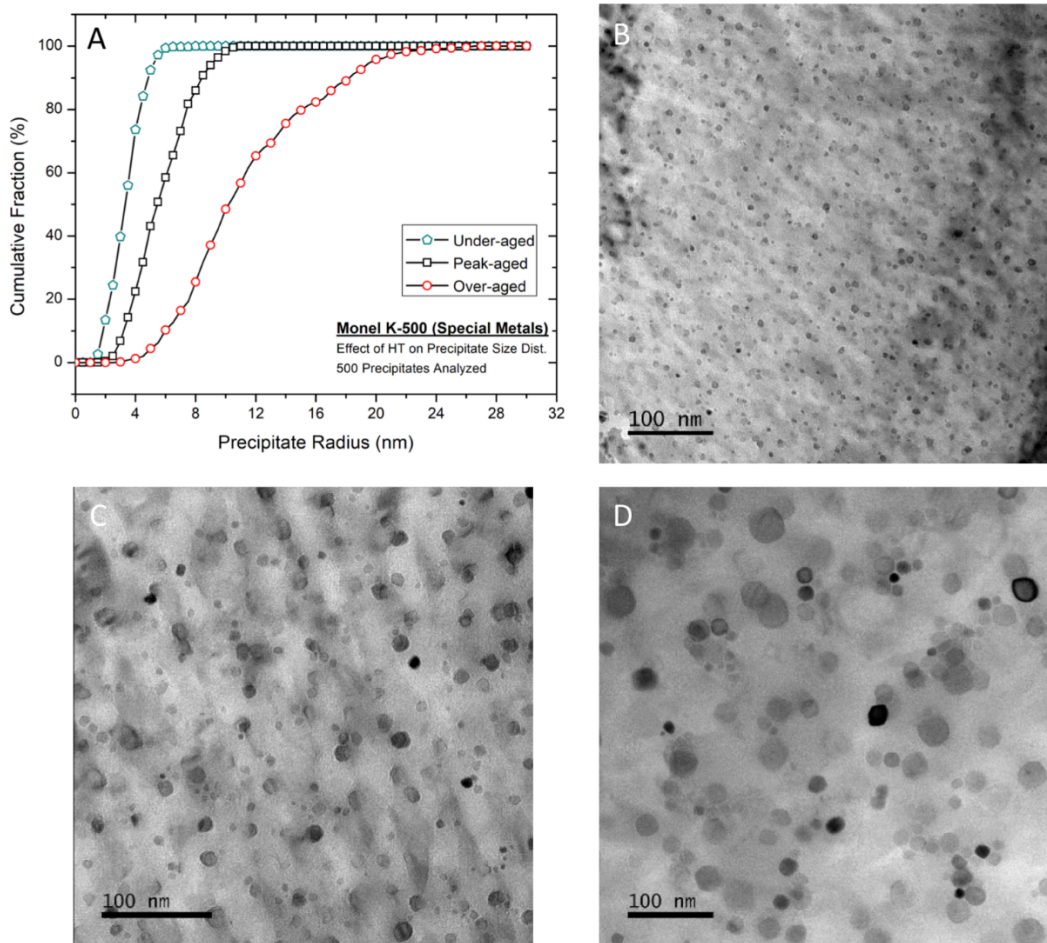


Figure 45 – (a) Plot of the γ' size distribution for each age-hardened heat treatment, based on the measurement of 500 precipitates, and representative micrographs of the γ' precipitate morphology for the (b) under-aged, (c) peak-aged, and (d) over-aged heat treatments.

Table 10 – Precipitate morphology characteristics as a function of heat treatment condition

Aging Condition	Average Radius (nm)	Std. Dev. (nm)
Non-aged	–	–
Under-aged	3.34	1.10
Peak-aged	5.67	1.95
Over-aged	11.22	4.55

4.5.4.1. Hydrogen trapping

Variations in precipitate morphology may influence HEAC susceptibility in Monel K-500 by affecting two parameters: (1) hydrogen trapping at the γ/γ' interface and (2) bulk slip morphology. Considering the former, improvements in the efficacy of hydrogen trapping have been previously argued to reduce the hydrogen available to participate in the fracture process [42]. However, this possibility is limited to closed systems, in which a finite hydrogen concentration is present. In the current work, which can be considered an open system, traps can be readily saturated as the hydrogen supply is effectively infinite. As such, the primary effect of variations in hydrogen trapping at the γ/γ' interface is not to reduce the amount of hydrogen available to participate in fracture processes, but to influence the rate at which hydrogen accumulates in the fracture process zone (*e.g.* the effective diffusivity).

Based on the work of Scully and coworkers [4,43], the γ/γ' interface is regarded as the predominant trap site in aged Monel K-500. Speculatively, variations in precipitate morphology could affect the trapping behavior at the γ/γ' interface by either (1) increasing the trap binding energy, as may occur if the interface coherency were reduced, and/or (2) increasing the trap density as precipitates grow. Regarding the trap binding energy, the misfit parameter calculated for the OA condition (0.00091) suggests that the γ' precipitates remain highly coherent with the matrix across the four tested heat treatments. As such, minimal variation in the trap binding energy for the γ/γ' interface should be expected for the conditions tested in the current study. This conjecture is supported by the work of Scully and coworkers [4,43], who observed that the γ' trap binding energy in aged Monel K-500 exhibited limited variability across numerous material heats and thermomechanical processing strategies ($\sim 12 \pm 5$ kJ/mol). Comparison of the reported hydrogen diffusivity (D_H ; which is inherently dependent on trapping [43]) for solution-treated Monel K-500 and various aged Monel K-500 conditions provides further support for a minimal variation in trap binding energy with heat treatment. Specifically, based on the applied technique, the D_H for the solution-treated condition was measured as $1.3\text{-}3.9 \times 10^{-14}$ m²/s, while various iterations of aged Monel K-500 exhibited D_H of $0.9\text{-}3.3 \times 10^{-14}$ m²/s [43]. The similar spread in measured D_H between the solution-treated and various aged conditions of Monel K-500 indicates (1) any effect from heat treatment is arguably within the spread of the

applied measurement techniques and (2) the γ' trap site is relatively weak, consistent with the low measured trap binding energy.

Considering the possibility of an enhanced trap density with increased aging time, Dey et al. noted that the volume fraction of γ' saturates after 2 hours during aging at 923 K [7], which suggests that the γ' volume fraction between the PA and OA heat treatments in the current study should be equivalent (~6-7 vol. % [7]). However, upon saturation of the precipitate volume fraction, the onset of Ostwald ripening (*i.e.* the growth of larger particles at the expense of smaller particles to reduce excess surface energy) will cause a reduction in the γ' interfacial area with additional aging time. Given that the γ/γ' interface is the primary trap site for Monel K-500 [43], the trap density should then *decrease* with aging time beyond 2 hours due to the reduction in interfacial area from particle coarsening effects [44], suggesting that the PA condition would have a higher trap density than the OA heat treatment. ***As such, the reported lack of appreciable variation in γ' trap binding energy with heat treatment, in addition to the reported similar values of effective diffusivity across different heat treatments, suggests that variations in hydrogen trapping induced by changes in precipitation morphology do not govern the observed HEAC behavior.***

4.5.4.2. Bulk slip morphology

It is well-established that the interaction between dislocations and strengthening precipitates changes as the precipitate size increases, with dislocation cutting mechanisms at small precipitates (*e.g.* shearing of particles) transitioning to bypass mechanisms at large precipitates (*e.g.* Orowan looping) [44]. These changes in dislocation-precipitate interactions strongly impact the mechanical properties of precipitation-hardened alloys, such as Monel K-500. For example, modifications in dislocation-precipitate interactions can readily explain the observed yield strength dependence on aging time shown in Figure 1 [44]. First, at short aging times (*i.e.* under-aged), the nucleation and subsequent growth of the γ' precipitates cause an increase in yield strength as progressively larger stresses are required to shear through precipitates of increased size. Eventually, the size of the particle becomes sufficiently large that the shearing of precipitates is less energetically favorable than the dislocation bypassing the precipitate via cross-slip, climb, etc. This point at which the energetics of the cutting and bypassing mechanisms are equivalent represents the peak-aged condition. Continued growth of the precipitates, which occurs via Ostwald ripening processes (large precipitates grow at the expense of small precipitates), increases the average spacing between precipitates, reducing their effectiveness as obstacles to dislocation motion. Therefore, the yield strength begins to decrease with additional precipitate growth (*i.e.* over-aged condition), with the slope of this descent dependent on precipitate characteristics (distribution, size, modulus, etc.) [44].

In addition to influencing first-order properties like yield strength, changes in dislocation-precipitate interactions may also affect HEAC susceptibility. First, literature suggests that alloys containing

shearable precipitates generally exhibit planar slip (*i.e.* slip only occurs on a limited number of slip systems), while alloys with precipitates necessitating bypass mechanisms deform by wavy slip (*i.e.* where slip occurs on multiple slip systems) [44]. Other factors may influence the propensity for planar slip (e.g. low stacking fault energy, short range ordering, large grain size, etc.), but for precipitation-hardened alloys, it is reasonable to consider dislocation-precipitate interactions as the predominant contribution [44]. Mechanistically, the propensity for planar slip in alloys with shearable precipitates arises from the reduction in effective diameter of the strengthening particles along the cutting plane with each passing dislocation. This action results in a continuously reduced resistance to shearing for subsequent dislocations gliding on the cutting plane; additional strain is then preferentially accommodated by continued slip along these “softened” planes as opposed to the activation of new slip systems [44]. Such ‘strain localization’ has been shown to adversely affect mechanical properties. For example, Sanders and Starke demonstrated that increased strain localization degraded the fatigue performance of Al-Li alloys by decreasing the resistance to fatigue crack initiation and increasing crack propagation rates due to cracking along localized slip bands [45]. Critically, the authors also noted that the impingement of these localized slip bands on grain boundaries produced noticeable ‘offsets’ in the boundary. These offsets were suggested to act as local stress concentrations, which led the authors to conclude that such disruptions likely serve as crack initiation sites [45].

In the context of HEAC, the local stress concentrations induced by strain localization in planar slip alloys would likely serve a dual role of increasing both the local stress *and* hydrogen concentration (since hydrogen preferentially diffuses to regions of increased hydrostatic stress [46]). As hydrogen has been shown to degrade the grain boundary cohesive strength [47], such increases in hydrogen concentration local to the boundary would act to further reduce the resistance to crack initiation. Moreover, it has been argued that strain localization is exacerbated in the presence of hydrogen [48]; the deleterious effect of such localized deformation forms a critical component of the well-known hydrogen-enhanced localized plasticity mechanism for hydrogen embrittlement [49,50]. Therefore, hydrogen effects on deformation may result in more severe grain boundary disruptions [50], which would act to further amplify the local stress and hydrogen concentrations. This conjecture that alloys exhibiting strain localization are more susceptible to HEAC is consistent with the findings of Bernstein and Thompson [51], who broadly reviewed the literature to identify links between metallurgy and susceptibility to stress corrosion cracking (such as HEAC). Specifically, the authors observed a recurring link between propensity for planar slip and increased susceptibility to stress corrosion cracking across multiple alloy systems, including Ti, Al, and Ni-base alloys. While the mechanistic interpretation of this finding was limited, the systematic link of propensity for planar slip and increased cracking susceptibility across multiple material systems strongly suggests that bulk slip morphology is a critical metallurgical variable for HEAC susceptibility.

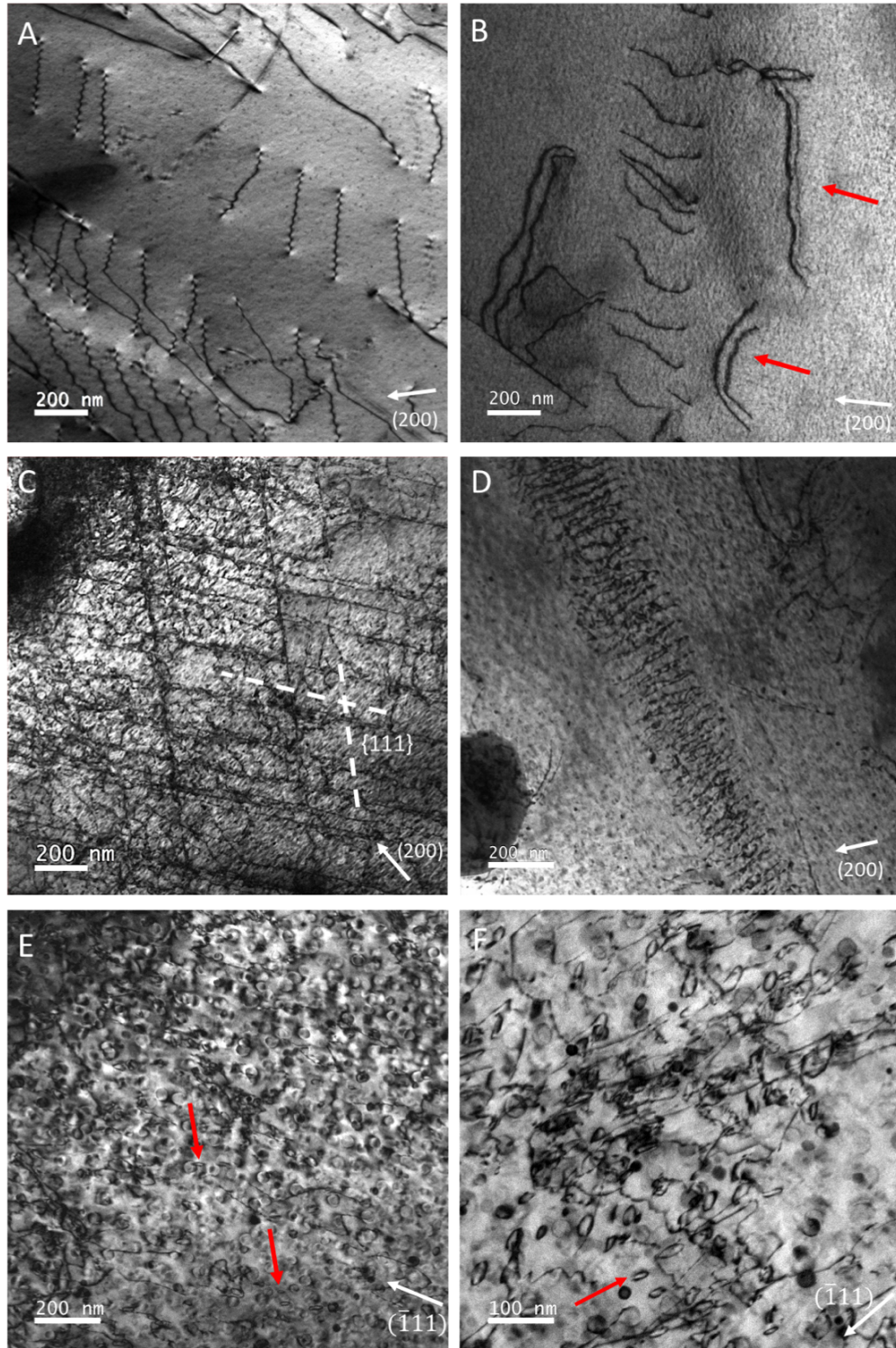


Figure 46 – Bright-field micrographs of representative bulk slip morphologies for the (a-b) under-aged, (c-d) peak-aged, and (e-f) over-aged heat treatments. The red arrows in (b) highlight two dislocation pairs, while the red arrows in (e-f) indicate evidence of looping. The diffraction vector associated with each condition is shown by the white arrows and the white dashed lines in (c) indicate the trace of the $\{111\}$ planes.

Considering the current study, a systematic evaluation of the dislocation patterning in the UA, PA, and OA conditions was conducted *via* transmission electron microscopy on foil specimens prepared from samples deformed to 2% total strain in compression. Two representative bright-field micrographs from each heat treatment, with the applicable diffraction condition noted by the white arrow, are shown in Figure 46. For the UA condition, planar arrays of dislocations were observed throughout the microstructure, with several examples shown in Figure 46a. Evidence of dislocation pairing was also observed, as indicated by the red arrows in Figure 46b. Note, the oscillating contrast in Figure 46a is not indicative of intense dislocation bending, but is instead a well-known absorption artifact for dislocations that are steeply tilted within the foil [52]. The PA heat treatment exhibited slip morphologies similar to the UA condition, with evidence of slip planarity based on the slip bands observed in Figure 46c and long planar arrays shown in Figure 46d. Analysis of the diffraction pattern for the image in Figure 46c (oriented proximate to the $\langle 110 \rangle$ zone axis) indicates that the observed bands aligned well with the trace of two $\{111\}$ planes, noted by the dashed white lines. Additionally, close examination of the planar array in Figure 46d reveals evidence of dislocation pairing within the array, as highlight by the red arrow. It should be noted that a limited number of dislocation loops were observed in the PA alloy (not shown), which is consistent with expectations for a material heat-treated to the PA condition (where a subset of precipitates is likely large enough to induce dislocation bypassing). However, the predominant slip morphologies observed in the PA heat treatment are consistent with planar slip. Finally, microscopy of the OA condition revealed widespread evidence of dislocation looping, with examples highlighted by the red arrows in Figure 46e-f. Close examination of the loops suggests that a subset have been “punched” out from the precipitate (a possible example is noted by the red arrow, Figure 46f), which would be strong evidence for the onset of cross-slip (and therefore, wavy slip).

These results align well with the findings of Dey et al. [6], who observed strong evidence of slip planarity and dislocation looping in Monel K-500 aged to similar conditions as the UA and OA heat treatments in the current study. Unfortunately, Dey et al. did not show micrographs for conditions similar to the PA heat treatment, other than stating that the planar arrays persisted for particle diameters beyond 10 nm (which is similar to PA condition; Table 10) [6]. Similar agreement was also observed between Dey et al.’s study and the current work when the dislocation patterning of the NA condition was evaluated via TEM. As shown by the representative micrograph in Figure 47, evidence of dislocation tangling (bottom left corner) and cross-slip suggests that the NA alloy is deforming via wavy slip. As discussed by Dey [6], this is consistent with stacking fault energy-based arguments, as the relatively high stacking fault energy of Ni is not significantly modified by the solute Cu addition. Considering these results in the context of the measured HEAC susceptibility (Figure 38), the UA and PA conditions, which exhibited the highest levels of HEAC susceptibility, both deform by planar slip, while the OA and NA conditions, which had reduced

HEAC susceptibility, exhibit wavy slip. *As such, in agreement with the generalizations made by Bernstein and Thompson, the current results indicate that HEAC susceptibility generally correlates with bulk slip morphology.*

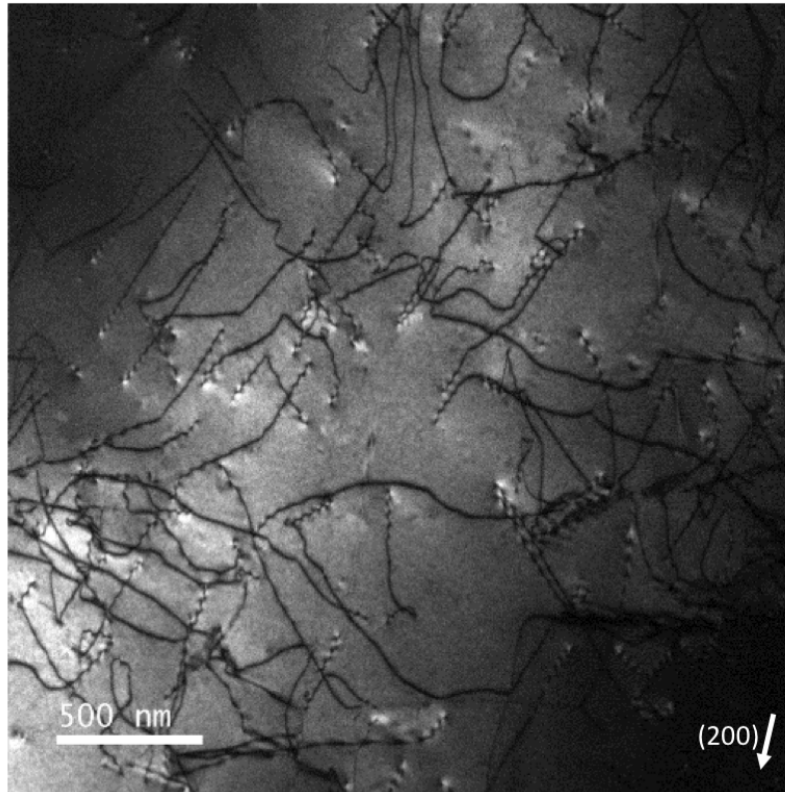


Figure 47 – Bright field micrograph of the bulk slip morphology in the non-aged condition, with the utilized diffraction vector indicated in lower right corner.

4.5.5. Summary and identified mechanistic knowledge gaps

In summary, the presented results suggest that the observed variation in HEAC susceptibility for different aging conditions of Monel K-500 correlates well with the propensity for slip localization. Other factors, such as grain boundary impurity concentration and hydrogen trapping, may still contribute to susceptibility, but the results herein indicate that such effects are likely complementary at best. The idea that planar slip increases HEAC susceptibility is supported by a broad literature database [51], but the extension of these experimental observations into mechanisms remains limited. In particular, it is unclear how these variations in bulk slip morphology (which were observed in the alloy bulk) influence deformation in the high-stress region proximate to a crack tip. Moreover, recent experiments suggest that hydrogen refines the dislocation substructure adjacent to the fracture surface [50], but the effect of variation in bulk slip morphology on this hydrogen-induced refinement is also unknown. In fact, the effect of hydrogen on dislocation processes in precipitation-hardened alloys as a function of heat treatment is largely unexplored,

thereby precluding even broad estimates of possible behavior. Given these clear knowledge gaps, the following two chapters present recent efforts to understand (1) the effect of hydrogen on bulk deformation processes in precipitation-hardened materials as a function of heat treatment and (2) how the conjoint action of bulk slip morphology and hydrogen may affect deformation processes local to the crack.

4.6. Conclusions

The HEAC susceptibility as function of heat treatment for a single heat of Monel K-500 isothermally aged to the non-aged, under-aged, peak-aged, and over-aged conditions was assessed *via* slow-rising stress intensity testing. The variations in possible heat treatment-sensitive metallurgical variables, including grain size, grain boundary character, grain boundary impurity concentration, yield strength, strain hardening, and precipitate morphology as a function of the applied heat treatments were then evaluated in the context of the measured HEAC susceptibility. This correlation revealed several critical insights into the effect of metallurgical variation on HEAC in Monel K-500:

4. Fracture mechanics testing revealed a strong variation in HEAC susceptibility amongst the tested heat treatments. Measurement of HEAC metrics (Figure 38) indicates that the under-aged heat treatment was the most susceptible to HEAC, followed by the PA condition, and then the OA condition. The NA heat treatment was found to be non-susceptible (over the K_I range tested) to HEAC, even at an applied potential of $-1200 \text{ mV}_{\text{SCE}}$.
5. The grain size and grain boundary character remained effectively constant across the evaluated heat treatment conditions, indicating that these parameters are not responsible for the observed differences in HEAC behavior.
6. An assessment of grain boundary impurity content as a function of heat treatment using Auger electron spectroscopy demonstrated that the impurity concentration increases with aging time. This observation was inconsistent with the measured HEAC susceptibility trends, as the OA condition was less susceptible than the UA and PA heat treatments, suggesting that grain boundary impurity concentration does not govern the observed HEAC behavior.
7. The influence of yield strength and strain hardening exponent was assessed by calculating the crack tip hydrostatic stress field for each heat treatment utilizing the plane strain Hutchinson-Rice-Rosengren solutions. Results correlated with the general trend in HEAC susceptibility, with the OA and NA heat treatments having reduced maximum hydrostatic stresses relative to the UA and PA conditions. However, these calculations did not capture the increased HEAC susceptibility of UA relative to the PA condition, suggesting that other factors govern HEAC susceptibility.
8. The variation in bulk slip morphology (*i.e.* wavy versus planar) as a function of heat treatment was evaluated via transmission electron microscopy. The NA and OA conditions were found to exhibit

features indicative of wavy slip, while the UA and PA heat treatments exhibited dislocation patterns consistent with planar slip. This characterization of planar slip alloys having increased HEAC susceptibility relative to wavy slip alloys is consistent with prior literature results, suggesting that bulk slip morphology strongly affects HEAC susceptibility.

4.7. Suggested Future Research Directions

Based on the work presented herein, several future research directions should be considered. First, as discussed in Section 4.5.3., it is possible that differences in crack tip stress field which modify the trends observed from the HRR solutions may arise closer to the crack tip if higher-order theories are employed. Towards this end, a finite element study utilizing strain gradient theories should be conducted to assess the crack tip stress field as a function of heat treatment for Monel K-500. Second, the observation that the OA condition exhibits reduced HEAC susceptibility relative to the UA and PA heat treatments suggests a possible pathway for modifying the QQ-N-286G standard [5] for Monel K-500 to improve HEAC resistance. However, before such a change can be implemented or even discussed, additional data are required to determine whether the observed behavior is limited to the current material heat (possibly due to the low observed yield strengths compared to the material heats tested in Chapter 3). In particular, it would be interesting to procure three different material heats of Monel K-500 and then perform the same heat treatment protocol and testing as completed herein. The test matrix should also be expanded to include additional ‘degrees’ of over-aging, such as specimens aged at 923 K for 10 and 25 hours, respectively, to determine whether the observed decrease in HEAC susceptibility persists closer to the peak-aged condition. Third, it would be interesting to rigorously assess the influence of grain boundary sulfur concentration by comparing the effect of heat treatment on a high-purity heat and a ‘high-sulfur’ (~50 ppm; which is still acceptable under the QQ-N-286G standard [5]) heat. In particular, a comparison of the high-purity UA, high-purity OA, high-sulfur UA, and high-sulfur OA would effectively determine whether or not sulfur provides a tangible contribution to heat-to-heat HEAC susceptibility variation in Monel K-500. Finally, considering the apparent importance of slip morphology, it is worthwhile to consider whether or not the Gerberich decohesion model [53] should be modified or in fact employed, given the assumed slip distribution in the derivation of the α'' and β' parameters. As was also suggested in Section 3.7, such findings could motivate the development/refinement of a stress-based micromechanical model for hydrogen-induced decohesion [54], which considers the synergistic interactions between mobile H-deformation interactions and the degradation of boundary cohesion by H present at the grain boundary (as was identified in Chapter 2).

4.8. Acknowledgements

Helpful discussions with Prof. Richard Gangloff, Prof. John Scully, and Prof. Sean Agnew, the assistance of Mr. Michael Ritzo and Mr. Adam Thompson in preparing TEM specimens, and the assistance of Mr. Denny Paul and Dr. John Hammond from Physical Electronics, USA with conducting the AES experiments are gratefully acknowledged.

4.9. References

- [1] R.P. Gangloff, H.M. Ha, J.T. Burns, J.R. Scully, Measurement and Modeling of Hydrogen Environment-Assisted Cracking in Monel K-500, *Metall. Mater. Trans. A.* 45 (2014) 3814–3834. doi:10.1007/s11661-014-2324-z.
- [2] A.S. Popernack, Loading Rate Effects on Hydrogen-Enhanced Cracking Behavior of Ni- and Co-Based Superalloys for Marine Applications, University of Virginia, 2017.
- [3] Z.D. Harris, J.D. Dolph, G.L. Pioszak, B.C. Rincon Troconis, J.R. Scully, J.T. Burns, The Effect of Microstructural Variation on the Hydrogen Environment-Assisted Cracking of Monel K-500, *Metall. Mater. Trans. A.* 47 (2016) 3488–3510. doi:10.1007/s11661-016-3486-7.
- [4] B.C.R. Troconis, Z.D. Harris, H. Ha, J.T. Burns, J.R. Scully, The effect of heat-to-heat variations in metallurgy and hydrogen-metal interactions on the hydrogen embrittlement of Monel K-500, *Mater. Sci. Eng. A.* 703 (2017) 533–550. doi:10.1016/j.msea.2017.07.019.
- [5] QQ-N-286G: Nickel-Copper-Aluminum Alloy, Wrought (UNS N05500), (2000).
- [6] G.K. Dey, R. Tewari, P. Rao, S.L. Wadekar, P. Mukhopadhyay, Precipitation hardening in nickel-copper base alloy monel K 500, *Metall. Trans. A.* 24 (1993) 2709–2719. doi:10.1007/BF02659495.
- [7] G.K. Dey, P. Mukhopadhyay, Precipitation in the Ni-Cu-base alloy Monel K-500, *Mater. Sci. Eng.* 84 (1986) 177–189. doi:10.1016/0025-5416(86)90236-3.
- [8] H. Tada P.C. Paris, and G.R. Irwin, *The Stress Analysis of Cracks Handbook*, Paris Productions Incorporated, St. Louis, MO, 1985.
- [9] N.E. Dowling, Fatigue at Notches and the Local Strain and Fracture Mechanics Approaches, *ASTM STP 677 Fract. Mech.* (1979) 247–273. doi:10.1520/STP34917S.
- [10] R.A. Smith, K.J. Miller, Fatigue cracks at notches, *Int. J. Mech. Sci.* 19 (1977) 11–22. doi:10.1016/0020-7403(77)90011-X.
- [11] J.K. Donald, J. Ruschau, Direct current potential difference fatigue crack measurement techniques, *Fatigue Crack Meas. Tech. Appl.* (1991) 11–37.
- [12] H.H. Johnson, Calibrating the Electric Potential Method for Studying Slow Crack Growth, *Mater. Res. Stand.* 5 (1965) 442–445.
- [13] K.-H. Schwalbe, D. Hellmann, Application of the Electrical Potential Method to Crack Length Measurements Using Johnson’s Formula, *J. Test. Eval.* 9 (1981) 218–221.
- [14] ASTM Standard E647-13: Standard Test Method for Measurement of Fatigue Crack Growth Rates, (2013). doi:10.1520/E0647-13E01.2.

- [15] V. Kumar, M.D. German, C.F. Shih, *An Engineering Approach for Elastic-Plastic Fracture Analysis*, Electric Power Research Institute, Palo Alto, CA, 1981.
- [16] Z.D. Harris, Private communication with Denny Paul, (2017).
- [17] R.P. Gangloff, Hydrogen Assisted Cracking of High Strength Alloys, in: I. Milne, R.O. Ritchie, B. Karihaloo (Eds.), *Compr. Struct. Integr.*, Elsevier Science, New York, NY, 2003: pp. 31–101.
- [18] C.E. Price, G.W. Henderson, The progression of bending fatigue in Monel K500, *Fatigue Fract. Eng. Mater. Struct.* 11 (988) 493–500.
- [19] R.P. Gangloff, H-Enhanced Deformation and Fracture in the Crack Tip Process Zone, in: B.P. Somerday, P. Sofronis (Eds.), *Mater. Perform. Hydrog. Environ. Proc. 2016 Int. Hydrog. Conf.*, ASME Press, 2016: pp. 1–35.
- [20] R.E. Reed-Hill, R. Abbaschian, *Physical metallurgy principles*, Van Nostrand, Princeton, 1994.
- [21] V. Rothova, M. Svoboda, J. Bursik, The effect of annealing conditions on grain growth and microstructure in nickel, in: *Met. 2009 Conf. Proc.*, 2009: pp. 1–8.
- [22] S.B. Lee, N.M. Hwang, D.Y. Yoon, M.F. Henry, Grain Boundary Faceting and Abnormal Grain Growth in Nickel, *Metall. Mater. Trans. A.* 31 (2000) 985–994.
- [23] T.P. Gabb, P.T. Kantzos, J. Telesman, J. Gayda, C.K. Sudbrack, B. Palsa, Fatigue resistance of the grain size transition zone in a dual microstructure superalloy disk, *Int. J. Fatigue.* 33 (2011) 414–426. doi:10.1016/j.ijfatigue.2010.09.022.
- [24] V. Randle, Grain boundary engineering: an overview after 25 years, *Mater. Sci. Technol.* 26 (2010) 253–261. doi:10.1179/026708309X12601952777747.
- [25] S. Bechtel, M. Kumar, B.P. Somerday, M.E. Launey, R.O. Ritchie, Grain-boundary engineering markedly reduces susceptibility to intergranular hydrogen embrittlement in metallic materials, *Acta Mater.* 57 (2009) 4148–4157. doi:10.1016/j.actamat.2009.05.012.
- [26] M. Frary, C.A. Schuh, Connectivity and percolation behaviour of grain boundary networks in three dimensions, *Philos. Mag.* 85 (2005) 1123–1143. doi:10.1080/14786430412331323564.
- [27] R.T. Holt, W. Wallace, Impurities and trace elements in nickel-base superalloys, *Int. Met. Rev.* (1976) 1–24.
- [28] P. Lejcek, Chapter 7: grain boundary segregation and related phenomena, in: P. Lejcek (Ed.), *Grain Bound. Segreg. Met.*, Springer, Berlin, 2010.
- [29] R.A. Mulford, Grain boundary segregation in Ni and binary Ni alloys doped with sulfur, *Metall. Trans. A.* 14 (1983) 865–870. doi:10.1007/BF02644289.
- [30] B. Ladna, H.K. Birnbaum, Surface and Grain-Boundary Segregation of Sulfur and Boron in Nickel, *Acta Metall.* 36 (1988) 745–755. doi:10.1016/0001-6160(88)90108-3.
- [31] S.M. Bruemmer, R.H. Jones, M.T. Thomas, D.R. Baer, Sulfur Induced Fracture Mode Transition of Nickel At Cathodic Potentials., *Scr. Metall.* 14 (1980) 1233–1237. doi:10.1016/0036-9748(80)90263-X.
- [32] S.M. Bruemmer, R.H. Jones, M.T. Thomas, D.R. Baer, Influence of sulfur, phosphorus, and

- antimony segregation on the intergranular hydrogen embrittlement of nickel, *Metall. Trans. A*. 14 (1983) 223–232. doi:10.1007/BF02651619.
- [33] M. Yamaguchi, M. Shiga, H. Kaburaki, Grain Boundary Decohesion by Impurity Segregation in a Nickel-Sulfur System, *Science* (80-.). 307 (2005) 393–398.
- [34] R.P. Messmer, C.L. Briant, The role of chemical bonding in grain boundary embrittlement, *Acta Metall.* 30 (1982) 457–467.
- [35] C.D. Taylor, M. Neurock, J.R. Scully, A First-Principles Model for Hydrogen Uptake Promoted by Sulfur on Ni(111), *J. Electrochem. Soc.* 158 (2011) F36–F44. doi:10.1149/1.3536470.
- [36] J.W. Cohron, E.P. George, L. Heatherly, C.T. Liu, R.H. Zee, Effect of low-pressure hydrogen on the room-temperature tensile ductility and fracture behavior of Ni3Al, *Intermetallics*. 4 (1996) 497–502. doi:10.1016/0966-9795(96)00039-8.
- [37] J.W. Hutchinson, Singular behaviour at the end of a tensile crack in a hardening material, *J. Mech. Phys. Solids*. 16 (1968) 13–31.
- [38] J.R. Rice, G.F. Rosengren, Plane strain deformation near a crack tip in a power-law hardening materials, *J. Mech. Phys. Solids*. 16 (1968) 1–12.
- [39] U. Komaragiri, S.R. Agnew, R.P. Gangloff, M.R. Begley, The role of macroscopic hardening and individual length-scales on crack tip stress elevation from phenomenological strain gradient plasticity, *J. Mech. Phys. Solids*. 56 (2008) 3527–3540. doi:10.1016/j.jmps.2008.08.007.
- [40] E. Martínez-Pañeda, C.F. Niordson, On fracture in finite strain gradient plasticity, *Int. J. Plast.* 80 (2016) 154–167. doi:10.1016/j.ijplas.2015.09.009.
- [41] E. Martinez-Paneda, C.F. Niordson, R.P. Gangloff, Strain gradient plasticity-based modeling of hydrogen environment assisted cracking, *Acta Mater.* 117 (2016) 321–332. doi:10.1016/j.actamat.2016.07.022.
- [42] H.K.D.H. Bhadeshia, Prevention of Hydrogen Embrittlement in Steels, *ISIJ Int.* 56 (2016) 24–36. doi:10.2355/isijinternational.ISIJINT-2015-430.
- [43] J. Ai, H.M. Ha, R.P. Gangloff, J.R. Scully, Hydrogen diffusion and trapping in a precipitation-hardened nickel–copper–aluminum alloy Monel K-500 (UNS N05500), *Acta Mater.* 61 (2013) 3186–3199. doi:10.1016/j.actamat.2013.02.007.
- [44] J.W. Martin, *Micromechanisms in particle-hardened alloys*, Cambridge University Press, Cambridge, UK, 1980.
- [45] T.H. Sanders, E.A. Starke, The effect of slip distribution on the monotonic and cyclic ductility of AlLi binary alloys, *Acta Metall.* 30 (1982) 927–939. doi:10.1016/0001-6160(82)90199-7.
- [46] W.W. Gerberich, Modelling hydrogen induced damage mechanisms in metals, in: R.P. Gangloff, B.P. Somerday (Eds.), *Gaseous Hydrog. Embrittlement Mater. Energy Technol.*, Woodhead Publishing, 2012: pp. 209–246.
- [47] A. Alvaro, I. Thue Jensen, N. Kheradmand, O.M. Løvvik, V. Olden, Hydrogen embrittlement in nickel, visited by first principles modeling, cohesive zone simulation and nanomechanical testing, *Int. J. Hydrogen Energy*. 40 (2015) 16892–16900. doi:10.1016/j.ijhydene.2015.06.069.

- [48] I.M. Robertson, The effect of hydrogen on dislocation dynamics, *Eng. Fract. Mech.* 65 (2001) 671–692.
- [49] H.K. Birnbaum, P. Sofronis, Hydrogen-enhanced localized plasticity—a mechanism for hydrogen-related fracture, *Mater. Sci. Eng. A.* 176 (1994) 191–202. doi:10.1016/0921-5093(94)90975-X.
- [50] I.M. Robertson, P. Sofronis, A. Nagao, M.L. Martin, S. Wang, D.W. Gross, et al., Hydrogen Embrittlement Understood, *Metall. Mater. Trans. B.* (2015). doi:10.1007/s11663-015-0325-y.
- [51] A.W. Thompson, I.M. Bernstein, The Role Of Metallurgical Variables In Hydrogen-Assisted Environmental Fracture, *Adv. Corros. Sci. Technol.* (1980) 53–175. doi:10.1007/978-1-4615-9065-1_2.
- [52] B. Fultz, J.M. Howe, *Transmission Electron Microscopy and Diffractometry of Materials*, 3rd Edition, 2008. doi:10.1017/CBO9781107415324.004.
- [53] W.W. Gerberich, R.A. Oriani, M. Lii, X. Chen, T. Foecke, The necessity of both plasticity and brittleness in the fracture thresholds of iron, *Philos. Mag. A.* 63 (1991) 363–376.
- [54] R.A. Oriani, A Mechanistic Theory of Hydrogen Embrittlement of Steels, *Berichte Der Bunsen-Gesellschaft Fur Phys. Chemie.* 76 (1972) 848–857.
- [55] V. Randle, D. Horton, Grain growth phenomena in nickel, *Scr. Metall. Mater.* 31 (1994) 891–895. doi:10.1016/0956-716X(94)90498-7.

Chapter 5. Effect of hydrogen on deformation behavior in Monel K-500

5.1. Overview

The effect of hydrogen on the deformation behavior of Monel K-500 as a function of isothermal heat treatment was assessed via uniaxial mechanical testing. Hydrogen-charged and non-charged specimens from four heat treatments, corresponding to the non-aged, under-aged, peak-aged, and over-aged conditions, were each strained to failure to facilitate comparison of fracture surface morphology, ductility, strength, and work hardening behavior. Results demonstrate that the ductility is significantly reduced for all tested heat treatments in the presence of hydrogen, which is corroborated by a consistent change in fracture surface morphology from ductile microvoid coalescence in the non-charged condition to brittle intergranular fracture in the hydrogen-charged condition. While the yield strength was found to be systematically enhanced for all heat treatments in the presence of hydrogen, the three precipitate-hardened conditions exhibited a >2x larger relative increase than the non-aged heat treatment, suggesting that hydrogen modifies dislocation-precipitate interactions. Examination of work hardening metrics corroborated this assessment as a clear deviation from trends established as a function of heat treatment in the non-charged condition were observed for both the initial work hardening rate and the Stage III slope. In particular, the peak-aged specimen tested in the hydrogen-charged condition exhibited a significant increase in initial hardening rate relative to the hydrogen-charged under-aged specimen, suggesting an onset of dislocation looping; such a striking increase between the under-aged and peak-aged heat treatments was not observed in the non-charged condition. Transmission electron microscopy of the hydrogen-charged peak-aged condition confirmed the onset of widespread dislocation looping, though planar slip bands characteristic of the non-charged condition were still observed. This result suggests that hydrogen induces the particle shearing-to-looping transition at smaller particle sizes; such an effect was unexpected as looping processes often involve dislocation cross-slip, which hydrogen has been argued to impede. An overview of possible mechanistic explanations for this observed behavior are presented, but the mechanism responsible is unclear, thereby underscoring the need for additional experiments to understand the effect of hydrogen on dislocation-precipitate interactions.

5.2. Introduction

The results of Chapter 4 demonstrate that the susceptibility of four different heat treatments of Monel K-500 to hydrogen environment-assisted cracking (HEAC) correlates well with the propensity for strain localization. Specifically, alloys heat treated to the non-aged and over-aged conditions, which were found to deform *via* wavy slip, exhibit reduced susceptibility relative to alloys in the under-aged and peak-aged conditions, which deform *via* planar slip. Such observations agreed well with literature data [1], which has established that planar slip alloys generally exhibit enhanced susceptibility to stress corrosion cracking (such as HEAC) relative to wavy slip alloys across multiple materials systems (e.g. Ti, Al, Ni alloys). However, extension of these correlations into mechanisms to explain the observed dependence on planar slip is complicated by two critical limitations. First, assessment of the bulk slip morphology is typically completed using transmission electron microscopy foils obtained from a tensile specimen strained on the order of a few percent. However, it is unclear whether these bulk observations are readily scalable to the high-stress region proximate to a crack tip. In particular, how variations in bulk slip morphology affect the deformation behavior at the crack tip is not well understood. Second, the majority of the studies examining bulk slip morphology were conducted in the absence of H. Given that exposure to H is a fundamental requirement of HEAC [2], the extrapolation of crack tip deformation behavior from bulk results obtained in the absence of H may not be representative of actual crack tip deformation processes.

The effect of H on deformation behavior has received extensive attention in the scientific literature, with the impetus for much of this work being Beachem's observation of small void-like features on the cleavage and intergranular facets in 4300-type steel exposed to 0.6 M NaCl [3]. Beachem took the presence of these ductile features as evidence that 'microscopic plasticity' governed H-assisted cracking, which led him to propose that H 'unlocks' dislocations such that they move and/or multiply at reduced stresses [3]. This interpretation was subsequently supported by the extensive *in-situ* observation of dislocation characteristics under a H atmosphere by Birnbaum and coworkers in an environmental TEM. Evidence that H caused enhanced dislocation velocities and reduced dislocation spacing in pile-ups was documented across numerous alloy systems [4], including Ti, Ni, Fe, 310 stainless steel, 316 stainless steel, Ni₃Al, 7xxx-series aluminum, and IN903, suggesting that the effect was ubiquitous for structural metals.

Additionally, this extensive characterization effort revealed that H restricted dislocation cross-slip, indicating that H promotes slip planarity [5]. In particular, it was argued that this restricted cross-slip was not solely due to a H-induced reduction in stacking fault energy (though H was estimated to reduce the stacking fault energy by ~20% [6]), but was instead a coupled effect between H influences on both the stacking fault energy and the repulsive force between partial dislocations. As demonstrated theoretically by Delafosse [7], H reduces the attraction between edge components in partial dislocations, leading to

increased repulsion, larger separation distances between the partial dislocations, and impeded cross-slip. Considering H-enhanced dislocation multiplication, Barnoush observed a reduction in the ‘pop-in’ load of H-charged specimens relative to non-charged specimens during nano-indentation experiments [8]. Given that, for a well-annealed material, the interaction volume of the nano-indenter can be considered smaller than the average dislocation spacing, the ‘pop-in’ load may be utilized to calculate the energy for homogeneous dislocation nucleation (HDN); the observed reduction in ‘pop-in’ load therefore suggests that H reduces the energy for HDN [8]. Similar results were also obtained by Kirchheim and coworkers [9,10]. In this work, sheets of H-charged and non-charged palladium (Pd) were cold-rolled to a 50% thickness reduction and then the dislocation density in each condition was estimated via X-ray diffraction (XRD) peak broadening experiments. Results indicated a 6x increase in dislocation density for Pd containing 0.75 at. % H, suggesting that H enhances dislocation multiplication [9]. These XRD results were consistent with TEM observations of the deformation microstructure, which showed increased dislocation densities in the H-charged Pd relative to the non-charged Pd [9]. Tensile testing of Pd charged to different H concentrations yielded further evidence for H-enhanced dislocation multiplication, as the strain hardening exponent was observed to strongly increase with H content [10].

While these studies provide an excellent description of the fundamental effects that H has on dislocation processes, attempts to extend these insights into more complicated, engineering-relevant alloys remain limited. For example, considering precipitation-hardened alloys, the effect of H on dislocation-precipitate interactions is largely unexplored [11]. In the context of HEAC, H-induced modifications in dislocation-precipitate interactions may have important ramifications on the observed bulk slip morphology, such as potentially increasing the precipitate size that can be sheared. This knowledge gap motivates a study to examine how H affects bulk slip morphology in precipitation-hardened alloys (such as Monel K-500), particularly as a function of aging condition.

Traditionally, evaluation of H effects on the bulk slip morphology is conducted by comparing dislocation patterning in the H-charged versus non-charged condition after deformation to a given strain level. For example, Robertson and coworkers have performed detailed TEM characterization of the deformation structure in pure Ni subjected to high-pressure torsion in the H-charged and non-charged condition [12]. In this study, specimens deformed to equivalent shear strains revealed a reduced dislocation cell diameter on average in the H-charged specimens compared to non-charged specimens, suggesting that H accelerates deformation processes (in agreement with the prior fundamental work on Pd [9,10]). However, this result was counter to other studies which showed no statistically significant refinement in the dislocation patterning of H-charged and non-charged Ni. Specifically, two studies examining TEM foils extracted from similarly strained H-charged and non-charged tensile specimens reported similar dislocation

patterning between the two conditions, indicating a lack of H influence [13,14]. These diametrically opposed results underscore the difficulty in assessing global deformation behavior solely through transmission electron microscopy, where the field of interrogation is effectively limited to a few μm^2 . Speculatively, the variability in these results is likely attributed to differences in dislocation patterning induced by variations in grain orientation. It is well known that grain orientation can have significant impacts on the observed dislocation patterning [15,16], suggesting that a macroscale approach to assessing dislocation characteristics may yield more consistent insights.

One macroscale pathway for assessing variations in bulk deformation behavior is through differences in measured work hardening parameters. For example, Cheng and coworkers utilized variations in work hardening data to understand the effect of heat treatment on deformation processes in AA6111 [17]. Considering the identified knowledge gap regarding the effect of H on dislocation-precipitate interactions, such an approach could provide insights on both *if* and *how* H modifies deformation behavior in precipitation-hardened alloys.

5.2.1. Chapter objective and research questions

The objective of this chapter is to systematically evaluate the influence of H on the mechanical behavior of Monel K-500 as a function of aging condition so as to understand how H affects dislocation-precipitate interactions. Towards this end, the chapter seeks to answer the following research questions:

7. How does H affect the mechanical properties (ductility, yield strength, etc.) as a function of aging condition in Monel K-500?
8. How does H affect the work hardening behavior as a function of aging condition in Monel K-500?
9. If H does affect dislocation-precipitate interactions, does it result in a change in bulk slip morphology and by what mechanism?

5.3. Experimental methods and material

5.3.1. Material

All experiments were conducted on a single heat of Monel K-500 procured in the form of a 6-m long, 16-mm diameter bar heat-treated to the solution-annealed condition. The as-received grain structure was nominally equiaxed with a supplier-reported average grain size of $\sim 10 \mu\text{m}$. Bulk composition was evaluated using inductively coupled plasma optical emission spectroscopy (ICP-OES), while glow discharge mass spectroscopy (GDMS) was utilized for trace elemental analysis; the measured composition is shown in Table 8. As described in Chapter 3, Monel K-500 is nominally composed of two phases: a face-centered cubic (FCC) Ni-Cu solid solution (γ) matrix and a homogenous distribution of highly coherent

(<0.1% misfit strain), spherical Ni₃(Al,X) precipitates (γ'), where X can be Ti, Cu, Mn, or Si, which have an ordered L1₂ structure [18–20].

Table 11 – Composition of the tested Monel K-500 heat (wt. % except Si, Zr, P, S, and B are in wppm)

Ni	Cu	Al	Ti	Mn	Fe	Si	Zr	P	S	B
62.3	31.8	2.96	0.59	0.7	0.78	850	310	69	31	1.2

Specimens for mechanical testing were heat-treated as follows to one of four targeted aging conditions based on the previously reported hardening curve (yield strength vs. isothermal aging time) for the tested material heat in Chapter 4. First, 38-mm long, 12.7-mm diameter cylindrical blanks were cut from the barstock and then solution-treated in a tube furnace for 1 hour at 1223 K, followed by an immediate water quench; this heat treatment represents the non-aged (NA) condition. Specimens targeted for the under-aged (UA), peak-aged (PA), or over-aged (OA) conditions were then age hardened at 923 K for times of 0.5, 5, or 50 hours, followed by an immediate water quench, respectively. After heat treating, each cylindrical blank was machined into two flat, rectangular tensile specimens with a nominal gage length, width, and thickness of 10.2 mm, 7.1 mm, and 3.2 mm, respectively.

5.3.2. Mechanical Testing

Uniaxial tensile tests, with the loading direction oriented along the bar's longitudinal axis, were performed on a servohydraulic load frame operated under actuator displacement control at a constant rate of 0.0041 mm/s, yielding a strain rate of $\sim 4 \times 10^{-4} \text{ s}^{-1}$ (calculated by dividing the displacement rate by the specimen gage length). Each specimen was tested until final fracture, with the specimen elongation actively monitored by an attached extensometer. Prior to straining, H-charged specimens, which had been continually stored under cryogenic temperatures (either in a cryogenic freezer at 223 K or immersed in LN₂), were held at room temperature (RT, $\sim 298 \text{ K}$) for precisely one hour, so as to allow H to redistribute and reach the equilibrium grain boundary H concentration for this temperature [21]. In addition to the employed extensometer, the true plastic strain was evaluated post-test through the calculation of the true plastic strain (ϵ_T) *via* the measured reduction in area (RA); the use of the true plastic strain allows for direct comparison between specimens, including those which exhibited necking. ϵ_T is calculated as follows:

$$\epsilon_T = -\ln(1 - RA) \quad (5.1)$$

where RA is the reduction in area, defined by:

$$RA = \frac{A_i^2 - A_f^2}{A_i^2} \quad (5.2)$$

where A_f and A_i are the final and initial cross-sectional areas of the gage section, respectively. Final area measurements were taken at the center of the specimen gage section using calibrated optical micrographs, while initial area measurements were made using digital calipers. The experimental work hardening rate (θ) was determined via numerically differentiating the true stress-true strain data using a 7-point ($n = 3$) polynomial method adapted from ASTM Standard E647 Appendix XI [22]. To smooth the data for presentation, the experimental work hardening rate vs. true strain curve was fit to a second-order exponential function using Matlab. For the H-charged conditions, additional specimens were deformed to incrementally higher strains, where the test was interrupted and the specimen removed for a future study (see Section 5.7). The stress-strain data from these interrupted specimens were also differentiated and then included in the fit so as to (1) show reproducibility of results and (2) improve the rigor of the fit. An example of this fitting procedure using the UA/H condition is shown in Figure 48, which was shown to agree well with the average experimental data.

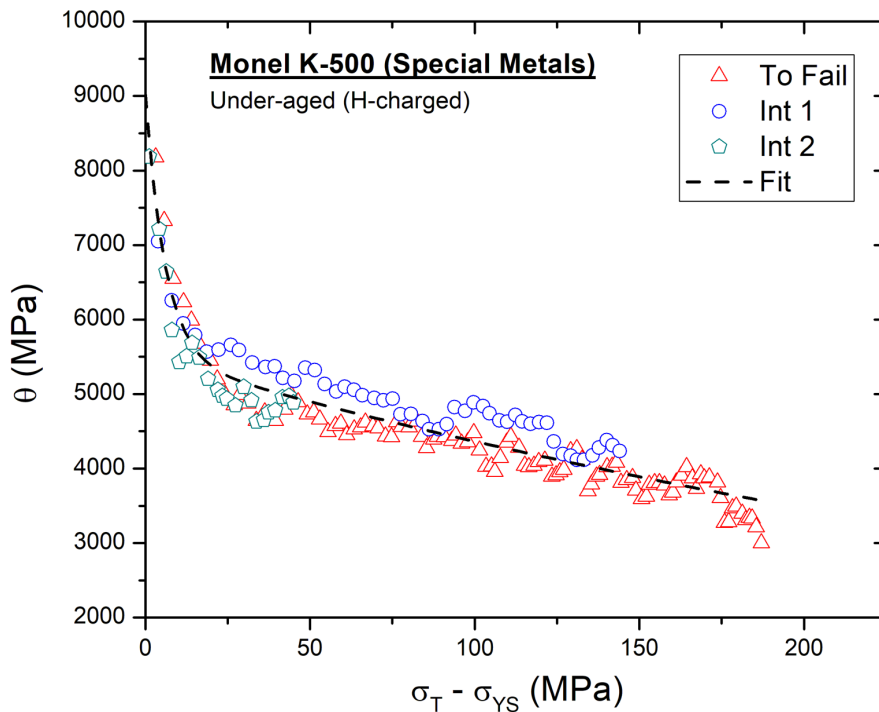


Figure 48 – Plot of the work hardening rate (θ) versus flow stress increase ($\sigma_T - \sigma_{YS}$) for the H-charged, under-aged specimen tested to failure as well as two tests which were interrupted at lower strains. The dashed black line represents the fit to the three data sets using a second-order exponential function.

5.3.3. Hydrogen Charging

Atomic H was introduced into a subset of the tensile specimens *via* thermal charging; a detailed explanation of this charging procedure is reported elsewhere [23,24]. Briefly, specimens were placed inside an autoclave mounted within a furnace, which was heated to a charging temperature of 573 K and then filled with 99.9999% pure H₂ gas until the target charging pressure of 96.5 MPa was reached. The system was then held at these conditions for approximately 144 hours to ensure the development of a uniform H concentration across the specimen diameter. Upon removal from the furnace, specimens were immediately stored in a cryogenic freezer maintained at 223 K and then later immersed under liquid nitrogen (LN₂) to minimize H egress prior to mechanical testing.

Literature establishes that the solubility of H in a Ni-Cu matrix is identical to that of H in pure Ni for alloys with <45% Cu by weight [25]. As such, the lattice H concentration under these charging conditions is expected to be approximately 70 parts per million (ppm) [23]. To determine whether this theoretical concentration was achieved, the H concentrations of four small pieces sectioned from the shoulder region of a tensile specimen from each aging condition were evaluated using an inert gas fusion analyzer. Based on these four replicates, average H concentrations of 180, 210, 220, and 220 ppm were measured in the NA, UA, PA, and OA specimens, respectively. Such concentrations approximately correspond to 1.08 atomic (at.) % H (NA), 1.26 at. % H (UA), and 1.32 at. % H (PA and OA). This substantial deviation between the theoretical and measured H concentration was unexpected and cannot be reasonably attributed to differences introduced by H trapped at grain boundaries, dislocations, or γ/γ' interfaces [23]. However, comparison of H uptake data previously generated for this material heat reveals an ~225-250% increase in diffusible H, depending on the applied potential, relative to a second material heat of Monel K-500 [26]. While the reasoning behind this enhanced H uptake in the current material heat is unknown, the ~250% increase in H content relative to expectations is consistent with the difference between the reported and theoretically calculated H concentrations. Considering the variation with heat treatment, the differences in measured H concentration between the aging conditions are likely due to H trapping at the γ/γ' interface [27] (or within in the γ' precipitate as suggested from simulations by Baskes et al. [28]), as thermal charging time was sufficiently long to allow for matrix saturation. It is possible that these differences in H concentration may affect the magnitude of H effects on mechanical behavior. As such, interpretations of results in the current study will predominantly focus on general trends with H for each treatment as opposed to directly comparing the heat treatments themselves.

5.3.4. Microscopy

The fracture surface morphology for each sample was examined using a Quanta 650 scanning electron microscope (SEM) operated in secondary electron mode with an accelerating voltage between 5-

10 keV. Foil specimens for transmission electron microscopy were taken from the gage section of the peak-aged H-charged (PA H) tensile specimen, with the foil plane parallel to the loading direction. Specimens were prepared as followed: the gage section from the specimen was progressively thinned using SiC papers, finishing at 1200 grit, to a final thickness of 100-110 μm . 3-mm diameter foils were then punched from this thin section using a Gatan disc puncher, further thinned to 80-90 μm using a Gatan disc grinder, and then electrochemically polished in a Fischione 110 twin jet polisher using a solution of 60% H_2SO_4 and 40% H_2O (by volume) at ambient temperature (296 to 298 K) with an applied voltage of 5 V. Transmission electron microscopy (TEM) was conducted using an FEI Titan equipped with a double-tilt specimen holder and operated at 300 keV.

5.4. Results

5.4.1 *Effect of H on stress-strain behavior and fractography*

Two specimens from each heat treatment, representing the H-charged and non-charged conditions, were strained to failure to determine the mechanical properties and the predominant fracture morphology for each heat treatment/hydrogen content combination. The true stress-true strain curves for the H-charged and non-charged specimens from each aging condition are shown in Figure 49. Note that the non-charged curves were truncated at the onset of necking, which was calculated using Considere's criterion: $\sigma_T = \theta$, where σ_T is true stress and θ is the work hardening rate [29]. Mechanical properties obtained from this testing are listed in Table 12.

Comparison of the flow curves for the H-charged versus non-charged conditions reveals several important differences. First, consistent with previous literature on hydrogen effects in Monel K-500 [30–32], a significant decrease in the reduction of area and true fracture strain was observed across all four tested aging conditions in the presence of hydrogen. Second, the ultimate tensile strength (derived from the engineering stress-strain curve; not shown) was also reduced in the presence of hydrogen, with measured decreases on the order of 100 MPa for the NA, UA, and PA conditions, while the OA condition decreased by a more modest 60 MPa. Third, the yield strength was found to increase with H-charging across the four aging conditions, with increases on the order of 100 MPa from the non-charged condition observed in the UA, PA, and OA specimens, while the NA exhibited an increase of ~ 50 MPa. Such results are consistent with the data presented in Chapter 2 for pure Ni, which also exhibited an increased yield strength in the H-charged condition.

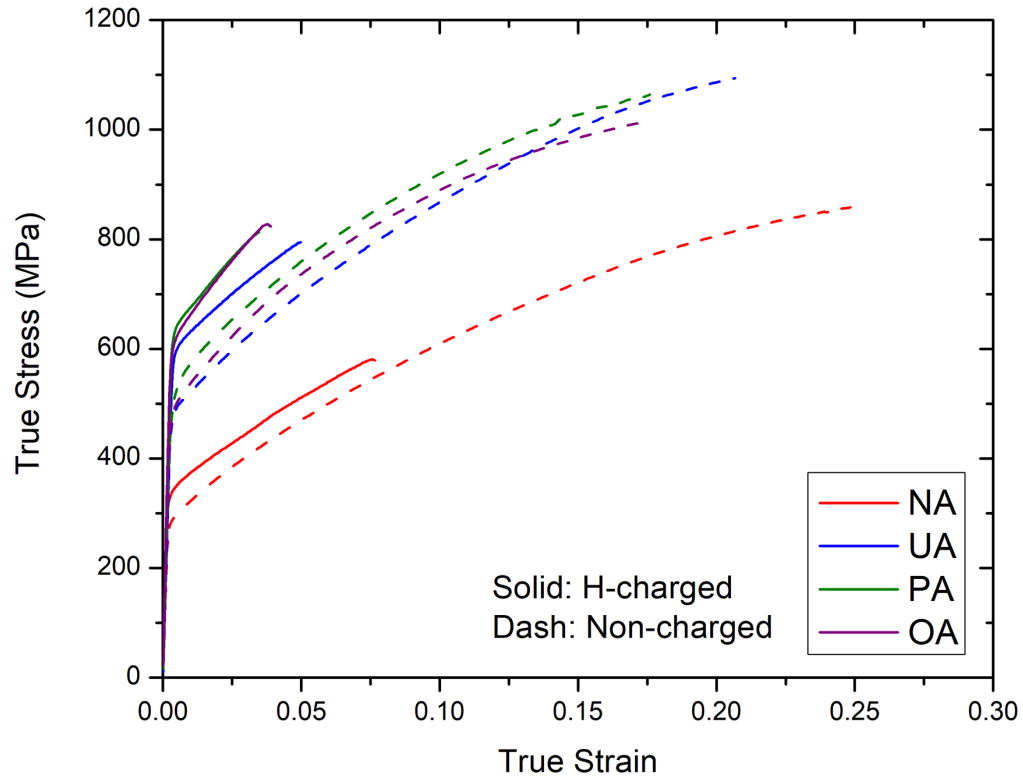


Figure 49 – True stress-true strain curves for the H-charged and non-charged specimens strained to failure for each heat treatment.

Table 12 – Mechanical properties as a function of heat treatment and hydrogen condition

Testing Condition	Yield Strength (MPa)	Ultimate Tensile Strength (MPa)	Reduction of Area (%)	True Fracture Strain
NA/H	345	538	8.7	0.091
NA/No H	294	670	50.0	0.693
UA/H	605	757	5.6	0.057
UA/No H	490	890	42.3	0.550
PA/H	641	786	5.5	0.056
PA/No H	526	894	38.1	0.479
OA/H	623	798	4.6	0.047
OA/No H	497	853	39.2	0.497

Fractography of the four heat treatments, shown in Figure 50 for the non-charged testing and Figure 51 for the H-charged testing, corroborates the observed reduction in ductility for each aging condition in the presence of hydrogen. Specifically, as shown in Figure 50, each heat treatment displayed extensive evidence of ductile failure *via* microvoid coalescence in the absence of H, consistent with the results of prior slow-strain rate testing of Monel K-500 in laboratory air [33]. The void morphology across the four conditions was generally similar, though on average, NA/No H (Figure 50a) may contain slightly larger voids relative to the other heat treatments, as would be expected given the increased strain-to-failure for the NA/No H condition (Figure 49). Considering the fractography of the H-charged testing, shown in Figure 51, each heat treatment exhibited widespread intergranular fracture. Critically, given the high hydrogen concentrations observed in this study, the observation of intergranular facets (as opposed to cleavage failure) and the measurable strains-to-failure on the order of 0.04-0.08 strongly suggests an absence of brittle hydrides. Examination of the intergranular facets at higher magnification (Figure 52) revealed striking differences in the observed slip traces as a function of heat treatment. In particular, as shown in Figure 52a and Figure 52d, NA/H and OA/H exhibited fine slip traces on the intergranular facets, while UA/H and (to a lesser extent) PA/H exhibit coarse slip traces (Figure 52b and Figure 52c, respectively).

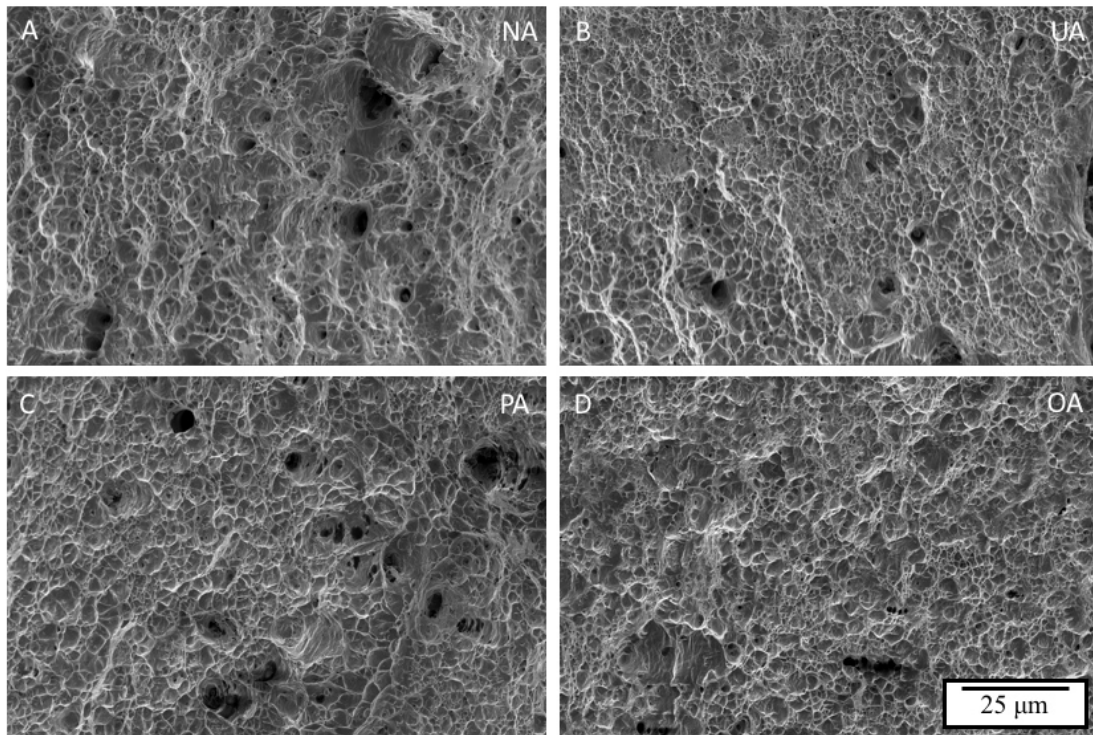


Figure 50 – Fractographs of the (a) non-aged, (b) under-aged, (c) peak-aged, and (d) over-aged heat treatments tested to failure in the non-charged condition.

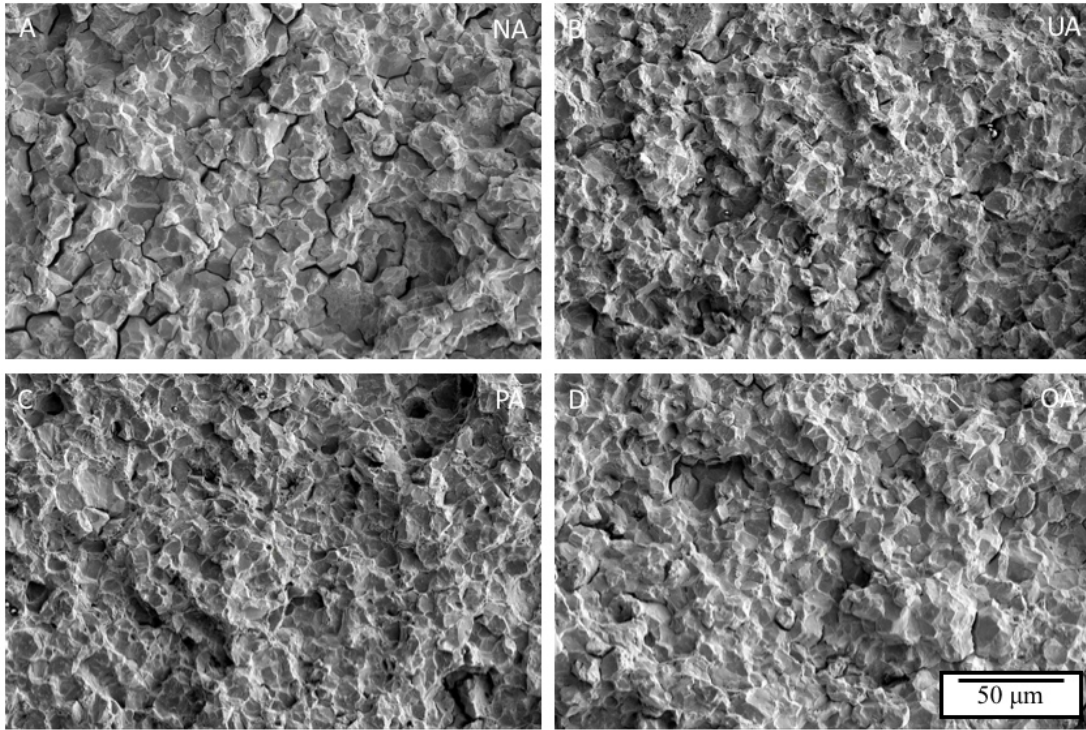


Figure 51 – Fractographs of the (a) non-aged, (b) under-aged, (c) peak-aged, and (d) over-aged heat treatments tested to failure in the hydrogen-charged condition.

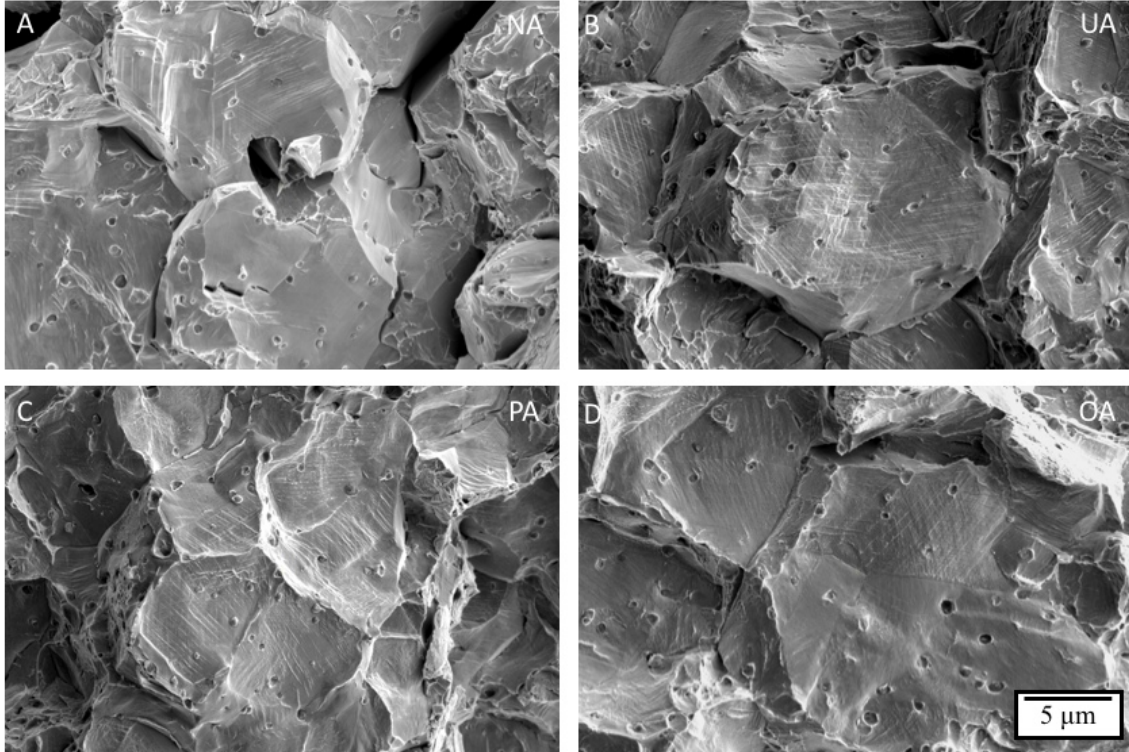


Figure 52 – High-magnification fractographs of the slip traces observed on intergranular facets in the (a) non-aged, (b) under-aged, (c) peak-aged, and (d) over-aged heat treatments tested to failure in the hydrogen-charged condition.

5.4.2. Effect of H on work hardening behavior

The work hardening rate (θ) versus the flow stress increase ($\sigma_T - \sigma_{YS}$) relationships for the non-charged and H-charged condition in each heat treatment are presented in Figure 53. First, each specimen, regardless of H and aging condition, displays an initial rapid decrease in work hardening rate at small ($\sigma_T - \sigma_{YS}$), which is related to the significant changes in slope within the elastic-plastic transition region of the true stress-true strain curve [17]. Second, beyond this transition region, each of the specimens exhibits an apparent linear decrease in the work hardening rate with increasing ($\sigma_T - \sigma_{YS}$). Clear variations in the character of this linear region arise among the tested specimens, both as a function of heat treatment and as a function of H. Considering the former, the NA/No H is found to generally exhibit the lowest work hardening rates, while the relative ordering of the UA/No H, PA/No H, and OA/No H evolves as the flow stress increases. Conversely, considering the role of H, the difference between H-charged and non-charged appears to become more evident as aging time increases. For example, NA/H exhibits a similar slope as NA/No H, while UA/H and PA/H exhibit significantly increased slopes relative to non-charged condition. Additionally, the magnitude of the difference in work hardening rate between the non-charged and H-charged specimens appears to increase with aging time. Specifically, while the NA/H and UA/H have similar (or lower) initial work hardening rates, the PA/H and OA/H exhibit work hardening rates on the order of 1000 MPa higher than the non-charged condition.

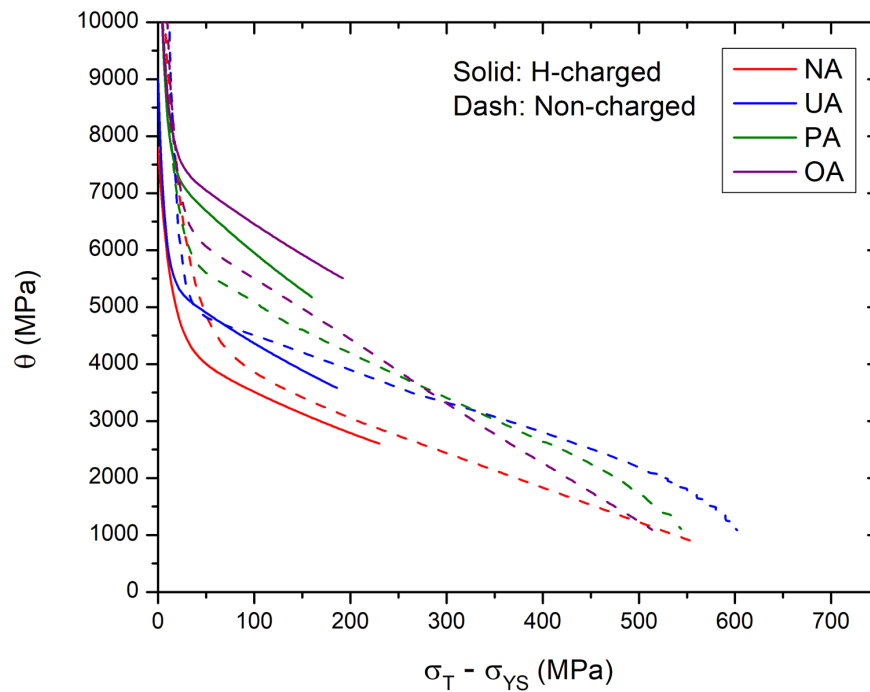


Figure 53 – Work hardening rate versus flow stress increase for the H-charged and non-charged specimens strained to failure for each heat treatment.

In order to quantitatively compare the work hardening behavior as a function of H and aging condition, it is convenient to define two parameters which describe the observed linear (termed “Stage III” in the literature) region: θ_{\max} and $-d\theta/d\sigma$. As demonstrated by Kocks and Mecking [34], these parameters can be readily determined graphically, as shown by Figure 54, from the y-intercept and slope, respectively, of a linear fit to the Stage III region. This fitting approach is based on the Voce relationship, which describes the linear θ vs $(\sigma_T - \sigma_{YS})$ relationship in the Stage III region and has been widely employed in the literature [34].

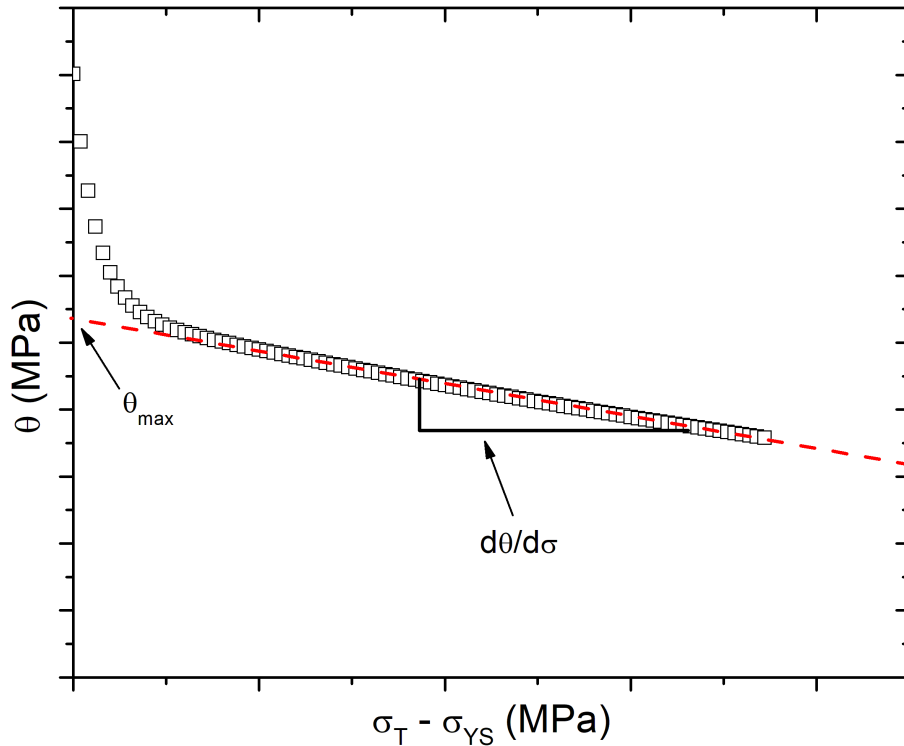


Figure 54 – Schematic demonstrating the graphical assessment of θ_{\max} and $d\theta/d\sigma$ based on a linear fit to the Stage III work hardening region.

Based on the definitions in Figure 54, θ_{\max} and $-d\theta/d\sigma$ were calculated from the work hardening data for each H/heat treatment combination and plotted in Figure 55a-b. Examination of Figure 55a reveals a distinct effect of H on the evolution of the θ_{\max} parameter with heat treatment. Specifically, for the non-charged condition, θ_{\max} was found to increase by a constant magnitude between each heat treatment (~ 700 MPa). Conversely, in the H-charged condition, while the NA and UA heat treatments exhibited θ_{\max} values similar to those measured in the non-charged condition (note that differences in $\theta_{\max} < 300\text{-}400$ MPa are not considered significant [35]), a large increase in θ_{\max} was observed for the PA/H (increase of ~ 1500 MPa relative to PA/No H), followed by another slight increase for the OA/H condition. A similarly clear effect of H was also observed for $-d\theta/d\sigma$, as shown in Figure 55b. Starting with the non-charged condition, similar

values of $-d\theta/d\sigma$ (≈ 6) were observed between the NA and UA heat treatments, followed by an increase to 8.1 and 10.6 for the PA and OA heat treatments, respectively. Conversely, upon adding H, $-d\theta/d\sigma$ was found to be increased for all heat treatments relative to the non-charged condition, with the exception of OA, which had a similar $-d\theta/d\sigma \approx 10.7$ for both conditions. In particular, $-d\theta/d\sigma$ for UA/H and PA/H were significantly elevated compared to their respective non-charged condition results.

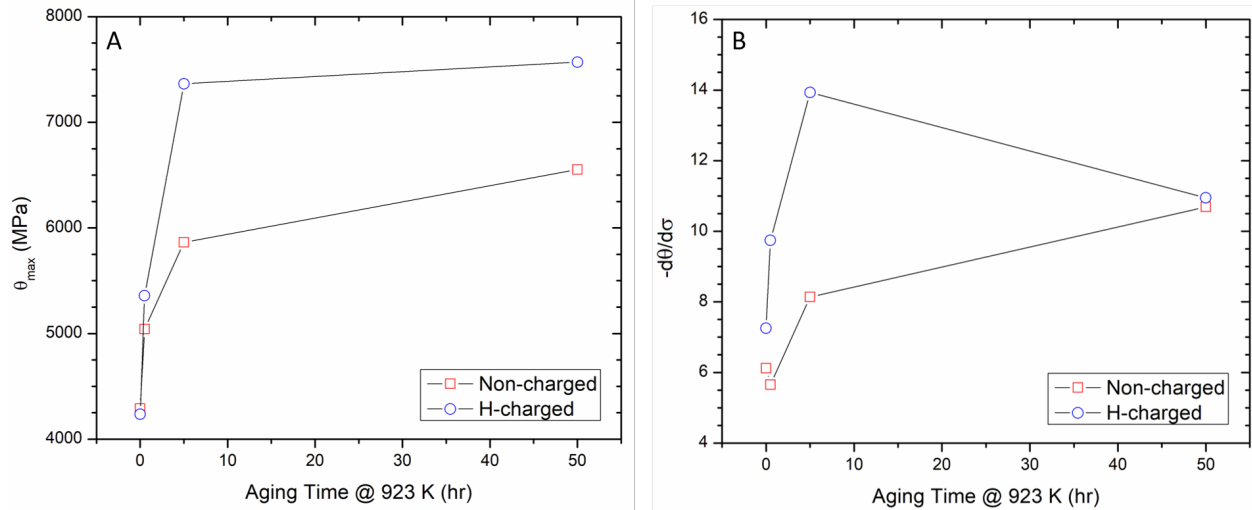


Figure 55 – Plot of (a) θ_{max} and (b) $-d\theta/d\sigma$ as a function of aging time and hydrogen. Parameters were obtained using the graphical method shown in Figure 54.

5.5. Discussion

The presented flow curves (Figure 49) and fractography (Figure 50 and Figure 51) demonstrate that the ductility and tensile strength (Table 12) of Monel K-500 are decreased in the presence of H across all four tested aging conditions. Moreover, analysis of work hardening curves (Figure 53) revealed a strong effect of H on Stage III work hardening behavior, as quantified by θ_{max} and $-d\theta/d\sigma$ (Figure 55a-b). In particular, significant increases in θ_{max} and $-d\theta/d\sigma$ were observed for the PA/H relative to PA/No H. Based on these findings, the following discussion will: (1) confirm the similarity in precipitate morphology between the non-charged and H-charged conditions, (2) evaluate the effect of H on mechanical behavior as a function of heat treatment, and (3) comment on the mechanistic implications of the current results.

5.5.1. Verification of similar precipitate morphologies between non-charged and H-charged conditions

A critical assumption of the current work is that the γ' morphology (*e.g.* size) and distribution is not appreciably modified during the thermal charging procedure utilized to introduce hydrogen into the tensile specimens. As discussed by Cheng et al. [17] and demonstrated by work hardening results for the

non-charged specimens in Figure 53, variations in the size of the precipitate could induce changes in the work hardening behavior that would complicate directly assessing the role of H. The extrapolation of γ' coarsening kinetics data previously obtained for Monel K-500 [19] to 573 K suggests that negligible growth (<0.01 nm) should be expected after 150 hours at 573 K. However, it has been previously shown that H can stabilize vacancies [36], which could cause an acceleration in the coarsening kinetics or assist in the nucleation of precipitates in the NA condition. To address the latter concern regarding nucleation, a 12.7-mm diameter, 2-mm thick disc specimen heat-treated to the NA condition was aged at 300°C for 335 hours. After annealing, the specimen was immediately water quenched and then polished flat for hardness testing. Ten Rockwell B (HRB) hardness measurements were taken from both the 300°C annealed NA specimen and a non-annealed NA specimen, which yielded an average hardness of 82.8 ± 2.1 HRB and 83.3 ± 2.7 HRB for the two conditions, respectively. As such, given the similarities in measured hardness, it was concluded that γ' nucleation did not occur during the thermal charging process. Second, to evaluate whether thermal charging affected the size distribution of the aged (UA, PA, and OA) heat treatments, a precipitate morphology analysis was completed using transmission electron microscopy on specimens prepared from the PA/H tensile specimen. A total of 375 precipitates were examined and the measured γ' size distribution was then compared to that obtained in Chapter 4 for the PA/No H condition. As shown by Figure 56, the two distributions are quite similar, suggesting that thermal H charging did not induce any significant changes in the γ' morphology or size distribution.

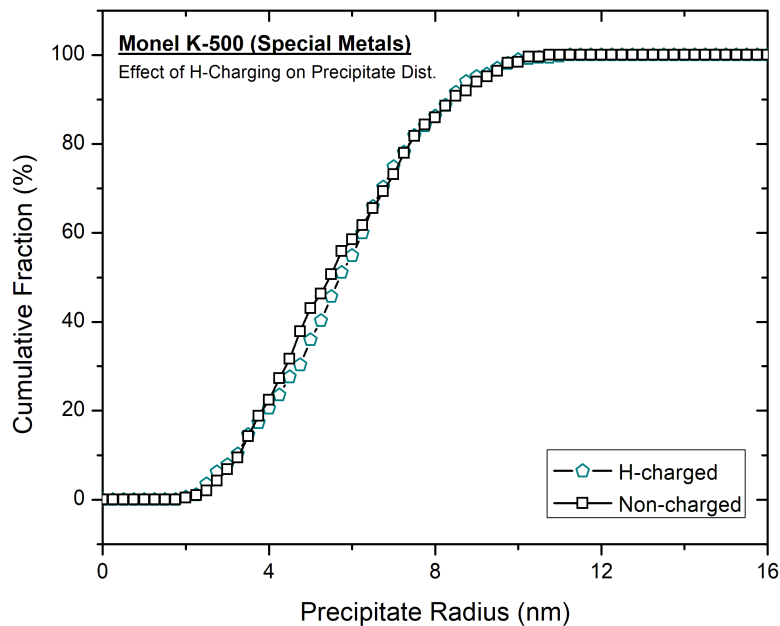


Figure 56 – Comparison of the γ' size distribution for the hydrogen-charged and non-charged specimens heat-treated to the peak-aged condition.

5.5.2. *Effect of hydrogen on the mechanical behavior of Monel K-500 as a function of heat treatment*

As demonstrated by the flow curves in Figure 49 and the work hardening metrics captured in Figure 55, tangible differences in mechanical behavior are observed in the presence of H for each heat treatment. First, considering the variation in yield strength as a function of heat treatment, the H-charged specimens exhibited an increased yield strength relative to the respective non-charged specimens in each of the tested aging conditions. However, comparison of the *change* in yield strength with H exposure indicates an apparent variation between the NA heat treatment versus the UA, PA, and OA heat treatments. Specifically, examination of Table 12 indicates that a difference in yield strength of 51 MPa was observed between the NA/H and NA/no H conditions, which can likely be attributed to H acting as a solute strengthener. Such an increase is consistent with the observations of Ulmer and Altstetter [37], who observed an increase in yield strength for 304 stainless steel on the order of 40-50 MPa/at. % of H. Therefore, if H contributions to yield strength are limited to solid solution strengthening effects, an increase on the order of 60-65 MPa would be expected between the H-charged and non-charged conditions for the UA, PA, and OA heat treatments (recall that UA/H contained 1.26 at. % H and that PA/H and OA/H contained 1.32 at. % H). However, as shown in Table 12, increases in yield strength of 115, 115, and 126 MPa were observed between the H-charged and non-charged conditions for the UA, PA, and OA heat treatments, respectively. Such increases in yield strength relative to expectations for H acting as a solid solution strengthener suggests that H may be affecting other strengthening mechanisms in the aged alloys. This difference is schematically shown in Figure 57 below. Given that the similar grain sizes across the four aging conditions (shown in Chapter 4) and the lack of cold work prior to straining, such differences are likely attributable to an H effect on precipitation hardening, which suggests that H modifies dislocation-precipitate interactions.

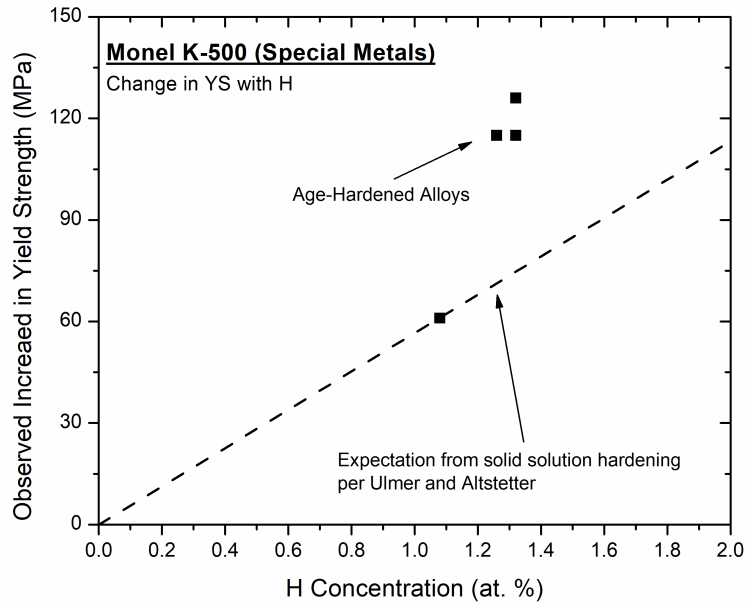


Figure 57 - Observed increase in yield strength versus hydrogen concentration. Note that the linear relationship for solid solution hardening is adapted based on the work of Ulmer and Altstetter [37].

The possibility that H may modify dislocation-precipitate interactions is directionally consistent with the observed variations in the initial hardening rate (θ_{\max}), shown in Figure 55a. Considering the non-charged condition, θ_{\max} is found to increase linearly with increased aging time, while a clear deviation from this linear trend is observed in the H-charged condition. Specifically, a significant increase in θ_{\max} is observed between H-charged UA and PA conditions. Given that variations in solute content are not expected to appreciably impact θ_{\max} [17,34], such differences are likely not attributable to the observed differences in H concentration. This conjecture is supported by the similarities in θ_{\max} between the H-charged and non-charged conditions in the NA and UA alloy. Historically, strong increases in work hardening behavior for different aging conditions in alloys hardened by secondary phases are attributed to two possible factors: (1) a transition to dislocation bypassing mechanisms (*i.e.* looping) and/or (2) constraint effects from non-deformable particles residing in a plastically-deforming matrix [17,38,39]. Considering the latter, impenetrable particles can contribute to the work hardening rate *via* image stresses due to elastic constraint (since the matrix is plastically deforming, but the particle is not), with the magnitude of this effect being equal to βGf [38], where β is a scaling factor on the order of 0.5, G is the shear modulus of the particle, and f is the particle volume fraction. Assuming a shear modulus of 77 GPa for Ni_3Al [40] and a γ' volume fraction of 6.5% [19], the work hardening contribution from non-deformable particles is estimated to be ~ 2500 MPa [38,39]. Considering the TEM results presented in Chapter 4, it is known that a transition

to non-shearable particles occurs in the non-charged condition between the PA and OA heat treatments. As such, a possible effect from elastic constraint would therefore arise between these two conditions. However, examination of Figure 55a indicates that the difference in θ_{\max} between the non-charged PA and OA heat treatments is ~ 700 MPa, which is significantly less than the ~ 2500 MPa expected based on the above calculation. As such, this large discrepancy indicates that the effect of elastic constraint does not explain the current results. Speculatively, this effect may not be applicable (or perhaps reduced in magnitude) in the current study due to the γ' precipitates remaining highly coherent, even after long aging times [19]. As such, atomic registry between the precipitate and matrix is maintained, which is not the case for the incoherent particles for which the elastic constraint theory was developed [38,39].

Considering the second possible explanation for the enhanced θ_{\max} in the PA/H alloy, as shown in Figure 58, transmission electron microscopy comparing the PA/H and PA/no H confirms the onset of dislocation bypassing in the H-charged condition. Specifically, while the development of planar bands along the trace of the $\{111\}$ planes (Figure 58a and c; planar bands indicated by red arrows) occurs in both the H-charged and non-charged PA alloys, examination at higher magnification reveals the widespread formation of dislocation loops (Figure 58b, red arrows) in the PA/H specimen. Such behavior is a significant change from the particle shearing observed in the PA/No H alloy, as demonstrated by the long planar array composed of dislocation pairs shown in Figure 58d. Finally, examination of the dislocation loop arrangement reveals the “stacking” of loops on parallel planes (left red arrow in Figure 58b), consistent with the Hirsch mechanism for looping [41]. Critically, the appearance of such ‘stacks’ suggests ready dislocation cross-slip [41], which is unexpected based on previous literature suggesting that H hinders cross-slip [6,7].

Lastly, considering the effect of H on $-d\theta/d\sigma$, Figure 55b indicates that $-d\theta/d\sigma$ either increases or remains constant in the presence of H. While the physical basis for this ‘dynamic recovery’ parameter is still debated in the literature [34,42–45], it is consistently related to the annihilation of dislocation line length (typically invoked via cross-slip processes [34,42]), with higher values of $-d\theta/d\sigma$ indicating increased rates of annihilation [17]. The observation of loop ‘stacks’ in Figure 58b in the PA/H alloy is directionally consistent with the observed increase in $-d\theta/d\sigma$ in Figure 55b, since such dislocation arrangements are known to form through complex cross-slip maneuvers [41,46]. As such, the current results in Figure 55b are notable as literature on H-dislocation interactions consistently suggests that H impedes dislocation annihilation processes [5–7], which would therefore result in H decreasing $-d\theta/d\sigma$ (*i.e.* closer to zero or less severe slope). In conclusion, while further interpretation of the enhanced $-d\theta/d\sigma$ are complicated by the ambiguous physical definition, taken together with the H-induced variations in yield strength and θ_{\max} , these results strongly suggest that H modifies dislocation-precipitate interactions.

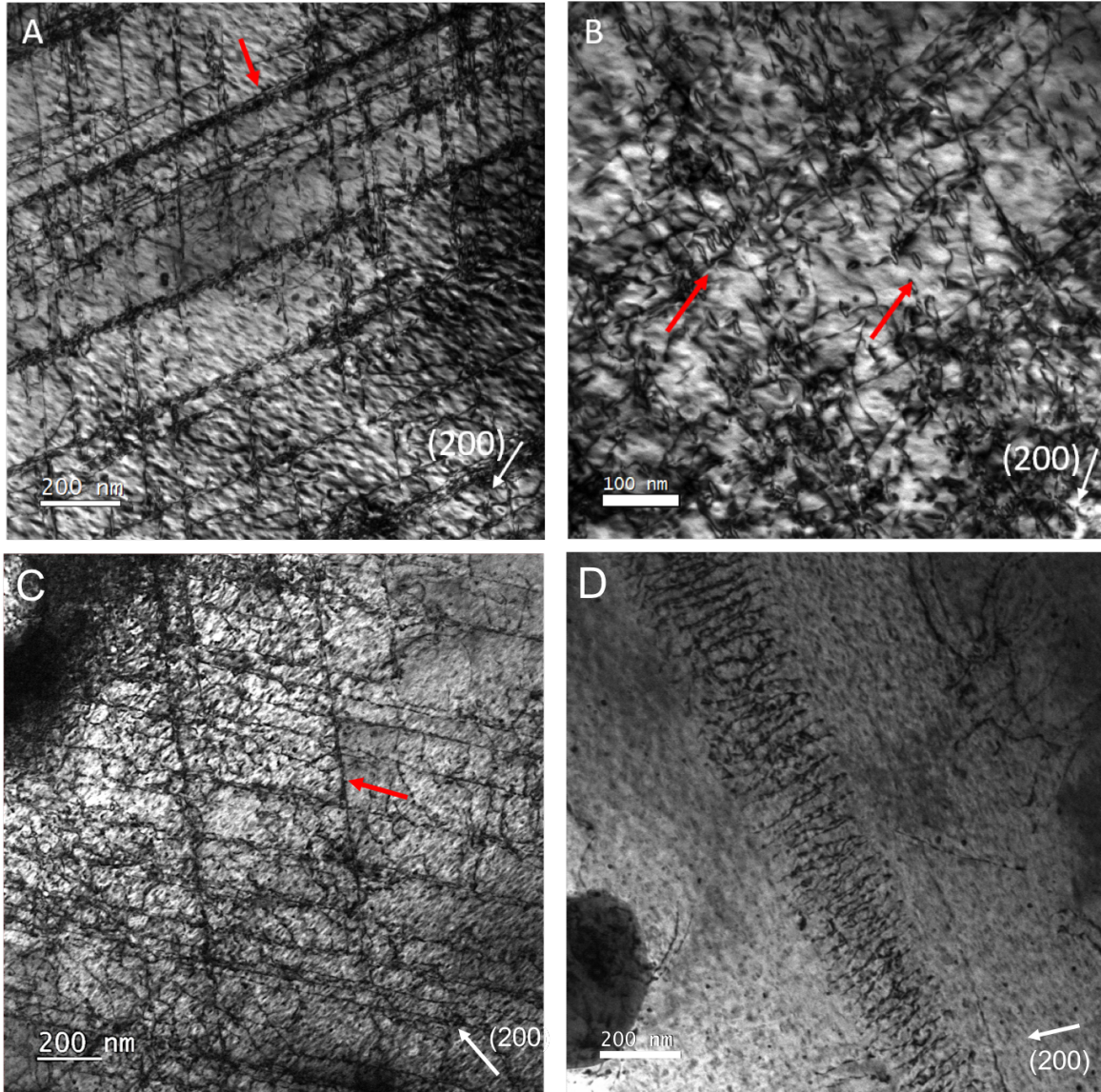


Figure 58 - Bright-field micrographs of the bulk slip morphology in the hydrogen-charged (a,b) and non-charged (c,d) peak-aged specimens tested to failure. The red arrow in (a) and (c) indicates planar slip bands oriented along the trace of the $\{111\}$ plane, while the red arrows in (b) indicates examples of dislocation looping.

5.5.3. Mechanistic interpretations

Mechanistically, the most tractable pathway for understanding the influence of H on precipitate-dislocation interactions would be to explain the observed onset of looping in the PA/H alloy. Given that a transition to looping will occur if the resistance to particle shearing is increased, this suggests that the observed behavior can be explained by six possible effects [44,47]: increases in particle size, chemical strengthening, order strengthening, coherency strengthening, modulus strengthening, and stacking fault strengthening. Considering each possibility in turn, Figure 56 demonstrates that the particle radius

distribution was effectively identical between the PA/H and PA/No H conditions, strongly suggesting that differences in size cannot explain the observed transition to looping. Chemical hardening, which would arise from the resistance to creating new interfaces as the particle is sheared, is also unlikely to have a tangible effect due to the low interfacial energy of the γ/γ' interface (which is confirmed by the spherical nature of the particles) [20]. Moreover, a mechanism by which hydrogen would increase the interfacial energy is unclear, given the evidence for H reducing interfacial energies (such as grain boundary energies) [48]. Differences from coherency strengthening can also be neglected since the stresses due to misfit strains are small (the misfit strain between γ/γ' is on the order of $<0.1\%$ for Monel K-500 [19,20]) and the presence of H would only reduce them further (since H has been shown to “shield” stresses [49]). Considering modulus strengthening, the similarity in shear moduli between the γ and γ' phases (assuming Ni for the γ), in which both are on the order of 70 GPa, would suggest that such an effect is unlikely to explain the onset of looping in the PA condition. Recent experiments have suggested that hydrogen can reduce the elastic modulus in Ni [50], but these findings are counter to atomistic modeling (which has been shown to accurately capture such elastic properties) that demonstrated that the elastic constants of Ni were insensitive to H, even at large concentrations [51]. Moreover, recent experiments by Hachet et al. have shown that the previously measured decreases in elastic properties with H in Ni can likely be attributed to enhanced vacancy concentrations and vacancy clustering, suggesting that H does not strongly affect elastic properties [52]. Stacking fault strengthening occurs when the stacking fault energy (SFE) of the precipitate is much lower than the matrix [44]. Given that the SFE in Ni_3Al is likely larger than the Ni-Cu matrix [53], such an effect can be neglected as well [20,54].

Finally, considering order hardening, this mechanism is regarded as the predominant contribution to strength in γ' -strengthened alloy and is linked to the generation of antiphase boundaries within the precipitate when dislocation shearing occurs [20,44]. As documented by Ardell [47], this strengthening mechanism is sensitive to variations in the antiphase boundary energy (APBE), with larger APBE values resulting in an increased resistance to shearing. Considering the current study, H-induced increases in the APBE could explain the transition from shearing to looping in the PA/H specimen, as this could increase the resistance of shearing sufficiently such that dislocation bypass mechanisms are more favorable. Computational results suggest that H may be trapped within the γ' precipitates [28], which would likely affect the APBE due to a well-known sensitivity to impurities [53]. However, the effect of H on the APBE for Ni_3Al has not been explicitly studied to date, thereby precluding a complete assessment of this possibility. In conclusion, while the mechanistic underpinnings for the observed change in deformation character for the PA/H specimen remain elusive, the current results establish that H appreciably modify precipitate-dislocation interactions in Monel K-500. Such results underscore the need to further explore the effect of H on fundamental deformation processes in precipitation-hardened alloys.

5.6. Conclusions

The influence of H on dislocation-precipitate interactions in a γ' -strengthened Ni-Cu superalloy was systematically evaluated through mechanical testing on four isothermal heat treatments. Analysis of these results, coupled with targeted microscopy of the PA heat treatments, revealed several important insights into H effects on deformation processes in precipitation-hardened alloys:

1. Specimens pre-charged with H exhibit increased yield strength and strongly reduced ductility, regardless of heat treatment, compared to non-charged specimens.
2. All heat treatments exhibited a clear transition in fracture morphology from ductile microvoid coalescence to brittle intergranular failure when pre-charged with H.
3. Analysis of the work hardening behavior revealed systematic differences between the non-charged and H-charged conditions. A strong increase in the initial work hardening rate was observed for the H-charged specimens relative to the non-charged specimens for the PA and OA conditions, while an enhanced Stage III slope was observed for the H-charged condition in the NA, UA, and PA conditions.
4. TEM of the deformation structure in the non-charged and H-charged PA specimens confirms that H induces an early transition from particle shearing to looping. Such results demonstrate that H appreciably affects dislocation-precipitate interactions, but the mechanism responsible for this effect is unclear.

5.7. Suggested Future Research Directions

There are several suggested research directions based on the work presented herein. First, given the clear modification of work hardening behavior in the presence of hydrogen across all four tested heat treatments, the effect of hydrogen-induced modifications in strain hardening and yield strength on the crack tip stress field should be explored. In particular, inclusion of these hydrogen-modified properties in strain gradient plasticity models, where stresses can be computed closer to the crack tip (and where such hydrogen-affected material properties likely occur) would be of interest. Second, a discrete dislocation dynamics modeling effort should be conducted to explore the effect of hydrogen on precipitate-dislocation interactions. In particular, it would be interesting to surround various sized precipitates with a given hydrogen concentration and then evaluate the dislocation motion as it shears or bypasses the particle. Perhaps such modeling efforts would provide further insights into the apparent increase in cross-slip for the PA heat treatment. With regards to current ongoing efforts, TEM will be conducted on the other H-charged conditions to determine the variation in dislocation morphology with heat treatment. Moreover, this effort will be coupled with TEM of specimens that were deformed to iteratively lower flow stress levels so as to

inform the deformation evolution behavior as a function of applied stress. Specimens in the non-charged condition will then be deformed to similar flow stress levels so as to enable a direct comparison of the deformation microstructure at equivalent “driving forces.”

5.8. Acknowledgements

The assistance of Dr. Joseph Ronevich, Dr. Chris San Marchi, and Mr. Jeff Campbell with H charging, the assistance of Mr. Michael Ritzo with TEM sample preparation and mechanical testing, and helpful discussions with Dr. Jishnu Bhattacharyya, Prof. Sean Agnew, Dr. Brian Somerday, and Prof. John Scully are gratefully acknowledged.

2.9. References

- [1] A.W. Thompson, I.M. Bernstein, The Role Of Metallurgical Variables In Hydrogen-Assisted Environmental Fracture, *Adv. Corros. Sci. Technol.* (1980) 53–175. doi:10.1007/978-1-4615-9065-1_2.
- [2] R.P. Gangloff, Critical issues in hydrogen assisted cracking of structural alloys, in: S. Shiilov (Ed.), *Environment Induc. Crack. Met.*, 2006: pp. 6337–6349.
- [3] C.D. Beachem, A new model for hydrogen-assisted cracking (hydrogen “embrittlement”), *Metall. Trans.* 3 (1972) 441–455. doi:10.1007/BF02642048.
- [4] I.M. Robertson, P. Sofronis, A. Nagao, M.L. Martin, S. Wang, D.W. Gross, et al., Hydrogen Embrittlement Understood, *Metall. Mater. Trans. B.* (2015). doi:10.1007/s11663-015-0325-y.
- [5] P.J. Ferreira, I.M. Robertson, H.K. Birnbaum, Hydrogen effects on the interaction between dislocations, *Acta Mater.* 46 (1998) 1749–1757. doi:10.1016/S1359-6454(97)00349-2.
- [6] I.M. Robertson, The effect of hydrogen on dislocation dynamics, *Eng. Fract. Mech.* 65 (2001) 671–692.
- [7] D. Delafosse, Hydrogen effects on the plasticity of face centred cubic (fcc) crystals, in: R.P. Gangloff, B.P. Somerday (Eds.), *Gaseous Hydrog. Embrittlement Mater. Energy Technol.*, Woodhead Publishing, 2012.
- [8] A. Barnoush, H. Vehoff, Recent developments in the study of hydrogen embrittlement: Hydrogen effect on dislocation nucleation, *Acta Mater.* 58 (2010) 5274–5285. doi:10.1016/j.actamat.2010.05.057.
- [9] Y.Z. Chen, H.P. Barth, M. Deutges, C. Borchers, F. Liu, R. Kirchheim, Increase in dislocation density in cold-deformed Pd using H as a temporary alloying addition, *Scr. Mater.* 68 (2013) 743–746. doi:10.1016/j.scriptamat.2013.01.005.
- [10] Y.Z. Chen, X.Y. Ma, X.H. Shi, T. Suo, C. Borchers, K.H. Zhang, et al., Hardening effects in plastically deformed Pd with the addition of H, *Scr. Mater.* 98 (2015) 48–51. doi:10.1016/j.scriptamat.2014.11.012.
- [11] A.M. Brass, D. Roux, J. Chêne, Role of secondary γ' precipitation and of hydrogen in the first stage of the plastic deformation of the ν matrix of a Ni base superalloy single crystal, *Mater. Sci. Eng. A.* 323 (2002) 97–102. doi:10.1016/S0921-5093(01)01349-1.

- [12] S. Wang, A. Nagao, K. Edalati, Z. Horita, I.M. Robertson, Influence of hydrogen on dislocation self-organization in Ni, *Acta Mater.* 135 (2017) 96–102. doi:10.1016/j.actamat.2017.05.073.
- [13] I.M. Robertson, H.K. Birnbaum, Effect of hydrogen on the dislocation structure of deformed nickel, *Scr. Metall.* 18 (1984) 269–274. doi:10.1016/0036-9748(84)90521-0.
- [14] W.A. McInteer, A.W. Thompson, I.M. Bernstein, The effect of hydrogen on the slip character of nickel, *Acta Metall.* 28 (1980) 887–894. doi:10.1007/BF02655107.
- [15] J.A. Wert, X. Huang, G. Winther, W. Pantleon, H.F. Poulsen, Revealing deformation microstructures, *Mater. Today.* 10 (2007) 24–32. doi:10.1016/S1369-7021(07)70206-7.
- [16] J. Jiang, T. Ben Britton, A.J. Wilkinson, The orientation and strain dependence of dislocation structure evolution in monotonically deformed polycrystalline copper, *Int. J. Plast.* 69 (2015) 102–117. doi:10.1016/j.ijplas.2015.02.005.
- [17] L.M. Cheng, W.J. Poole, J.D. Embury, D.J. Lloyd, The influence of precipitation on the work-hardening behavior of the aluminum alloys AA6111 and AA7030, *Metall. Mater. Trans. A.* 34 (2003) 2473–2481. doi:10.1007/s11661-003-0007-2.
- [18] J.R. Davis, ed., Nickel, Cobalt, and Their Alloys: ASM Specialty Handbook, in: 2000: pp. 167–188.
- [19] G.K. Dey, P. Mukhopadhyay, Precipitation in the Ni-Cu-base alloy Monel K-500, *Mater. Sci. Eng.* 84 (1986) 177–189. doi:10.1016/0025-5416(86)90236-3.
- [20] G.K. Dey, R. Tewari, P. Rao, S.L. Wadekar, P. Mukhopadhyay, Precipitation hardening in nickel-copper base alloy monel K 500, *Metall. Trans. A.* 24 (1993) 2709–2719. doi:10.1007/BF02659495.
- [21] D.H. Lassila, H.K. Birnbaum, The effect of diffusive hydrogen segregation on fracture of polycrystalline nickel, *Acta Metall.* 34 (1986) 1237–1243. doi:10.1016/0001-6160(86)90010-6.
- [22] ASTM Standard E647-13: Standard Test Method for Measurement of Fatigue Crack Growth Rates, (2013). doi:10.1520/E0647-13E01.2.
- [23] S. Bechtel, M. Kumar, B.P. Somerday, M.E. Launey, R.O. Ritchie, Grain-boundary engineering markedly reduces susceptibility to intergranular hydrogen embrittlement in metallic materials, *Acta Mater.* 57 (2009) 4148–4157. doi:10.1016/j.actamat.2009.05.012.
- [24] B.P. Somerday, J.A. Campbell, K.L. Lee, J.A. Ronevich, C. San Marchi, Enhancing safety of hydrogen containment components through materials testing under in-service conditions, *Int. J. Hydrogen Energy.* (2016) 4–11. doi:10.1016/j.ijhydene.2016.04.189.
- [25] F. Jones, R. Pehlke, Solubility of hydrogen in solid Ni–Co and Ni–Cu alloys, *Metall. Trans.* 2 (1971). <http://link.springer.com/article/10.1007/BF02814909>.
- [26] R.P. Gangloff, H.M. Ha, J.T. Burns, J.R. Scully, Measurement and Modeling of Hydrogen Environment-Assisted Cracking in Monel K-500, *Metall. Mater. Trans. A.* 45 (2014) 3814–3834. doi:10.1007/s11661-014-2324-z.
- [27] J. Ai, H.M. Ha, R.P. Gangloff, J.R. Scully, Hydrogen diffusion and trapping in a precipitation-hardened nickel–copper–aluminum alloy Monel K-500 (UNS N05500), *Acta Mater.* 61 (2013) 3186–3199. doi:10.1016/j.actamat.2013.02.007.

- [28] M.I. Baskes, J.E. Angelo, N.R. Moody, SAND-94-8741C: Atomistic calculations of hydrogen interactions with Ni₃Al grain boundaries and Ni/Ni₃Al interfaces, 1994.
- [29] R.E. Reed-Hill, R. Abbaschian, Physical metallurgy principles, Van Nostrand, Princeton, 1994.
- [30] J.A. Harris, R.C. Scarberry, C.D. Stephens, Effects of Hydrogen on Engineering Properties of MONEL Nickel-Copper Alloy K-500, Corrosion. 28 (1972) 57–62.
- [31] K.D. Eford, Failure of Monel Ni-Cu-Al Alloy K-500 Bolts in Seawater, Mater. Perform. 24 (1985) 37–40.
- [32] L.H. Wolfe, M.W. Joosten, Failures of Nickel/Copper Bolts in Subsea Applications, SPE Prod. Eng. 3 (1988) 382–386. doi:10.2118/16632-PA.
- [33] B.C.R. Troconis, Z.D. Harris, H. Ha, J.T. Burns, J.R. Scully, The effect of heat-to-heat variations in metallurgy and hydrogen-metal interactions on the hydrogen embrittlement of Monel K-500, Mater. Sci. Eng. A. 703 (2017) 533–550. doi:10.1016/j.msea.2017.07.019.
- [34] U.F. Kocks, H. Mecking, Physics and phenomenology of strain hardening: The FCC case, Prog. Mater. Sci. 48 (2003) 171–273. doi:10.1016/S0079-6425(02)00003-8.
- [35] Z.D. Harris, Personal communication with Warren Poole and Sean Agnew, (2017).
- [36] S.K. Lawrence, Y. Yagodzinskyy, H. Hanninen, E. Korhonen, F. Tuomisto, Z.D. Harris, et al., Effects of grain size and deformation temperature on hydrogen-enhanced vacancy formation in Ni alloys, Acta Mater. 128 (2017) 218–226. doi:10.1016/j.actamat.2017.02.016.
- [37] D.G. Ulmer, C.J. Altstetter, Hydrogen-induced strain localization and failure of austenitic stainless steels at high hydrogen concentrations, Acta Metall. Mater. 39 (1991) 1237–1248. doi:10.1016/0956-7151(91)90211-i.
- [38] J.W. Martin, Micromechanisms in particle-hardened alloys, Cambridge University Press, Cambridge, UK, 1980.
- [39] L.M. Brown, D.R. Clarke, Work hardening due to internal stresses in composite materials, Acta Metall. 23 (1975) 821–830. doi:10.1016/0001-6160(75)90198-4.
- [40] D.E. Kim, S.L. Shang, Z.K. Liu, Effects of alloying elements on elastic properties of Ni₃Al by first-principles calculations, Intermetallics. 18 (2010) 1163–1171. doi:10.1016/j.intermet.2010.02.024.
- [41] F.J. Humphreys, P.B. Hirsch, The Deformation of Single Crystals of Copper and Copper-Zinc Alloys Containing Alumina Particles. II. Microstructure and Dislocation-Particle Interactions, Proc. R. Soc. A Math. Phys. Eng. Sci. 318 (1970) 73–92. doi:10.1098/rspa.1970.0134.
- [42] Y. Estrin, Dislocation-Density-Related Constitutive Modeling, in: A.S. Krausz, K. Krausz (Eds.), Unified Const. Laws Plast. Deform., Academic Press, 1996: pp. 69–107.
- [43] D. Kuhlmann-Wilsdorf, Theory of plastic deformation: - properties of low energy dislocation structures, Mater. Sci. Eng. A. 113 (1989) 1–41. doi:10.1016/0921-5093(89)90290-6.
- [44] A.S. Argon, Strengthening mechanisms in crystal plasticity, Oxford University Press, 2008.
- [45] E. Nes, Modelling of work hardening and stress saturation in FCC metals, Prog. Mater. Sci. 41

- (1997) 129–193. doi:10.1016/S0079-6425(97)00032-7.
- [46] Y. Xiang, D.J. Srolovitz, L.T. Cheng, W. E, Level set simulations of dislocation-particle bypass mechanisms, *Acta Mater.* 52 (2004) 1745–1760. doi:10.1016/j.actamat.2003.12.016.
- [47] A.J. Ardell, Precipitation hardening, *Metall. Trans. A.* 16 (1985) 2131–2165. doi:10.1007/BF02670416.
- [48] S. Jothi, T.N. Croft, S.G.R. Brown, Influence of grain boundary misorientation on hydrogen embrittlement in bi-crystal nickel, *Int. J. Hydrogen Energy.* (n.d.). doi:http://dx.doi.org/10.1016/j.ijhydene.2014.07.020.
- [49] H.K. Birnbaum, P. Sofronis, Hydrogen-enhanced localized plasticity—a mechanism for hydrogen-related fracture, *Mater. Sci. Eng. A.* 176 (1994) 191–202. doi:10.1016/0921-5093(94)90975-X.
- [50] S.K. Lawrence, B.P. Somerday, M.D. Ingraham, D.F. Bahr, Probing the Effect of Hydrogen on Elastic Properties and Plastic Deformation in Nickel Using Nanoindentation and Ultrasonic Methods, *Jom.* 70 (2018) 1068–1073. doi:10.1007/s11837-018-2850-z.
- [51] M. Wen, A. Barnoush, K. Yokogawa, Calculation of all cubic single-crystal elastic constants from single atomistic simulation: Hydrogen effect and elastic constants of nickel, *Comput. Phys. Commun.* 182 (2011) 1621–1625. doi:10.1016/j.cpc.2011.04.009.
- [52] G. Hachet, A. Metsue, A. Oudriss, X. Feugas, Influence of hydrogen on the elastic properties of nickel single crystal: A numerical and experimental investigation, *Acta Mater.* 148 (2018) 280–288. doi:10.1016/j.actamat.2018.01.056.
- [53] Y.F. Wen, J. Sun, J. Huang, First - Principles study of stacking fault energies in Ni3Al intermetallic alloys, *Trans. Nonferrous Met. Soc. China (English Ed.)* 22 (2012) 661–664. doi:10.1016/S1003-6326(11)61229-6.
- [54] D. Raynor, J.M. Silcock, Strengthening Mechanisms in γ' Precipitating Alloys, *Met. Sci.* 4 (1970) 121–130. doi:10.1179/msc.1970.4.1.121.

Chapter 6. Initial assessment of near-crack wake deformation structure

6.1. Overview

The initial results of a multiple length-scale approach to assessing the deformation proximate to the crack wake are presented, with particular emphasis on leveraging high-resolution electron backscatter diffraction (HR-EBSD) to evaluate the geometrically necessary dislocation (GND) density distribution. The GND density distribution is evaluated for a peak-aged Monel K-500 specimen that was tested under slow-rising K conditions in 0.6 M NaCl at $-1200 \text{ mV}_{\text{SCE}}$. An evaluation of the GND density distribution reveals that deformation is highly localized to the crack wake, with GND metrics decaying to a constant level after 25-40 μm . Moreover, the average GND density was qualitatively observed to increase with increasing K_{I} , in agreement with the expectations from strain gradient plasticity theories. Finally, neighboring grains were found to exhibit different distributions of GND density, despite experiencing nominally similar K_{I} , underscoring the importance of grain orientation when attempting to compare dislocation patterning.

6.2. Introduction

Recent efforts to mechanistically understand the role of hydrogen-enhanced deformation in creating the conditions for hydrogen-assisted cracking has led to the widespread utilization of a focused ion beam (FIB)/transmission electron microscopy (TEM) approach for assessing the deformation structure proximate to the fracture surface [1]. In particular, Robertson and coworkers have leveraged this technique to characterize the effect of hydrogen on deformation structure evolution across numerous alloy systems, including: polycrystalline nickel [2,3], polycrystalline iron [4], 300-series stainless steels [5], ferritic-pearlitic steel [6], martensitic steel [7], and equimolar alloys [8,9]. In each case, the authors noted that the deformation structure was more refined in the presence of hydrogen as compared to testing in laboratory air. Similar findings have also been reported by other authors in polycrystalline Fe [10–12] and are directionally consistent with X-ray diffraction peak broadening experiments (and TEM) conducted on cold-rolled Pd [13]. Such observations have subsequently been used as evidence to advance the view that hydrogen-induced degradation is predominantly driven by hydrogen-plasticity interactions, resulting in the formulation of the hydrogen-enhanced, plasticity-mediated decohesion mechanism [1].

While this proposed mechanism enjoys considerable experimental support from the aforementioned FIB/TEM experiments, several outstanding questions must still be addressed regarding the significance of the underlying evidence. First, as noted by Keller et al. based on the examination of dislocation structure evolution as a function of strain in pure Ni tensile specimens [14], the measured grain-to-grain variation in both dislocation cell diameter and type is not insignificant. Specifically, standard deviations reaching between 30 and 50% of the mean cell diameter can be observed within a single specimen deformed to a given level of strain [14]; such behavior suggests that differences in grain orientation can significantly influence the observed dislocation patterning, as has been extensively documented in the literature [15–17]. However, despite this well-known influence, many of the noted studies have not held this variable constant when comparing deformation structures from specimens tested in hydrogen versus those tested in air. Moreover, given the observed statistical variation in cell diameter within a single specimen [14], it is reasonable to question whether the examination of a single FIB/TEM specimen can be considered globally representative. Such experimental complications may explain why two studies comparing deformation structures in hydrogen-charged versus non-charged Ni did not observe any evidence of deformation refinement in the hydrogen condition [18,19].

Second, experiments conducted on fatigue [5] and monotonically [7] loaded specimens did not examine the deformation structure at a constant stress intensity (K). Given that the stress/strain field proximate to the crack is explicitly dependent on the applied stress intensity [20], it is reasonable to expect

that such differences could give rise to variations in the observed dislocation patterning. Such a possibility is supported by strain gradient plasticity theories, which predict an appreciable increase in the geometrically necessary dislocation (GND) density proximate to the crack tip with increasing K [21]. Finally, the inherent limitation of the TEM/FIB approach is the small material area sampled during characterization, which is typically on the order of tens of μm^2 . Given this areal limitation, in addition to the previously noted complications of grain orientation and applied driving force, the use of characterization techniques which can inform deformation behavior at larger length scales may be worthwhile, particularly if such methods can preserve 100 nm-level resolution.

Towards this end, the calculation of GND densities proximate to the crack wake using high-resolution electron backscatter diffraction (HR-EBSD) via cross-correlation techniques offers promise due to an attractive combination of spatial resolution (>75 nm) and sampling area ($\sim 100\text{s}-1000\text{s}$ of μm^2) [22–24]. This approach has been extensively applied by Wilkinson and coworkers to characterize deformation distributions induced by a wide range of processes, including: Cu deformed in tension [25], blocked slip bands in Ti [26], thermal stress effects from carbides in a Ni-base superalloy [27], after fatigue in Ti-6Al-4V [28], and from microstructurally-small crack growth from inclusions in a Ni-based superalloy [29]. Given the widespread successful use of this characterization strategy, the following study will seek to employ this approach to assess near-crack wake deformation as a possible complementary technique to FIB/TEM.

6.2.1. Chapter objective and research question

The objective of this chapter is to present the initial results of a HR-EBSD study which sought to evaluate near-fracture surface deformation characteristics for a Ni-base superalloy specimen which exhibited hydrogen environment-assisted cracking (HEAC). Fundamentally, this goal of this effort is to evaluate whether or not differences in bulk alloy characteristics (such as slip morphology) affect the deformation behavior proximate to the crack tip. Once this relationship has been established, this multiple length-scale approach could then enable the assessment of the local failure criterion on a grain-by-grain basis. Such insights would then be leveraged to inform the development of physically-based models for hydrogen cracking. However, given that this work is on-going, the following chapter will only seek to inform the reader about recent efforts to develop and implement this characterization approach. In particular, the chapter will attempt to provide an initial assessment of how does GND density distribution evolve with:

1. Depth from the crack wake
2. Stress intensity (K)

3. Grain orientation

6.3. Experimental methods and material

6.3.1. Material

All experiments were conducted on a single-edge notched tension specimen of Monel K-500, which had been heat-treated to the peak-aged (PA) condition using the following protocol: solution treated for 1 hour at 1223 K, followed by an immediate water quench, and then aging for 5 hours at 623 K, followed by an immediate water quench. HEAC was induced via slow-rising K testing at a constant elastic $dK/dt = 0.33 \text{ MPa}\sqrt{\text{m/hr}}$ while immersed in 0.6 M NaCl at an applied potential of $-1200 \text{ mV}_{\text{SCE}}$. Additional details of the testing methodology are provided in Chapter 4.

6.3.2. Bulk specimen preparation

After HEAC testing was complete, the fracture surface was excised from the gage section using a low-speed cutoff saw. To ensure that extraneous deformation was not introduced during this process, the saw cut was made at least 3 mm away from the fracture surface. An EBSD study characterizing the depth of saw damage (not shown) indicates that the maximum extent of damage is less than 600 μm , suggesting that the cut was made sufficiently far from the fracture surface to preclude saw-induced artifacts. After the sample was excised, the sample thickness (B; $\sim 2.68 \text{ mm}$) was progressively thinned using SiC papers and diamond slurries, finishing with a 1 μm slurry, to a final thickness of 1.4 mm. Similarly, after the thickness of the sample was thinned, the sample height was reduced from $\sim 3 \text{ mm}$ to 500-600 μm using SiC papers and diamond slurries, also finishing with the 1 μm slurry. During these thinning steps, extensive care was taken to minimize polishing-induced damage from lower grit sizes to the specimen by removing at least 3x the average particle size of the preceding SiC grinding paper before advancing to next grit size. For example, since the supplier-reported average particle size for the 400-grit SiC paper is $\sim 22 \mu\text{m}$, a minimum of 66 μm (typically 70 μm) was removed using the 600-grit SiC paper before advancing to the 800-grit SiC paper. As such, after the polishing steps were completed, the final specimen dimensions were $\sim 1.4 \text{ mm} \times 12.5 \text{ mm} \times 0.6 \text{ mm}$ (W x L x H). The width value of 1.4 mm was selected so as to ensure that the sample was evaluated in a region which exhibited a plane strain stress state [20].

After polishing, an argon broad-beam ion mill (Hitachi IM4000) was utilized to expose a cross-section of material at a surface condition suitable for HR-EBSD. An example of this cross-section is shown in Figure 59 below. Briefly, the sample was mounted such the ion mill beam (represented by the red arrow in Figure 59) impinged on the ‘bottom’ surface of the specimen, in a direction perpendicular to the fracture surface (indicated by the white dashed line in Figure 59). Given that localized heating of the specimen may occur during broad-beam ion milling, an EBSD study (not shown) was conducted using cold-rolled Monel

K-500 prepared using the above polishing procedure so as to identify the optimal parameters for cross-sectioning. Characterization of the kernel average misorientation (KAM) via EBSD before and after ion milling revealed no observable effect for a two-hour cross-section mill completed using an accelerating voltage of 6 keV (which was sufficient to mill through the $\sim 600 \mu\text{m}$ thickness of the test specimen). Typical ‘cross-section’ dimensions are $800\text{-}1000 \mu\text{m}$ in width and between $25\text{-}75 \mu\text{m}$ in depth. After the completion of ion milling, the specimen was soaked in acetone to remove residue mounting wax, followed by a second soak in methanol to remove the acetone film. The advantage of this cross-section approach is the ability to (1) expose the region proximate to the crack wake with negligible edge rounding, thereby facilitating characterization to within $300\text{-}500 \text{ nm}$ of the fracture surface and (2) expose a region at a specific crack length so as to evaluate the deformation behavior at a specific K of interest. For the current study, a K of $\sim 45 \text{ MPa}\sqrt{\text{m}}$ was targeted so as to enable the assessment of multiple grains at a similar crack tip driving force.

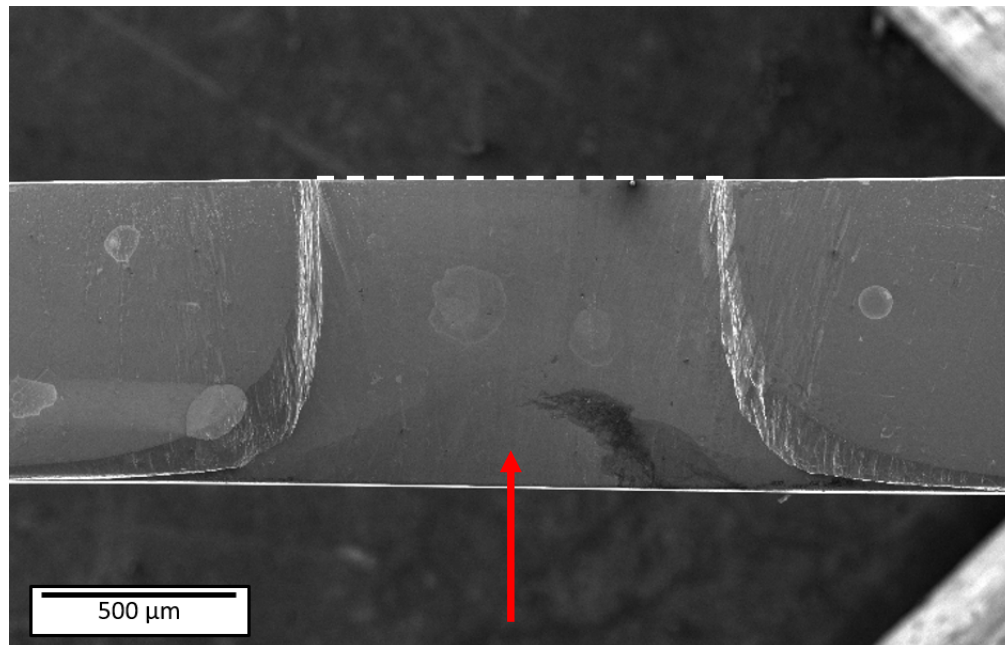


Figure 59 – Example of the cross-section exposed after Ar broad-beam ion milling. The red arrow notes the impingement direction of the Ar ions, while the white dashed line reflects the location of the fracture surface.

6.3.3. Electron backscatter diffraction and calculation of geometrically necessary dislocation density maps

Electron backscatter diffraction (EBSD) was completed at a magnification of $350\times$ to allow for the broad assessment of relative misorientation (as a proxy for deformation) ‘far’ from the fracture surface ($\sim 200\text{-}300 \mu\text{m}$). These ‘global’ EBSD maps were collected using a FEI Helios DB SEM/FIB that was

equipped with the Oxford Symmetry EBSD detector. Pertinent scan parameters were an accelerating voltage of 30 keV, probe current of 3.2 nA, 2x2 binning, and a step size of 400 nm. HR-EBSD maps were then collected over the near-fracture surface region examined via broad-scale EBSD at a magnification of 1500x using an accelerating voltage of 30 keV, probe current of 3.2 nA, 2x2 binning, and a step size of 150 nm.

The Kikuchi patterns collected during HR-EBSD are utilized to generate maps of the GND density using the commercial cross-correlation analysis software, CrossCourt4. The advantage of calculating GND densities using cross-correlation methods is the significant improvement in resolution relative to traditional Hough transform approaches [30]. As described by Britton and coworkers (and schematically shown in Figure 60) [30,31], the GND calculation occurs as follows. First, reference patterns to which each pixel (for a given grain) will be compared are selected based on pattern quality and the kernel average misorientation. Given that strain-free references for each grain/sub-grain were not collected for this work (since a strain-free location does not exist within the sample), all calculated values are relative as opposed to absolute. Once a suitable set of reference patterns has been selected, each Kikuchi pattern collected during the HR-EBSD scan is divided into separate regions of interest (ROIs). The number of ROIs used in the calculation can be increased to reduce error, but at the expense of exponentially longer computational times. In the current study, 20 ROIs were used. Next, the cross-correlation function of each of these 20 ROIs is then calculated, resulting in a “cross-correlation function peak”. The relative shift in this peak between each of the reference and sample ROIs is then utilized to generate the deformation gradient tensor for the Kikuchi pattern of interest, which can then be used to calculate the strain and rotation for the evaluated pixel relative to the reference pattern. Additional passes using a remapping procedure, which corrects for errors induced by large rotations between the reference and test pattern, can then be employed to improve calculation quality [31]. Once these shifts are known, the local curvature about the pixel of interest can then be calculated, which is known to be related to the geometrically necessary dislocation density via the Nye tensor [30]. It is important to recognize that for FCC materials, the Nye tensor is under-constrained due to the large number of possible slip systems (12 versus 9 strain components in the curvature tensor), which results in multiple solutions. The ‘correct’ solution to the Nye tensor is then selected based on the principle that the dislocation line energy will be minimized [30]. For a complete description of this calculation strategy, the reader is referred to the reviews by Britton and coworkers [30,31].

There are two critical experimental parameters when collecting Kikuchi patterns for GND analysis: step size and binning mode [23]. Regarding the former, Ruggles et al. demonstrated that the calculated GND density can be highly dependent on the applied step size [24]. However, he also noted that a step size ‘plateau’ existed for the calculated GND density, where the density was independent of step size, between

step sizes of 100-800 nm [24]. As such, in the current study, all HR-EBSD scans were collected using a step size of 150 nm, which is squarely in the middle of the identified invariant region. Second, increased binning of the camera pixels to improve signal (at the expense of increased noise) can affect the GND calculation by degrading the pattern quality, with the effect becoming acute when 8x8 binning is employed [23]. However, Jiang et al. demonstrated that the binning effect on calculated GND density was negligible between 1x1 (no binning) and 2x2 binning [23]. As such, a 2x2 binning mode is utilized in all HR-EBSD scans collected in the current study.

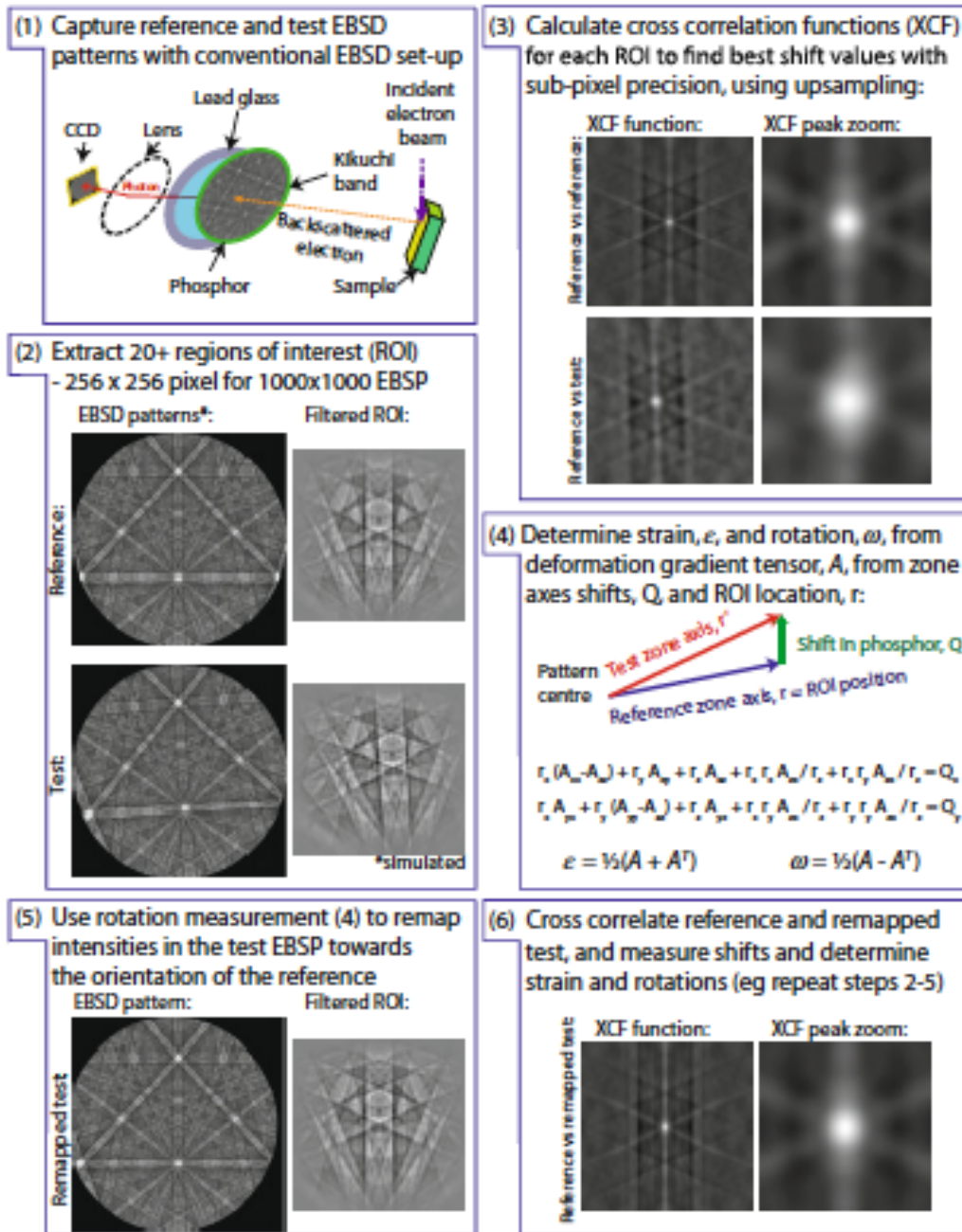


Figure 60 – Schematic documenting the cross-correlation calculation procedure. Taken from [31].

6.4. Results

The ion mill-exposed cross-section for the PA -1200 mV_{SCE} specimen is shown in Figure 61, where the white dashed lines delineate the region to be evaluated *via* HR-EBSD. Examination of the micrographs indicates that the ion mill successfully exposed the fracture surface without inducing substantial surface rounding. Moreover, the clearly observed grain structure in the micrograph suggests that the surface

condition as-milled is sufficient for EBSD. Close examination of the micrograph reveals ‘streaking’ patterns on the exposed surface oriented parallel to the impingement direction during ion milling. These streaks are a well-known artifact of broad-beam ion milling and are exacerbated by the presence of secondary phases that have different milling rates than the matrix (such as the TiC particles in Monel K-500). Such streaking may modify the subsequent GND analysis due to subtle shifts in the detector-sample geometry (from rounding). However, such effects would manifest in increased error, which can be quantified during the GND analysis via differences in the cross-correlation peak height for the reference and test pattern (XCF height) or the mean angular error in the pattern rotation [30]. Examination of the error metrics for calculated GND maps revealed no discernable increase in error over such features, suggesting that their influence is minimal. Regardless, such features are clearly non-ideal and, as discussed in Section 6.5, efforts are underway to utilize a Xe-based plasma focused ion beam instrument for cross-sectioning, which would effectively eliminate the observed streaking and improve the locational accuracy of the cross-sectioning (i.e. more reliably cross-section at the K of interest).

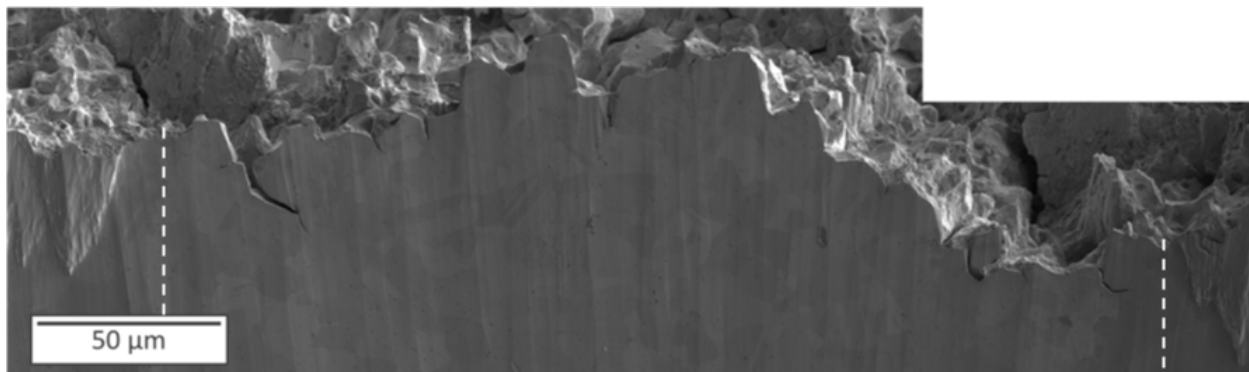


Figure 61 – Micrograph of the ion-mill cross-section, with the white dashed lines indicating the bounds of the HR-EBSD characterization and are consistent with the black dashed lines in Figure 62.

The evolution of the total stress intensity (K_I) over the exposed cross-section is shown in Figure 62, with the black dashed lines in Figure 62 corresponding to the white dashed lines in Figure 61. This crack length versus K_I relationship was corrected for the effect of crack tip plasticity on the dcPD-measured crack growth using the procedure outlined by Popernack [32]. Specifically, Popernack demonstrated that the true crack growth kinetics could be calculated by subtracting the resolution limit obtained during dry N_2 testing from the dcPD-measured crack growth rates generated during HEAC testing [32]. As such, the K_I for a given crack length can be reliably obtained and correlated with the observed deformation behavior, thereby enabling (1) a comparison of deformation as a function of K_I across a single specimen and/or (2) the comparison of deformation at a single K_I across multiple specimens.

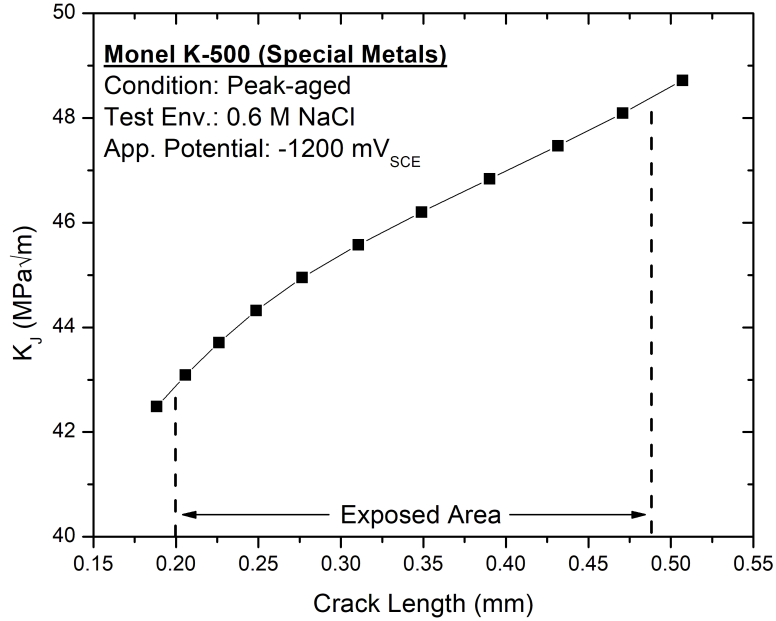


Figure 62 – Plot showing the total stress intensity (K_j) sampled over the exposed cross-section. Note that the crack length is measured relative to the end of the fatigue precrack (see Chapter 4 for additional details of testing). The black dashed lines correspond to the white dashed lines in Figure 61.

The inverse pole figure map with orientations relative to the Z-axis (IPF-Z; Z axis is out of the page) collected for the cross-sectional area is shown in Figure 63a, with along with the respective calculated kernel average misorientation (KAM [33]) map in Figure 63b. Examination of the KAM map (Figure 63b) reveals that the KAM values (which can be considered a proxy for GNDs [34]) effectively decay to a constant level at depths between 10-25 μm from the crack wake. This steep gradient in the KAM metric from the crack wake indicates that the deformation pertinent to hydrogen environment-assisted cracking is highly localized to the fracture plane. To quantify this degree of localization, the approximate depth where the KAM reaches the bulk level can be compared to the expected plane strain plastic zone size, which can be estimated by the Irwin relationship as follows [20]:

$$r_p = \frac{1}{3\pi} \left(\frac{K}{\sigma_{YS}} \right)^2 \quad (6.1)$$

Assuming $K \approx 45 \text{ MPa}\sqrt{\text{m}}$ and $\sigma_{YS} = 572 \text{ MPa}$ (from Chapter 4), this calculation indicates that the deformation decreases to the bulk level at approximately 4-5% of the plane strain plastic zone size ($\sim 650 \mu\text{m}$).

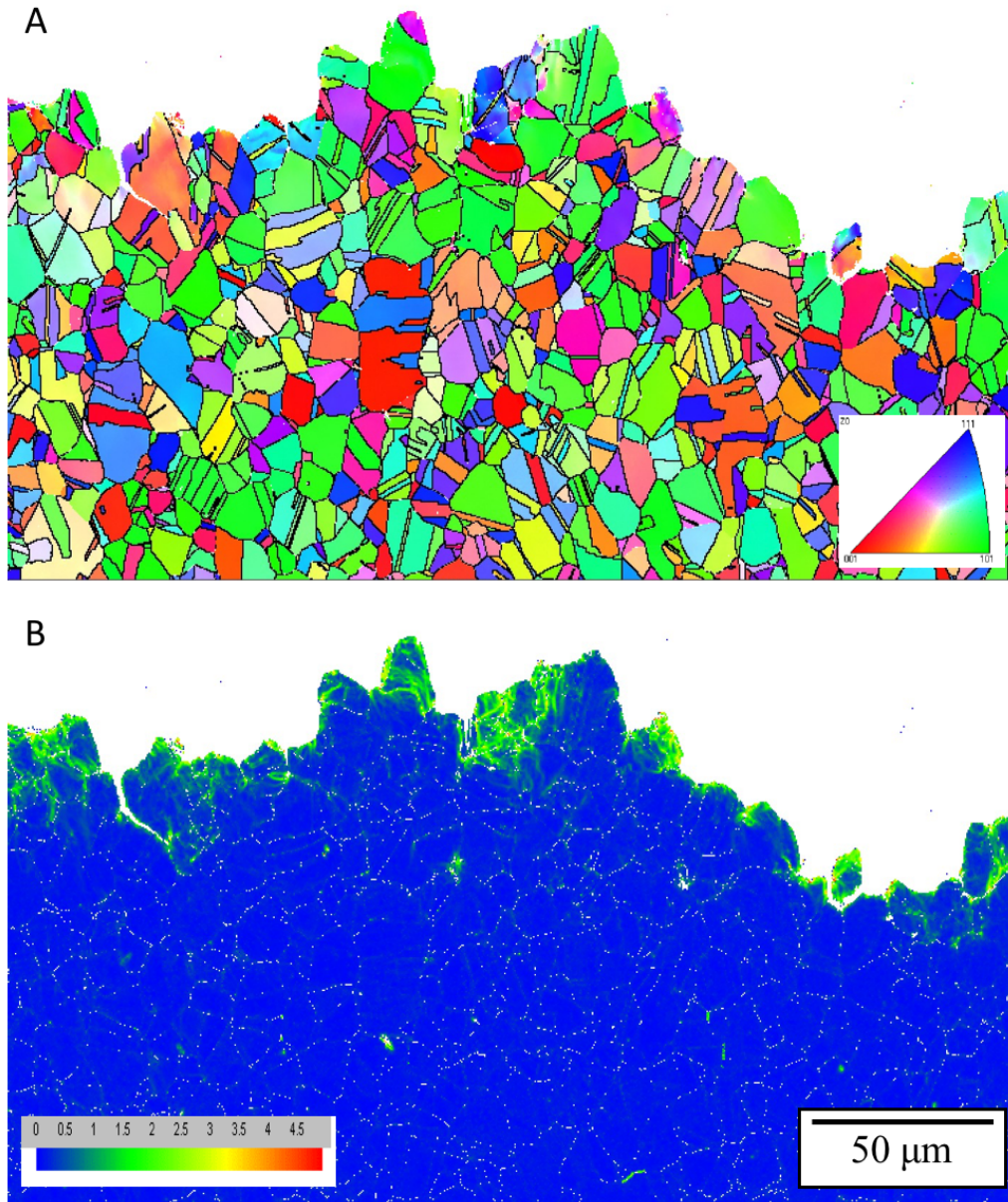


Figure 63 – (a) Inverse pole figure map with grain orientations relative to the Z-axis (out of the page) and (b) kernel average misorientation map for the peak-aged specimen tested in 0.6 M NaCl at $-1200 \text{ mV}_{\text{SCE}}$. Note that the kernel average misorientation legend is in degrees.

This observation that deformation is highly localized to the fracture plane is consistent with the calculated GND density maps collected using HR-EBSD (shown in Figure 64), which demonstrates that the calculated GND density rapidly decreases to a constant level after $\sim 25\text{-}40 \mu\text{m}$ from the fracture surface. Two other interesting trends are noted with regards to the GND density. First, as shown by the red arrows, adjacent grains which experienced nominally similar K_I have significantly different distributions of GND

density. In particular, the left grain (*i.e.* lower K_I) shows a strongly concentrated GND density at the fracture surface, while the right grain exhibits a more diffuse distribution. Second, qualitative examination of the GND density as a function of K_I suggests an apparent increase in average GND density with increasing K_I (*i.e.* moving from left to right in Figure 64). Finally, the importance of appropriate reference pattern selection is highlighted by grain indicated by the black arrow. Due to the grain being split between two separate HR-EBSD scans, two separate reference patterns were selected, which resulted in disparate calculation results. Sensitivity analyses are currently underway to better understand the variation implicit to reference selection.

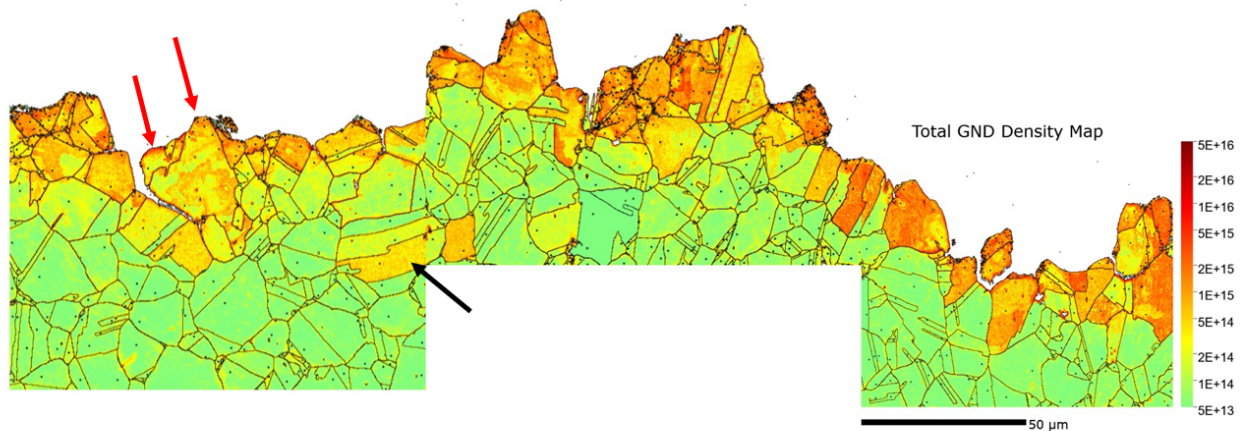


Figure 64 – Geometrically dislocation density map calculated using cross-correlation techniques from high-resolution EBSD scans. The red arrows indicate two adjacent grains which exhibit different distributions of GND density, while the black arrow indicates the effects of poor reference pattern selection. Note that the units are in m^{-2} and that the scale is logarithmic.

6.5. Discussion

The KAM map (Figure 63b) and GND map (Figure 64) demonstrate that the deformation pertinent to hydrogen environment-assisted cracking is highly localized to the fracture surface, with deformation metrics decreasing to a constant level after distances <5 - 10% of the plastic zone size. This difference in depth between the KAM and GND maps demonstrates the utility of the HR-EBSD technique's improved resolution relative to standard EBSD techniques. Second, the GND density appears to increase as the K_I increased, in agreement with expectations from strain gradient plasticity theories [21]. Finally, a non-negligible variation in GND density distribution was observed between different grains which experience similar crack tip driving forces; such an observation underscores the importance of accounting for grain orientation effects when comparing dislocation patterning from different specimens [15]. While these initial results are still being analyzed, the qualitative observations highlight the promise of this broad-scale approach to understanding the deformation behavior pertinent to environmental cracking problems.

Current efforts are focused on (1) improving the GND analysis (*i.e.* improved reference selection, optimized sample preparation, etc.) and (2) validating the GND analysis through transmission electron microscopy. Regarding the former, sensitivity studies are underway to better understand the effect of reference selection on obtained results. Additionally, a collaboration with NASA Langley Research Center has been established to investigate the utility of using a Xe-based plasma FIB for performing sample cross-sectioning. Considering the latter, while an exact replication of the GND density distribution is not expected in the TEM (since the total dislocation density is also composed of “statistically stored dislocations”), the ability to qualitatively evaluate the deformation character across different specimens, loading conditions, grain orientations, etc., over a large sampling area would still be informative. Attempts to examine the near-fracture surface deformation first required the development of a FIB lift-out protocol which effectively eliminates near-surface damage induced during FIB specimen preparation; the results of this study are shown in Appendix I. Work is now on-going to prepare TEM specimens for scanning TEM (STEM) from the cross-section shown in Figure 61 to validate the observed dislocation distributions.

6.6. Conclusions

The initial results of a multiple length-scale characterization strategy were presented, with emphasis placed on leveraging HR-EBSD to calculate the GND density distributions proximate to the crack wake of a specimen which failed due to hydrogen environment-assisted cracking. Results indicate three interesting trends: (1) deformation is highly localized to the fracture surface, (2) the average GND density appears to increase with increasing K_I , and (3) the GND distribution for an approximately constant K_I can differ from grain-to-grain. Current work is focused on improving the GND analysis through targeted sensitivity studies and validating the GND approach via complementary STEM.

6.8. Acknowledgements

The assistance of Adam Thompson with sample preparation and Dr. Tim Ruggles with optimizing the GND analysis as well as helpful discussion with Prof. Sean Agnew are all gratefully acknowledged.

6.9. References

- [1] I.M. Robertson, P. Sofronis, A. Nagao, M.L. Martin, S. Wang, D.W. Gross, et al., Hydrogen Embrittlement Understood, *Metall. Mater. Trans. B.* (2015). doi:10.1007/s11663-015-0325-y.
- [2] M.L. Martin, B.P. Somerday, R.O. Ritchie, P. Sofronis, I.M. Robertson, Hydrogen-induced intergranular failure in nickel revisited, *Acta Mater.* 60 (2012) 2739–2745. doi:10.1016/j.actamat.2012.01.040.
- [3] S. Wang, A. Nagao, K. Edalati, Z. Horita, I.M. Robertson, Influence of hydrogen on dislocation self-organization in Ni, *Acta Mater.* 135 (2017) 96–102. doi:10.1016/j.actamat.2017.05.073.
- [4] S. Wang, M.L. Martin, P. Sofronis, S. Ohnuki, N. Hashimoto, I.M. Robertson, Hydrogen-induced

- intergranular failure of iron, *Acta Mater.* 69 (2014) 275–282. doi:10.1016/j.actamat.2014.01.060.
- [5] M.L. Martin, P. Sofronis, I.M. Robertson, T. Awane, Y. Murakami, A microstructural based understanding of hydrogen-enhanced fatigue of stainless steels, *Int. J. Fatigue.* 57 (2013) 28–36. doi:10.1016/j.ijfatigue.2012.08.009.
- [6] S. Wang, A. Nagao, P. Sofronis, I.M. Robertson, Hydrogen-modified dislocation structures in a cyclically deformed ferritic-pearlitic low carbon steel, *Acta Mater.* 144 (2018) 164–176. doi:10.1016/j.actamat.2017.10.034.
- [7] A. Nagao, C.D. Smith, M. Dadfarnia, P. Sofronis, I.M. Robertson, The role of hydrogen in hydrogen embrittlement fracture of lath martensitic steel, *Acta Mater.* 60 (2012) 5182–5189. doi:10.1016/j.actamat.2012.06.040.
- [8] K.E. Nygren, K.M. Bertsch, S. Wang, H. Bei, A. Nagao, I.M. Robertson, Hydrogen embrittlement in compositionally complex FeNiCoCrMn FCC solid solution alloy, *Curr. Opin. Solid State Mater. Sci.* 22 (2018) 1–7. doi:10.1016/j.cossms.2017.11.002.
- [9] K.E. Nygren, S. Wang, K.M. Bertsch, H. Bei, A. Nagao, I.M. Robertson, Hydrogen embrittlement of the equi-molar FeNiCoCr alloy, *Acta Mater.* 157 (2018) 218–227. doi:10.1016/j.actamat.2018.07.032.
- [10] Y. Ogawa, D. Birenis, H. Matsunaga, A. Thøgersen, Ø. Prytz, O. Takakuwa, et al., Multi-scale observation of hydrogen-induced, localized plastic deformation in fatigue-crack propagation in a pure iron, *Scr. Mater.* 140 (2017) 13–17. doi:10.1016/j.scriptamat.2017.06.037.
- [11] D. Birenis, Y. Ogawa, H. Matsunaga, O. Takakuwa, J. Yamabe, Ø. Prytz, et al., Interpretation of hydrogen-assisted fatigue crack propagation in BCC iron based on dislocation structure evolution around the crack wake, *Acta Mater.* 156 (2018) 245–253. doi:10.1016/j.actamat.2018.06.041.
- [12] Y. Ogawa, D. Birenis, H. Matsunaga, O. Takakuwa, J. Yamabe, Ø. Prytz, et al., The role of intergranular fracture on hydrogen-assisted fatigue crack propagation in pure iron at a low stress intensity range, *Mater. Sci. Eng. A.* 733 (2018) 316–328. doi:10.1016/j.msea.2018.07.014.
- [13] Y.Z. Chen, H.P. Barth, M. Deutges, C. Borchers, F. Liu, R. Kirchheim, Increase in dislocation density in cold-deformed Pd using H as a temporary alloying addition, *Scr. Mater.* 68 (2013) 743–746. doi:10.1016/j.scriptamat.2013.01.005.
- [14] C. Keller, E. Hug, R. Retoux, X. Feugas, TEM study of dislocation patterns in near-surface and core regions of deformed nickel polycrystals with few grains across the cross section, *Mech. Mater.* 42 (2010) 44–54. doi:10.1016/j.mechmat.2009.09.002.
- [15] J.A. Wert, X. Huang, G. Winther, W. Pantleon, H.F. Poulsen, Revealing deformation microstructures, *Mater. Today.* 10 (2007) 24–32. doi:10.1016/S1369-7021(07)70206-7.
- [16] N. Hansen, X. Huang, G. Winther, Grain orientation, deformation microstructure and flow stress, *Mater. Sci. Eng. A.* 494 (2008) 61–67. doi:10.1016/j.msea.2007.10.086.
- [17] X. Huang, N. Hansen, Grain orientation dependence of microstructure in aluminium deformed in tension, *Scr. Mater.* 37 (1997) 1–7. doi:10.1016/S1359-6462(97)00072-9.
- [18] I.M. Robertson, H.K. Birnbaum, Effect of hydrogen on the dislocation structure of deformed nickel, *Scr. Metall.* 18 (1984) 269–274. doi:10.1016/0036-9748(84)90521-0.

- [19] W.A. McInTeer, A.W. Thompson, I.M. Bernstein, The effect of hydrogen on the slip character of nickel, *Acta Metall.* 28 (1980) 887–894. doi:10.1007/BF02655107.
- [20] T.L. Anderson, *Fracture Mechanics: Fundamentals and Applications*, 3rd ed., Taylor & Francis, 2005.
- [21] E. Martinez-Paneda, C.F. Niordson, R.P. Gangloff, Strain gradient plasticity-based modeling of hydrogen environment assisted cracking, *Acta Mater.* 117 (2016) 321–332. doi:10.1016/j.actamat.2016.07.022.
- [22] A.J. Wilkinson, G. Meaden, D.J. Dingley, High-Resolution Elastic Strain Measurement from Electron Backscatter Diffraction Patterns: New Levels of Sensitivity, *Ultramicroscopy.* 106 (2006) 307–313. doi:http://dx.doi.org/10.1016/j.ultramic.2005.10.001.
- [23] J. Jiang, T.B. Britton, A.J. Wilkinson, Measurement of geometrically necessary dislocation density with high resolution electron backscatter diffraction: Effects of detector binning and step size, *Ultramicroscopy.* 125 (2013) 1–9. doi:10.1016/j.ultramic.2012.11.003.
- [24] T.J. Ruggles, T.M. Rampton, A. Khosravani, D.T. Fullwood, The effect of length scale on the determination of geometrically necessary dislocations via EBSD continuum dislocation microscopy, *Ultramicroscopy.* 164 (2016) 1–10. doi:10.1016/j.ultramic.2016.03.003.
- [25] J. Jiang, T.B. Britton, A.J. Wilkinson, Evolution of dislocation density distributions in copper during tensile deformation, *Acta Mater.* 61 (2013) 7227–7239. doi:10.1016/j.actamat.2013.08.027.
- [26] T. Benjamin Britton, A.J. Wilkinson, Stress fields and geometrically necessary dislocation density distributions near the head of a blocked slip band, *Acta Mater.* 60 (2012) 5773–5782. doi:10.1016/j.actamat.2012.07.004.
- [27] P.S. Karamched, A.J. Wilkinson, High resolution electron back-scatter diffraction analysis of thermally and mechanically induced strains near carbide inclusions in a superalloy, *Acta Mater.* 59 (2011) 263–272. doi:10.1016/j.actamat.2010.09.030.
- [28] P.D. Littlewood, A.J. Wilkinson, Geometrically necessary dislocation density distributions in cyclically deformed Ti-6Al-4V, *Acta Mater.* 60 (2012) 5516–5525. doi:10.1016/j.actamat.2012.07.003.
- [29] J. Jiang, J. Yang, T. Zhang, J. Zou, Y. Wang, F.P.E. Dunne, et al., Microstructurally sensitive crack nucleation around inclusions in powder metallurgy nickel-based superalloys, *Acta Mater.* 117 (2016) 333–344. doi:10.1016/j.actamat.2016.07.023.
- [30] T.B. Britton, J.L.R. Hickey, Understanding deformation with high angular resolution electron backscatter diffraction (HR-EBSD), *IOP Conf. Ser. Mater. Sci. Eng.* 304 (2018). doi:10.1088/1757-899X/304/1/012003.
- [31] T. Ben Britton, J. Jiang, P.S. Karamched, A.J. Wilkinson, Probing deformation and revealing microstructural mechanisms with cross-correlation-based, high-resolution electron backscatter diffraction, *Jom.* 65 (2013) 1245–1253. doi:10.1007/s11837-013-0680-6.
- [32] A.S. Popernack, *Loading Rate Effects on Hydrogen-Enhanced Cracking Behavior of Ni- and Co-Based Superalloys for Marine Applications*, University of Virginia, 2017.
- [33] L.N. Brewer, D.P. Field, C.C. Merriman, Mapping and Assessing Plastic Deformation Using EBSD, in: A.J. Schwartz, M. Kumar, B.L. Adams, D.P. Field (Eds.), *Electron Backscatter Diffr.*

Mater. Sci., Springer, 2009: pp. 251–262.

- [34] C. Moussa, M. Bernacki, R. Besnard, N. Bozzolo, About quantitative EBSD analysis of deformation and recovery substructures in pure Tantalum, IOP Conf. Ser. Mater. Sci. Eng. 89 (2015). doi:10.1088/1757-899X/89/1/012038.

Chapter 7. Summary and conclusions

7.1. Overview

This chapter summarizes the key conclusions emerging from the work completed in the dissertation.

7.2. Summary and Key Conclusions

1. The influence of deformation temperature, and therefore mobile H-deformation interactions, on H-induced intergranular cracking in polycrystalline nickel was systematically evaluated through targeted mechanical testing at ambient (where such interactions are possible) and cryogenic temperatures (where such interactions cannot occur due to kinetic limitations). In-depth microscopy-based analyses of separate specimens tested to increasing strain levels at both deformation temperatures revealed that the initiation of intergranular microcracks in hydrogen-charged Ni-201 (for a hydrogen concentration of 4000 appm) was predominantly attributed to the initial grain boundary hydrogen concentration (*i.e.* concentration prior to deformation) and that mobile H-deformation interactions only provide a secondary contribution to intergranular microcrack initiation. Conversely, intergranular microcrack evolution was enhanced at ambient temperature relative to 77 K, but a mechanistic interpretation of this finding is complicated by the likely concurrent influences of mobile H-deformation interactions and H redistribution to the stress centers created by microcracks.
2. The influence of microstructure variation on hydrogen environment-assisted cracking (HEAC) of Monel K-500 was evaluated across five nominally peak-aged heats of material (all of which satisfy the governing material specification) *via* slow-rising stress intensity loading while immersed in 0.6 M NaCl solution under cathodic polarizations. Limited heat-to-heat variation in HEAC susceptibility was observed when the lots were tested at an applied potential of $-950 \text{ mV}_{\text{SCE}}$, while significant heat-to-heat variations in HEAC susceptibility were observed at the less aggressive applied potential of $-850 \text{ mV}_{\text{SCE}}$, suggesting that metallurgical influences become dominant at low hydrogen overpotentials. An attempt was made to correlate the variation in HEAC susceptibility at $-850 \text{ mV}_{\text{SCE}}$ with variations in metallurgical features across the tested material heats, including grain size, impurity segregation, grain boundary character and connectivity, hydrogen-metal interactions, crack path deflection due to grain size, yield strength, and strain hardening. However, no specific trend between these individual metallurgical parameters and HEAC susceptibility metrics was identified, suggesting a combinatory and/or synergistic influence of multiple metallurgical features.

3. The HEAC susceptibility as function of heat treatment for a single heat of Monel K-500 isothermally aged to the non-aged, under-aged, peak-aged, and over-aged conditions was assessed *via* slow-rising stress intensity testing in 0.6 M NaCl. The variation in heat-treatment sensitive properties, including: grain size, grain boundary character, impurity segregation to grain boundaries, yield strength, strain hardening, hydrogen trapping, and bulk slip morphology, was then compared to the observed variations in HEAC susceptibility. Results indicate that HEAC susceptibility only correlates well with variations in bulk slip morphology. Specifically, the less-susceptible non-aged and over-aged conditions were found to exhibit features indicative of wavy slip, while the susceptible under-aged and peak-aged heat treatments exhibited dislocation patterns consistent with planar slip.
4. The effect of hydrogen on the deformation behavior of Monel K-500 as a function of the four isothermal heat treatments was evaluated via uniaxial mechanical testing. The ductility was found to be significantly reduced for all tested heat treatments in the presence of hydrogen, which was further corroborated by a consistent change in fracture surface morphology from microvoid coalescence in the non-charged condition to intergranular fracture in the hydrogen-charged condition. The yield strength was found to be systematically enhanced for all heat treatments in the presence of hydrogen, though the three precipitate-hardened conditions exhibited a >2x larger relative increase than the non-aged heat treatment, suggesting that hydrogen modifies dislocation-precipitate interactions. This result was corroborated by an analysis of the work hardening behavior, which revealed characteristic deviations from the non-charged work hardening behavior. In particular, the peak-aged specimen tested in the hydrogen-charged condition exhibited a significant increase in initial hardening rate relative to the hydrogen-charged under-aged specimen, suggesting an onset of dislocation looping. Subsequent TEM of the peak-aged hydrogen-charged alloy confirmed the widespread onset of dislocation looping, but a mechanistic explanation for this modification remains unclear.
5. The GND density distribution was evaluated proximate to the fracture surface (over a K_I from 43 to 48 MPa \sqrt{m}) of a peak-aged Monel K-500 specimen that was tested under slow-rising K conditions in 0.6 M NaCl at -1200 mV_{SCE}. This analysis indicates that deformation is highly localized to the crack wake, with GND metrics decaying to a constant level after 25-40 μm . Moreover, the average GND density was qualitatively observed to increase with increasing K_I , in agreement with the expectations from strain gradient plasticity theories. Finally, neighboring grains were found to exhibit different distributions of GND density, despite experiencing nominally similar K_I , underscoring the importance of grain orientation when attempting to compare dislocation patterning.

Appendix I: Mitigation of focused ion beam-induced damage

The following section describes ancillary work to which the author contributed as a co-primary performer which sought to demonstrate the efficacy of a combined electron-beam/ion-beam platinum deposition strategy when performing FIB lift-outs of surface-sensitive samples, such as those that will be evaluated based on the continuing work from Chapter 6.

A.1. Overview

It is well known that damage induced by impinging Ga^+ ions during focused ion beam (FIB) milling of transmission electron microscopy (TEM) specimens can obfuscate subsequent TEM characterization, especially in the near-surface region of the TEM foil. Numerous strategies for minimizing this damage have been invoked, with the most common being the deposition of a Pt ‘strap’ at the area of interest. However, damage can still occur in the near-surface region during this Pt deposition step and the variation in the character and extent of this damage with applied Pt deposition parameter, especially in complex structural alloys, is not well characterized. In this study, the damage induced in an aerospace Al alloy (AA7075-T651) during five different Pt deposition protocols is examined using TEM. Results indicate extensive variations in damage character and depth amongst the applied Pt deposition protocols, with damage being effectively eliminated using a combined electron-beam/ion-beam Pt deposition strategy. Results are found to be in good agreement with Monte Carlo-based simulations of ion implantation and the implications of these findings on recent experiments in the fracture mechanics community are explored.

A.2. Introduction

Focused ion beam (FIB) milling with Ga^+ ions is a common technique for the preparation of transmission electron microscopy (TEM) specimens due to several distinct advantages over traditional TEM sample preparation strategies [1–3]. In particular, FIB milling enables one to obtain TEM samples: (1) from specific regions of interest with high spatial precision, (2) in a relatively time-efficient manner, and (3) with modestly-sized regions of electron transparency. However, a critical shortcoming of the FIB milling approach is the possibility of specimen damage from the impinging Ga^+ ions [4,5]. This damage can occur in several forms, depending on specimen composition/microstructure, ion beam current and accelerating voltage, and the impingement geometry. For example, studies have shown that FIB milling with Ga^+ ions can cause: (1) the formation of an amorphous surface layer (which can reach a thickness of >100 nm [6]), (2) the injection of dislocations and vacancies through knock-on processes [7], (3) the formation of Ga intermetallic phases in certain metallic materials [8,9], (4) the implantation of Ga into the specimen bulk (with local compositions being reported as high as 20 at. % [10]), (5) preferential grain

growth/texture evolution in metallic materials [11], and (6) phase transformations such as the $\gamma \rightarrow \alpha$ transformation in steels [12,13].

As this damage can obfuscate the interpretation of any subsequent TEM characterization, numerous methodologies have been suggested for mitigating FIB-induced artifacts. Of these different approaches, the most common mitigation strategy is the deposition of a protective Pt ‘strap’ over the region of interest prior to FIB milling. Briefly, the Pt strap is deposited as follows [2]: (1) a precursor gas (*e.g.* $C_9H_{16}Pt$) is introduced into the chamber *via* a fine nozzle located near the specimen surface, causing (2) the precursor gas to adsorb onto the specimen surface, where (3) the incident beam (either electron or ion) causes a decomposition of the precursor gas into volatile and nonvolatile components, which results in (4) the volatile components (hydrogen and carbon) leaving the surface and the deposition of the nonvolatile Pt. This Pt strap provides two advantages: (1) it protects the underlying material from a direct interaction with the ion beam (I-beam) during FIB milling and (2) it ensures a smooth surface, which has been shown to minimize ‘curtaining’ from surface irregularities [2]. However, a critical limitation of this protection scheme is that the ions impinging on the specimen surface during the initial stages of the Pt deposition process (*i.e.* until a critical thickness is achieved) can cause damage that is predominantly localized to the near-surface region [14–16].

Understanding the implications of this surface-localized damage layer is particularly pertinent given the increased interest in leveraging FIB milling to prepare TEM specimens from the fracture surfaces of metallic components. For example, several recent studies have utilized FIB milling to examine the near-fracture surface deformation structure generated during both cyclic and monotonic loading in Ni and Fe-based alloys [17,18]. Such experiments are especially of interest to the environmental cracking community, where the localized environment-material interactions occurring proximate to the crack tip are expected to govern alloy susceptibility [19]. Critically, as FIB milling enables the opportunity to directly examine the microstructure in the near-crack tip region, it is now possible to correlate changes in environment, loading protocol, and metallurgy with local deformation behavior and the concomitant effect on crack growth kinetics. Such insights could then be used to mechanistically inform models for environmental cracking, validate theories for crack tip mechanical fields, and understand the role of individual microstructural features on the fracture process. However, decoupling the deformation/microstructure evolution induced from damage during FIB milling from that generated during loading is non-trivial. Numerous studies on mitigating FIB-induced damage have been published, with particular focus on understanding damage character in Si and pure metals [5,9,10,20–22]. However, extension of these results into more complex engineering-relevant alloys is complicated by the possible influences of prior cold working, precipitation hardening, and other alloy modifications. Additionally, a small number of studies suggest that depositing

an initial layer of Pt using the electron beam (E-beam) can effectively mitigate damage induced during I-beam deposition [14,23]. Other authors have suggested using materials such as sputter-deposited Au and Cr or polymeric sheets for a similar ‘initial barrier’ purpose [5,16,24]. Despite being widely available, the use of E-beam Pt prior to depositing I-beam Pt is generally not utilized in the literature, particularly on structural alloys which have complex microstructures. These knowledge gaps motivate a study to better understand the extent of damage as a function of applied Pt deposition parameters, as well as the efficacy of the E-beam/I-beam strategy to prevent such damage in structural alloys.

The objective of this work is to evaluate the near-surface FIB-induced damage induced by commonly employed Pt deposition strategies in the aerospace alloy AA7075-T651. Transmission electron microscopy is employed to quantify the depth of the FIB-induced damage as a function of applied Pt deposition parameters. These findings are then compared with the results of Monte Carlo simulations of ion bombardment. The impact of these results are then discussed in the context of preparing TEM specimens from fracture surfaces. These data will enhance the understanding of how FIB-induced damage depends on Pt deposition parameters, thereby enabling optimization of the damage mitigation strategy for such surface-sensitive specimens.

A.3. Material and Methods

All experiments were conducted on AA7075-T651, which was procured in the form of a 50.8-mm thick plate. This alloy was selected due to the high likelihood of susceptibility to FIB-induced damage (based on a previous study on FIB damage in Al alloys [25]) as well as its technological relevance as a widely-utilized aerospace alloy. Microstructure details for this plate of material are reported elsewhere [26,27]. For this study, two small sections (termed Block 1 and Block 2) were taken from the plate such that the thickness of each section was centered at a depth of 8.5 mm from the surface. Block 1 had dimensions (L x W x H) of 12.15 mm x 7.60 mm x 7.06 mm, while Block 2 was 8.88 mm x 5.80 mm x 7.59 mm. Five different Pt deposition protocols, termed Samples 1-5 and shown in Figure 65, were evaluated in this work. Samples 1-4 were separately excised from a surface of Block 1 that was cut using a low-speed saw; this saw-cut surface was used so as to simulate the damage and uneven surface topography of a fracture surface. The primary objective for Samples 1-4 was to determine the extent of damage that occurs during different Pt deposition strategies, so as to inform which Pt deposition protocol best prevented damage for subsequent use on Sample 5. Sample 5 was excised from Block 2, which was cold-rolled to ~50% of the original thickness and then polished to a surface finish of 0.1 μm using diamond slurries. Polishing prior to the Pt deposition was completed to remove the recrystallized surface layer induced by adiabatic heating from the rolling process. Critically, the removal of this recrystallized layer formed during rolling enabled any observed recrystallization in the FIB-prepared TEM specimen to be solely attributed to

FIB damage. Moreover, as this cold-worked specimen is expected to contain a significantly increased dislocation density relative to Samples 1-4, the driving force for recrystallization from either FIB-induced temperature increases or imparted strain from impinging Ga^+ ions is expected to be elevated, thereby making Sample 5 more susceptible to FIB damage than Samples 1-4.

Damage induced from each Pt deposition protocol was examined *via* TEM using a FEI Titan operated at 300 keV. TEM specimens were prepared using the following lift-out procedure. First, Pt was deposited over an approximate area of $10\ \mu\text{m} \times 3\ \mu\text{m}$ using the protocols shown in Figure 65. A trench was then milled about the Pt deposition area with the sample surface oriented normal to the I-beam. All samples were trenched using a stepped trench technique with an accelerating voltage of 30 keV and an I-beam current of 9.0 nA. An OmniProbe micromanipulator was used to remove the specimen from the sample bulk and then attach the excised sample to a 3-mm diameter Cu TEM half-grid. Each sample was then incrementally thinned to electron transparency (thickness $\approx 100\text{-}150\ \text{nm}$) using the I-beam (specimen surface was oriented perpendicular to I-beam), finishing with an accelerating voltage of 30 KeV and a beam current of 90 pA. The extent of FIB-induced near-surface damage was then quantified by measuring the average damage depth under the Pt layer across the TEM specimen width at ten equidistant points.

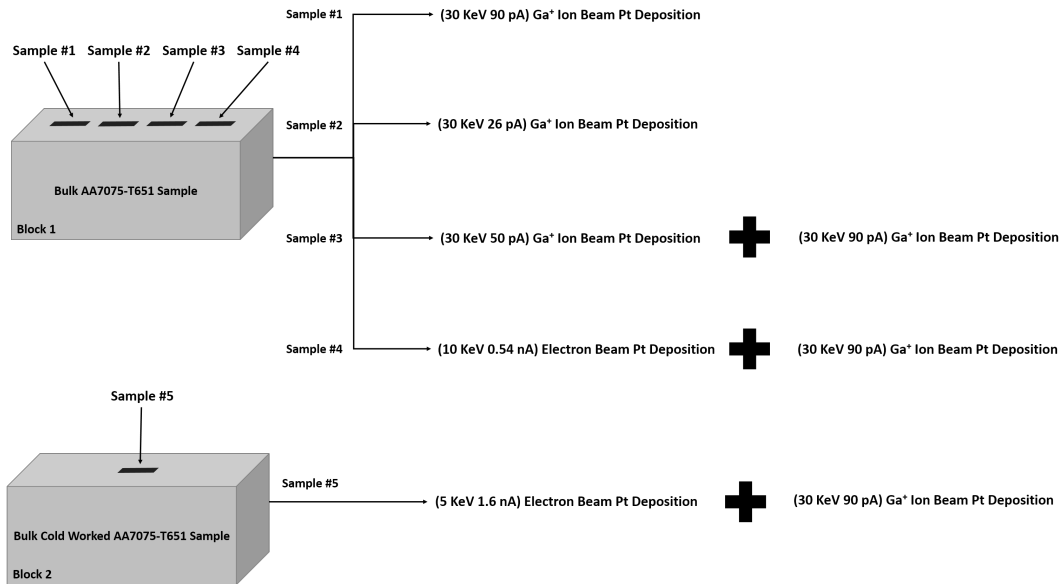


Figure 65 – Overview of applied Pt deposition protocols for each TEM sample.

To evaluate the efficacy of suggested E-beam Pt deposition thicknesses, Monte Carlo simulations of the Ga^+ ion implantation were conducted using the SRIM software package [28]. Calculations of the Ga^+ ion and recoiled atom distributions were completed using 30 keV Ga^+ ions impinging perpendicular to an amorphous 250-nm thick Pt layer. This layer thickness was utilized to enable the simultaneous evaluation

of the likely range of E-beam Pt layer thicknesses (*e.g.* 50-150 nm). The density of the Pt layer was reduced to 7.50 g/cm^3 (~35% of crystalline Pt) based on previous composition measurements of E-beam Pt deposited using $\text{C}_9\text{H}_{16}\text{Pt}$ (~22% Pt, 73% C, and 5% O; in at. %) [29]. As the density will likely vary with deposition parameters, in addition to expected improvements in Pt deposition purity as new FIB systems are developed, results are also plotted for calculations which used Pt densities of 4.29 g/cm^3 and 10.72 g/cm^3 (corresponding to ~20 and ~50% of crystalline Pt, respectively) to account for such differences/improvements. The upper-bound density of 50% was selected to reflect that Pt deposited using $\text{C}_9\text{H}_{16}\text{Pt}$ is generally C-rich [23] and no efforts were made in this study to modify the E-beam Pt purity post-deposition [30].

A.4. Results

TEM micrographs of each Pt deposition condition taken at two different magnifications are shown in Figure 66; three general observations can be made from these micrographs. First, extensive damage (extending greater than $1 \mu\text{m}$ into the TEM specimen) was observed in Samples 2 and 3 (Figure 66c-d and Figure 66e-f, respectively). Damage is broadly characterized as any microstructural feature which is not observed in the bulk foil; a clear example of such differences is shown in Figure 66e, with the FIB-induced damage indicated by the red arrow. Second, the sample prepared using standard I-beam current values (Sample 1, 90 pA) still exhibits a noticeable damage layer, but the damage depth is significantly less than that found in the 'low' I-beam current specimens (Samples 2 and 3.) Third, depositions which utilized the E-beam to deposit an initial layer of Pt before switching to I-beam deposition exhibit minimal damage (Samples 4 and 5) as shown in Figure 66g-h and Figure 66i-j, respectively.

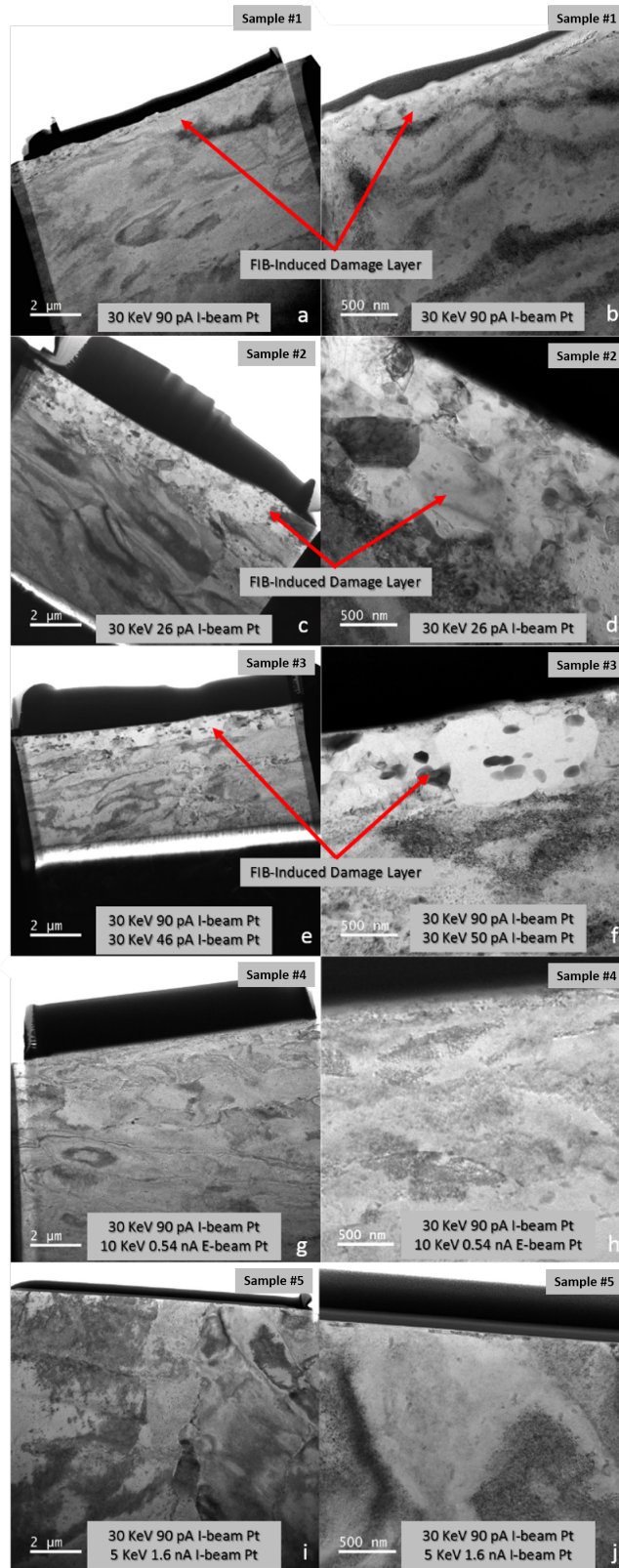


Figure 66 – Overview TEM micrographs at two different magnifications for (a,b) Sample 1, (c,d) Sample 2, (e,f) Sample 3, (g,h) Sample 4, and (i,j) Sample 5.

High-magnification images of the Pt-Al interface for Samples 1 and 4 are shown in Figure 67. These micrographs clearly demonstrate the advantages of using an initial E-beam Pt deposition step (Sample 4; Figure 67b) as the damage is noticeably reduced relative to the I-beam specimen (Sample 1; Figure 67a). Critically, as Sample 1 and 4 were prepared from the same sample but have different damage depths, these images conclusively establish that the observed damage layer in Sample 1 is due to the Pt deposition process and is not an artifact from other steps in the sample preparation process (e.g. the saw cut). Figure 68a shows high magnification images of Sample 5, which was extensively cold-rolled and then prepared with a thicker E-beam Pt layer (prior to I-beam deposition) than Sample 4 (~110 vs. ~45 nm for Sample 4). It is noteworthy that this sample exhibits a continuous, unaltered microstructure (*i.e.* negligible change/gradient in microstructure), even immediately proximate to the Pt-Al interface, suggesting minimal damage occurred in this specimen during Pt deposition. Additional evidence for this negligible microstructural gradient in Sample 5 is shown in Figure 68b, where the sample has been tilted to show the deformation substructure proximate to the specimen surface. Clearly, the deformation structure appears unaltered up to the Pt-Al interface. These results strongly suggest that FIB-induced damage was effectively mitigated by the applied E-beam/I-beam Pt deposition strategy. To quantitatively compare the FIB-induced damage depth from the five employed Pt deposition protocols, ten measurements of the damage layer thickness were made at equally spaced intervals across the width of each specimen. The average damage layer for each condition from these measurements is shown graphically in Figure 69. As expected from the micrographs presented in Figure 66, Samples 2 and 3 exhibit the largest average damage depths (1351 and 825 nm, respectively), which are both deeper than the damage observed in Sample 1 (388 nm). However, these three samples are all significantly elevated compared to the damage found in Samples 4 and 5, which were prepared using the combined E-beam/I-beam Pt deposition strategies (67 and 7 nm, respectively).

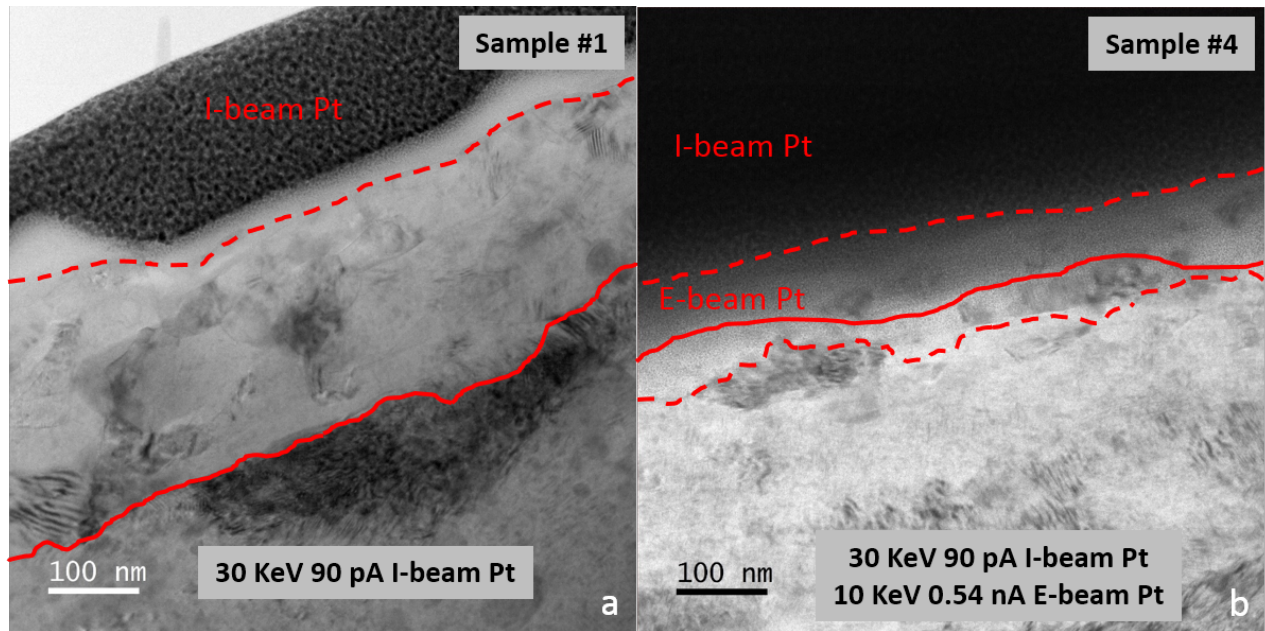


Figure 67 – High magnification TEM micrographs of the Pt/Al interface for (a) Sample 1 and (b) Sample 4. Red lines indicate the transition in damage character as well as the location of interfaces between E-beam Pt, I-beam Pt, and the Al alloy.

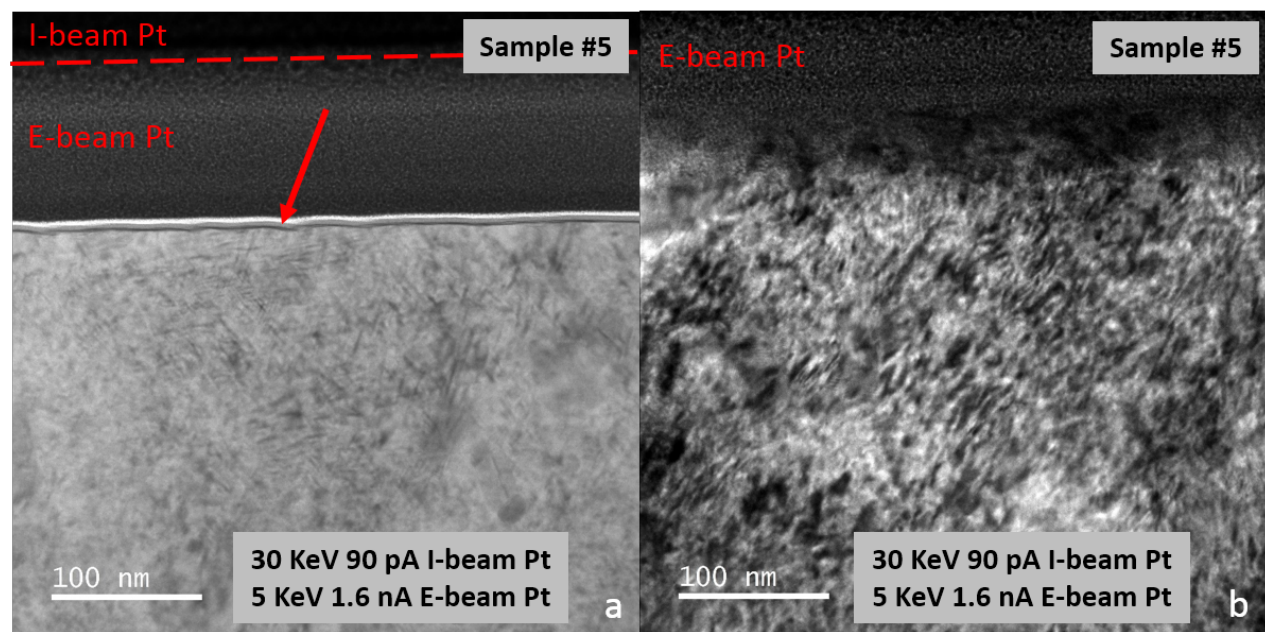


Figure 68 - High magnification TEM micrographs of the Pt/Al interface for (a) Sample 5 un-tilted and (b) Sample 5 tilted to show continuity of deformation. In (a), the red dashed line indicates the transition between the E-beam Pt and I-beam Pt, while the red arrow indicates the ‘damage’ used for calculating the damage depth shown in Figure 69.

In addition to the different damage depths, the character of the damage appears to differ between samples. For example, a clear gradient in microstructure is observed in Samples 1-3 (Figure 66 and Figure 67a), but not in Samples 4 and 5 (Figure 67b and Figure 68a). In particular, the ‘high’ I-beam current sample (Sample 1) contains an Al material layer which appears to be dislocation and precipitate-free (bright region between red dashed line and I-beam Pt layer in Figure 67a). Conversely, Samples 2 and 3 (Figure 66) do not appear to have such an amorphous region, but instead exhibit a microstructure similar to that expected after recrystallization. Finally, regarding the damage observed in Sample 5 (white and gray layer in Figure 68a, indicated by the red arrow), it is speculated that this ‘damage’ is either an oxide layer or damage induced during polishing prior to Pt deposition. However, as the origin of the damage cannot be rigorously determined, it is conservatively attributed to the FIB for the purposes of this comparison. Additional postulation on the details of the observed microstructure for each specimen is presented in the Discussion.

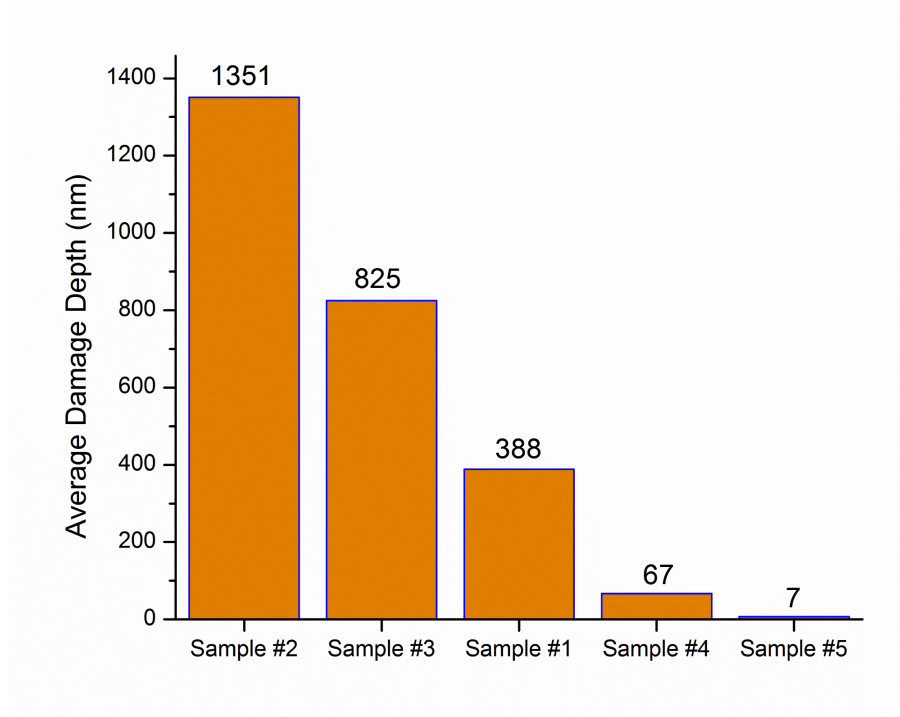


Figure 69 – Average damage depth for each Pt deposition strategy based on ten equidistant measurements across the TEM specimen width.

A.5. Discussion

The results shown in Figure 66, Figure 67, Figure 68, and Figure 69 demonstrate that for AA7075-T651: (1) the damage layer induced in the near-surface region by impinging Ga^+ ions during I-beam Pt deposition varies extensively with I-beam deposition parameters and (2) the use of a combined E-beam/I-

beam Pt deposition strategy greatly reduces such damage. In the following discussion, we: (1) qualitatively evaluate the observed damage depth and character for each condition based on the findings of previous studies and (2) outline the implications of the presented results in the context of efforts to understand near-surface deformation using specimens excised from crack wakes.

A.5.1 Effect of Pt Deposition Approach on Damage Depth

The observed dependence of FIB-induced damage depth on Pt deposition strategy for AA7075-T651 shown in Figure 66 (and quantitatively in Figure 69) are consistent with the findings of previous studies. For example, it was expected that the ‘low’ I-beam current specimens would exhibit the largest damage depth. As discussed extensively elsewhere [2], the advantage of utilizing a ‘low’ I-beam current during Pt deposition is a reduction in the I-beam milling rate. However, the beneficial impact of this decrease in milling rate on the induced damage is countered by a concomitant decrease in the decomposition rate of the Pt precursor gas, which can decrease the Pt layer growth rate. Therefore, while the milling rate is reduced under such ‘low’ I-beam currents, the time required to deposit a Pt layer that is sufficiently thick to stop the impinging Ga^+ ions is increased, thereby allowing more damage to accumulate relative to higher I-beam currents [2]. Such a decrease in damage depth with increasing beam current (for modest beam currents; *i.e.* < 100 pA) is consistent with the observed damage depth in Samples 2, 3, and 1 (Figure 66 and Figure 67), where the employed I-beam current was 26, 50, and 90 pA, respectively.

A small number of prior studies have shown that the damage layer induced during I-beam Pt deposition can be reduced by first depositing a Pt layer using the E-beam [14,23]. This use of the E-beam for the initial deposition, while having sufficient energy to decompose the Pt precursor gas (albeit slowly relative to the I-beam), is not expected to induce damage at typical accelerating voltages in an SEM (*i.e.* < 30 keV), especially in metallic specimens. Therefore, as long as the E-beam Pt deposition is made sufficiently thick to stop Ga^+ ions from interacting with the specimen, negligible damage should be imparted during the subsequent ‘finishing’ I-beam Pt deposition. Literature suggests that ~ 50 nm of E-beam Pt is necessary to eliminate I-beam damage in Si [23], but the results presented herein indicate that this may not be adequate for AA7075-T651. As shown in Figure 67b, a small layer of near-surface damage (area between the red dashed and solid line) was observed in Sample 4, which contained ~ 45 nm of E-beam Pt, while no such damage was observed in the Sample 5 (despite being more susceptible to possible recrystallization due to an increased dislocation density) which contained ~ 110 nm of E-beam Pt (Figure 68a). As such, the present results suggest that, while 50 nm of E-beam Pt will certainly reduce I-beam damage, at least 100 nm of E-beam Pt should be deposited to nominally eliminate I-beam damage during Pt deposition at 30 keV on Al alloys. This approach was effective even under conditions where the sample contains significant deformation (Sample 5), as would be the case in a near-fracture surface location.

These experimental observations on the effect of E-beam Pt layer thickness are consistent with the results from Monte Carlo-based simulations of ion implantation from the SRIM software package [28]. Several observations can be made from the calculated normalized distribution of Ga⁺ ions as a function of depth, shown in Figure 70. First, it is clear that the peak damage location is between 10-30 nm of the Pt surface, depending on Pt layer density, which indicates that the previously suggested 50-nm thick E-beam Pt layer [23] will shield the underlying specimen from the worst of the Ga⁺ ion penetration. Second, in all three cases, a non-negligible fraction of the Ga⁺ ions will penetrate beyond 50 nm, suggesting that a 50 nm E-beam layer thickness is not sufficient to completely preclude damage during subsequent I-beam Pt deposition. Third, an E-beam Pt layer depth of >100 nm is sufficiently thick to effectively stop all Ga⁺ ions from reaching the specimen for the most likely E-beam Pt density values (based on composition; between 7.5 and 10.72 g/cm³). Finally, the simulation results suggest that an E-beam Pt layer thickness of >150 nm would likely preclude specimen damage at all evaluated density values. Taken together, the experimental findings presented in Figure 69 and the modeling results shown in Figure 70 demonstrate the effectiveness of the E-beam Pt deposition strategy in mitigating near-surface damage during I-beam Pt deposition.

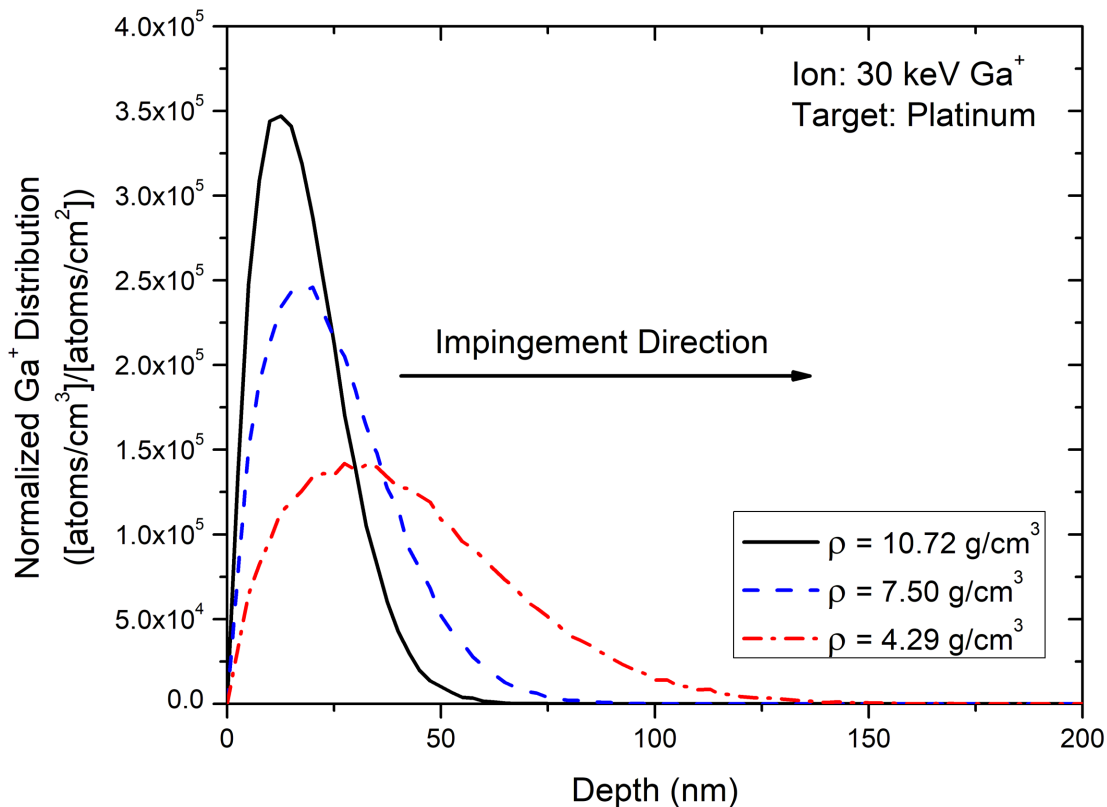


Figure 70 - Normalized Ga⁺ ion distribution as a function of depth from the Pt surface calculated using Monte Carlo-based simulations for three different Pt density values. Calculations were completed using 30 keV Ga⁺ ions impinging from a source oriented perpendicular to the Pt layer surface.

A.5.2 Effect of Pt Deposition Approach on Damage Character

The focus of the current study is to evaluate the efficacy of various Pt deposition strategies in preventing damage; as such, an extensive damage characterization effort is outside of the scope of the current work. However, it is pertinent to note the apparent variations in damage character with Pt deposition parameters. Considering the micrographs presented in Figure 66d and Figure 66f (Sample 2 and 3, respectively), the presence of nominally equiaxed grains (as opposed to the pancake-type grains expected in a rolled AA7075 microstructure) suggests that the near-surface region has recrystallized in the ‘low’ I-beam current specimens – an inference which is supported by the clear reduction in deformation relative to the bulk material observed deeper in the TEM foil. Conversely, the specimen prepared using only a 30 keV, 90 pA I-beam deposition (Sample 1) exhibits two ‘layers’ of damage. As shown in Figure 67a, a region which appears to be completely dislocation-free and likely amorphous (area between I-beam Pt and dashed red line in Figure 67a) can be found immediately adjacent to the Pt-Al interface. Beneath this first layer, a second region is observed which also appears to have a reduced dislocation density relative to the bulk foil, as was found on Samples 2 and 3. These observations strongly suggest that the near-surface region of specimens prepared using only I-beam Pt deposition strategies was appreciably modified. Moreover, the variation in damage character, despite each TEM sample being excised in an identical manner from the same region of the bulk specimen and finished with a sufficiently thick Pt layer to avoid damage during milling, strongly implies that the noted damage is due to the differences in I-beam Pt deposition parameters. That such microstructural changes occur *during* the I-beam Pt deposition process is significant as I-beam Pt deposition is most commonly used for preventing FIB-induced damage during milling.

Literature suggests that this recovery/recrystallization of the near-surface region could be attributed to irradiation effects and/or thermal effects [5,11,31]. Concerning the former, irradiation of Cu with Ga⁺ ions for 360 seconds at 30 KeV and 30 pA resulted in extensive recrystallization and grain growth in the irradiated surface region as well as the development of a strong <110> texture [11]. Based on these results, it was suggested that recrystallization/grain growth is driven by the orientation-dependence of ion channeling. Specifically, grains which have a non-channeling orientation will have increased interactions with the ion beam, thereby resulting in an increased generation of defects with such grains. As the defect density is locally increased, there is an appreciable increase in free energy in the non-channeling grains, which is then relieved through the growth of grains which are well-oriented for channeling. Considering thermal effects, it has been suggested that impinging Ga⁺ ions can cause localized heating of the specimen surface, which may be sufficient to induce recovery and recrystallization. For example, it was reported that the brief irradiation of Au/Ni bilayers with 30 keV Ga⁺ ions during specimen placement resulted in microstructural variations equivalent to annealing the specimen for several minutes at 400°C [31]. However,

while either of these processes may be active (or even work synergistically) during ion impingement, decoupling the relative influence of these two potential contributions is complicated by their likely simultaneous nature. Such complications in determining the source of observed damage will also obfuscate evaluating damage-like features which may have been present prior to TEM sample preparation.

Critically, examination of the damage near the Pt-Al interface in samples prepared using the combined E-beam/I-beam strategy (Figure 67 and Figure 68) suggests that such irradiation and/or thermal effects can be neutralized if a sufficiently thick E-beam Pt layer is deposited. In particular, a sample which was severely deformed so as to contain an increased dislocation density (and therefore have increased sensitivity to recovery/recrystallization) exhibited a continuous microstructure even immediately adjacent to the Pt-Al interface. Tilting of the TEM foil (Figure 68b) confirms the continuity of strong contrast (likely due to deformation), even proximate to the interface, further supporting the assessment that a sufficiently thick E-beam Pt layer can eliminate near-surface damage induced during I-beam Pt deposition. Moreover, the results of Monte Carlo-based simulations (Figure 70) indicates that an E-beam Pt layer of >100 nm is sufficiently thick to effectively prevent the interaction between Ga⁺ ions and the underlying specimen. Such mitigation of these specimen-ion interactions has important implications for preparing TEM samples from near-surface regions.

A.5.3 Implications on the Characterization of Near-Surface Microstructure

Despite its inherent simplicity and widespread availability, the use of E-beam Pt as a mitigation scheme is not well-documented in the FIB damage literature nor is it widely employed in microstructural studies which utilized FIB milling for TEM sample preparation. For example, several recent studies have sought to employ FIB milling as a means by which to examine the near-fracture surface region of specimens exposed to aggressive environments so as to better understand the deformation processes governing material failure [17,18,32,33]. In particular, FIB extraction of TEM specimens from the crack wake evaluate the role of hydrogen in causing premature fracture of metallic structural components *via* TEM characterization of the dislocation structure [34]. It has been hypothesized that the processes responsible for this ‘hydrogen embrittlement’ phenomenon (and other fracture processes) occur close to the crack tip (< 1 μm) [19], indicating that damage induced during I-beam Pt deposition could complicate the interpretation of such experiments. Examination of methods employed in these studies reveals a consistent use of only I-beam Pt deposition strategies, as well as evidence of near-surface damage in FIB-prepared specimens (often observed as a bright white line immediately beneath the surface; similar to that shown in Figure 67a). Conversely, other studies have employed a ‘low’ I-beam current during Pt deposition to reduce the observed damage [17]; the current results (Figure 66d and Figure 66f) demonstrate that such a protocol can cause more extensive damage than the typically utilized I-beam current of 90 pA. The current results

demonstrate that an E-beam/I-beam Pt deposition strategy enables unambiguous characterization of the damage structure in the high interest region within 100 nm of the crack surface. Such a protocol offers additional insights to prior efforts where the experimental complications associated with Pt induced damage forced analysis of “bulk” microstructures further away from the Pt deposition region [33]. In conclusion, the present results demonstrate that the combined E-beam/I-beam strategy can be utilized to enable rigorous characterization of these near-surface regions, thereby enabling the direct evaluation of proposed mechanisms for hydrogen-induced premature fracture and other failure processes.

A.6. Conclusions

The influence of Pt deposition strategy on the damage induced in the near-surface region of FIB-prepared specimens of AA7075-T651 was systematically examined using transmission electron microscopy, resulting in several important insights:

1. The depth and character of damage induced during I-beam Pt deposition was found to strongly depend on the employed deposition parameters for AA7075-T651.
2. The use of a combined E-beam/I-beam Pt deposition strategy, in which ~110 nm of Pt was initially deposited using the E-beam, was found to effectively eliminate damage during I-beam Pt deposition in AA7075-T651. This observation is consistent with the results of Monte Carlo-based modeling of ion implantation.
3. Mitigation of this near-surface damage suggests that the combined E-beam/I-beam Pt deposition strategy could be employed to enable the examination of near-surface damage processes in AA7075-T651. This efficacy of this deposition strategy is expected to extend to other alloy systems.

A.7. Acknowledgements

Discussions with Prof. James Fitz-Gerald, Prof. Sean Agnew, Prof. James Howe, and Dr. Helge Heinrich at the University of Virginia are gratefully acknowledged. The use of the FIB at the United States Naval Research Laboratory (hosted by Dr. Keith Knippling) is also sincerely appreciated. This work was supported through the AFSOR YIP Contract #FA9550-16-1-0211.

A.8. References

- [1] P.R. Munroe, The application of focused ion beam microscopy in the material sciences, *Mater. Charact.* 60 (2009) 2–13. doi:10.1016/j.matchar.2008.11.014.
- [2] N. Yao, *Focused ion beam systems: basics and applications*, 2007. doi:10.1017/CBO9780511600302.

- [3] L.A. Giannuzzi, F.A. Stevie, Introduction to focused ion beams: Instrumentation, theory, techniques and practice, 2005. doi:10.1007/b101190.
- [4] J. Mayer, L.A. Giannuzzi, T. Kamino, J. Michael, TEM Sample Preparation and FIB-Induced Damage, *MRS Bull.* 32 (2007) 400–407. doi:10.1557/mrs2007.63.
- [5] N.I. Kato, Reducing focused ion beam damage to transmission electron microscopy samples, *J. Electron Microsc.* (Tokyo). 53 (2004) 451–458. doi:10.1093/jmicro/dfh080.
- [6] L.A. Giannuzzi, F.A. Stevie, A review of focused ion beam milling techniques for TEM specimen preparation, *Micron.* 30 (1999) 197–204.
- [7] S. Lee, J. Jeong, Y. Kim, S.M. Han, D. Kiener, S.H. Oh, FIB-induced dislocations in Al submicron pillars: Annihilation by thermal annealing and effects on deformation behavior, *Acta Mater.* 110 (2016) 283–294. doi:10.1016/j.actamat.2016.03.017.
- [8] M.W. Phaneuf, J. Li, J.D. Casey Jr, Gallium phase formation in Cu and other FCC metals during near-normal incidence Ga-FIB milling and techniques to avoid this phenomenon, *Microsc. Microanal.* 8 (2002) 52–53. doi:http://dx.doi.org/http://dx.doi.org/.
- [9] J. Yu, J. Liu, J. Zhang, J. Wu, TEM investigation of FIB induced damages in preparation of metal material TEM specimens by FIB, *Mater. Lett.* 60 (2006) 206–209. doi:10.1016/j.matlet.2005.08.018.
- [10] D. Kiener, C. Motz, M. Rester, M. Jenko, G. Dehm, FIB damage of Cu and possible consequences for miniaturized mechanical tests, *Mater. Sci. Eng. A.* 459 (2007) 262–272. doi:10.1016/j.msea.2007.01.046.
- [11] J.R. Michael, Focused Ion Beam Induced Microstructural Alterations: Texture Development, Grain Growth, and Intermetallic Formation, *Microsc. Microanal.* 17 (2011) 386–397.
- [12] R.P. Babu, S. Irukuvarghula, A. Harte, M. Preuss, Nature of gallium focused ion beam induced phase transformation in 316L austenitic stainless steel, *Acta Mater.* 120 (2016) 391–402. doi:10.1016/j.actamat.2016.08.008.
- [13] K.E. Knipling, D.J. Rowenhorst, R.W. Fonda, G. Spanos, Effects of focused ion beam milling on austenite stability in ferrous alloys, *Mater. Charact.* 61 (2010) 1–6. doi:10.1016/j.matchar.2009.09.013.
- [14] S. Lipp, Investigations on the topology of structures milled and etched by focused ion beams, *J. Vac. Sci. Technol. B Microelectron. Nanom. Struct.* 14 (1996) 3996. doi:10.1116/1.588630.

- [15] R.M. Langford, A.K. Petford-Long, Preparation of transmission electron microscopy cross-section specimens using focused ion beam milling, *J. Vac. Sci. Technol. A Vacuum, Surfaces, Film.* 19 (2001) 2186–2193. doi:10.1116/1.1378072.
- [16] B.W. Kempshall, L. a. Giannuzzi, B.I. Prenitzer, F. a. Stevie, S.X. Da, Comparative evaluation of protective coatings and focused ion beam chemical vapor deposition processes, *J. Vac. Sci. Technol. B Microelectron. Nanom. Struct.* 20 (2002) 286. doi:10.1116/1.1445165.
- [17] M.L. Martin, B.P. Somerday, R.O. Ritchie, P. Sofronis, I.M. Robertson, Hydrogen-induced intergranular failure in nickel revisited, *Acta Mater.* 60 (2012) 2739–2745. doi:10.1016/j.actamat.2012.01.040.
- [18] S. Wang, A. Nagao, P. Sofronis, I.M. Robertson, Hydrogen-modified dislocation structures in a cyclically deformed ferritic-pearlitic low carbon steel, *Acta Mater.* 144 (2018) 164–176. doi:10.1016/j.actamat.2017.10.034.
- [19] R.P. Gangloff, H-Enhanced Deformation and Fracture in the Crack Tip Process Zone, in: B.P. Somerday, P. Sofronis (Eds.), *Mater. Perform. Hydrog. Environ. Proc. 2016 Int. Hydrog. Conf.*, ASME Press, 2016: pp. 1–35.
- [20] S. Rubanov, P.R. Munroe, FIB-induced damage in silicon, *J. Microsc.* 214 (2004) 213–221. doi:10.1111/j.0022-2720.2004.01327.x.
- [21] J.P. McCaffrey, M.W. Phaneuf, L.D. Madsen, Surface damage formation during ion-beam thinning of samples for transmission electron microscopy, *Ultramicroscopy.* 87 (2001) 97–104. doi:10.1016/S0304-3991(00)00096-6.
- [22] J. Huang, M. Loeffler, W. Moeller, E. Zschech, Ga contamination in silicon by Focused Ion Beam milling: Dynamic model simulation and Atom Probe Tomography experiment, *Microelectron. Reliab.* 64 (2016) 390–392. doi:10.1016/j.microrel.2016.07.087.
- [23] Platinum Deposition Technical Note (PN 4035 272 21851-D), Hillsboro, OR, 2007.
- [24] T. Vermeij, E. Plancher, C.C. Tasan, Preventing damage and redeposition during focused ion beam milling: The “umbrella” method, *Ultramicroscopy.* 186 (2018) 35–41. doi:10.1016/j.ultramic.2017.12.012.
- [25] K.A. Unocic, M.J. Mills, G.S. Daehn, Effect of gallium focused ion beam milling on preparation of aluminium thin foils, *J. Microsc.* 240 (2010) 227–238. doi:10.1111/j.1365-2818.2010.03401.x.
- [26] J. Papazian, E.L. Anagnostou, R.J. Christ, S.J. Engel, D. Fridline, D. Hoitsma, J. Madsen, J. Nardiello, J. Payne, R.P. Silberstein, G. Welsh, J.B. Whiteside, DARPA/NCG structural integrity

- prognosis system, HR0011-04-C-0003, DARPA, Arlington, VA, 2009.
- [27] J.T. Burns, J.M. Larsen, R.P. Gangloff, Driving forces for localized corrosion-to-fatigue crack transition in Al–Zn–Mg–Cu, *Fatigue Fract. Eng. Mater. Struct.* (2011) no-no. doi:10.1111/j.1460-2695.2011.01568.x.
- [28] J.F. Ziegler, M.D. Ziegler, J.P. Biersack, SRIM - The stopping and range of ions in matter (2010), *Nucl. Instruments Methods Phys. Res. Sect. B Beam Interact. with Mater. Atoms.* 268 (2010) 1818–1823. doi:10.1016/j.nimb.2010.02.091.
- [29] O. Yavas, C. Ochiai, M. Takai, Y.K. Park, C. Lehrer, S. Lipp, L. Frey, H. Ryssel, a. Hosono, S. Okuda, Field emitter array fabricated using focused ion and electron beam induced reaction, *J. Vac. Sci. Technol. B Microelectron. Nanom. Struct.* 18 (2000) 976. doi:10.1116/1.591310.
- [30] E. Villamor, F. Casanova, P.H.F. Trompenaars, J.J.L. Mulders, Embedded purification for electron beam induced Pt deposition using MeCpPtMe₃, *Nanotechnology.* 26 (2015). doi:10.1088/0957-4484/26/9/095303.
- [31] X. Cen, K. van Benthem, Ion beam heating of kinetically constrained nanomaterials, *Ultramicroscopy.* 186 (2018) 30–34. doi:10.1016/j.ultramic.2017.12.005.
- [32] S. Wang, A. Nagao, K. Edalati, Z. Horita, I.M. Robertson, Influence of hydrogen on dislocation self-organization in Ni, *Acta Mater.* 135 (2017) 96–102. doi:10.1016/j.actamat.2017.05.073.
- [33] Y.J. Ro, S.R. Agnew, R.P. Gangloff, Effect of Environment on Fatigue Crack Wake Dislocation Structure in Al-Cu-Mg, *Metall. Mater. Trans. A.* 43A (2012) 2275–2292. doi:DOI 10.1007/s11661-012-1089-5.
- [34] I.M. Robertson, P. Sofronis, A. Nagao, M.L. Martin, S. Wang, D.W. Gross, K.E. Nygren, Hydrogen Embrittlement Understood, *Metall. Mater. Trans. B.* (2015). doi:10.1007/s11663-015-0325-y.

Appendix II: Relevant publications and presentations

Several manuscripts are either published or in review regarding work completed to date. For brevity, the details, author contribution, and abstract for each published manuscript has been placed below for review by the committee. Full-length manuscripts for each of the listed peer-reviewed journal publications will be provided electronically. For manuscripts currently being prepared, the proposed title, likely author order, status/author contribution, and a brief description are included; these manuscripts are listed in order of completion percentage. Finally, a list of contributed conference presentations by the author is provided; this list is augmented with planned presentations that have already been accepted by the respective conference.

A2.1. Published/Submitted Peer-Reviewed Journal Articles

1. J.T. Burns, **Z.D. Harris**, J.D. Dolph, and R.P. Gangloff, “Measurement and Modeling of Hydrogen Environment-Assisted Cracking in a Ni-Cu-Al-Ti Superalloy”, *Metallurgical and Material Transactions A*, vol. 47, pp. 990-997, 2016.
 - a. **Contribution:** The author assisted in interpretation of data, performed SEM imaging, and contributed to manuscript preparation.
 - b. **Abstract:** This research improves H decohesion mechanism-based modeling of intergranular stress corrosion cracking in a Ni-Cu superalloy, Monel K-500. New cracking data plus improved model parameters lead to accurate predictions of the cathodic potential dependencies of K_{TH} and H-diffusion limited da/dt_{II} for Monel K-500 under slow-rising K in 0.6 M NaCl solution. Experiments and modeling demonstrate that IGSCC is eliminated for applied potentials more positive than a critical level between -900 mV_{SCE} and -840 mV_{SCE} , but slow-subcritical cracking persists by a microvoid-based mechanism.
2. **Z.D. Harris**, J.D. Dolph, G.L. Pioszak, B.C. Rincon Troconis, J.R. Scully, and J.T. Burns, “The Effect of Microstructure Variation on the Hydrogen Environment-Assisted Cracking of Monel K-500”, *Metallurgical and Material Transactions A*, vol. 47, pp. 3488-3510, 2016.
 - a. **Contribution:** The author performed data analysis/interpretation, conducted micromechanical modeling, performed SEM imaging, and led the writing and editing efforts on the manuscript.
 - b. **Abstract:** The influence of microstructure variation on hydrogen environment-assisted cracking (HEAC) of Monel K-500 was evaluated using five nominally peak-aged lots of material tested under slow-rising stress intensity loading while immersed in NaCl solution under cathodic polarizations. Minimal variation in HEAC resistance amongst material lots was observed for an applied potential of -950 mV_{SCE} (E_{app} , vs. saturated calomel), whereas lot-to-lot variability in the fracture morphology demonstrates a significant difference in the HEAC resistance at the less negative potential of -850 mV_{SCE} , suggesting that relatively severe H environments produce sufficient crack-tip H to minimize the impact of metallurgical differences. Sensitivity analyses accomplished by varying the inputs used in decohesion-based, micromechanical models imply significant variations in HEAC resistance are possible for realistic changes in grain boundary toughness, hydrogen uptake behavior, and yield strength. Grain size, impurity segregation (including the effects of

gettering elements), grain boundary character/connectivity, and crack path tortuosity are also considered in the context of HEAC susceptibility. Yield strength, global hydrogen content, as well as impurity segregation to grain boundaries, especially boron and sulfur, are speculatively considered to be the dominant contributions in determining HEAC resistance. Modifications that would incorporate the effects of grain boundary segregation are proposed for the K_{TH} model; detailed validation of such changes require high fidelity and quantitative inputs for the degree of grain boundary segregation. Regardless, fracture mechanics-based HEAC results, detailed microstructure characterization, and micromechanical modeling were successfully coupled to gain insights into the influences governing the microstructure-dependent HEAC susceptibility of Monel K-500.

3. S.K. Lawrence, Y. Yagodzinsky, H. Hanninen, E. Korhonen, F. Tuomisto, **Z.D. Harris**, and B.P. Somerday, “Effects of Grain Size and Deformation Temperature on Hydrogen-Enhanced Vacancy Formation in Ni Alloys”, *Acta Materialia*, vol. 128, pp. 218-226, 2017.
 - a. **Contribution:** The author assisted with mechanical testing and manuscript preparation.
 - b. **Abstract:** Positron annihilation spectroscopy and thermal desorption spectroscopy experiments were combined to ascertain the role of hydrogen on generation of vacancies and vacancy clusters in Ni alloys. The effects of grain size and deformation temperature are emphasized for pure Ni single crystals and polycrystalline Ni-201 alloy samples with two grain sizes that were thermally pre-charged with 3000 appm hydrogen. Variation in positron lifetime and intensity suggests that hydrogen enhances and stabilizes vacancies and vacancy clusters. Additionally, grain boundaries and the regions adjacent to them are preferential sites for vacancy and cluster formation. Hydrogen-altered vacancies and vacancy clusters are manifest in yield behavior differences: uniform vacancy distributions augment strength increases after hydrogen charging; enhanced yield strength during cryogenic deformation is ascribed to an ‘Orowan type’ strengthening mechanism while cross-slip restriction dominates hardening behavior at room temperature.
4. B.C. Rincon Troconis, **Z.D. Harris**, H.M. Ha, J.T. Burns, and J.R. Scully, “The Effect of Heat-to-Heat Variations in Metallurgy and Hydrogen-Metal Interactions on Hydrogen Embrittlement of Monel K-500”, *Materials Science and Engineering: A*, vol. 703, pp. 533-550, 2017.
 - a. **Contribution:** The author assisted with SEM imaging of fracture surfaces, data analysis of slow-strain rate tensile test experiments, manuscript preparation, and macroscale modeling to predict breaking stress as a function of applied potential and diffusible hydrogen concentration.
 - b. **Abstract:** The influence of heat-to-heat variations on the hydrogen embrittlement susceptibility of age-hardened Monel K-500 (UNS N05500) was evaluated through detailed characterization of metallurgical attributes and hydrogen interactions, coupled with notched tensile specimen embrittlement metrics. Four nominally peak-aged material heats of Monel K-500 were assessed using slow strain rate tensile (SSRT) testing while immersed in 0.6 M NaCl solution and exposed to cathodic polarization levels ranging from -0.850 to -1.1 VSCE. Despite each of the four heats meeting the US Federal Procurement Specification QQ-N-286G, the hydrogen embrittlement susceptibility was found to vary extensively between the tested material heats. Characterization of microstructural features, composition, and hydrogen-metal interactions were performed to facilitate correlation between material property and susceptibility trends. Results suggest that subtle differences

in grain boundary chemistry and H uptake behavior may contribute to heat-to-heat variations in hydrogen embrittlement susceptibility of Monel K-500. Conversely, parameters including yield strength, hydrogen diffusivity, hydrogen production rate, grain boundary character, and grain size do not independently control the observed variations in susceptibility. Based on these experimental results, a macroscale framework for assessing the degradation in fracture stress as a function of applied potential is proposed and possible avenues for framework improvement are suggested.

5. **Z.D. Harris**, S.K. Lawrence, D.L. Medlin, G. Guetard, J.T. Burns, and B.P. Somerday, “Elucidating the contribution of mobile hydrogen-deformation interactions to hydrogen-induced intergranular cracking in polycrystalline nickel”, *Acta Materialia*, vol. 158, pp. 180-192, 2018.
 - a. **Contribution:** The author performed mechanical testing, fractography/microscopy, analysis, interpretation, and manuscript preparation.
 - b. **Abstract:** Uniaxial mechanical testing conducted at room temperature (RT) and 77 K on hydrogen-exposed nickel was coupled with targeted microscopy to evaluate the influence of deformation temperature, and therefore mobile hydrogen (H)-deformation interactions, on intergranular cracking in nickel. Results from interrupted tensile tests conducted at cryogenic temperatures (77 K), where mobile H-deformation interactions are effectively precluded, and RT, where mobile H-deformation interactions are active, indicate that mobile H-deformation interactions are not an intrinsic requirement for hydrogen-induced intergranular fracture. Moreover, an evaluation of the true strain for intergranular microcrack initiation for testing conducted at RT and 77 K suggests that H which is segregated to grain boundaries prior to the onset of straining dominates the H-induced fracture process for the prescribed H concentration of 4000 appm. Finally, recent experiments suggesting that H-induced fracture is predominately driven by mobile H-deformation interactions, as well as the increased susceptibility of coherent twin boundaries to H-induced crack initiation, are re-examined in light of these new results.
6. A.W. Thompson, **Z.D. Harris**, and J.T. Burns, “Examination of focused ion beam-induced damage during platinum deposition in the near-surface region of an aerospace aluminum alloy”, *Micron*, in review.
 - a. **Contribution:** The author designed the study, performed transmission electron microscopy, interpreted results, performed Monte-Carlo simulations, and wrote the manuscript.
 - b. **Abstract:** It is well known that damage induced by impinging Ga⁺ ions during focused ion beam (FIB) milling of transmission electron microscopy (TEM) specimens can obfuscate subsequent TEM characterization, especially in the near-surface region of the TEM foil. Numerous strategies for minimizing this damage have been invoked, with the most common being the deposition of a Pt ‘strap’ at the area of interest. However, damage can still occur in the near-surface region during this Pt deposition step and the variation in the character and extent of this damage with applied Pt deposition parameter, especially in complex structural alloys, is not well characterized. In this study, the damage induced in an aerospace Al alloy (AA7075-T651) during five different Pt deposition protocols is examined using TEM. Results indicate extensive variations in damage character and depth amongst the applied Pt deposition protocols, with damage being effectively eliminated using a combined electron-beam/ion-beam Pt deposition strategy. Results are found to be

in good agreement with Monte Carlo-based simulations of ion implantation and the implications of these findings on recent experiments in the fracture mechanics community are explored.

A2.2. Published Peer-Reviewed Conference Proceedings

1. **Z.D. Harris**, S.K. Lawrence, G. Guetard, J.T. Burns, and B.P. Somerday, “The Influence of Deformation Temperature on the Initiation of Hydrogen-Induced Intergranular Cracking in Nickel”, in *Material Performance in Hydrogen Environments: Proceedings of the 2016 International Hydrogen Conference*, B.P. Somerday and P. Sofronis, eds., pp. 358-366.
 - a. **Contribution:** The author performed mechanical testing, fractography/microscopy, analysis, interpretation, and manuscript preparation.
 - b. **Abstract:** The influence of deformation temperature on the initiation of hydrogen-induced intergranular cracking was evaluated through testing at ambient temperature and 77 K, corresponding to conditions where hydrogen-deformation interactions are possible and effectively precluded, respectively. Uniaxial tensile testing of hydrogen-charged specimens, coupled with detailed microscopy of sectioned specimens, facilitated the assessment of the total number and cumulative length of intergranular microcracks as a function of true strain. Hydrogen-induced microcracks were found to initiate at true strains of 0.12 and 0.2 when tested at ambient temperature and 77 K, respectively. These results suggest that hydrogen segregated to the grain boundary prior to deformation dominates the initiation of hydrogen-induced intergranular microcracks, while hydrogen-deformation interactions provide an important, but ultimately secondary, contribution.
2. **Z.D. Harris** and J.T. Burns, “The Effect of Heat Treatment on Hydrogen Environment-Assisted Cracking of Monel K-500”, in *Material Performance in Hydrogen Environments: Proceedings of the 2016 International Hydrogen Conference*, B.P. Somerday and P. Sofronis, eds., pp. 367-376.
 - a. **Contribution:** The author performed alloy heat treatments and characterization, fracture mechanics experiments, data analysis, and manuscript preparation.
 - b. **Abstract:** The influence of heat treatment on hydrogen environment-assisted cracking of Monel K-500 was evaluated through slow-rising stress intensity loading of two ageing conditions while immersed in NaCl solution under cathodic polarizations. Results indicate that both the non-aged and over-aged conditions were immune to HEAC at potentials more positive than $-1000 \text{ mV}_{\text{SCE}}$, while both were susceptible at $-1200 \text{ mV}_{\text{SCE}}$. Crack growth kinetics and fractography confirm the enhanced susceptibility of the over-aged material at $-1200 \text{ mV}_{\text{SCE}}$; **K_{TH} of 16 and 17 MPa $\sqrt{\text{m}}$ and da/dt_{II} of 4×10^{-6} and $4 \times 10^{-5} \text{ mm/s}$ were observed for the non-aged and over-aged conditions, respectively.** These differences are discussed in the context of possible changes in microstructure, with particular emphasis on sulfur segregation to grain boundaries and global slip morphology.
3. **Z.D. Harris** and J.T. Burns, “The Effect of Grain Boundary Sulfur on Hydrogen Environment-Assisted Cracking of Monel K-500”, in *2017 Department of Defense-Allied Nations Technical Corrosion Conference*, Paper No. 2017-854213.
 - a. **Contribution:** The author performed alloy heat treatment and characterization, data analysis, and manuscript preparation.
 - b. **Abstract:** Monel K-500 is susceptible to hydrogen environment-assisted cracking (HEAC) when exposed to cathodic polarizations while immersed in marine environments.

Numerous studies have sought to understand the causal factors governing HEAC susceptibility in Monel K-500; recent literature has specifically focused on the influence of metallurgical variations, but only modest correlations between measured parameters and HEAC susceptibility were observed. However, macroscale results suggest that grain boundary (GB) sulfur may influence Monel K-500's resistance to HEAC. This study investigates the effect of GB sulfur on HEAC by comparing the results of previous high-fidelity fracture mechanics experiments with direct measurements of the GB sulfur concentration via Auger electron spectroscopy (AES). AES experiments were conducted on a model alloy which was heat-treated to two conditions, representing "high" and "low" GB sulfur concentrations, as well as four engineering heats obtained from different suppliers. Results suggest that while GB sulfur content may affect HEAC, it does not govern susceptibility; the influence of applied heat treatment on HEAC of Monel K-500 is discussed and critical future experiments are proposed.

A2.3. Contributed Conference Presentations

1. "Effect of Lot-to-Lot Variation on Hydrogen Environment-Assisted Cracking Susceptibility of Monel K-500", **Z.D. Harris**, J.D. Dolph, and J.T. Burns, *2015 Department of Defense – Allied Nations Technical Corrosion Conference*, Pittsburgh, PA, November 2015.
2. "Do Hydrogen-Deformation Interactions Aid Intergranular Cracking?", **Z.D. Harris**, S.K. Lawrence, J.T. Burns, and B.P. Somerday, *2016 International Hydrogen Conference*, Moran, WY, September 2016.
3. "The Influence of Microstructural Variation on the Hydrogen Environment-Assisted Cracking Susceptibility of Monel K-500", **Z.D. Harris**, B.C. Rincon Troconis, J.R. Scully, and J.T. Burns, *TMS 2017*, San Diego, CA, March 2017.
4. "The Effect of Heat Treatment on Hydrogen Environment-Assisted Cracking of Monel K-500", **Z.D. Harris** and J.T. Burns, *International Conference on Fracture (ICF14)*, Rhodes, Greece, June 2017.
5. "The Effect of Grain Boundary Sulfur on Hydrogen Environment-Assisted Cracking of Monel K-500", **Z.D. Harris** and J.T. Burns, *2017 Department of Defense – Allied Nations Technical Corrosion Conference*, Birmingham, AL, August 2017.
6. "The Effect of Heat Treatment on Hydrogen Environment-Assisted Cracking in a Ni-Cu Superalloy", **Z.D. Harris** and J.T. Burns, *3rd International Conference on Hydrogen and Metals (SteelyHydrogen 2018)*, Ghent, Belgium, May 2018. **Awarded Best Presentation/Paper of the conference.**
7. "Effect of Loading Rate on Hydrogen Environment-Assisted Cracking in Monel K-500", **Z.D. Harris**, A.S. Popernack, K. Amino, and J.T. Burns, *2018 Department of Defense – Technical Corrosion Collaboration Annual Meeting*, Hattiesburg, MS, August 2018.

8. "Characterization of near-fracture surface deformation from fatigue loading of AA7075-T651 exposed to high altitude environments", **Z.D. Harris**, A.W. Thompson, and J.T. Burns, *International Conference on Fatigue and Damage of Structural Materials XII*, Hyannis, MA, September 2018.
9. "Elucidating the role of localized deformation on hydrogen environment-assisted cracking susceptibility in a precipitation-hardened Ni-base superalloy", **Z.D. Harris** and J.T. Burns, accepted for presentation at *TMS 2019*, San Antonio, TX, March 2019.
10. "The effect of hydrogen and aging condition on the deformation and fracture behavior of a precipitation-hardened Ni-base superalloy", **Z.D. Harris**, J.J. Bhattacharyya, M.A. Ritzo, J.A. Ronevich, S.R. Agnew, and J.T. Burns, accepted for presentation at *TMS 2019*, San Antonio, TX, March 2019.
11. "Assessing the loading rate dependence of hydrogen environment-assisted cracking in a Ni-Cu superalloy", **Z.D. Harris**, A.S. Popernack, B.P. Somerday, and J.T. Burns, accepted for presentation at the *19th International ASTM/ESIS Symposium on Fatigue and Fracture Mechanics*, Denver, CO, May 2019.